

WGOTHIC Application to AP600 and AP1000



WESTINGHOUSE NON-PROPRIETARY CLASS 3

WCAP-15862
Revision 1
(Class 2 WCAP-15846 Revision 1)

WGOTHIC Application to AP600 and AP1000

**J. Woodcock, T. S. Andreychek, L. Conway, T. Elicson, A. Forgie, J. A. Gresham,
R. Haessler, T. O'Donnell, R. Ofstun, D. R. Spencer, M. Sredzienski, M. Wills**

Nuclear Safety Analysis

March 2004

Westinghouse Electric Company LLC
P.O. Box 355
Pittsburgh, PA 15230-0355

© 2004 Westinghouse Electric Company LLC
All Rights Reserved

MASTER TABLE OF CONTENTS

LIST OF TABLES xi
LIST OF FIGURES xix
LIST OF ACRONYMS AND ABBREVIATIONS xxxiii

1 INTRODUCTION

1.1 OBJECTIVE 1-1
1.2 AP600 CONTAINMENT DBA REPORTS 1-1
 1.2.1 Accident Specification and Phenomena Identification and
 Ranking Table Report 1-1
 1.2.2 Scaling Report 1-3
 1.2.3 Heat and Mass Transfer Correlations Report 1-5
 1.2.4 WGOTHIC Code Description and Validation 1-5
 1.2.5 SSAR 1-6
1.3 AP1000 CONTAINMENT DBA REPORTS 1-6
1.4 APPLICATIONS REPORT CONTENT SUMMARY 1-8
1.5 USE OF LST AND VALIDATION RESULTS 1-10
 1.5.1 LST Matrix Tests 1-11
 1.5.2 Use of LST Separate Effects Data 1-12
 1.5.3 LST Confirmation of Phenomena 1-12
 1.5.4 Code Comparison to LST as an Integral Test 1-13
 1.5.5 Lumped Parameter Biases 1-13
1.6 INTERFACE WITH DCD CALCULATIONS 1-13
 1.6.1 Upgrade of WGOTHIC Version 4.1 to Version 4.2 1-14
 1.6.2 Changes in the Evaluation Model Input 1-14
1.7 CONCLUSIONS 1-15
1.8 REFERENCES 1-15

2 TEST AND ANALYSIS PROCESS OVERVIEW AND HIGH AND MEDIUM RANKED CONTAINMENT PHENOMENA

2.1 INTRODUCTION 2-1
2.2 ELEMENT 1 - AP600 PCS REQUIREMENTS AND CODE CAPABILITIES 2-1
2.3 ELEMENT 2 - ASSESS CODE VERSUS TESTS AND IMPORTANT PROCESSES 2-3
2.4 ELEMENT 3 - ASSESS UNCERTAINTIES AND DEVELOP BOUNDING MODELS 2-6
2.5 ELEMENT 4 - PERFORM DBA CALCULATIONS AND COMPARE TO SUCCESS CRITERIA 2-7
2.6 CONCLUSIONS 2-8
2.7 REFERENCES 2-8

MASTER TABLE OF CONTENTS (cont.)

3 OVERVIEW OF WGOthic

3.1 INTRODUCTION 3-1

3.2 OVERVIEW OF THE CODE DEVELOPMENT AND VALIDATION 3-1

3.3 THE WGOthic CLIME MODEL 3-11

3.4 GENERAL CLIME EQUATIONS 3-14

3.5 INTEGRATION OF THE WESTINGHOUSE CLIME MODEL INTO GOthic 3-19

3.6 REFERENCES 3-22

4 DESCRIPTION OF AP600 PLANT GEOMETRY IN WGOthic EVALUATION MODEL

4.1 INTRODUCTION 4-1

4.2 AP600 PLANT GEOMETRY IN WGOthic MODEL 4-2

4.2.1 Reactor Cavity Description 4-4

4.2.2 Reactor Coolant Drain Tank (RCDT) Cavity Description 4-13

4.2.3 Southeast Accumulator Cavity 4-19

4.2.4 Northeast Accumulator Cavity 4-25

4.2.5 East Steam Generator Cavity (Upper and Lower) 4-30

4.2.6 West Steam Generator Cavity (Upper and Lower) 4-39

4.2.7 North CMT Cavity 4-48

4.2.8 South CMT Cavity 4-61

4.2.9 Chemical and Volume Control Cavity 4-69

4.2.10 Refueling Room 4-75

4.2.11 Internal Refueling Water Storage Tank (IRWST) 4-82

4.2.12 Cylindrical Central Room 4-89

4.2.13 Above-Deck East Steam Generator Compartment 4-95

4.2.14 Above-Deck West Steam Generator Compartment 4-102

4.2.15 South Inner-Half Annulus Compartment 4-109

4.2.16 North Inner-Half Annulus Compartment 4-116

4.2.17 North Mid-Quarter Annulus Compartment 4-123

4.2.18 West Mid-Quarter Annulus Compartment 4-131

4.2.19 South Mid-Quarter Annulus Compartment 4-140

4.2.20 East Mid-Quarter Annulus Compartment 4-147

4.2.21 North Outer Quarter Annulus Compartment 4-154

4.2.22 West Outer Quarter Annulus Compartment 4-161

4.2.23 South Outer Quarter Annulus Compartment 4-168

4.2.24 East Outer Quarter Annulus Compartment 4-175

4.2.25 East Quarter Inner Dome Compartment 4-182

4.2.26 North Quarter Inner Dome Compartment 4-186

4.2.27 West Quarter Inner Dome Compartment 4-190

MASTER TABLE OF CONTENTS (cont.)

| | | |
|-------------|---|-------|
| 4.2.28 | South Quarter Inner Dome Compartment | 4-192 |
| 4.2.29 | East Quarter Outer Dome Compartment | 4-199 |
| 4.2.30 | North Quarter Outer Dome Compartment | 4-203 |
| 4.2.31 | West Quarter Outer Dome Compartment | 4-207 |
| 4.2.32 | South Quarter Outer Dome Compartment | 4-211 |
| 4.2.33 | Outside Containment Upflow Annulus Volumes | 4-215 |
| 4.2.34 | Outside Containment Downflow Annulus Volumes | 4-220 |
| 4.2.35 | PCS Chimney Volume | 4-224 |
| 4.3 | CONDUCTOR TYPE DESCRIPTIONS | 4-226 |
| 4.4 | CLIME NODING DESCRIPTION | 4-244 |
| 4.4.1 | Wet Stacks | 4-244 |
| 4.4.2 | Dry Stacks | 4-260 |
| 4.4.3 | Passive Cooling System Flow | 4-272 |
| 4.4.4 | Condensate Film Stripping | 4-274 |
| 4.5 | INITIAL AND BOUNDARY CONDITIONS | 4-274 |
| 4.5.1 | Initial Conditions | 4-274 |
| 4.5.2 | Boundary Conditions | 4-291 |
| 4.5.3 | Conclusions | 4-294 |
| 4.6 | AP600 CONTAINMENT EVALUATION MODEL SUMMARY | 4-297 |
| 4.7 | SUMMARY OF EVALUATION MODEL TRANSIENT CALCULATIONS | 4-319 |
| 4.7.1 | LOCA Evaluation Model Base Case Results Summary | 4-319 |
| 4.7.2 | MSLB Evaluation Model Base Case Results Summary | 4-324 |
| 4.8 | REFERENCES | 4-353 |
| APPENDIX 4A | AP600 PLANT GEOMETRY UPDATE | 4A-1 |
| APPENDIX 4B | WGOthic EVALUATION MODEL HEAT SINK CHANGES FOR ITAAC | 4B-1 |
| 5 | INITIAL AND BOUNDARY CONDITIONS | |
| 5.1 | INTRODUCTION | 5-1 |
| 5.2 | INITIAL CONDITION SENSITIVITY CASES | 5-1 |
| 5.3 | INITIAL CONTAINMENT HUMIDITY | 5-3 |
| 5.4 | INITIAL CONTAINMENT PRESSURE | 5-4 |
| 5.5 | INITIAL CONTAINMENT TEMPERATURE | 5-9 |
| 5.6 | AMBIENT HUMIDITY | 5-12 |
| 5.7 | AMBIENT TEMPERATURE | 5-15 |
| 5.8 | SENSITIVITY TO DROP MODELING ASSUMPTIONS | 5-20 |
| 5.9 | CONCLUSIONS | 5-20 |

MASTER TABLE OF CONTENTS (cont.)

6 METEOROLOGICAL EFFECTS ON PCS PERFORMANCE 6-1

6.1 INTRODUCTION 6-1

6.2 WIND-INDUCED TURBULENCE 6-1

6.2.1 Summary of Wind Tunnel Tests 6-1

6.2.2 Tracking of a Wind-Driven Particle 6-3

6.2.3 Containment Time Constants 6-3

6.2.4 Wind-Induced Oscillation Effect on Heat Transfer Coefficient 6-5

6.2.5 WGOTHIC Evaluation Model Basis 6-5

6.3 RECIRCULATION OF CHIMNEY EFFLUENT 6-7

6.3.1 Summary of Literature Review 6-7

6.3.2 Evaluation of Effect of Recirculation 6-8

6.3.3 WGOTHIC Evaluation Model Basis 6-9

6.4 CONCLUSIONS 6-10

6.5 REFERENCES 6-10

7 BASIS AND METHOD FOR CALCULATING THE PCS WATER EVAPORATION
RATE FOR THE AP600 AND AP1000 CONTAINMENT DBA EVALUATION MODELS

7.1 INTRODUCTION 7-1

7.2 WATER APPLICATION AND DISTRIBUTION 7-3

7.2.1 Containment Shell Surface Coating 7-3

7.2.2 PCS Water Distribution Weir Description and Operation 7-5

7.2.3 PCS Water Distribution Testing Results 7-8

7.2.4 Delivered PCS Water Flow Rate versus Time 7-10

7.2.5 Time to Establish Steady State Water Coverage 7-10

7.3 WATER COVERAGE BASIS 7-14

7.3.1 Water Distribution Film Flow Rate, Γ_{dist} 7-14

7.3.2 Minimum Film Flow Rate, Γ_{min} 7-16

7.4 EFFECT OF TWO-DIMENSIONAL (2-D) HEAT CONDUCTION
THROUGH THE CONTAINMENT SHELL 7-18

7.4.1 Geometry of the Wet and Dry Vertical Stripes on the
Containment Outside Steel Surface 7-18

7.4.2 Inside and Outside Heat Transfer Boundary Conditions for the
Conduction Model 7-19

7.4.3 2-D Conduction (ANSYS) Model Description 7-20

7.4.4 Enhanced Evaporation due to 2-D Conduction 7-21

7.4.5 Insights from the PCS Large-Scale Testing 7-21

MASTER TABLE OF CONTENTS (cont.)

| | | |
|-------|---|------|
| 7.5 | THE CONTAINMENT EVALUATION MODEL TREATMENT OF WATER COVERAGE | 7-31 |
| 7.5.1 | PCS Film Coverage Model | 7-31 |
| 7.5.2 | WGOthic Model | 7-36 |
| 7.6 | SUMMARY OF SUPPORTING TESTS AND SELECTED ANALYSIS | 7-39 |
| 7.6.1 | Westinghouse Wet Flat Plate Test | 7-39 |
| 7.6.2 | Small-Scale Tests | 7-39 |
| 7.6.3 | Large-Scale Tests (LSTs) | 7-40 |
| 7.6.4 | Estimated Range of Film Coverage Parameters | 7-49 |
| 7.6.5 | Containment Shell Heatup Analysis | 7-51 |
| 7.7 | AP600 CONTAINMENT DBA EVALUATION MODEL FILM COVERAGE SENSITIVITIES | 7-54 |
| 7.7.1 | Sensitivity of the Evaluation Model to the Input PCS Film Flow Rate | 7-54 |
| 7.7.2 | Sensitivity to the Water Coverage Area | 7-54 |
| 7.7.3 | Conservatism in the Assumed Time Delay for Application of the PCS Film | 7-60 |
| 7.8 | CONCLUSIONS AND SUMMARY | 7-63 |
| 7.9 | NOMENCLATURE | 7-65 |
| 7.10 | REFERENCES | 7-66 |
| | APPENDIX 7A PHYSICS OF LIQUID FILMS ON THE AP600 CONTAINMENT SHELL | 7A-1 |
| 8 | CONTAINMENT PRESSURE SENSITIVITY DURING BLOWDOWN | |
| 8.1 | INTRODUCTION | 8-1 |
| 8.2 | METHOD | 8-1 |
| 8.3 | ANALYSIS | 8-2 |
| 8.4 | CONCLUSIONS | 8-2 |
| 9 | CIRCULATION AND STRATIFICATION WITHIN CONTAINMENT | |
| 9.1 | INTRODUCTION | 9-4 |
| 9.1.1 | Definitions | 9-14 |
| 9.1.2 | Lumped Parameter Biases and Capabilities | 9-14 |
| 9.2 | LARGE-SCALE TEST RESULTS | 9-17 |
| 9.2.1 | LOCA Configuration | 9-18 |
| 9.2.2 | MSLB Configuration | 9-19 |
| 9.2.3 | Method to Address Distortions in LST Stratification Data | 9-20 |
| 9.2.4 | Application of Modeling Methods Developed for NUPEC M-4-3 Lumped Parameter Model | 9-22 |

MASTER TABLE OF CONTENTS (cont.)

| | | |
|--------------|--|-------|
| 9.3 | CIRCULATION AND STRATIFICATION ASSESSMENT FOR THE LOSS-OF-COOLANT ACCIDENT | 9-26 |
| 9.3.1 | LOCA Break Scenarios | 9-27 |
| 9.3.2 | <u>W</u> GOTHIC Containment Evaluation Model for LOCA | 9-34 |
| 9.4 | MAIN STEAMLINE BREAK (MSLB) | 9-44 |
| 9.4.1 | Break Locations | 9-44 |
| 9.4.2 | <u>W</u> GOTHIC Containment Evaluation Model for MSLB | 9-45 |
| 9.4.3 | MSLB Sensitivity Results | 9-46 |
| 9.5 | CONCLUSIONS | 9-48 |
| 9.6 | REFERENCES | 9-50 |
| APPENDIX 9.A | THERMAL AND CIRCULATION EFFECTS OF DROPS DURING A LOCA | 9.A-1 |
| APPENDIX 9.B | EFFECTS OF STRATIFICATION ON HEAT SINK UTILIZATION | 9.B-1 |
| APPENDIX 9.C | ADDITIONAL INFORMATION ON CONTAINMENT CIRCULATION AND STRATIFICATION | 9.C-1 |
| APPENDIX 9.D | BASIS FOR ASSUMING HOMOGENEOUS BULK CONDITIONS FOR AP600 AND AP1000 CONTAINMENT PRESSURE DESIGN BASIS ANALYSIS | 9.D-1 |
| 10 | NOMINAL INPUTS AND CORRELATIONS SENSITIVITIES | |
| 10.1 | INTRODUCTION | 10-1 |
| 10.2 | SENSITIVITY STUDY RESULTS | 10-1 |
| 10.2.1 | Sensitivity Study Cases for LOCA | 10-5 |
| 10.2.2 | Sensitivity Study Case for MSLB | 10-10 |
| 10.3 | CONCLUSIONS | 10-10 |
| 10.4 | REFERENCES | 10-11 |
| 11 | TIMESTEP SENSITIVITY | |
| 11.1 | INTRODUCTION | 11-1 |
| 11.2 | METHODOLOGY | 11-1 |
| 11.3 | RESULTS | 11-2 |
| 11.4 | SUMMARY | 11-3 |
| 11.5 | REFERENCES | 11-6 |

MASTER TABLE OF CONTENTS (cont.)

12 SENSITIVITY TO CLIME NODING

- 12.1 INTRODUCTION 12-1
 - 12.1.1 Background 12-1
 - 12.1.2 Problem Statement 12-3
 - 12.1.3 Approach 12-3
 - 12.1.4 Selected Parameters 12-4
 - 12.1.5 Success Criteria 12-4
- 12.2 MODEL DESCRIPTIONS 12-5
 - 12.2.1 Simple Annulus Clime Model 12-5
 - 12.2.2 AP600 Containment Model 12-7
- 12.3 RESULTS 12-8
 - 12.3.1 Simple Annulus Clime Model 12-8
 - 12.3.2 AP600 Containment Model 12-10
- 12.4 SUMMARY 12-12
 - 12.4.1 Simple Annulus Clime Model Noding Study 12-12
 - 12.4.2 AP600 Containment Model Clime Noding Study 12-12
- 12.5 REFERENCES 12-12

13 DESCRIPTION OF AP1000 PLANT GEOMETRY IN WGOTHIC EVALUATION MODEL

- 13.1 INTRODUCTION 13-1
- 13.2 AP1000 PLANT GEOMETRY IN WGOTHIC MODEL 13-3
 - 13.2.1 Reactor Cavity Description 13-7
 - 13.2.2 Reactor Coolant Drain Tank (RCDT) Cavity Description 13-13
 - 13.2.3 Southeast Accumulator Cavity 13-19
 - 13.2.4 Northeast Accumulator Cavity 13-24
 - 13.2.5 East Steam Generator Cavity (Upper and Lower) 13-29
 - 13.2.6 West Steam Generator Cavity (Upper and Lower) 13-38
 - 13.2.7 North CMT Cavity 13-46
 - 13.2.8 South CMT Cavity 13-58
 - 13.2.9 Chemical and Volume Control Cavity 13-67
 - 13.2.10 Refueling Room 13-74
 - 13.2.11 Internal Refueling Water Storage Tank (IRWST) 13-81
 - 13.2.12 Cylindrical Central Rooms 13-89
 - 13.2.13 Above-Deck East Steam Generator Compartment 13-94
 - 13.2.14 Above-Deck West Steam Generator Compartment 13-101
 - 13.2.15 South Inner-Half Annulus Compartment 13-108
 - 13.2.16 North Inner-Half Annulus Compartment 13-114
 - 13.2.17 North Mid-Quarter Annulus Compartment 13-122
 - 13.2.18 West Mid-Quarter Annulus Compartment 13-130
 - 13.2.19 South Mid-Quarter Annulus Compartment 13-137

MASTER TABLE OF CONTENTS (cont.)

13.2.20 East Mid-Quarter Annulus Compartment 13-144
13.2.21 North Outer Quarter Annulus Compartment 13-150
13.2.22 West Outer Quarter Annulus Compartment 13-157
13.2.23 South Outer Quarter Annulus Compartment 13-164
13.2.24 East Outer Quarter Annulus Compartment 13-171
13.2.25 East Quarter Inner Dome Compartment 13-178
13.2.26 North Quarter Inner Dome Compartment 13-182
13.2.27 West Quarter Inner Dome Compartment 13-186
13.2.28 South Quarter Inner Dome Compartment 13-188
13.2.29 East Quarter Outer Dome Compartment 13-195
13.2.30 North Quarter Outer Dome Compartment 13-199
13.2.31 West Quarter Outer Dome Compartment 13-203
13.2.32 South Quarter Outer Dome Compartment 13-207
13.2.33 Outside Containment Upflow Annulus Volumes 13-211
13.2.34 Outside Containment Downflow Annulus Volumes 13-216
13.2.35 PCS Chimney Volume 13-220
13.3 CONDUCTOR TYPE DESCRIPTIONS 13-222
13.4 CLIME NODING DESCRIPTION 13-253
13.4.1 Wet Stacks 13-253
13.4.2 Dry Stacks 13-271
13.4.3 Passive Cooling System Flow 13-286
13.4.4 Condensate Film Stripping 13-289
13.5 INITIAL AND BOUNDARY CONDITIONS 13-289
13.5.1 Initial Conditions 13-289
13.5.2 Boundary Conditions 13-304
13.5.3 Conclusions 13-307
13.6 AP1000 CONTAINMENT EVALUATION MODEL SUMMARY 13-310
13.7 SUMMARY OF EVALUATION MODEL TRANSIENT CALCULATIONS 13-334
13.7.1 LOCA Transient Response Results Summary 13-334
13.7.2 MSLB Transient Response Results Summary 13-335
13.8 WGOthic CONTAINMENT MINIMUM PRESSURE CALCULATION
FOR SMALL-BREAK LOCA AND LONG-TERM COOLING 13-343
13.9 REFERENCES 13-346

14 LOCA MASS AND ENERGY RELEASE CALCULATION METHODOLOGY
14.1 INTRODUCTION 14-1
14.2 BLOWDOWN MASS AND ENERGY RELEASE CALCULATION 14-2
14.3 POST-BLOWDOWN MASS AND ENERGY RELEASE CALCULATION 14-2
14.4 COMPARISON OF SATAN/SPREADSHEET RELEASES WITH
WCOBRA-TRAC CALCULATED RELEASES 14-9
14.5 SUMMARY AND CONCLUSIONS 14-14
14.6 REFERENCES 14-14

LIST OF TABLES

| | | |
|------------|--|-------|
| Table 2-1 | Phenomena Identification and Ranking Table - Summary of High and Medium Ranked Phenomena | 2-4 |
| Table 3-1 | GOTHIC Validation Tests | 3-5 |
| Table 3-2 | GOTHIC Phenomenological Models Validated by Test | 3-6 |
| Table 3-3 | Operating Range Comparison for AP600 and AP1000 Heat and Mass Transfer Parameters | 3-10 |
| Table 4-1 | Central Cylindrical Room Parameters | 4-90 |
| Table 4-2 | Flow Paths for the Cylindrical Central Volumes | 4-91 |
| Table 4-3 | Above-Deck East Steam Generator Compartment Parameters | 4-95 |
| Table 4-4 | Flow Paths for the Above-Deck East Steam Generator Volumes | 4-96 |
| Table 4-5 | Above-Deck West Steam Generator Compartment Parameters | 4-102 |
| Table 4-6 | Flow Paths for the Above-Deck West Steam Generator Volumes | 4-103 |
| Table 4-7 | South Inner-Half Annulus Compartment Parameters | 4-109 |
| Table 4-8 | Flow Paths for the South Inner-Half Annulus Volumes | 4-110 |
| Table 4-9 | North Inner-Half Annulus Compartment Parameters | 4-116 |
| Table 4-10 | Flow Paths for the North Inner-Half Annulus Volumes | 4-117 |
| Table 4-11 | North Mid-Quarter Annulus Compartment Parameters | 4-124 |
| Table 4-12 | Flow Paths for the North Mid-Quarter Annulus Volumes | 4-125 |
| Table 4-13 | West Mid-Quarter Annulus Compartment Parameters | 4-132 |
| Table 4-14 | Flow Paths for the West Mid-Quarter Annulus Volumes | 4-133 |
| Table 4-15 | South Mid-Quarter Annulus Compartment Parameters | 4-140 |
| Table 4-16 | Flow Paths for the South Mid-Quarter Annulus Volumes | 4-146 |
| Table 4-17 | East Mid-Quarter Annulus Compartment Parameters | 4-147 |
| Table 4-18 | Flow Paths for the East Mid-Quarter Annulus Volumes | 4-148 |
| Table 4-19 | North Outer Quarter Annulus Compartment Parameters | 4-154 |
| Table 4-20 | Flow Paths for the North Outer Quarter Annulus Volumes | 4-156 |
| Table 4-21 | West Outer Quarter Annulus Compartment Parameters | 4-162 |
| Table 4-22 | Flow Paths for the West Outer Quarter Annulus Volumes | 4-163 |
| Table 4-23 | South Outer Quarter Annulus Compartments Parameters | 4-169 |
| Table 4-24 | Flow Paths for the South Outer Quarter Annulus Volumes | 4-170 |
| Table 4-25 | East Outer Quarter Annulus Compartment Parameters | 4-176 |
| Table 4-26 | Flow Paths for the East Outer Quarter Annulus Volumes | 4-177 |
| Table 4-27 | East Quarter Inner Dome Compartment Parameters | 4-182 |
| Table 4-28 | Flow Paths for the East Quarter Inner Dome Volumes | 4-183 |
| Table 4-29 | North Quarter Inner Dome Compartment Parameters | 4-187 |
| Table 4-30 | Flow Paths for the North Quarter Inner Dome Volumes | 4-187 |
| Table 4-31 | West Quarter Inner Dome Compartment Parameters | 4-190 |
| Table 4-32 | Flow Paths for the West Quarter Inner Dome Volumes | 4-193 |
| Table 4-33 | South Quarter Inner Dome Compartment Parameters | 4-195 |

LIST OF TABLES (cont.)

| | | |
|------------|---|-------|
| Table 4-34 | Flow Paths for the South Quarter Inner Dome Volumes | 4-196 |
| Table 4-35 | East Quarter Outer Dome Compartment Parameters | 4-199 |
| Table 4-36 | Flow Paths for the East Quarter Outer Dome Volumes | 4-200 |
| Table 4-37 | North Quarter Outer Dome Compartment Parameters | 4-203 |
| Table 4-38 | Flow Paths for the North Quarter Outer Dome Volumes | 4-204 |
| Table 4-39 | West Quarter Outer Dome Compartment Parameters | 4-207 |
| Table 4-40 | Flow Paths for the West Quarter Outer Dome Volumes | 4-208 |
| Table 4-41 | South Quarter Outer Dome Compartment Parameters | 4-211 |
| Table 4-42 | Flow Paths for the South Quarter Outer Dome Volumes | 4-212 |
| Table 4-43 | Outside Containment Upflow Annulus Volume Parameters | 4-215 |
| Table 4-44 | Flow Paths for the Outside Containment Upflow Annulus | 4-216 |
| Table 4-45 | Outside Containment Downflow Annulus Volume Parameters | 4-220 |
| Table 4-46 | Flow Paths for the Outside Containment Downflow Annulus | 4-221 |
| Table 4-47 | PCS Chimney Volume Parameters | 4-224 |
| Table 4-48 | Flow Paths for the PCS Chimney | 4-224 |
| Table 4-49 | Conductor Material Properties | 4-227 |
| Table 4-50 | Conductor 1 – 0.1" Thick Carbon Steel | 4-227 |
| Table 4-51 | Conductor 2 – 0.03" Thick Carbon Steel | 4-229 |
| Table 4-52 | Conductor 3 – 0.06" Thick Carbon Steel | 4-229 |
| Table 4-53 | Conductor 4 – 0.105" Thick Carbon Steel | 4-229 |
| Table 4-54 | Conductor 5 – 0.1007" Thick Carbon Steel | 4-229 |
| Table 4-55 | Conductor 6 – 0.1044" Thick Carbon Steel | 4-230 |
| Table 4-56 | Conductor 7 – 0.158" Thick Carbon Steel | 4-230 |
| Table 4-57 | Conductor 8 – 0.132" Thick Carbon Steel | 4-230 |
| Table 4-58 | Conductor 9 – 0.210" Thick Carbon Steel | 4-230 |
| Table 4-59 | Conductor 10 – 0.2448" Thick Carbon Steel | 4-231 |
| Table 4-60 | Conductor 11 – 0.252" Thick Stainless Steel | 4-231 |
| Table 4-61 | Conductor 12 – 0.252" Thick Carbon Steel | 4-231 |
| Table 4-62 | Conductor 13 – 0.284" Thick Carbon Steel | 4-231 |
| Table 4-63 | Conductor 14 – 0.404" Thick Carbon Steel | 4-232 |
| Table 4-64 | Conductor 15 – 0.504" Thick Stainless Steel | 4-232 |
| Table 4-65 | Conductor 16 – 0.854" Thick Carbon Steel | 4-232 |
| Table 4-66 | Conductor 17 – 0.996" Thick Stainless Steel | 4-232 |
| Table 4-67 | Conductor 18 – 0.81" Thick Carbon Steel | 4-233 |
| Table 4-68 | Conductor 19 – 1.57" Thick Carbon Steel | 4-233 |
| Table 4-69 | Conductor 20 – 1.63" Thick Carbon Steel | 4-233 |
| Table 4-70 | Conductor 21 – 1.754" Thick Carbon Steel | 4-233 |
| Table 4-71 | Conductor 22 – 1.998" Thick Carbon Steel | 4-234 |
| Table 4-72 | Conductor 23 – 3.014" Thick Carbon Steel | 4-234 |

LIST OF TABLES (cont.)

| | | |
|-------------|--|-------|
| Table 4-73 | Conductor 24 – 4.399" Thick Stainless Steel | 4-234 |
| Table 4-74 | Conductor 25 – 4.874" Thick Carbon Steel | 4-234 |
| Table 4-75 | Conductor 26 – 3.0" Thick Stainless Steel | 4-235 |
| Table 4-76 | Conductor 27 – 25.04" Thick Concrete | 4-235 |
| Table 4-77 | Conductor 28 – 25.0" Thick Concrete | 4-235 |
| Table 4-78 | Conductor 29 – 25.0" Thick Concrete | 4-236 |
| Table 4-79 | Conductor 30 – 36.0" Thick Concrete | 4-236 |
| Table 4-80 | Conductor 31 – 25.0" Thick Concrete | 4-236 |
| Table 4-81 | Conductor 32 – 24.5" Thick Concrete | 4-237 |
| Table 4-82 | Conductor 33 – 24.5" Thick Concrete | 4-237 |
| Table 4-83 | Conductor 34 – 24.5" Thick Concrete | 4-237 |
| Table 4-84 | Conductor 35 – 24.5" Thick Concrete | 4-238 |
| Table 4-85 | Conductor 36 – 24.0" Thick Concrete | 4-238 |
| Table 4-86 | Conductor 37 – 49.0" Thick Concrete | 4-238 |
| Table 4-87 | Conductor 38 – 48.5" Thick Concrete | 4-239 |
| Table 4-88 | Conductor 39 – 48.5" Thick Concrete | 4-239 |
| Table 4-89 | Conductor 40 – 48.5" Thick Carbon Steel | 4-239 |
| Table 4-90 | Conductor 41 – 49.0" Thick Concrete | 4-240 |
| Table 4-91 | Conductor 42 – 48.0" Thick Concrete | 4-240 |
| Table 4-92 | Conductor 43 – 48.5" Thick Concrete | 4-240 |
| Table 4-93 | Conductor 44 – 48.5" Thick Concrete | 4-241 |
| Table 4-94 | Conductor 45 – 48.0" Thick Concrete | 4-241 |
| Table 4-95 | Conductor 46 – 49.0" Thick Concrete | 4-241 |
| Table 4-96 | Conductor 47 – 49.0" Thick Concrete | 4-242 |
| Table 4-97 | Conductor 48 – 49.0" Thick Concrete | 4-242 |
| Table 4-98 | Conductor 49 – 25.0" Thick Concrete | 4-242 |
| Table 4-99 | Conductor 50 – 48.5" Thick Concrete | 4-243 |
| Table 4-100 | Conductor 51 – 2.0" Thick Carbon Steel | 4-243 |
| Table 4-101 | Conductor 52 – Dummy Baffle | 4-243 |
| Table 4-102 | Evaluation Model Function for the AP600 PCS Film Flow | 4-272 |
| Table 4-103 | Outside Containment Initial Conditions | 4-275 |
| Table 4-104 | Inside Containment Initial Conditions | 4-276 |
| Table 4-105 | LOCA Boundary Conditions Represented by Forcing Functions in the AP600 Evaluation Model | 4-277 |
| Table 4-106 | MSLB Boundary Conditions Represented by Forcing Functions in the AP600 Evaluation Model | 4-277 |
| Table 4-107 | Basis for Geometric Inputs | 4-294 |
| Table 4-108 | Basis for LOCA and MSLB Mass and Energy Inputs | 4-295 |
| Table 4-109 | Basis for PCS Inputs | 4-296 |

LIST OF TABLES (cont.)

| | | |
|-------------|--|--------|
| Table 4-110 | Summary of Containment Volumes and Heat Sinks Model Node Listing | 4-298 |
| Table 4-111 | Master List of Flow Paths in AP600 Evaluation Model | 4-300 |
| Table 5-1 | Initial Conditions | 5-1 |
| Table 5-2 | Initial Conditions Sensitivity Analysis Cases | 5-2 |
| Table 5-3 | Summary of Pressure Results for LOCA Initial Condition Sensitivity Studies | 5-3 |
| Table 5-4 | Summary of Pressure Results for MSLB Initial Condition Sensitivity Studies | 5-3 |
| Table 7-1 | Ranges of the Film Coverage Parameters in the PCS Tests | 7-4 |
| Table 7-2 | Summary of the Phase 3 Water Distribution Test | 7-9 |
| Table 7-3 | Elevation D Heat Flux Comparison From PCS Large-Scale Tests RC048C and RC050C | 7-29 |
| Table 7-4 | Elevation E Heat Flux Comparison From PCS Large-Scale Tests RC048C and RC050C | 7-30 |
| Table 7-5 | Clime Wetted Perimeter and Basis for <u>W</u> GOTHIC Model | 7-37 |
| Table 7-6 | Summary of STC Heated Flat Plate Tests | 7-41 |
| Table 7-7 | Summary of Small-Scale Tests | 7-43 |
| Table 7-8 | Summary of Large-Scale Tests | 7-47 |
| Table 7-9 | Estimated Shell Heat Flux and Film Temperature | 7-50 |
| Table 7-10 | Comparison of the Range of Film Coverage Parameters | 7-51 |
| Table 7-11 | Transient Dry Shell Temperature Increase | 7-53 |
| Table 9-1 | Circulation and Stratification Evaluation Summary | 9-5 |
| Table 9-2 | AP600 Flow Areas Connecting to North and South CMT Compartments (excluding Dead-Ended Compartment Connections) | 9-24 |
| Table 10-1 | Nominal Inputs and Correlations Sensitivity Results | 10-2 |
| Table 11-1 | Timestep Sensitivity Results | 11-2 |
| Table 11-2 | Timestep Limit Results | 11-3 |
| Table 12-1 | Input Parameters for Annulus Clime Model Sensitivity Study | 12-6 |
| Table 12-2 | Predicted Heat Removal Rates for Various Clime Noding Schemes | 12-9 |
| Table 13-1 | Central Cylindrical Room Parameters | 13-89 |
| Table 13-2 | Flow Paths for the Cylindrical Central Volumes | 13-93 |
| Table 13-3 | Above-Deck East Steam Generator Compartment Parameters | 13-94 |
| Table 13-4 | Flow Paths for the Above-Deck East Steam Generator Volumes | 13-95 |
| Table 13-5 | Above-Deck West Steam Generator Compartment Parameters | 13-101 |
| Table 13-6 | Flow Paths for the Above-Deck West Steam Generator Volumes | 13-102 |
| Table 13-7 | South Inner-Half Annulus Compartment Parameters | 13-108 |
| Table 13-8 | Flow Paths for the South Inner-Half Annulus Volumes | 13-109 |
| Table 13-9 | North Inner-Half Annulus Compartment Parameters | 13-115 |
| Table 13-10 | Flow Paths for the North Inner-Half Annulus Volumes | 13-116 |
| Table 13-11 | North Mid-Quarter Annulus Compartment Parameters | 13-123 |
| Table 13-12 | Flow Paths for the North Mid-Quarter Annulus Volumes | 13-124 |

LIST OF TABLES (cont.)

| | | |
|-------------|---|--------|
| Table 13-13 | West Mid-Quarter Annulus Compartment Parameters | 13-130 |
| Table 13-14 | Flow Paths for the West Mid-Quarter Annulus Volumes | 13-131 |
| Table 13-15 | South Mid-Quarter Annulus Compartment Parameters | 13-138 |
| Table 13-16 | Flow Paths for the South Mid-Quarter Annulus Volumes | 13-139 |
| Table 13-17 | East Mid-Quarter Annulus Compartment Parameters | 13-144 |
| Table 13-18 | Flow Paths for the East Mid-Quarter Annulus Volumes | 13-145 |
| Table 13-19 | North Outer Quarter Annulus Compartment Parameters | 13-151 |
| Table 13-20 | Flow Paths for the North Outer Quarter Annulus Volumes | 13-152 |
| Table 13-21 | West Outer Quarter Annulus Compartment Parameters | 13-158 |
| Table 13-22 | Flow Paths for the West Outer Quarter Annulus Volumes | 13-159 |
| Table 13-23 | South Outer Quarter Annulus Compartments Parameters | 13-165 |
| Table 13-24 | Flow Paths for the South Outer Quarter Annulus Volumes | 13-166 |
| Table 13-25 | East Outer Quarter Annulus Compartment Parameters | 13-172 |
| Table 13-26 | Flow Paths for the East Outer Quarter Annulus Volumes | 13-173 |
| Table 13-27 | East Quarter Inner Dome Compartment Parameters | 13-178 |
| Table 13-28 | Flow Paths for the East Quarter Inner Dome Volumes | 13-180 |
| Table 13-29 | North Quarter Inner Dome Compartment Parameters | 13-183 |
| Table 13-30 | Flow Paths for the North Quarter Inner Dome Volumes | 13-183 |
| Table 13-31 | West Quarter Inner Dome Compartment Parameters | 13-186 |
| Table 13-32 | Flow Paths for the West Quarter Inner Dome Volumes | 13-189 |
| Table 13-33 | South Quarter Inner Dome Compartment Parameters | 13-191 |
| Table 13-34 | Flow Paths for the South Quarter Inner Dome Volumes | 13-192 |
| Table 13-35 | East Quarter Outer Dome Compartment Parameters | 13-195 |
| Table 13-36 | Flow Paths for the East Quarter Outer Dome Volumes | 13-196 |
| Table 13-37 | North Quarter Outer Dome Compartment Parameters | 13-199 |
| Table 13-38 | Flow Paths for the North Quarter Outer Dome Volumes | 13-200 |
| Table 13-39 | West Quarter Outer Dome Compartment Parameters | 13-203 |
| Table 13-40 | Flow Paths for the West Quarter Outer Dome Volumes | 13-204 |
| Table 13-41 | South Quarter Outer Dome Compartment Parameters | 13-207 |
| Table 13-42 | Flow Paths for the South Quarter Outer Dome Volumes | 13-208 |
| Table 13-43 | Outside Containment Upflow Annulus Volume Parameters | 13-211 |
| Table 13-44 | Flow Paths for the Outside Containment Upflow Annulus | 13-212 |
| Table 13-45 | Outside Containment Downflow Annulus Volume Parameters | 13-216 |
| Table 13-46 | Flow Paths for the Outside Containment Downflow Annulus | 13-217 |
| Table 13-47 | PCS Chimney Volume Parameters | 13-220 |
| Table 13-48 | Flow Paths for the PCS Chimney | 13-220 |
| Table 13-49 | Conductor Material Properties | 13-222 |
| Table 13-50 | Conductor 1 – 0.1" Thick Carbon Steel | 13-224 |
| Table 13-51 | Conductor 2 – 0.024" Thick Carbon Steel | 13-224 |

LIST OF TABLES (cont.)

| | | |
|-------------|---|--------|
| Table 13-52 | Conductor 3 – 0.124" Thick Carbon Steel | 13-224 |
| Table 13-53 | Conductor 4 – 0.20944" Thick Carbon Steel | 13-224 |
| Table 13-54 | Conductor 5 – 0.1007" Thick Carbon Steel | 13-225 |
| Table 13-55 | Conductor 6 – 0.2088" Thick Carbon Steel | 13-225 |
| Table 13-56 | Conductor 7 – 0.292" Thick Carbon Steel | 13-225 |
| Table 13-57 | Conductor 8 – 0.288" Thick Carbon Steel | 13-225 |
| Table 13-58 | Conductor 9 – 0.5056" Thick Carbon Steel | 13-226 |
| Table 13-59 | Conductor 10 – 0.4896" Thick Carbon Steel | 13-226 |
| Table 13-60 | Conductor 11 – 0.504" Thick Stainless Steel | 13-226 |
| Table 13-61 | Conductor 12 – 0.504" Thick Carbon Steel | 13-226 |
| Table 13-62 | Conductor 13 – 0.6112" Thick Carbon Steel | 13-227 |
| Table 13-63 | Conductor 14 – 0.404" Thick Carbon Steel | 13-227 |
| Table 13-64 | Conductor 15 – 0.504" Thick Stainless Steel | 13-227 |
| Table 13-65 | Conductor 16 – 1.708" Thick Carbon Steel | 13-227 |
| Table 13-66 | Conductor 17 – 1.992" Thick Stainless Steel | 13-228 |
| Table 13-67 | Conductor 18 – 1.636" Thick Carbon Steel | 13-228 |
| Table 13-68 | Conductor 19 – 2.524" Thick Carbon Steel | 13-228 |
| Table 13-69 | Conductor 20 – 1.762" Thick Carbon Steel | 13-229 |
| Table 13-70 | Conductor 21 – 3.508" Thick Carbon Steel | 13-229 |
| Table 13-71 | Conductor 22 – 3.996" Thick Carbon Steel | 13-229 |
| Table 13-72 | Conductor 23 – 3.028" Thick Carbon Steel | 13-229 |
| Table 13-73 | Conductor 24 – 0.96" Thick Stainless Steel | 13-230 |
| Table 13-74 | Conductor 25 – 5.028" Thick Carbon Steel | 13-230 |
| Table 13-75 | Conductor 26 – 6.0" Thick Stainless Steel | 13-230 |
| Table 13-76 | Conductor 27 – 30.028" Thick Concrete | 13-231 |
| Table 13-77 | Conductor 28 – 24.012" Thick Concrete | 13-232 |
| Table 13-78 | Conductor 29 – 39.028" Thick Concrete | 13-233 |
| Table 13-79 | Conductor 30 – 36.0" Thick Concrete | 13-233 |
| Table 13-80 | Conductor 31 – 30.014" Thick Concrete | 13-234 |
| Table 13-81 | Conductor 32 – 24.014" Thick Concrete | 13-235 |
| Table 13-82 | Conductor 33 – 24.008" Thick Concrete | 13-235 |
| Table 13-83 | Conductor 34 – 24.022" Thick Concrete | 13-236 |
| Table 13-84 | Conductor 35 – 17.0" Thick Concrete | 13-236 |
| Table 13-85 | Conductor 36 – 24.0" Thick Concrete | 13-237 |
| Table 13-86 | Conductor 37 – 48.028" Thick Concrete | 13-237 |
| Table 13-87 | Conductor 38 – 54.022" Thick Concrete | 13-238 |
| Table 13-88 | Conductor 39 – 150.014" Thick Concrete | 13-238 |
| Table 13-89 | Conductor 40 – 13.514" Thick Concrete | 13-239 |
| Table 13-90 | Conductor 41 – 48.014" Thick Concrete | 13-239 |

LIST OF TABLES (cont.)

| | | |
|--------------|--|--------|
| Table 13-91 | Conductor 42 – 12" Thick Concrete | 13-240 |
| Table 13-92 | Conductor 43 – 150" Thick Concrete | 13-240 |
| Table 13-93 | Conductor 44 – 150" Thick Concrete | 13-241 |
| Table 13-94 | Conductor 45 – 150.0" Thick Concrete | 13-241 |
| Table 13-95 | Conductor 46 – 48" Thick Concrete | 13-242 |
| Table 13-96 | Conductor 47 – 77.5" Thick Concrete | 13-242 |
| Table 13-97 | Conductor 48 – 48" Thick Concrete | 13-243 |
| Table 13-98 | Conductor 49 – 24" Thick Concrete | 13-243 |
| Table 13-99 | Conductor 50 – 48" Thick Concrete | 13-244 |
| Table 13-100 | Conductor 51 – 2.0" Thick Carbon Steel | 13-244 |
| Table 13-101 | Conductor 52 – Dummy Baffle | 13-244 |
| Table 13-102 | Conductor 53 – 18" Thick Concrete | 13-245 |
| Table 13-103 | Conductor 54 – 106" Thick Concrete | 13-246 |
| Table 13-104 | Conductor 55 – 6" Thick Concrete | 13-246 |
| Table 13-105 | Conductor 56 – Floor Framing | 13-247 |
| Table 13-106 | Conductor 57 – CMT | 13-247 |
| Table 13-107 | Conductor 58 – Containment Shell Below Deck | 13-247 |
| Table 13-108 | Conductor 59 – 0.8" Thick Steel | 13-248 |
| Table 13-109 | Conductor 60 – 0.6" Stainless Steel | 13-248 |
| Table 13-110 | Conductor 61 – 0.3" Thick Steel | 13-248 |
| Table 13-111 | Conductor 62 – 1.5" Thick Steel | 13-249 |
| Table 13-112 | Conductor 63 – 1.08" Thick Steel | 13-249 |
| Table 13-113 | Conductor 64 – 3.34" Thick Stainless Steel | 13-249 |
| Table 13-114 | Conductor 65 – 8.5" Thick Stainless Steel | 13-249 |
| Table 13-115 | Conductor 66 – 0.7" Stainless Steel | 13-250 |
| Table 13-116 | Conductor 67 – 0.6624" Thick Steel | 13-250 |
| Table 13-117 | Conductor 68 – 1.625" Thick Steel | 13-250 |
| Table 13-118 | Conductor 69 – 0.33264" Thick Steel | 13-250 |
| Table 13-119 | Conductor 70 – 9" Thick Steel | 13-251 |
| Table 13-120 | Conductor 71 – 4.2" Thick Steel | 13-251 |
| Table 13-121 | Conductor 72 – 0.392" Thick Steel | 13-251 |
| Table 13-122 | Conductor 73 – 1.0" Thick Steel | 13-252 |
| Table 13-123 | Conductor 74 – 0.54" Thick Steel | 13-252 |
| Table 13-124 | Conductor 75 – 7.735" Thick Steel | 13-252 |
| Table 13-125 | Evaluation Model Function for the AP1000 PCS Film Flow | 13-287 |
| Table 13-126 | Outside Containment Initial Conditions | 13-290 |
| Table 13-127 | Inside Containment Initial Conditions | 13-291 |

LIST OF TABLES (cont.)

| | | |
|--------------|--|--------|
| Table 13-128 | LOCA Boundary Conditions Represented by Forcing Functions in the AP1000 Evaluation Model | 13-292 |
| Table 13-129 | MSLB Boundary Conditions Represented by Forcing Functions in the AP1000 Evaluation Model | 13-292 |
| Table 13-130 | Basis for Geometric Inputs | 13-307 |
| Table 13-131 | Basis for LOCA Mass and Energy Inputs | 13-308 |
| Table 13-132 | Basis for PCS Inputs | 13-309 |
| Table 13-133 | Containment Volumes and Heat Sinks Model Node Listing | 13-311 |
| Table 13-134 | Master List of Flow Paths in the AP1000 Containment Evaluation Model | 13-313 |
| Table 13-135 | LOCA Transient Sequence of Events | 13-337 |
| Table 13-136 | <u>W</u> GOTHIC Assumptions for Minimum Pressure Calculation | 13-344 |
| Table 14-1 | DECLG LOCA Energy Release Modeling | 14-4 |

LIST OF FIGURES

| | | |
|-------------|---|------|
| Figure 1-1 | Relationship of AP600 Containment DBA Reports | 1-2 |
| Figure 2-1 | PCS Test and Analysis Process Overview | 2-2 |
| Figure 3-1 | Summary of GOTHIC Historical Development | 3-2 |
| Figure 3-2 | GOTHIC Modeling Features | 3-3 |
| Figure 3-3 | Summary of <u>W</u> GOTHIC Historical Development | 3-7 |
| Figure 3-4 | Westinghouse-GOTHIC Clime Wall Source Term Models | 3-13 |
| Figure 3-5 | Clime Finite Difference Model Definitions | 3-15 |
| Figure 3-6 | Clime Routines Flow Control Outline | 3-21 |
| Figure 4-1 | Cutaway View of the 100-foot Elevation of the AP600 Including Major Components | 4-5 |
| Figure 4-2 | Cutaway View of the 100-foot Elevation of the AP600 Excluding Major Components | 4-6 |
| Figure 4-3 | Reactor Cavity | 4-7 |
| Figure 4-4 | Reactor Cavity Cross-Section – AA | 4-8 |
| Figure 4-5 | Reactor Cavity Cross-Section – BB | 4-9 |
| Figure 4-6 | Reactor Coolant Drain Tank Cavity | 4-14 |
| Figure 4-7 | Reactor Coolant Drain Tank Cross-Section – AA | 4-15 |
| Figure 4-8 | Southeast Accumulator Cavity | 4-20 |
| Figure 4-9 | Southeast Accumulator Cavity Cross-Section – BB | 4-21 |
| Figure 4-10 | Northeast Accumulator Cavity | 4-26 |
| Figure 4-11 | Northeast Accumulator Cavity Cross-Section – BB | 4-27 |
| Figure 4-12 | East Steam Generator Cavity | 4-31 |
| Figure 4-13 | East Steam Generator Cavity Cross-Section – AA | 4-32 |
| Figure 4-14 | East Steam Generator Cavity Cross-Section – BB | 4-33 |
| Figure 4-15 | West Steam Generator Cavity | 4-41 |
| Figure 4-16 | West Steam Generator Cavity Cross-Section – AA | 4-42 |
| Figure 4-17 | West Steam Generator Cavity Cross-Section – BB | 4-43 |
| Figure 4-18 | North CMT Cavity | 4-49 |
| Figure 4-19 | North CMT Cavity Cross-Section – AA | 4-50 |
| Figure 4-20 | North CMT Cavity Cross-Section – BB | 4-51 |
| Figure 4-21 | South CMT Cavity | 4-62 |
| Figure 4-22 | South CMT Cavity Cross-Section – AA | 4-63 |
| Figure 4-23 | South CMT Cavity Cross-Section – BB | 4-64 |
| Figure 4-24 | Chemical and Volume Control Cavity | 4-71 |
| Figure 4-25 | Chemical and Volume Control Cavity Cross-Section – AA | 4-72 |
| Figure 4-26 | Refueling Canal | 4-76 |
| Figure 4-27 | Refueling Canal Cross-Section – AA | 4-77 |
| Figure 4-28 | Internal Refueling Water Storage Tank (IRWST) | 4-83 |
| Figure 4-29 | IRWST Cross-Section – AA | 4-84 |
| Figure 4-30 | South Inner-Half Annulus Compartment | 4-92 |

LIST OF FIGURES (cont.)

Figure 4-31 Cylindrical Central Room Cross-Section – BB 4-93
Figure 4-32 Cylindrical Central Room Cross-Section – AA 4-94
Figure 4-33 Above-Deck East Steam Generator Compartment 4-97
Figure 4-34 Above-Deck East Steam Generator Room Cross-Section – BB 4-98
Figure 4-35 Above-Deck East Steam Generator Room Cross-Section – AA 4-99
Figure 4-36 Above-Deck West Steam Generator Compartment 4-104
Figure 4-37 Above-Deck West Steam Generator Compartment Cross-Section – BB 4-105
Figure 4-38 Above-Deck West Steam Generator Compartment Cross-Section – AA 4-106
Figure 4-39 South Inner-Half Annulus Compartment 4-111
Figure 4-40 South Inner-Half Annulus Cross-Section – BB 4-112
Figure 4-41 South Inner-Half Annulus Cross-Section – AA 4-113
Figure 4-42 North Inner-Half Annulus Compartment 4-118
Figure 4-43 North Inner-Half Annulus Cross-Section – BB 4-119
Figure 4-44 North Inner-Half Annulus Cross-Section – AA 4-120
Figure 4-45 North Mid-Quarter Annulus Compartment 4-126
Figure 4-46 North Mid-Quarter Annulus Cross-Section – BB 4-127
Figure 4-47 North Mid-Quarter Annulus Cross-Section – AA 4-128
Figure 4-48 West Mid-Quarter Annulus Compartment 4-134
Figure 4-49 West Mid-Quarter Annulus Cross-Section – BB 4-135
Figure 4-50 West Mid-Quarter Annulus Cross-Section – AA 4-136
Figure 4-51 South Mid-Quarter Annulus Compartment 4-141
Figure 4-52 South Mid-Quarter Annulus Cross-Section – BB 4-142
Figure 4-53 South Mid-Quarter Annulus Cross-Section – AA 4-143
Figure 4-54 East Mid-Quarter Annulus Compartment 4-149
Figure 4-55 East Mid-Quarter Annulus Cross-Section – BB 4-150
Figure 4-56 East Mid-Quarter Annulus Cross-Section – AA 4-151
Figure 4-57 North Outer Quarter Annulus Cross-Section 4-157
Figure 4-58 North Outer Quarter Annulus Cross-Section – BB 4-158
Figure 4-59 North Outer Quarter Annulus Cross-Section – AA 4-159
Figure 4-60 West Outer Quarter Annulus Compartment 4-164
Figure 4-61 West Outer Quarter Annulus Cross-Section – BB 4-165
Figure 4-62 West Outer Quarter Annulus Cross-Section – AA 4-166
Figure 4-63 South Outer Quarter Annulus Compartment 4-171
Figure 4-64 South Outer Quarter Annulus Cross-Section – BB 4-172
Figure 4-65 South Outer Quarter Annulus Cross-Section – AA 4-173
Figure 4-66 East Outer Quarter Annulus Compartment 4-178
Figure 4-67 East Outer Quarter Annulus Cross-Section – BB 4-179
Figure 4-68 East Outer Quarter Annulus Cross-Section – AA 4-180
Figure 4-69 East Quarter Inner Dome Cross-Section – BB 4-184
Figure 4-70 East Quarter Inner Dome Cross-Section – AA 4-185

LIST OF FIGURES (cont.)

| | | |
|--------------|---|-------|
| Figure 4-71 | North Quarter Inner Dome Cross-Section – BB | 4-188 |
| Figure 4-72 | North Quarter Inner Dome Cross-Section – AA | 4-189 |
| Figure 4-73 | West Quarter Inner Dome Cross-Section – BB | 4-191 |
| Figure 4-74 | West Quarter Inner Dome Cross-Section – AA | 4-194 |
| Figure 4-75 | South Quarter Inner Dome Cross-Section – BB | 4-197 |
| Figure 4-76 | South Quarter Inner Dome Cross-Section – AA | 4-198 |
| Figure 4-77 | East Quarter Outer Dome Cross-Section – BB | 4-201 |
| Figure 4-78 | East Quarter Outer Dome Cross-Section – AA | 4-202 |
| Figure 4-79 | North Quarter Outer Dome Cross-Section – BB | 4-205 |
| Figure 4-80 | North Quarter Outer Dome Cross-Section – AA | 4-206 |
| Figure 4-81 | West Quarter Outer Dome Cross-Section – BB | 4-209 |
| Figure 4-82 | West Quarter Outer Dome Cross-Section – AA | 4-210 |
| Figure 4-83 | South Quarter Outer Dome Cross-Section – BB | 4-213 |
| Figure 4-84 | South Quarter Outer Dome Cross-Section – AA | 4-214 |
| Figure 4-85 | Outside Containment Upflow Annulus Cross-Section – BB | 4-217 |
| Figure 4-86 | Outside Containment Downflow Annulus Cross-Section – BB | 4-222 |
| Figure 4-87 | PCS Chimney Cross-Section – BB | 4-225 |
| Figure 4-88 | WGOTHIC Conductor Noding Example | 4-228 |
| Figure 4-89 | Wet/Dry Clime Modeling Diagram | 4-245 |
| Figure 4-90 | Containment , Baffle, Shield Building Modeling with Climes | 4-246 |
| Figure 4-91 | Wet Stack Clime Numbering Diagram | 4-247 |
| Figure 4-92 | Dry Stack Clime Numbering Diagram | 4-261 |
| Figure 4-93 | AP600 Evaluation Model LOCA Function 3: PCS Evaporation Limited Film Flow Rate | 4-273 |
| Figure 4-94 | AP600 Evaluation Model LOCA Function 2: IRWST Drain Rate | 4-278 |
| Figure 4-95 | AP600 Evaluation Model LOCA Function 4: Liquid Drop Model Control | 4-279 |
| Figure 4-96 | AP600 Evaluation Model LOCA Function 5: Liquid Mass Break Flow | 4-280 |
| Figure 4-97 | AP600 Evaluation Model LOCA Function 6: Liquid Break Enthalpy | 4-281 |
| Figure 4-98 | AP600 Evaluation Model LOCA Function 7: Steam Mass Break Flow | 4-282 |
| Figure 4-99 | AP600 Evaluation Model LOCA Function 8: Steam Break Enthalpy | 4-283 |
| Figure 4-100 | AP600 Evaluation Model LOCA Function 11: Thermal Conductor Heat Transfer Coefficient Control | 4-284 |
| Figure 4-101 | AP600 Evaluation Model LOCA Function 12: Steam Mass ADS Flow | 4-285 |
| Figure 4-102 | AP600 Evaluation Model LOCA Function 13: PCS Annular Sump Drain Rate ... | 4-286 |
| Figure 4-104 | AP600 Evaluation Model MSLB Function 12: Steam Break Enthalpy | 4-288 |
| Figure 4-105 | AP600 Evaluation MSLB Function 13: Short-Term MSLB Steam Mass Break Flow | 4-289 |
| Figure 4-106 | AP600 Evaluation Model MSLB Function 13: Long-Term MSLB Steam Mass Break Flow | 4-290 |

LIST OF FIGURES (cont.)

| | | |
|---------------|---|-------|
| Figure 4-107 | AP600 <u>W</u> GOTHIC Evaluation Model Section B-B | 4-310 |
| Figure 4-108 | AP600 <u>W</u> GOTHIC Evaluation Model Section A-A | 4-311 |
| Figure 4-109 | AP600 <u>W</u> GOTHIC Evaluation Model 135'-3" Elevation | 4-312 |
| Figure 4-110 | AP600 <u>W</u> GOTHIC Evaluation Model 148'-0" Elevation | 4-313 |
| Figure 4-111 | AP600 <u>W</u> GOTHIC Evaluation Model 170'-0" Elevation | 4-314 |
| Figure 4-112 | AP600 <u>W</u> GOTHIC Evaluation Model 189'-6" Elevation | 4-315 |
| Figure 4-113 | AP600 <u>W</u> GOTHIC Evaluation Model 209'-0" Elevation | 4-316 |
| Figure 4-114 | AP600 <u>W</u> GOTHIC Evaluation Model 224'-9" Elevation | 4-317 |
| Figure 4-115 | AP600 <u>W</u> GOTHIC Evaluation Model 240'-6" Elevation | 4-318 |
| Figure 4-116 | AP600 <u>W</u> GOTHIC Evaluation Model 254'-4" Elevation | 4-328 |
| Figure 4-117 | Below-Deck Compartments and Flowpaths | 4-329 |
| Figure 4-118a | LOCA Break Pools Below the CMT Room Floor (107'-2") | 4-330 |
| Figure 4-118b | LOCA Break Pools in the Accumulator and CVS Cavities | 4-331 |
| Figure 4-119 | LOCA Below-Deck Water Levels Above 107'-2" | 4-332 |
| Figure 4-120 | LOCA IRWST Water Level | 4-333 |
| Figure 4-121a | LOCA Pressure History: Short-Term | 4-334 |
| Figure 4-121b | LOCA Pressure History: Long-Term | 4-335 |
| Figure 4-122 | LOCA Steam Concentration for East Quarter Compartments | 4-336 |
| Figure 4-123 | LOCA Steam Concentration for West Quarter Compartments | 4-337 |
| Figure 4-124 | LOCA Temperature Distribution for East Quarter Compartments | 4-338 |
| Figure 4-125 | LOCA Temperature Distribution for West Quarter Compartments | 4-339 |
| Figure 4-126a | Temperature Distribution for Central Cylindrical Regions | 4-340 |
| Figure 4-126b | Temperature Distribution for the Dome Regions | 4-341 |
| Figure 4-127 | Air Temperature Distribution in the PCS Annulus - LOCA Event | 4-342 |
| Figure 4-128 | Air Flow Through the PCS Annulus - LOCA Event | 4-343 |
| Figure 4-129a | LOCA Gas Circulation Pattern in the Upper East Steam Generator Compartment . | 4-344 |
| Figure 4-129b | LOCA Gas Circulation Pattern in the East Outer Quarter Compartments | 4-345 |
| Figure 4-130a | LOCA Gas Circulation Pattern in the Upper West Steam Generator Compartment | 4-346 |
| Figure 4-130b | LOCA Gas Circulation Pattern in the West Outer Quarter Compartments | 4-347 |
| Figure 4-131 | LOCA Gas Circulation Pattern Across the Operating Deck | 4-348 |
| Figure 4-132 | LOCA Steam Pressure Ratios Between the CMT Room Floor and the Operating Deck | 4-349 |
| Figure 4-133 | LOCA Steam Pressure Ratios at the Operating Deck Inside the 50.975' Radius | 4-350 |
| Figure 4-134 | MSLB Temperature Distribution | 4-351 |
| Figure 4-135 | MSLB Pressure History | 4-352 |
| Figure 5-1 | Case 1 - Initial Containment Humidity Sensitivity - LOCA | 5-5 |
| Figure 5-2 | Case 8 - Initial Containment Humidity Sensitivity - MSLB | 5-6 |

LIST OF FIGURES (cont.)

| | | |
|-------------|---|------|
| Figure 5-3 | Case 2 - Initial Containment Pressure Sensitivity - LOCA | 5-7 |
| Figure 5-4 | Case 9 - Initial Containment Pressure Sensitivity - MSLB | 5-8 |
| Figure 5-5 | Case 3 - Initial Containment Temperature Sensitivity - LOCA | 5-10 |
| Figure 5-6 | Case 10 - Initial Containment Temperature Sensitivity - MSLB | 5-11 |
| Figure 5-7 | Case 4 - Ambient Humidity Sensitivity at 115°F Ambient Temperature - LOCA | 5-13 |
| Figure 5-8 | Case 11 - Ambient Humidity Sensitivity at 115°F Ambient Temperature - MSLB | 5-14 |
| Figure 5-9 | Case 5 - Ambient Temperature Sensitivity - LOCA | 5-16 |
| Figure 5-10 | Case 12 - Ambient Temperature Sensitivity - MSLB | 5-17 |
| Figure 5-11 | Case 7 - Film Temperature Sensitivity - LOCA | 5-18 |
| Figure 5-12 | Case 14 - Film Temperature Sensitivity - MSLB | 5-19 |
| Figure 5-13 | Blowdown Drop Fraction Sensitivity - LOCA | 5-21 |
| Figure 6-1 | Particle Path Through AP600 PCS With and Without Wind | 6-4 |
| Figure 6-2 | 1D Containment Shell Model Inside Temperature Results | 6-6 |
| Figure 7-1 | Illustration of PCS Water Distribution Weir Assembly | 7-7 |
| Figure 7-2 | Minimum Delivered PCS Water Flow Rate | 7-11 |
| Figure 7-3 | Weir Outflow | 7-12 |
| Figure 7-4 | Comparison of Water Distribution Model to Phase 3 Water Distribution Test Results | 7-15 |
| Figure 7-5 | Determination of Gamma-Min from LST, SST, and Flat Plate Data | 7-17 |
| Figure 7-6 | Normalized Water Evaporation Rate (2-D/1D Conduction) versus Overall Containment Wetted Fraction | 7-22 |
| Figure 7-7 | Containment Steel Shell Temperature Gradients (°F) with 2-D Heat Conduction; 20 psig, 25% Wetted | 7-23 |
| Figure 7-8 | Containment Steel Shell Thermal Flux Gradients (Btu/hr-ft ²) in Y-Direction; 20 psig, 25% Wetted | 7-24 |
| Figure 7-9 | Containment Steel Shell Total Thermal Flux (Btu/hr-ft ²); 20 psig, 25% Wetted | 7-25 |
| Figure 7-10 | Thermal Flux in Y-Direction on Outside Surface of Containment Wall [Btu/hr-ft ²] | 7-26 |
| Figure 7-11 | Thermal Flux in Y-direction on Inside Surface of Containment Wall [Btu/hr-ft ²] | 7-27 |
| Figure 7-12 | Large-Scale Test Water Coverage Pattern | 7-45 |
| Figure 7-13 | Sensitivity to the Input PCS Film Flow Rate | 7-55 |
| Figure 7-14 | Comparison of Peak Containment Pressure as Function of PCS Coverage Area | 7-57 |
| Figure 7-15 | PCS Runoff Flow Rates as a Function of Coverage Area | 7-58 |
| Figure 7-16 | Comparison of Evaporation Model Peak Pressure with 100% and 50% Constant Coverage Models | 7-59 |
| Figure 7-17 | Comparison of Evaporation Model PCS Runoff Flow Rate with 100% and 50% Constant Coverage Models | 7-61 |
| Figure 7-18 | Difference in the Integrated Energy Transferred to the Top of the Dome (with PCS Film Applied at 35 and 337 Seconds) | 7-62 |

LIST OF FIGURES (cont.)

| | | |
|-------------|--|------|
| Figure 8-1 | Comparison of Single-Node Model with EM Pressure Curve | 8-3 |
| Figure 8-2 | Comparison of Response with No Heat Sinks to EM Response | 8-4 |
| Figure 9-1 | Measured Steam Concentrations for LST | 9-52 |
| Figure 9-2 | LST with Diffuser Under Steam Generator - Steam Flow 0.11-0.17 lb/sec - Internal Fluid Temperature - Group 1 | 9-53 |
| Figure 9-3 | LST with Diffuser Under Steam Generator - Steam Flow 0.11-0.17 lb/sec - Saturation Temperature - Group 1 | 9-54 |
| Figure 9-4 | LST with Diffuser Under Steam Generator - Steam Flow 0.11-0.17 lb/sec - Internal Steam Pressure Ratio - Group 1 | 9-55 |
| Figure 9-5 | LST with Diffuser Under Steam Generator - Steam Flow 0.11-0.17 lb/sec - Internal Fluid Temperature - Group 2 | 9-56 |
| Figure 9-6 | LST with Diffuser Under Steam Generator - Steam Flow 0.11-0.17 lb/sec - Saturation Temperature - Group 2 | 9-57 |
| Figure 9-7 | LST with Diffuser Under Steam Generator - Steam Flow 0.11-0.17 lb/sec - Internal Steam Pressure Ratio - Group 2 | 9-58 |
| Figure 9-8 | LST with Diffuser Under Steam Generator - Steam Flow 0.27-0.36 lb/sec - Internal Fluid Temperature | 9-59 |
| Figure 9-9 | LST with Diffuser Under Steam Generator - Steam Flow 0.27-0.36 lb/sec - Saturation Temperature | 9-60 |
| Figure 9-10 | LST with Diffuser Under Steam Generator - Steam Flow 0.27-0.36 lb/sec - Internal Steam Pressure Ratio | 9-61 |
| Figure 9-11 | LST with Diffuser Under Steam Generator - Steam Flow 0.49-0.62 lb/sec - Internal Fluid Temperature - Group 1 | 9-62 |
| Figure 9-12 | LST with Diffuser Under Steam Generator - Steam Flow 0.49-0.26 lb/sec - Saturation Temperature - Group 1 | 9-63 |
| Figure 9-13 | LST with Diffuser Under Steam Generator - Steam Flow 0.49-0.62 lb/sec - Internal Steam Pressure Ratio - Group 1 | 9-64 |
| Figure 9-14 | LST with Diffuser Under Steam Generator - Steam Flow 0.49-0.62 lb/sec - Internal Fluid Temperature - Group 2 | 9-65 |
| Figure 9-15 | LST with Diffuser Under Steam Generator - Steam Flow 0.49-0.62 lb/sec - Saturation Temperature - Group 2 | 9-66 |
| Figure 9-16 | LST with Diffuser Under Steam Generator - Steam Flow 0.49-0.62 lb/sec - Internal Steam Pressure Ratio - Group 2 | 9-67 |
| Figure 9-17 | LST with Diffuser Under Steam Generator - Steam Flow 0.76-0.84 lb/sec - Internal Fluid Temperature | 9-68 |
| Figure 9-18 | LST with Diffuser Under Steam Generator - Steam Flow 0.76-0.84 lb/sec - Saturation Temperature | 9-69 |
| Figure 9-19 | LST with Diffuser Under Steam Generator - Steam Flow 0.76-0.84 lb/sec - Internal Steam Pressure Ratio | 9-70 |

LIST OF FIGURES (cont.)

| | | |
|-------------|---|------|
| Figure 9-20 | LST with Diffuser Under Steam Generator - Steam Flow 1.10-1.20 lb/sec - Internal Fluid Temperature | 9-71 |
| Figure 9-21 | LST with Diffuser Under Steam Generator - Steam Flow 1.10-1.20 lb/sec - Saturation Temperature | 9-72 |
| Figure 9-22 | LST with Diffuser Under Steam Generator - Steam Flow 1.10-1.20 lb/sec - Internal Steam Pressure Ratio | 9-73 |
| Figure 9-23 | LST with Diffuser Under Steam Generator - Steam Flow 1.54-1.68 lb/sec - Internal Fluid Temperature | 9-74 |
| Figure 9-24 | LST with Diffuser Under Steam Generator - Steam Flow 1.54-1.68 lb/sec - Saturation Temperature | 9-75 |
| Figure 9-25 | LST with Diffuser Under Steam Generator - Steam Flow 1.54-1.68 lb/sec - Internal Steam Pressure Ratio | 9-76 |
| Figure 9-26 | LST with Diffuser Up 6 Feet - Steam Flow 0.76 & 1.68 lb/sec - Internal Fluid Temperature | 9-77 |
| Figure 9-27 | LST with Diffuser Up 6 Feet - Steam Flow 0.76 & 1.68 lb/sec - Saturation Temperature | 9-78 |
| Figure 9-28 | LST with Diffuser Up 6 Feet - Steam Flow 0.76 & 1.68 lb/sec - Internal Steam Pressure Ratio | 9-79 |
| Figure 9-29 | LST with Steam Injection: 3 Inch Pipe - Steam Flow 0.76 - 0.95 lb/sec - Internal Fluid Temperature | 9-80 |
| Figure 9-30 | LST with Steam Injection: 3 Inch Pipe - Steam Flow 0.76 - 0.95 lb/sec - Saturation Temperature | 9-81 |
| Figure 9-31 | LST with Steam Injection: 3 Inch Pipe - Steam Flow 0.76 - 0.95 lb/sec - Internal Steam Pressure Ratio | 9-82 |
| Figure 9-32 | LST with Steam Injection: 3 Inch Pipe - Steam Flow 1.25 - 1.31 lb/sec - Internal Fluid Temperature | 9-83 |
| Figure 9-33 | LST with Steam Injection: 3 Inch Pipe - Steam Flow 1.25 - 1.31 lb/sec - Saturation Temperature | 9-84 |
| Figure 9-34 | LST with Steam Injection: 3 Inch Pipe - Steam Flow 1.25 - 1.31 lb/sec - Internal Steam Pressure Ratio | 9-85 |
| Figure 9-35 | CMT Compartment Layout | 9-86 |
| Figure 9-36 | Simplified AP600 Containment Diagram | 9-87 |
| Figure 9-37 | <u>W</u> GOTHIC Calculated LOCA Blowdown Steam Pressure Ratio for Jet Momentum Dissipated in SG East Compartment | 9-88 |
| Figure 9-38 | <u>W</u> GOTHIC Calculated AP600 Containment Pressure - Sensitivity to Loss Coefficients for LOCA Jet Momentum Dissipated in SG East Compartment | 9-89 |
| Figure 9-39 | <u>W</u> GOTHIC Calculated Flow Pattern - Sensitivity to Loss Coefficients for LOCA Jet Momentum Dissipated in SG East Compartment at 20 Seconds | 9-90 |
| Figure 9-40 | <u>W</u> GOTHIC Calculated Flow Pattern - Sensitivity to Loss Coefficients for LOCA Jet Momentum Dissipated in SG East Comp. at 1000 Seconds | 9-91 |

LIST OF FIGURES (cont.)

Figure 9-41 WGOTHIC Calculated Flow Pattern - Sensitivity to Loss Coefficients for
LOCA Jet Momentum Dissipated in SG East Comp. at 1550 Seconds 9-92

Figure 9-42 WGOTHIC Calculated Flow Pattern - Sensitivity to Loss Coefficients for
LOCA Jet Momentum Dissipated in SG East Comp. at 80050 Seconds 9-93

Figure 9-43 WGOTHIC Calculated AP600 Containment Heat Removal Rates - LOCA
Jet Momentum Dissipated in SG East Compartment 9-94

Figure 9-44 WGOTHIC Calculated AP600 Containment Steam Pressure Ratio for
LOCA Jet Momentum Dissipated in SG East Compartment 9-95

Figure 9-45 WGOTHIC Calculated AP600 Cont. Pressure - Sensitivity to Heat
Transfer Coefficient for Study of Undissipated Jet Effects During a LOCA 9-96

Figure 9-46 WGOTHIC Calculated AP600 Containment Pressure-LOCA Jet
Momentum Dissipated in SG East Compartment 9-97

Figure 9-46A WGOTHIC Calculated AP600 Containment Below-Deck Compartment
Pressure for LOCA Jet Momentum Dissipated in SG East Compartment 9-98

Figure 9-47 WGOTHIC Calculated Flow Pattern - LOCA Jet Momentum Dissipated
in SG East Compartment at 20 Seconds 9-99

Figure 9-48 WGOTHIC Calculated Flow Pattern - LOCA Jet Momentum Dissipated
in SG East Compartment at 1000 Seconds 9-100

Figure 9-49 WGOTHIC Calculated Flow Pattern - LOCA Jet Momentum Dissipated
in SG East Compartment at 1500 Seconds 9-101

Figure 9-50 WGOTHIC Calculated Flow Pattern - LOCA Jet Momentum Dissipated
in SG East Compartment at 8000 Seconds 9-102

Figure 9-51 Details of WGOTHIC Flow Paths to Above-Deck Region from CMT,
Refueling Canal, and IRWST 9-103

Figure 9-52 WGOTHIC Calculated AP600 Containment Pressure - LOCA Plume
Rising into CMT Room 9-104

Figure 9-53 WGOTHIC Calculated Flow Pattern - LOCA Plume Rising into
CMT Room at 1000 Seconds 9-105

Figure 9-54 WGOTHIC Calculated Flow Pattern - LOCA Plume Rising into
CMT Room at 1400 Seconds 9-106

Figure 9-55 WGOTHIC Calculated AP600 Containment Heat Removal Rates -
LOCA Plume Rising into CMT Room 9-107

Figure 9-56 WGOTHIC Calculated AP600 Containment Pressure - LOCA Plume
Rising into CMT Room and SG Compartments 9-108

Figure 9-57 WGOTHIC Calculated Flow Pattern - LOCA Plume Rising into
CMT Room and SG Compartments at 1000 Seconds 9-109

Figure 9-58 WGOTHIC Calculated Flow Pattern - LOCA Plume Rising into
CMT Room and SG Compartments at 1500 Seconds 9-110

Figure 9-59 WGOTHIC Calculated AP600 Containment Heat Removal Rates -
LOCA Plume Rising into CMT Room and SG Compartments 9-111

LIST OF FIGURES (cont.)

| | | |
|--------------|--|-------|
| Figure 9-60 | <u>WGOTHIC</u> Calculated AP600 Containment Steam Pressure Ratio for MSLB Above-Deck | 9-112 |
| Figure 9-61 | <u>WGOTHIC</u> Calculated AP600 Containment Pressure - MSLB Above Operating Deck | 9-113 |
| Figure 9-62 | <u>WGOTHIC</u> Calculated AP600 Containment Pressure - MSLB in CMT Room | 9-114 |
| Figure 10-1 | LOCA Sensitivities to Nominal Inputs and Correlations | 10-3 |
| Figure 10-2 | MSLB Sensitivity to Nominal Inputs and Correlations | 10-4 |
| Figure 10-3 | Comparison of Evaluation Model and Nominal Mass Release | 10-8 |
| Figure 10-4 | Comparison of Evaluation Model and Nominal Energy Release | 10-9 |
| Figure 11-1 | AP600 Containment LOCA Transient Pressure Prediction with Full, One-Half, and One-Quarter Timesteps | 11-4 |
| Figure 11-2 | AP600 Timestep Comparison, Percentage Difference in Predicted Pressures Between Successive Code Versions | 11-5 |
| Figure 12-1 | Westinghouse-GOTHIC Clime Wall Source Term Models | 12-13 |
| Figure 12-2 | Simplified Line Diagram of Annulus Clime Model | 12-14 |
| Figure 12-3 | Noding Diagram, 8 Clime Node Model | 12-15 |
| Figure 12-4 | Comparison of Transient Heat Transfer Rates; Case 1 | 12-16 |
| Figure 12-5 | Comparison of Transient Heat Transfer Rates; Case 2 | 12-17 |
| Figure 12-6 | Comparison of Transient Heat Transfer Rates; Case 3 | 12-18 |
| Figure 12-7 | Comparison of Transient Heat Transfer Rates; Case 4 | 12-19 |
| Figure 12-8 | Comparison of Transient Heat Transfer Rate Differences; Case 1 | 12-20 |
| Figure 12-9 | Comparison of Transient Heat Transfer Rate Differences; Case 2 | 12-21 |
| Figure 12-10 | Comparison of Transient Heat Transfer Rate Differences; Case 3 | 12-22 |
| Figure 12-11 | Comparison of Transient Heat Transfer Rate Differences; Case 4 | 12-23 |
| Figure 12-12 | Comparison of Heat Flux Profiles; Time t = 2000 Seconds; Case 1 | 12-24 |
| Figure 12-13 | Comparison of Heat Flux Profiles; Time t = 2000 Seconds; Case 2 | 12-25 |
| Figure 12-14 | Comparison of Heat Flux Profiles; Time t = 2000 Seconds; Case 3 | 12-26 |
| Figure 12-15 | Comparison of Heat Flux Profiles; Time t = 2000 Seconds; Case 4 | 12-27 |
| Figure 12-16 | Comparison of Film Temperature Profiles; Time t = 2000 Seconds; Case 1 | 12-28 |
| Figure 12-17 | Comparison of Film Temperature Profiles; Time t = 2000 seconds; Case 2 | 12-29 |
| Figure 12-18 | Comparison of Film Temperature Profiles; Time t = 2000 seconds; Case 3 | 12-30 |
| Figure 12-19 | Comparison of Film Temperature Profiles; Time t = 2000 seconds; Case 4 | 12-31 |
| Figure 12-20 | Comparison of Air Temperature Profiles; Time t = 2000 seconds; Case 1 | 12-32 |
| Figure 12-21 | Comparison of Air Temperature Profiles; Time t = 2000 seconds; Case 2 | 12-33 |
| Figure 12-22 | Comparison of Air Temperature Profiles; Time t = 2000 seconds; Case 3 | 12-34 |
| Figure 12-23 | Comparison of Air Temperature Profiles; Time t = 2000 seconds; Case 4 | 12-35 |
| Figure 12-24 | AP600 Containment Model Clime Noding Pattern | 12-36 |
| Figure 12-25 | AP600 Containment Model Double Vertical Clime Noding Pattern | 12-37 |
| Figure 12-26 | AP600 Containment Model Double Stack Clime Noding Pattern | 12-38 |
| Figure 12-27 | AP600 Containment Model Double Mesh Point Clime Noding Pattern | 12-39 |

LIST OF FIGURES (cont.)

Figure 12-28 Pressure History, AP600 Containment Model; Double Clime 12-40
Figure 12-29 Wet Heat Flux vs. Clime; AP600 Containment Model, Base Case 12-41
Figure 12-30 Wet Heat Flux vs. Clime; AP600 Containment Model, Double Clime 12-42
Figure 12-31 Dry Heat Flux vs. Clime; AP600 Containment Model, Base Case 12-43
Figure 12-32 Dry Heat Flux vs. Clime; AP600 Containment Model, Double Clime 12-44
Figure 12-33 Film Temperature vs. Clime; AP600 Containment Model,
Base Case 12-45
Figure 12-34 Film Temperature vs. Clime; AP600 Containment Model,
Double Clime 12-46
Figure 12-35 Dry Surface Temperature vs. Clime; AP600 Containment Model,
Base Case 12-47
Figure 12-36 Dry Surface Temperature vs. Clime; AP600 Containment Model,
Double Clime 12-48
Figure 12-37 Annulus Pressure vs. Clime; AP600 Containment Model,
Base Case 12-49
Figure 12-38 Annulus Pressure vs. Clime; AP600 Containment Model,
Double Clime 12-50
Figure 12-39 Air Temperature vs. Clime; AP600 Containment Model, Base Case 12-51
Figure 12-40 Air Temperature vs. Clime; AP600 Containment Model, Double Clime 12-52
Figure 12-41 Air Density vs. Clime; AP600 Containment Model, Base Case 12-53
Figure 12-42 Air Density vs. Clime; AP600 Containment Model, Double Clime 12-54
Figure 12-43 Air Velocity vs. Clime; AP600 Containment Model, Base Case 12-55
Figure 12-44 Air Velocity vs. Clime; AP600 Containment Model, Double Clime 12-56
Figure 12-45 Heat Rejection History Comparison, AP600 Containment Model;
Double Clime Sensitivity Case 12-57
Figure 12-46 Integrated Heat Rejection Comparison, AP600 Containment Model;
Double Clime Sensitivity Case 12-58
Figure 12-47 Pressure History Comparison, AP600 Containment Model;
Double Stack Sensitivity Case 12-59
Figure 12-48 Heat Rejection History Comparison, AP600 Containment Model;
Double Stack Sensitivity Case 12-60
Figure 12-49 Integrated Heat Rejection Comparison, AP600 Containment Model;
Double Stack Sensitivity Case 12-61
Figure 12-50 Pressure History Comparison, AP600 Containment Model;
Double Mesh Sensitivity Case 12-62
Figure 12-51 Heat Rejection History Comparison, AP600 Containment Model;
Double Mesh Sensitivity Case 12-63
Figure 12-52 Integrated Heat Rejection Comparison, AP600 Containment Model;
Double Mesh Sensitivity Case 12-64

LIST OF FIGURES (cont.)

| | | |
|--------------|--|--------|
| Figure 13-1a | A Comparison of AP600 and AP1000 Containment Model Noding Structures | 13-2 |
| Figure 13-1 | Cutaway View of the 100-foot Elevation of the AP1000 Including Major Components | 13-4 |
| Figure 13-2 | Cutaway View of the 100-foot Elevation of the AP1000 Excluding Major Components | 13-5 |
| Figure 13-3 | Reactor Cavity | 13-8 |
| Figure 13-4 | Reactor Cavity Cross-Section – AA | 13-9 |
| Figure 13-5 | Reactor Cavity Cross-Section – BB | 13-10 |
| Figure 13-6 | Reactor Coolant Drain Tank Cavity | 13-14 |
| Figure 13-7 | Reactor Coolant Drain Tank Cross-Section – AA | 13-15 |
| Figure 13-8 | Southeast Accumulator Cavity | 13-20 |
| Figure 13-9 | Southeast Accumulator Cavity Cross-Section – BB | 13-21 |
| Figure 13-10 | Northeast Accumulator Cavity | 13-25 |
| Figure 13-11 | Northeast Accumulator Cavity Cross-Section – BB | 13-26 |
| Figure 13-12 | East Steam Generator Cavity | 13-30 |
| Figure 13-13 | East Steam Generator Cavity Cross-Section – AA | 13-31 |
| Figure 13-14 | East Steam Generator Cavity Cross-Section – BB | 13-32 |
| Figure 13-15 | West Steam Generator Cavity | 13-39 |
| Figure 13-16 | West Steam Generator Cavity Cross-Section – AA | 13-40 |
| Figure 13-17 | West Steam Generator Cavity Cross-Section – BB | 13-41 |
| Figure 13-18 | North CMT Cavity | 13-47 |
| Figure 13-19 | North CMT Cavity Cross-Section – AA | 13-48 |
| Figure 13-20 | North CMT Cavity Cross-Section – BB | 13-49 |
| Figure 13-21 | South CMT Cavity | 13-59 |
| Figure 13-22 | South CMT Cavity Cross-Section – AA | 13-60 |
| Figure 13-23 | South CMT Cavity Cross-Section – BB | 13-61 |
| Figure 13-24 | Chemical and Volume Control Cavity | 13-68 |
| Figure 13-25 | Chemical and Volume Control Cavity Cross-Section – AA | 13-69 |
| Figure 13-26 | Refueling Canal | 13-75 |
| Figure 13-27 | Refueling Canal Cross-Section – AA | 13-76 |
| Figure 13-28 | Internal Refueling Water Storage Tank (IRWST) | 13-82 |
| Figure 13-29 | IRWST Cross-Section – AA | 13-83 |
| Figure 13-30 | South Inner-Half Annulus Compartment | 13-90 |
| Figure 13-31 | Cylindrical Central Room Cross-Section – BB | 13-91 |
| Figure 13-32 | Cylindrical Central Room Cross-Section – AA | 13-92 |
| Figure 13-33 | Above-Deck East Steam Generator Compartment | 13-96 |
| Figure 13-34 | Above-Deck East Steam Generator Room Cross-Section – BB | 13-97 |
| Figure 13-35 | Above-Deck East Steam Generator Room Cross-Section – AA | 13-98 |
| Figure 13-36 | Above-Deck West Steam Generator Compartment | 13-103 |
| Figure 13-37 | Above-Deck West Steam Generator Compartment Cross-Section – BB | 13-104 |

LIST OF FIGURES (cont.)

| | | |
|--------------|--|--------|
| Figure 13-38 | Above-Deck West Steam Generator Compartment Cross-Section – AA | 13-105 |
| Figure 13-39 | South Inner-Half Annulus Compartment | 13-110 |
| Figure 13-40 | South Inner-Half Annulus Cross-Section – BB | 13-111 |
| Figure 13-41 | South Inner-Half Annulus Cross-Section – AA | 13-112 |
| Figure 13-42 | North Inner-Half Annulus Compartment | 13-117 |
| Figure 13-43 | North Inner-Half Annulus Cross-Section – AA | 13-118 |
| Figure 13-44 | North Inner-Half Annulus Cross-Section – AA | 13-119 |
| Figure 13-45 | North Mid-Quarter Annulus Compartment | 13-125 |
| Figure 13-46 | North Mid-Quarter Annulus Cross-Section – BB | 13-126 |
| Figure 13-47 | North Mid-Quarter Annulus Cross-Section – AA | 13-127 |
| Figure 13-48 | West Mid-Quarter Annulus Compartment | 13-132 |
| Figure 13-49 | West Mid-Quarter Annulus Cross-Section – BB | 13-133 |
| Figure 13-50 | West Mid-Quarter Annulus Cross-Section – AA | 13-134 |
| Figure 13-51 | South Mid-Quarter Annulus Compartment | 13-140 |
| Figure 13-52 | South Mid-Quarter Annulus Cross-Section – BB | 13-141 |
| Figure 13-53 | South Mid-Quarter Annulus Cross-Section – AA | 13-142 |
| Figure 13-54 | East Mid-Quarter Annulus Compartment | 13-146 |
| Figure 13-55 | East Mid-Quarter Annulus Cross-Section – BB | 13-147 |
| Figure 13-56 | East Mid-Quarter Annulus Cross-Section – AA | 13-148 |
| Figure 13-57 | North Outer Quarter Annulus Cross-Section | 13-153 |
| Figure 13-58 | North Outer Quarter Annulus Cross-Section – BB | 13-154 |
| Figure 13-59 | North Outer Quarter Annulus Cross-Section – AA | 13-155 |
| Figure 13-60 | West Outer Quarter Annulus Compartment | 13-160 |
| Figure 13-61 | West Outer Quarter Annulus Cross-Section – BB | 13-161 |
| Figure 13-62 | West Outer Quarter Annulus Cross-Section – AA | 13-162 |
| Figure 13-63 | South Outer Quarter Annulus Compartment | 13-167 |
| Figure 13-64 | South Outer Quarter Annulus Cross-Section – BB | 13-168 |
| Figure 13-65 | South Outer Quarter Annulus Cross-Section – AA | 13-169 |
| Figure 13-66 | East Outer Quarter Annulus Compartment | 13-174 |
| Figure 13-67 | East Outer Quarter Annulus Cross-Section – BB | 13-175 |
| Figure 13-68 | East Outer Quarter Annulus Cross-Section – AA | 13-176 |
| Figure 13-69 | East Quarter Inner Dome Cross-Section – BB | 13-179 |
| Figure 13-70 | East Quarter Inner Dome Cross-Section – AA | 13-181 |
| Figure 13-71 | North Quarter Inner Dome Cross-Section – BB | 13-184 |
| Figure 13-72 | North Quarter Inner Dome Cross-Section – AA | 13-185 |
| Figure 13-73 | West Quarter Inner Dome Cross-Section – BB | 13-187 |
| Figure 13-74 | West Quarter Inner Dome Cross-Section – AA | 13-190 |
| Figure 13-75 | South Quarter Inner Dome Cross-Section – BB | 13-193 |
| Figure 13-76 | South Quarter Inner Dome Cross-Section – AA | 13-194 |
| Figure 13-77 | East Quarter Outer Dome Cross-Section – BB | 13-197 |

LIST OF FIGURES (cont.)

| | | |
|---------------|--|--------|
| Figure 13-78 | East Quarter Outer Dome Cross-Section – AA | 13-198 |
| Figure 13-79 | North Quarter Outer Dome Cross-Section – BB | 13-201 |
| Figure 13-80 | North Quarter Outer Dome Cross-Section – AA | 13-202 |
| Figure 13-81 | West Quarter Outer Dome Cross-Section – BB | 13-205 |
| Figure 13-82 | West Quarter Outer Dome Cross-Section – AA | 13-206 |
| Figure 13-83 | South Quarter Outer Dome Cross-Section – BB | 13-209 |
| Figure 13-84 | South Quarter Outer Dome Cross-Section – AA | 13-210 |
| Figure 13-85 | Outside Containment Upflow Annulus Cross-Section – BB | 13-213 |
| Figure 13-86 | Outside Containment Downflow Annulus Cross-Section – BB | 13-218 |
| Figure 13-87 | PCS Chimney Cross-Section – BB | 13-221 |
| Figure 13-88 | <u>W</u> GOTHIC Conductor Noding Example | 13-223 |
| Figure 13-89 | Wet/Dry Clime Modeling Diagram | 13-254 |
| Figure 13-90 | Containment, Baffle, Shield Building Modeling with Climes | 13-255 |
| Figure 13-91 | Wet Stack Clime Numbering Diagram | 13-256 |
| Figure 13-92 | Dry Stack Clime Numbering Diagram | 13-272 |
| Figure 13-93 | AP1000 Evaluation Model LOCA Function 3: PCS Evaporation Limited Film Flow Rate | 13-288 |
| Figure 13-94 | AP1000 Evaluation Model LOCA Function 2: IRWST Drain Rate | 13-293 |
| Figure 13-95 | AP1000 Evaluation Model LOCA Function 4: Drop Diameter Multiplier | 13-294 |
| Figure 13-96 | AP1000 Evaluation Model LOCA Function 5: Two-Phase Mass Flow | 13-295 |
| Figure 13-97 | AP1000 Evaluation Model LOCA Function 6: Two-Phase Enthalpy | 13-296 |
| Figure 13-98 | AP1000 Evaluation Model LOCA Function 7: Steam Phase Mass Flow | 13-297 |
| Figure 13-99 | AP1000 Evaluation Model LOCA Function 8: Steam Phase Enthalpy | 13-298 |
| Figure 13-100 | AP1000 Evaluation Model Function 9: Blowdown Heat Transfer Coefficient Multiplier | 13-299 |
| Figure 13-101 | ADS Evaluation Model Function 10: ADS-4 Steam Flow Rate | 13-300 |
| Figure 13-102 | AP1000 Evaluation Model Function 11: Sump Drain Rate | 13-301 |
| Figure 13-103 | AP1000 Evaluation Model Functions 14, 16, 18 and 20: MSLB Mass Flow Rate | 13-302 |
| Figure 13-104 | AP1000 Evaluation Model Functions 13, 15, 17 and 19: MSLB Enthalpy | 13-303 |
| Figure 13-105 | AP1000 <u>W</u> GOTHIC Evaluation Model Section B-B | 13-323 |
| Figure 13-106 | AP1000 <u>W</u> GOTHIC Evaluation Model Section A-A | 13-324 |
| Figure 13-107 | AP1000 <u>W</u> GOTHIC Evaluation Model 135'-3" Elevation | 13-325 |
| Figure 13-108 | AP1000 <u>W</u> GOTHIC Evaluation Model 148'-0" Elevation | 13-326 |
| Figure 13-109 | AP1000 <u>W</u> GOTHIC Evaluation Model 170'-0" Elevation | 13-327 |
| Figure 13-110 | AP1000 <u>W</u> GOTHIC Evaluation Model 189'-6" Elevation | 13-328 |
| Figure 13-111 | AP1000 <u>W</u> GOTHIC Evaluation Model 209' Elevation | 13-329 |
| Figure 13-112 | AP1000 <u>W</u> GOTHIC Evaluation Model 226'-0" Elevation | 13-330 |
| Figure 13-113 | AP1000 <u>W</u> GOTHIC Evaluation Model 250'-3" Elevation | 13-331 |
| Figure 13-114 | AP1000 <u>W</u> GOTHIC Model 266' Elevation | 13-332 |

LIST OF FIGURES (cont.)

| | | |
|---------------|---|--------|
| Figure 13-115 | AP1000 <u>W</u> GOTHIC Evaluation Model 279'-10" Elevation | 13-333 |
| Figure 13-116 | Containment Pressure | 13-338 |
| Figure 13-117 | Riser Air Temperatures | 13-338 |
| Figure 13-118 | Annulus Flow Rate | 13-339 |
| Figure 13-119 | External Shell Heat Rate | 13-339 |
| Figure 13-120 | Sump/CMT Compartment Liquid Levels | 13-340 |
| Figure 13-121 | East SG Compartment Liquid Level | 13-340 |
| Figure 13-122 | West SG Compartment Liquid Level | 13-341 |
| Figure 13-123 | Refueling Cavity Liquid Level | 13-341 |
| Figure 13-124 | AP1000 Containment Response for Full DER MSLB | 13-342 |
| Figure 13-125 | <u>W</u> GOTHIC Minimum Pressure Response for DEDVI Break – Small-Break LOCA Phase | 13-345 |
| Figure 14.3-1 | Spreadsheet Mass and Energy Release Schematic | 14-8 |
| Figure 14.4-1 | Mass Release Comparison | 14-10 |
| Figure 14.4-2 | Energy Release Comparison | 14-10 |
| Figure 14.4-3 | Mass Release Comparison | 14-11 |
| Figure 14.4-4 | Energy Release Comparison | 14-11 |
| Figure 14.4-5 | Integrated Mass Comparison | 14-12 |
| Figure 14.4-6 | Integrated Energy Comparison | 14-12 |
| Figure 14.4-7 | LOCA Transient Comparison | 14-13 |

LIST OF ACRONYMS AND ABBREVIATIONS

| | |
|----------------|--|
| CFD | Computational Fluid Dynamics |
| CMT | Core Makeup Tank |
| CVS | Chemical and Volume Control System |
| DBA | Design Basis Accident |
| DBE | Design Basis Event |
| DECLG | Double-Ended Cold Leg Guillotine |
| EM | Evaluation Model |
| HDR | Heissdampfreaktor |
| HVAC | Heating, Ventilation, and Air Conditioning |
| IRWST | Internal Refueling Water Storage Tank |
| LOCA | Loss-of-Coolant Accident |
| LST | Large-Scale Tests |
| M&E | Mass & Energy |
| MIT | Massachusetts Institute of Technology |
| MSLB | Main Steamline Break |
| NAI | Numerical Applications, Inc. |
| NUPEC | Nuclear Power Engineering Corporation |
| PCS | Passive Containment Cooling System |
| PIRT | Phenomena Identification and Ranking Table |
| RCS | Reactor Coolant System |
| SG | Steam Generator |
| SRP | Standard Review Plan |
| SSAR | Standard Safety Analysis Report |
| STC | Science & Technology Center |
| TS | Technical Specifications |
| UWO | University of Western Ontario |
| <u>WGOTHIC</u> | Westinghouse-GOTHIC |

Section 1

Introduction

TABLE OF CONTENTS

LIST OF FIGURES iii

1.0 INTRODUCTION 1-1

1.1 OBJECTIVE 1-1

1.2 AP600 CONTAINMENT DBA REPORTS 1-1

1.2.1 Accident Specification and Phenomena Identification and
Ranking Table Report 1-1

1.2.2 Scaling Report 1-3

1.2.3 Heat and Mass Transfer Correlations Report 1-5

1.2.4 WGOTHIC Code Description and Validation 1-5

1.2.5 SSAR 1-6

1.3 AP1000 CONTAINMENT DBA REPORTS 1-6

1.4 APPLICATIONS REPORT CONTENT SUMMARY 1-8

1.5 USE OF LST AND VALIDATION RESULTS 1-10

1.5.1 LST Matrix Tests 1-11

1.5.2 Use of LST Separate Effects Data 1-12

1.5.3 LST Confirmation of Phenomena 1-12

1.5.4 Code Comparison to LST as an Integral Test 1-13

1.5.5 Lumped Parameter Biases 1-13

1.6 INTERFACE WITH DCD CALCULATIONS 1-13

1.6.1 Upgrade of WGOTHIC Version 4.1 to Version 4.2 1-14

1.6.2 Changes in the Evaluation Model Input 1-14

1.7 CONCLUSIONS 1-15

1.8 REFERENCES 1-15

LIST OF FIGURES

Figure 1-1 Relationship of AP600 Containment DBA Reports 1-2

1.0 INTRODUCTION

1.1 OBJECTIVE

The computer code used for both the AP600 and AP1000 containment pressure design basis accident (DBA) analyses is WGOTHIC. WGOTHIC is used to calculate a conservative containment pressure transient response and to specify temperatures for equipment qualification. The containment DBA analysis makes use of the lumped parameter approach which is based on 30 years of nuclear industry experience. The industry experience has identified lumped parameter limitations and biases that are due primarily to the oversimplification of the momentum formulation. Limitations and biases have been identified based on international tests at different scales (Section 9). Biases and conservatism are applied to models for important phenomena in the WGOTHIC Evaluation Model to develop a bounding methodology, so that containment pressure is conservatively estimated.

This report describes specific modeling and defines methods used to develop conservative input for the WGOTHIC code to create a bounding Containment Evaluation Model. Using design parameters specified in the Design Control Document (DCD), the licensing basis Containment Evaluation Model is used to calculate the design basis pressures and temperatures reported in the DCD. (See Section 1.6 for a discussion of updates made for DCD calculations.)

1.2 AP600 CONTAINMENT DBA REPORTS

As shown in Figure 1-1, this report fits into the framework of licensing documentation which defines the containment DBA methods. Following is a brief summary of the purposes of the AP600 containment DBA reports.

1.2.1 Accident Specification and Phenomena Identification and Ranking Table Report

WCAP-14812 (Ref. 1.1) describes the containment and passive containment cooling system (PCS), defines DBA accidents, identifies success criteria, and ranks the importance of phenomena that must be considered. A cross-reference to relevant tests and test data reports is also included. A systematic process has been followed to identify and rank phenomena, including input and review by members of industry, academia, and regulatory authorities.

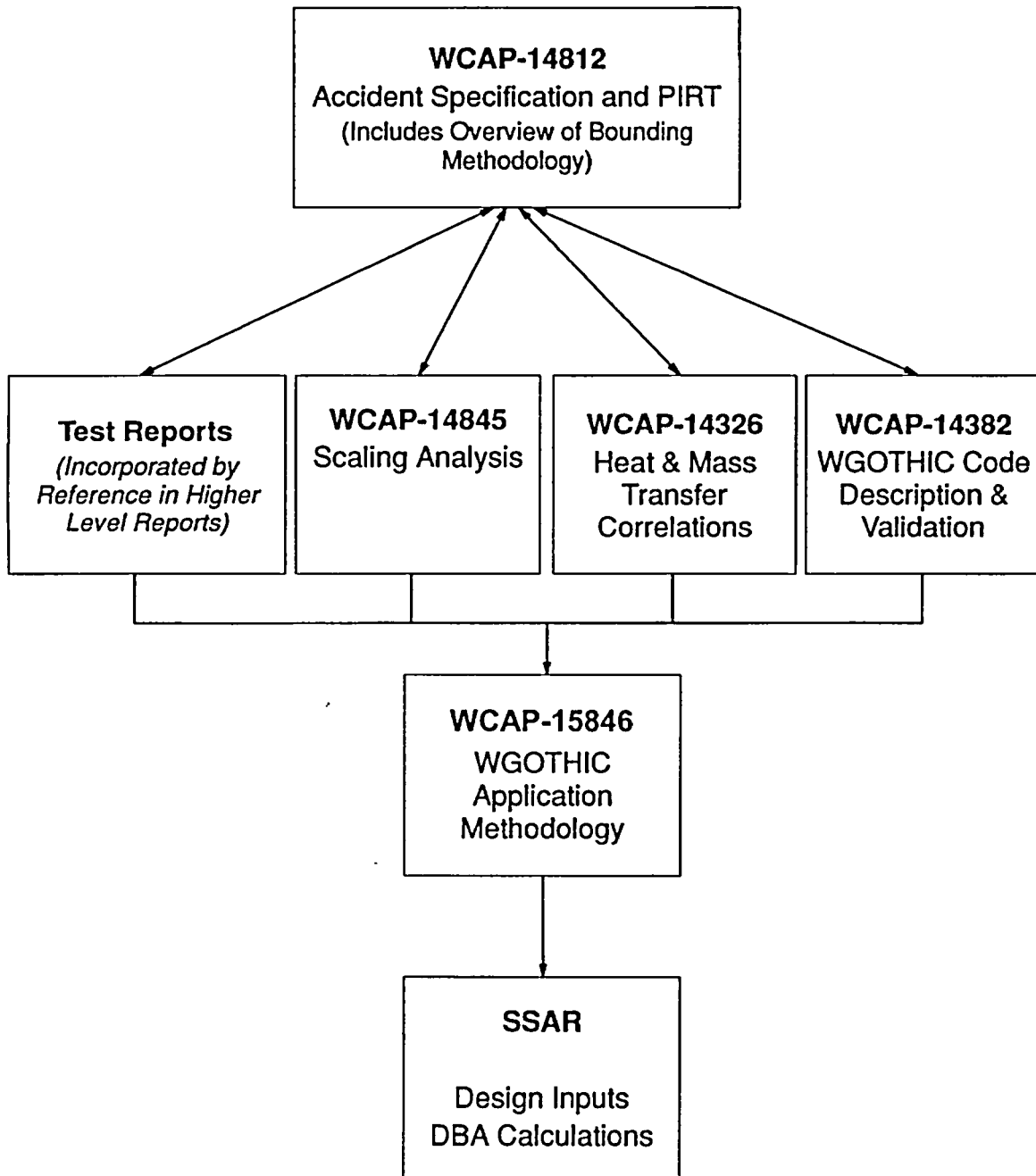


Figure 1-1 Relationship of AP600 Containment DBA Reports

As a convenient vehicle for defining the Evaluation Model approach, the following information is provided in WCAP-14812 for each phenomenon:

- Phenomena identification ranking table (PIRT) ranking
- Basis for PIRT ranking
 - Test results
 - Scaling results
 - Sensitivity studies
 - Expert review
- How phenomena are implemented in the Evaluation Model
- Justification of Evaluation Model treatment of phenomenon
 - Test experience
 - Modeling guidance
 - Sensitivity studies
- Evaluation Model treatment of uncertainty

1.2.2 Scaling Report

The application of scaling to a specific methodology is related to the type of analysis being performed and the regulatory needs to be satisfied. The regulations require supporting documentation for the use and sufficiency of the database to develop bounding models for the full-scale AP600 containment pressure transient. The objectives for the scaling of the AP600 pressure transient and the approximately 1/8 geometric scale test vessel, called the Large-Scale Test (LST), are derived from regulations and regulatory guides. WCAP-14845 (Ref. 1.2) describes how scaling has been used to derive the appropriate nondimensional parameters and their AP600 ranges to examine phenomena for bottom-up model validation. Separate Effects Tests (SETs) are identified and the test parameter ranges compared to AP600 ranges to show sufficiency of the test database for application to containment DBAs. Scaling is used to identify distortions in the LST that are then addressed in the bounding methodology.

The following shows how objectives are met for scaling in support of AP600 containment DBA methods.

The scaling analysis in WCAP-14845 (Ref. 1.2) satisfies the three stated objectives for AP600 containment pressure scaling. The conclusions of the scaling analysis are:

1. Support Development of Bounding Methodology (PIRT Confirmation)

The scaling analysis confirmed the identification in the PIRT (Reference 1.1, Table 4-1) of high ranked phenomena. The high ranked phenomena inside containment are the break source, gas compliance, and condensation on the shell and heat sinks. The high ranked phenomena outside containment are evaporation of the external liquid film and the PCS natural circulation flow rate. In addition, the scaling analysis confirmed the PIRT ranking of lower order phenomena including convection and radiation heat transfer, liquid film conductance, and liquid film energy transport.

The high ranked phenomena and the parameters that most strongly affect them are the ones that must be bounded in the evaluation model. Phenomena and how they are bounded in the evaluation model are described in Section 4.4 of Reference 1.1.

The net effect of these is an evaluation model that bounds all the dominant processes so as to produce the maximum pressure response.

2. Specify Individual Model Constitutive Relations.

The range of AP600 dimensionless groups for each of the separate effects test database has been shown to be adequately covered.

Appropriate constitutive relations and models were identified for each of the dominant phenomena and parameters in 1 above:

Condensation and evaporation are modeled using conventional free and forced convection mass transfer relationships, characterized by Reynolds, Grashof, and Schmidt numbers. The range of these dimensionless variables necessary to cover AP600 operation was defined and separate effects tests were identified and used to validate the selected mass transfer correlations. The range of dimensionless variables in the data were shown to encompass the expected range of operation in AP600.

3. Investigate Use of LST to Validate Elements of the Bounding Evaluation Model

Steady state heat and mass transfer correlations have been shown to be applicable for the AP600 double-ended cold-leg guillotine (DECLG) loss-of-coolant accident (LOCA) and main steam line break (MSLB) DBA pressure transients. The LST was used as a source of separate effects data to validate condensation and evaporation mass transfer, film stability, and circulation and stratification models as discussed under 1 and 2 above. Component level distortions in the LST were addressed

by using local measurements of temperature, concentration, and velocity from the LST, and by supplementing the LST data with data from other sources when the range of LST parameters was insufficient to cover AP600 operation.

The scaling analysis shows the three dominant system level phenomena for the transient phase are the break source energy addition, the gas volume, and the heat sink surface area dependent condensation energy removal rate. The scaling analysis shows that the LST system level phenomena are distorted in the transient phase relative to AP600, but are well-scaled in the quasi-steady phase.

The LST is therefore not used as a system level representation of AP600 transient pressure response. However, the steady-state LST data is acceptable for use as separate effects data for the following models:

- Internal condensation
- Internal above-deck steam distribution
- External dry heat transfer
- External water coverage (film stability)

The use of the LST in support of code validation is summarized in Section 1.4.

1.2.3 Heat and Mass Transfer Correlations Report

WCAP-14326 (Ref. 1.3) documents the analytical and experimental bases for heat and mass transfer correlations associated with:

- Condensation mass transfer
- Evaporation mass transfer
- Convective heat transfer
- Liquid film thermal resistance

For modeling convenience, an explicit representation of the liquid film thermal resistance is modeled, with condensation or evaporation occurring at the film surface. This is in contrast to the more traditional approach of combining mass transfer and liquid film resistance and then using the solid surface temperature. The explicit representation allows clearer treatment of elements of uncertainty in mass transfer and liquid film over the AP600 range of conditions.

1.2.4 WGOthic Code Description and Validation

WCAP-14382 (Ref. 1.4) documents the implementation of "climes" subroutines in the GOTHIC code. Climes are used to represent heat and mass transfer on the containment shell, shield building, and baffle. The report shows comparisons to the LST using both lumped parameter and distributed parameter models,

identifies lumped parameter biases and competing effects based on the LST calculations, and describes the derivation of nodding guidance for the AP600 Evaluation Model. WGOTHIC verification and validation has been completed using calculations of separate effects tests (Reference 1.4, Section 4 and Reference 1.3, Sections 3.1 and 3.3). An assessment of the effects of a WGOTHIC Solver Upgrade from 1.2 (used in Reference 1.4) to 4.1 has shown that code validation conclusions remain valid (Reference 1.7).

1.2.5 SSAR

The methodology in the WGOTHIC Application Report is used, along with design input specified in Section 1.6, to perform the licensing basis DBA containment calculations reported in the AP600 SSAR, Chapter 6.2.

1.3 AP1000 CONTAINMENT DBA REPORTS

Both the AP1000 and AP600 employ a Passive Containment Cooling System (PCS). The AP1000 containment structure is taller, but maintains the same diameter and internal layout as the AP600. A detailed comparison of the AP600 and AP1000 plant designs is provided in WCAP-15612 (Reference 1.8).

The capability requirements for the AP1000 Containment Evaluation Model are the same as AP600. To be able to model the PCS, the Evaluation Model must be able to model:

- The transport of break mass and energy (steam) to the containment shell
- The condensation of steam on the inside surface of the containment shell
- The transport of the condensate film on the inside surface of the containment shell
- The conduction of heat through the containment shell
- The transport and heating of the applied liquid film on the outside surface of the containment shell
- Evaporation from the applied liquid film on the outside surface of the containment shell and
- The natural draft cooling air flowing through the downcomer, riser and chimney of the shield building.

Westinghouse developed special subroutines to mechanistically calculate the heat and mass transfer and to track the liquid films for the PCS. These subroutines were appended to the GOTHIC version 4.0 code to create WGOTHIC version 4.2.

To determine the applicability of using the WGOTHIC code (version 4.2) and AP600 Containment Evaluation Model methodology for performing the AP1000 containment DBA analyses, Westinghouse:

- Reviewed the AP600 containment PIRT (WCAP-14812) for application to the AP1000
- Reviewed the AP600 containment scaling analysis (WCAP-14845) for application to the AP1000 and
- Compared the test data ranges of the important dimensionless parameters for heat and mass transfer and water coverage with the operating range for the AP1000.

The AP600 containment PIRT was reviewed to determine if there were any new phenomena or any change in the importance ranking of the existing phenomena with respect to the AP1000 containment and reactor coolant system (RCS) design changes. This review was documented in WCAP-15613 (Reference 1.9, Section 2.6). No new phenomena were identified and there were no significant changes in the ranking of phenomena as a result of the AP1000 design changes.

An LST scaling assessment was performed for AP1000 and compared with AP600 (Reference 1.9, Section 4.2). Due to its relatively low and constant steam injection flow rate, the LST was not well scaled to model the blowdown transient for either AP600 or AP1000. The steady-state LST data were determined to be acceptable for use as a source of separate effects test data for internal condensation, above-deck steam distribution, external heat transfer, and external water coverage.

The ranges of the dimensionless parameters for the heat and mass transfer correlations were examined to determine if the existing test data covered the AP1000 operating range (Reference 1.9, Section 4.2). The test data covered the upper range of the AP1000 dimensionless parameters for the heat and mass transfer correlations in the important riser region of the annulus. Therefore, the correlations were also considered to be valid for the AP1000 containment Evaluation Model.

Experimental test data and correlations were reviewed to determine if the increase in containment height would affect the circulation within the open volume above the operating deck. Both the correlations and test data suggest that increasing the containment height would increase the turbulence and improve the mixing (see Section 9C).

An alternate analysis methodology was used to independently assess the degree of mixing in the open volume above the operating deck. Detailed, 2-dimensional slice Computational Fluid Dynamics (CFD) models representing this region were constructed for both the AP600 and the AP1000 (Reference 1.9, Section 4.2). The flow and velocity patterns for the AP600 and AP1000 were very similar. Both models predicted cold falling plumes near the walls and a hot rising plume near the center of the volume. Except for the small layers very close to the walls and within the central plume, the temperature profile within the volume was nearly uniform. Therefore, based on the experimental test data, correlations, and results from the alternate

analysis approach, the well-mixed assumption for this region was also considered to be valid for the AP1000 Containment Evaluation Model.

The operating ranges of the liquid film coverage parameters for AP600 and AP1000 were compared to the composite PCS test data. The test data covered the operating range of the important film coverage parameters (minimum film Reynolds number and maximum heat flux) for both AP600 and AP1000. Therefore, the constant coverage area input values and the model for calculating the evaporation-limited PCS water flow rate input that was used for AP600 are also applicable to the AP1000.

In summary, both the AP600 and AP1000 employ the same passive containment cooling system design features so the events and phenomena to be analyzed in the AP1000 Containment Evaluation Model are the same as the AP600. The range of important dimensionless parameters from the PCS test data covers the operating range of both the AP600 and AP1000, so the WGOTHIC heat and mass transfer correlations remain acceptable. Since the containment designs are similar and since the heat and mass transfer correlations remain acceptable, WGOTHIC source code changes are not required for the AP1000 Containment Evaluation Model. Therefore, a containment evaluation model that uses the same bounding methodology that was accepted by the NRC for the AP600 should also be acceptable for the AP1000.

1.4 APPLICATIONS REPORT CONTENT SUMMARY

The Introduction outlines the containment DBA analysis approach, summarizes the use of the LST, and shows how the Evaluation Model methods are incorporated in the containment DBA analysis reported in SSAR 6.2 for long-term loss-of-coolant accidents (LOCA) and main steamline breaks (MSLB). Subsequent sections document elements of the methodology, as follows.

Section 2 contains a summary of high and medium ranked phenomena. This section describes the process used to develop the bounding Containment Evaluation Model. Each step or element in the process is briefly described, and those phenomena that were determined to be of high or medium rank are presented, with a summary of how those phenomena are addressed by the WGOTHIC Evaluation Model.

Section 3 presents an overview of the Westinghouse-GOTHIC code package. The WGOTHIC features, development history, and validation programs are briefly described. The models and features that were added by Westinghouse to adapt GOTHIC to model the PCS are also described. (See Section 1.5 for summary of WGOTHIC code updates for DCD analysis.)

Section 4 presents the geometric input for the WGOTHIC design basis Evaluation Model of the AP600 using design inputs specified in this report. In this section, the code inputs are described for the AP600 model geometry. The code inputs include free volumes, elevations, heat sink characteristics, and boundary conditions. Graphics are included which aid in visualizing both the AP600 layout and the WGOTHIC model of the AP600. The methodology defined in this section is used for the Evaluation Model. (See Section 1.6 and Appendices 4.A and 4.B for input model updates for the DCD analysis.)

Section 5 contains a number of sensitivity cases varying the initial conditions assumed for the design basis analyses. These include sensitivities on initial containment humidity, initial containment pressure, initial containment temperature, outside humidity, outside temperature, and boundary condition drop assumptions. Except as noted specifically for a sensitivity study, all sensitivities in this report are based on the base case Evaluation Model described in Section 4. This section provides the basis for choosing the conservative initial conditions assumed for the DBA analyses.

Section 6 describes the effects of meteorological changes on the performance of the PCS. In this section the effects of PCS effluent entrainment into the PCS inlet are studied. In addition to recirculation, the effects of wind on PCS performance are identified. The results of these studies show that wind effects are beneficial to containment cooling since they augment the natural draft velocity that develops during PCS operation. The effluent recirculation due to inversions or strong winds is shown to have a negligible effect on PCS performance and containment pressure response.

Section 7 supplies the methodology for calculating the PCS applied water flow rate input for the Containment Evaluation Model. Based on conservatively bounding liquid film test data from various tests, the coverage and evaporation rate are conservatively calculated, and only the amount of water which evaporates is applied to the Evaluation Model. Thus, there is a conservative bound on the amount of evaporative cooling credited in the Evaluation Model. The implementation of evaporation limited flow applied in the Evaluation Model also conservatively underpredicts subcooled liquid film heat removal from containment. The basis for the delay time in the application of the film as well as the coverage areas and other parameters are presented. Sensitivities to coverage area and other parameters are presented which demonstrate the conservatism in the method used to determine the water coverage.

Section 8 presents the sensitivity of the AP600 blowdown pressurization transient. The PCS model that uses climes is compared to a single volume model of the AP600 created based on Standard Review Plan (SRP) methodologies. The single volume model uses WGOTHIC conductors to model the containment shell instead of the clime model and uses the Uchida heat transfer correlation instead of the Westinghouse-developed clime heat and mass transfer correlations. The results of this comparison show that there is very little difference between the two models for the blowdown phase of the transient. A sensitivity to heat sinks during blowdown is also presented.

Section 9 addresses circulation and stratification within the AP600 containment. Circulation and stratification can be affected by break location, orientation, and type, in addition to nodding assumptions. The effects of circulation and stratification inside the containment are assessed for an MSLB and the various time phases (i.e., blowdown, refill, peak pressure, and long-term) of a LOCA. The effects of circulation above the operating deck for both the AP600 and AP1000 were also examined in Reference 1.9, Section 4.2. Based on these results, biases have been incorporated into the Containment Evaluation Model as described in Sections 4, 13 and 9.

Section 10 describes the conservatism contained in some Evaluation Model assumptions made for the design basis LOCA and MSLB analysis that are intended to maximize the peak pressure. In this section, the conservatism in the heat and mass transfer biases, the initial conditions for inside and outside of containment, PCS water temperature, material properties, steel-concrete gap, external annulus loss coefficient, dead-ended compartment modeling biases, and the LOCA mass and energy releases are described in a step-wise fashion. The final result is a quantification of the conservatism contained in the Evaluation Model in the above parameter. Based on these sensitivities, there is approximately 13 psi of margin in the AP600 design basis analysis second peak pressure as compared to the nominal case second peak. Since the nominal case maximum pressure occurs during blowdown, there is approximately 11.5 psi of margin in the maximum calculated pressure between the AP600 design basis case and the nominal case. It should be noted that the nominal case only credits conservatisms that can be readily quantified. A similar sensitivity for the net effect of parameters important in the MSLB analysis is also provided.

Section 11 describes the sensitivity of WGOTHIC to changes in the calculated timestep size. The timestep selection logic was modified to reduce the calculated timestep by one-half and by one-quarter in separate cases. The results of this sensitivity show that the solution is stable, in that the pressure transients did not change appreciably as the timestep size was reduced. This result supports the conclusion that the timestep logic used in WGOTHIC is acceptable.

Section 12 examines the sensitivity of the predicted containment pressure transient to changes in clime noding. Results support the noding used to represent volumes, elevations, and azimuthal segments in the external annulus, as well as the numerical mesh pattern through conductors.

Section 13 presents the geometric input for the WGOTHIC design basis Evaluation Model of the AP1000 using design inputs specified in this report. In this section, the code inputs are described for the AP1000 model geometry. The code inputs include free volumes, elevations, heat sink characteristics, and boundary conditions. Graphics are included which aid in visualizing both the AP1000 layout and the WGOTHIC model of the AP1000. The methodology defined in this section is used for the licensing basis DCD Evaluation Model.

The methodology specified in the above sections is used, together with design inputs specified in Section 1.6, to perform the licensing basis calculations in Section 6.2 of the DCD.

1.5 USE OF LST AND VALIDATION RESULTS

In the mid-1980s, Westinghouse developed the LST as an integral test to provide steady-state heat and mass transfer data for a geometrically similar model of the AP600 containment vessel. The focus was on long-term transient behavior, because that is where the passive containment design, with no credited active heat removal system, differed significantly from the current containment test databases. Because of limitations of scale (power-to-volume and power-to-area ratios, and steam supply), the LST matrix was

selected to vary boundary conditions parametrically to obtain data over a range of parameters. Specific passive containment pressure transients were not simulated with the LST.

The LST was designed to provide steady-state heat and mass transfer data in an integral setting, that is, with external evaporation and internal condensation acting simultaneously, for a geometrically similar model of the AP600 containment vessel (Reference 1.5, Section 3.2.4.2). The use of the LST has been supported through the application of scaling methodologies that have evolved during the 1990s.

As discussed in subsection 1.2.2, local data from the LST has been combined with other SETs and integral effects tests (IETs) at different scales to provide supporting data for the following phenomena:

- Dry external riser annulus heat transfer
- External liquid film stability
- Internal condensation mass transfer
- Internal stratification

1.5.1 LST Matrix Tests

The LST matrix was developed to contain parametric variations that examined various extremes and combinations of boundary condition effects. In this way, the LST was ranged similarly to a SET.

In addition to the more obvious matrix test parameters, such as steam flow, experience with the international containment test database pointed to the need to examine the effects of boundary condition parameters on distributions of noncondensables inside containment. The following provides a brief overview of the parametric variations included in the LST matrix (Ref. 1.6, Tables 1.3-1, 1.3-2, and 1.3-3).

- The LST matrix was designed to cover a range of pressure. Air and helium were used as noncondensables, and steam was used as the working fluid. Therefore, the important thermodynamic properties of the containment atmosphere in both the AP600 and AP1000 are preserved.
- Water flow rates, and thus shell coverage, were varied to obtain various degrees of coverage and to examine water film behavior through complete dryout on the sidewall. In addition to quantitative recorded test data, videotapes and engineering notes were taken to characterize the qualitative behavior of the liquid film.
- The matrix was defined to address the effect of external cooling on stratification which has been suggested in international tests (Appendix 9.C). For example, LST 219.1 applied water to the external shell surface starting from dry conditions. To gain further insight, additional parametric variation of external transients were examined in LST 214.1, 215.1, 216.1, 221.1, by suddenly varying water coverage and air flow rates during the course of a test. This is in addition to the test-to-test parametric variations in external conditions.

- Transients initiated by a larger "blowdown" steam flow rate, relative to the steady-state tests, were included. The LST did not include blowdown mass flow rates scaled to the AP600 or AP1000 due to limitations on steam supply. The LST blowdown transients (LST 220.1, 221.1, 222.1, 222.2) include the influence of an initial rapid pressurization on the subsequent quasi-steady heat and mass transfer rates. The transients also provided code validation of transient performance with reductions in steam flow.
- Tests were included to examine the influence of break elevation and momentum (LST 222.1, 222.2, 222.3, 222.4) to support evaluation of the various LOCA and MSLB break locations and orientations.
- Tests with initial vacuum (LST 223.1) and initially pressurized to two atmospheres (LST 224.1, 224.2) were included to range the effect of noncondensable content in the containment.
- Tests were included to provide parameter variations specifically to validate elements of the Evaluation Model. These parameter variations were external loss coefficient (LST 215.1); natural convection (LST 206.1, 211.1, 214.1, 215.1) versus the fan used at various speeds to replace the external density head; and circumferential variations in inlet blockage (LST 215.1).
- In the containment DBA, there is no appreciable source of hydrogen to containment (Ref. 1.1, Section 4.4.2E). As part of the DBA testing program, data were taken to supplement the literature for postulated severe accidents. Helium was introduced into the LST primarily to study the effects of additional noncondensables. Helium was shown to be a good simulant of hydrogen in the German HDR tests. Sampling of noncondensable content (LST 212.1, 217.1, 218.1, 219.1, 220.1, 221.1, 222.1, 222.2, 222.3, 222.4, 223.1, 224.1, 224.2) was included at four elevations, including helium content measurement where applicable.

1.5.2 Use of LST Separate Effects Data

Scaling has been used to assess the use of the LST to supplement the smaller scale separate effects data (Ref. 1.2, Sections 10.1 and 11.3). Separate effects test data from the LST is used to support validation of the condensation correlation applied to the inner steel shell surface (Ref. 1.3, Section 3.9) and to examine potential stratification effects in an enclosed volume in an integral setting with external cooling (Section 9). Water coverage and film stability data were used to develop a bounding model to address the effects of film stability (Section 7). External dry heat transfer data have been used to supplement convective heat transfer data (Ref. 1.3, Section 3.5).

1.5.3 LST Confirmation of Phenomena

The LST data have been used to validate the system scaling equation used to support the identification and ranking of phenomena (Ref. 1.2, Section 10.2).

1.5.4 Code Comparison to LST as an Integral Test

Analyses of the LST have been completed using the WGOTHIC lumped parameter momentum formulation. In the LST calculations, nominal properties and nominal test boundary and initial conditions were used to isolate the biases inherent in the computer code, independent of conservatism included in the Evaluation Model. This allowed the examination of the known lumped parameter biases, and quantification of the effects of compensating errors in lumped parameter results. The method to address the lumped parameter biases, as well as the method used to address phenomena for the Evaluation Model are documented (Ref. 1.1, Section 4.4).

The containment DBA analysis approach is based on the lumped parameter formulation. Examination of LST WGOTHIC lumped parameter results identified compensating effects (velocity and steam concentration) that have been bounded in the application to the AP600 and the AP1000 by using free convection on interior surfaces. By using free convection, the effect of computed velocity is eliminated, and effects of steam concentration distribution can then be separately bounded.

1.5.5 Lumped Parameter Biases

The lumped parameter Evaluation Model does not resolve internal velocity and concentration fields due to its simplified momentum model and large lumped volumes. Comparisons between preliminary versions of the Evaluation Model and the system level LST response showed that pressure was reasonably well predicted, with a modest conservative margin. Examination of internal processes clearly identified the existence of competing internal effects in which the excessive velocities predicted by the lumped parameter model overpredicted the velocity component of mass transfer, while overmixing underpredicted the steam concentration component of mass transfer. Consequently, these competing effects in predictions are addressed. The effect of overpredicted velocities was resolved by using only free convection for internal heat and mass transfer, thereby eliminating velocity from the condensation correlation. The overmixing issue was resolved by examining and biasing the effects of circulation and stratification in the Evaluation Model as discussed in Section 9.

1.6 INTERFACE WITH DCD CALCULATIONS

The licensing basis containment DBA pressure analysis reported in Section 6.2 of the DCD is performed with the WGOTHIC Evaluation Model, defined by methodology described herein. The following design inputs are required as input to the Evaluation Model methodology:

- PCS delivered flow as a function of time assuming failure of one PCCWST drain valve to open.
- Conservatively calculated mass and energy releases as a function of time, using approved methodology (DCD 6.2.1.3.2 for LOCA and DCD 6.2.1.4 for MSLB).

- Appropriate Technical Specification and Site Interface Parameters for initial and boundary conditions (DCD 16.1, Section 3.6 and 2.3).

The results of the Evaluation Model are used for design pressure evaluation and equipment qualification condition specifications, as reported in DCD Appendix 3D. Evaluation Model methodology considers DBA phenomena so that the predicted containment pressure has sufficient margin to bound uncertainty in important parameters. The temperature of the break room node is the maximum temperature in containment and is used for input to equipment qualification envelopes to bound the effects of temperature distributions.

1.6.1 Upgrade of WGOTHIC Version 4.1 to Version 4.2

The DCD DBA pressure transients (DECLG LOCA and MSLB) have been calculated using WGOTHIC version 4.2. Identified errors in the WGOTHIC clime subroutines, that were previously evaluated to have no significant impact on pressure results, have been corrected. The changes that were made to WGOTHIC version 4.1 to create version 4.2 are as follows.

- Created a new clime subroutine, gvel, to provide cell-centered velocity direction for the clime calculations, to allow correct determination of assisting versus opposed convection in the downcomer
- Replaced the modified GOTHIC ccvel subroutine, supplied by NAI, with the GOTHIC 4.0 ccvel subroutine and corrected the error in effective flow area calculation
- Replaced the single precision constants with double precision constants in subroutines mixed.f and props1.f
- Increased the array dimensions for the GOTHIC conductors

Thus, known errors in the WGOTHIC clime subroutines have been corrected. In addition, known errors reported for GOTHIC version 4.0, the basis for WGOTHIC versions 4.0 and beyond, have been evaluated and determined not to be applicable to sections of coding exercised by the evaluation model.

Verification and validation of the code changes has been completed. As part of the validation effort, a regression test was performed to confirm that the change from WGOTHIC version 4.1 to version 4.2 had no effect on calculated peak pressure.

1.6.2 Changes in the Evaluation Model Input

Calculations, which provide the geometric data (free volume, hydraulic diameter, pool area, flow path parameters) for input to the WGOTHIC containment pressure DBA, have been updated to be consistent with the latest drawings. Applicable modifications have been made to the AP600 Containment Evaluation Model

input to reflect the changes in geometry, a more conservative approach for the MSLB has been implemented by moving the break node to a higher elevation, and changes to metal heat sinks to include only those verified by ITAAC, as described in Appendices 4.A and 4.B.

The sensitivity calculations in this report were performed with WGOTHIC Solver version 4.1 and plant geometry described in the body of Section 4. An evaluation of the effects of WGOTHIC Solver version 4.2 and input modification described in Appendices 4.A and 4.B has been performed to show that the changes to internal containment parameters do not affect the case-to-case sensitivities used to select the limiting extremes for internal initial and boundary conditions. Since the internal heat sinks reach their maximum thermal effectiveness well before the DECLG LOCA peak pressure is reached, the changes do not significantly impact the sensitivities used to select limiting scenarios for circulation and stratification. The small change to internal pressure, and thus the related small change to internal temperature boundary condition for the containment shell, does not affect the sensitivities for clime vertical noding and conductor mesh. Similarly, the changes do not affect external condition case-to-case results. The changes also do not invalidate the time step study. Therefore, the sensitivities performed in this report, remain valid.

1.7 CONCLUSIONS

This report defines a methodology which yields conservative pressure calculation and temperature envelopes. Evaluation Model methodology is cross referenced to PIRT phenomena in Reference 1.1, Section 4.4. The licensing basis DBA calculation is presented in Section 6.2 of the DCD.

1.8 REFERENCES

- 1.1 WCAP-14812, "Accident Specification and Phenomena Evaluation for AP600 Passive Containment Cooling System," Rev. 2, April 1998.
- 1.2 WCAP-14845, Revision 3, "Scaling Analysis for AP600 Containment Pressure During Design Basis Accidents," March 1998.
- 1.3 WCAP-14326, "Experimental Basis for the AP600 Containment Vessel Heat and Mass Transfer Correlations," Rev. 2, April 1998.
- 1.4 WCAP-14382, "WGOTHIC Code Description and Validation," May 1995.
- 1.5 WCAP-14141, "AP600 Test and Analysis Plan for Design Certification," Rev. 1, April 1995.
- 1.6 WCAP-14135, "Final Data Report for PCS Large-Scale Tests, Phase 2 and Phase 3," Revision 1, April 1997.

- 1.7 WCAP-14967, "Assessment of Effects of WGOTHIC Solver Upgrade from Version 1.2 to 4.1," September 1997.
- 1.8 WCAP-15612, "AP1000 Plant Description and Analysis Report," M. Corletti et al., December 2000.
- 1.9 WCAP-15613, "AP1000 PIRT and Scaling Assessment," February 2001.

Section 2

**Test and Analysis Process Overview and
High and Medium Ranked
Containment Phenomena**

TABLE OF CONTENTS

LIST OF TABLES iii

LIST OF FIGURES iii

2.1 INTRODUCTION 2-1

2.2 ELEMENT 1 - AP600 PCS REQUIREMENTS AND CODE CAPABILITIES 2-1

2.3 ELEMENT 2 - ASSESS CODE VERSUS TESTS AND IMPORTANT PROCESSES 2-3

2.4 ELEMENT 3 - ASSESS UNCERTAINTIES AND DEVELOP BOUNDING
MODELS 2-6

2.5 ELEMENT 4 - PERFORM DBA CALCULATIONS AND COMPARE TO SUCCESS
CRITERIA 2-7

2.6 CONCLUSIONS 2-8

2.7 REFERENCES 2-8

LIST OF TABLES

Table 2-1 Phenomena Identification and Ranking Table - Summary of High
and Medium Ranked Phenomena 2-4

LIST OF FIGURES

Figure 2-1 PCS Test and Analysis Process Overview 2-2

2.1 INTRODUCTION

The Evaluation Model for the passive containment cooling system (PCS) design basis accident (DBA) has been developed using elements of scaling (top-down and bottom-up modeling of the integrated components), testing, and analysis (bottom-up phenomenological models and evaluations), similar to the methodology for Code Scaling Applicability and Uncertainty (Ref. 2.1). Results have been used to identify bounding models and input values for use in the DBA Evaluation Model. The results of the DBA analyses provide conservative predictions of design basis transient pressure and temperature response for the containment.

The development of the PCS DBA methodology has followed an approach which can be organized into the four elements shown in Figure 2-1. The elements include tasks, that together provide a structured, traceable, and practical method for

- Specifying the scenario
- Identifying phenomena important to the transient
- Evaluating data and scale effects
- Documenting and validating the computer code
- Assessing margins and uncertainties
- Developing and applying the Evaluation Model

The process is represented by a once-through flow diagram for simplicity. The actual process included many iterations between the various tasks. For example, to better represent the observations of the large-scale containment test (LST) dome temperature distribution, due to the subcooling of the film applied to the LST, the initial WGOTHIC code version used in 1992 was augmented by the addition of a model for convective heat transport for the liquid film. In addition, extensive review by representatives of regulatory agencies, industry, and academia were incorporated into the process (Ref. 2.2). The end result is documentation which describes the PCS DBA Evaluation Model and its bases in an auditable, traceable manner. Following is a brief description of the four elements of the process used to develop the methodology.

2.2 ELEMENT 1 - PCS REQUIREMENTS AND CODE CAPABILITIES

The PCS DBA methodology development process began with a review of the AP600 design and DBA scenarios and an identification of phenomena important for AP600 containment pressurization. From this review, an initial test program was defined and a computer code was selected.

A PIRT was developed to identify the key thermal-hydraulic phenomena which govern the transients of interest. The PIRT (Ref. 2.2, Section 4) ranks phenomena according to their relative importance to the particular transient phase of interest. The PIRT process included input and review by representatives of academia and regulatory authorities, and cross-functional Westinghouse technical reviews. The bases for high, medium, and low rankings are documented in the PIRT. A key result of the PIRT is that the dominant phenomenon for

PCS Test and Analysis Process Overview

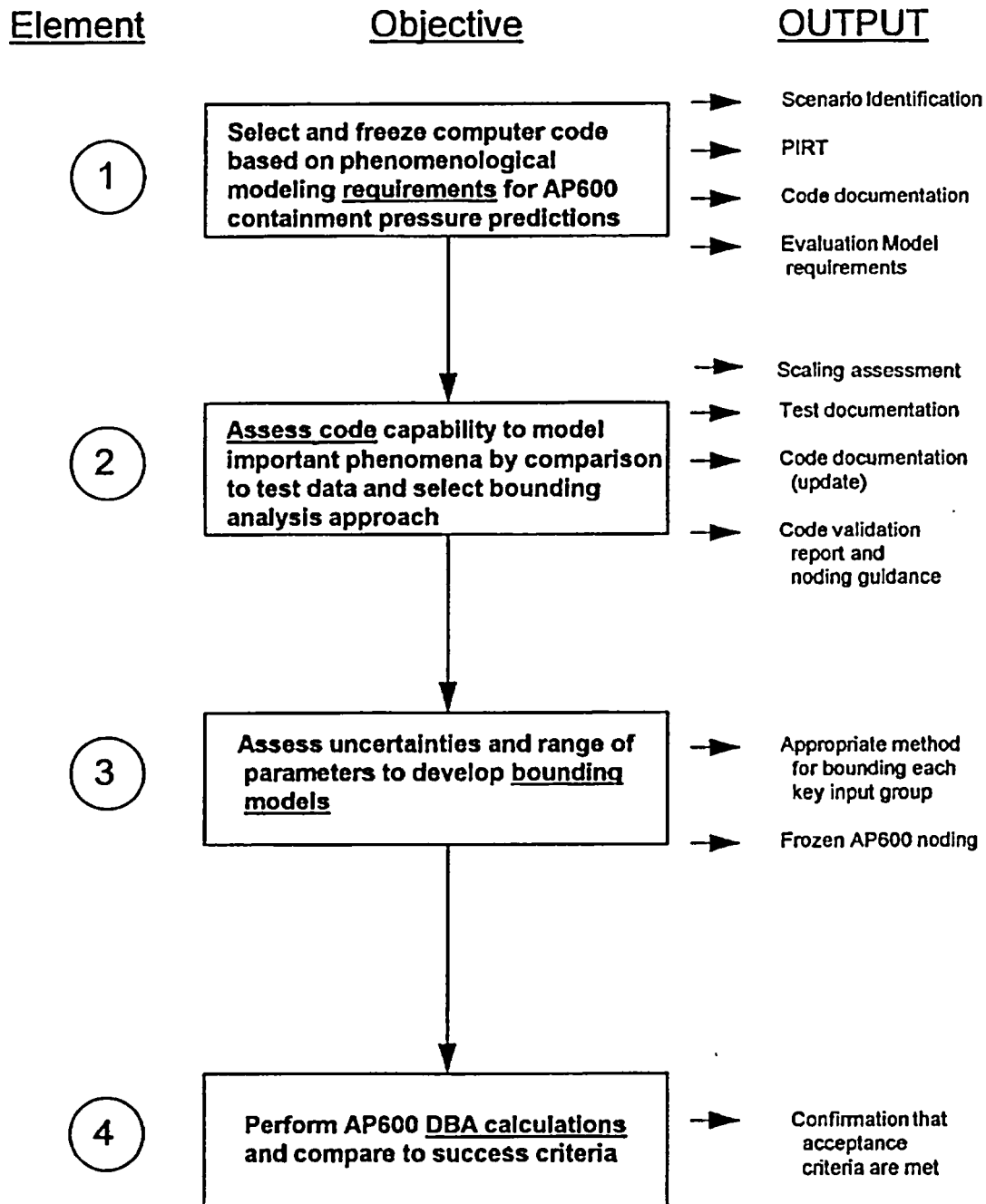


Figure 2-1 PCS Test and Analysis Process Overview

transferring heat from the containment is mass transfer— condensation on the inside and evaporation on the outside. The mass and energy release boundary condition imposed on the problem is the primary driver of the containment pressure response, and is ranked high. For the loss-of-coolant accident (LOCA) scenario, pressurization is mitigated primarily by internal volume compliance during blowdown, and by internal heat sinks below deck, from blowdown through the transition period when the PCS cooling begins to dominate and turns the pressure around. PCS heat removal dominates the long-term LOCA response. The main steamline break (MSLB) transient is mitigated primarily by volume compliance and internal heat sinks. A summary of the high and medium ranked phenomena is shown in Table 2-1. As described in Reference 2.10, Section 2.6, the AP1000 design changes do not affect the PIRT or the results of the AP600 PIRT confirmation that are documented in Reference 2.9.

In parallel with bottom-up phenomena evaluations, the WGOTHIC computer code was selected, upgraded, and frozen to allow explicit modeling of many of the phenomena identified in the initial review. As the scaling analysis and testing programs progressed, code upgrades were completed to better model experimental results according to guidelines consistent with computer code lifecycle management. Hand calculations and spreadsheets were used to verify correct programming of the upgrades as documented within the Westinghouse QA program. Documentation of the code used in the Evaluation Model consists of base GOTHIC 4.0 documentation (Refs. 2.3, 2.4, 2.5) and upgrades to create WGOTHIC 4.2 (Section 3).

2.3 ELEMENT 2 - ASSESS CODE VERSUS TESTS AND IMPORTANT PROCESSES

Analyses and computer code validations were used to identify the most appropriate models and biases to use in the PCS DBA Evaluation Model. The PCS test results were documented, including separate effects (Ref. 2.6) and integral effects (Ref. 2.7). The PCS test data and other data from the literature were used to provide input to code validation (Ref. 2.8). Validation was used to study how the oversimplification inherent in the lumped parameter WGOTHIC model applies to the AP600. The lumped parameter limitations lead to the potential for compensating errors, so that a methodology to bound the effects of compensating errors was identified (Ref. 2.8, page 8-9). The effect of lumped parameter momentum formulation and nodding on WGOTHIC results was an important output of validation. Insight from validation was used to develop a bounding Evaluation Model in Element 3.

A scaling evaluation of AP600 was performed (Ref. 2.9) which provided additional confirmation of the PIRT phenomena and ranking. Scaling identified the appropriate nondimensional parameters, the effects of facility scales, and the ranges of parameters expected in AP600. Scaling was also used to identify distortions in the LST facility and to evaluate the effect of distortions on the use of the LST for studying lumped parameter code biases.

The results of scaling, testing, and code validation were used to establish a bounding analysis approach for each of the PIRT phenomena, documented in Reference 2.2, Section 4.4.

| Table 2-1 Phenomena Identification and Ranking Table - Summary of High and Medium Ranked Phenomena | | | |
|--|--|--|---|
| Phenomenon * | Effect on Containment | Pi Groups | Where Addressed |
| Break Source Mass and Energy (1A) | The mass and energy source for containment pressurization | $\pi_{p,g,brk,enth}$ $\pi_{p,g,brk,work}$ $\pi_{p,work,d}$ $\pi_{p,work,n}$ | Scaling Analysis |
| Gas Compliance (2C) | Stores mass and energy in atmosphere, increasing pressure | $\pi_{p,r}$ | Scaling Analysis |
| Initial Conditions Inside (4A, 4B, 4C) | Temperature, humidity, pressure affect noncondensables and energy storage | parameter | Initial Conditions Section 5 |
| Containment Solid Heat Sinks (3), Pool (5), Drops (1), and Shell (7) | Store energy (and remove mass from atmosphere) reducing pressure | $\pi_{p,g,j}$ $\pi_{p,work,j}$ | Scaling Analysis |
| Internal Heat Sink Conduction (3D, 5E, 7F) and Heat Capacity (3E, 5A, 7G) | Limits conduction heat transfer into heat sinks, shell, or pool, and through shell. Stratification in the break pool can affect the effective heat capacity of the pool. | parameter | Scaling Analysis |
| Heat Transfer Through Horizontal Liquid Films (3C) | Water on and noncondensable gases near upward facing horizontal surfaces limit heat and mass transfer to horizontal heat sinks | parameter | Scaling Analysis |
| Condensation Mass Transfer (3F, 5B, 7C) | The first-order transport process that removes mass and energy from the containment gas | $\pi_{p,work,j}$ | Scaling Analysis |
| Break Source Direction and Elevation (1B), Momentum (1C), and Density (1D) | Direction, elevation, density, and momentum can dominate circulation and affect condensation rate. | parameter | Circulation and Stratification, Section 9 |
| Circulation and Stratification (2A) | Intercompartment Flow (Circulation) and stratification can affect the distribution of steam (and noncondensables) near heat sinks for condensation heat removal. | parameters | |
| Intercompartment Flow (2B) | | | |
| Source Fog (2D) | Affects circulation and stratification via buoyancy | parameter | |

| Table 2-1 Phenomena Identification and Ranking Table - Summary of High and Medium Ranked Phenomena (cont.) | | Effect on Containment | Pi Groups | Where Addressed |
|--|---|---|--|-----------------------------------|
| Evaporation Mass Transfer (7N) | | First-order transport process that removes mass and energy from the evaporating external shell | $\pi_{e,fg,esx}$ $\pi_{p,g,brk,work}$ $\pi_{p,work,d}$ $\pi_{r,work,n}$ | Scaling Analysis |
| | PCS Natural Circulation (9A, 13A) | Convective air flow provides convective heat and mass transfer from containment shell. | parameter | Scaling Analysis |
| | Liquid Film Flow Rate (8A), Water Temperature (8B), Film Stability (8C) | Affects the upper limit for water coverage on the external shell and amount of water available for evaporation. | parameter | Film Stability, Section 7 |
| Liquid Film Energy Transport (7E, 7M) | | <i>Inside:</i> Carries condensation energy to the IRWST and break pool. <i>Outside:</i> Absorbs energy rejected by the external shell surface. | $\pi_{e,t,if}$ See note 1 | Scaling Analysis |
| Convection Heat Transfer (3G, 7H, 10A, 10B) | | A second order transport process that removes energy from the containment gas, and from the external shell. | $\pi_{p,q,j}$ $\pi_{e,q,esx} + \pi_{e,q,dex}$ Note 2 | Scaling Analysis |
| Radiation Heat Transfer (3H, 7I) | | A second order transport process that removes energy from the containment gas and from the external shell. | $\pi_{p,q,j}$ $\pi_{e,q,esx} + \pi_{e,q,dex}$ Note 2 | Scaling Analysis |
| Baffle Conduction (10D) and Baffle Leakage Paths (10G) | | Conduction through the baffle into downcomer volume and leakage paths can influence the external natural circulation flow rates | $\pi_{e,q,bf}$ $\pi_{e,q,bfx}$ None for leakage | PIRT Sections 4.4.10D and 4.4.10G |

* Indicators in parentheses refer to phenomena in the "Phenomena Identification and Ranking According to Effect on Containment Pressure" (Reference 2.2, Table 4-1).

Note 1. The fraction of the internal condensation carried away by the liquid film is defined by the ratio: $\pi_{e,t,j}/(\pi_{e,t,j} + \pi_{e,fg,j})$, for each heat sink j. The fraction of the external shell heat rejection that goes into the subcooled heat capacity of the external liquid is defined by the ratio: $\pi_{e,q,esx}/(\pi_{e,q,esx} + \pi_{e,q,esx} + \pi_{e,fg,esx} + \pi_{e,q,dex})$. The pi group values for AP600 are presented in Reference 2.9, Section 8.

Note 2. Inside containment $\pi_{p,q,j}$ represents the pressure effect of sensible heat transfer. The sensible heat transfer is approximately 1/2 radiation heat transfer and 1/2 convection heat transfer. Outside containment $\pi_{e,q,esx} + \pi_{e,q,dex}$ represents the sum of the dry and evaporating shell sensible heat transfer, that is approximately 1/2 radiation heat transfer and 1/2 convection heat transfer.

2.4 ELEMENT 3 - ASSESS UNCERTAINTIES AND DEVELOP BOUNDING MODELS

Uncertainties were assessed, and together with the results of code validation, were used to develop a method of applying the WGOTHIC lumped parameter formulation to create a bounding DBA Evaluation Model. Key results are summarized as follows.

It is worthwhile noting how representative high-ranked phenomena are addressed for the AP600 PCS in the context of understanding this overview. In this regard, some background on lumped parameter containment codes follows, and then a summary is given of how uncertainties are handled for two representative phenomena, the heat and mass transfer rate correlations, and circulation and stratification.

The application of WGOTHIC lumped parameter formulation for the PCS Evaluation Model has been justified by conservatively addressing lumped parameter biases (Appendix 9C, Section 9.C.3.4). Lumped parameter containment codes have been used for nuclear power plant licensing calculations for over 30 years. Limitations of the lumped parameter approach for containment modeling are documented in the literature. Generally, lumped parameter codes can reasonably predict global parameters, such as pressure, but the lumped parameter formulation oversimplifies physics when local details are important. For containment analysis, details within a volume are important when the physics of stratification within a volume or entrainment into jets or plumes is important. Coupling of the WGOTHIC lumped parameter nodes, with one or more distributed parameter volumes to gain some resolution of the details within a volume, can increase the accuracy of the solution. However, while distributed parameter calculations were used to help understand test results, the use of such more detailed models was not practical for PCS DBA calculations due to computing requirements.

Complex thermal hydraulic models may produce results that match or bound test data but may also include compensating errors. Sufficient data were obtained on the important variables in the LST to isolate compensating errors in the lumped parameter model. Studies of LST calculations have shown that the compensating errors in lumped parameter calculations arise from offsetting effects of steam concentration and velocity. Because the jet source is numerically expanded to uniformly fill the volume flow area in a lumped parameter node, numerical entrainment leads to high predicted velocities in the above-deck region and a resultant homogenization of the containment. Mixing of noncondensables from the below-deck region in the LST penalizes PCS heat transfer because the noncondensables from below-deck penalize condensation rates. Overpredicting velocities benefits PCS heat transfer because of forced convection enhancement. In the Evaluation Model, the competing effects are addressed by using only free convection inside containment, thereby eliminating the influence of velocity overprediction. This results in a bounding prediction relative to the potential for compensating errors.

After developing an understanding of lumped parameter model performance, bounding approaches to address important phenomena, summarized in Table 2-1, were developed. Uncertainties are addressed by quantifying a bias and distribution for a phenomenon or by studying the range of expected containment conditions and

establishing an upper bound approach. Examples of the two approaches follow, using mass transfer correlation and circulation and stratification.

Separate effects tests (SETs) and LST data have been used to select appropriate heat and mass transfer correlations from the literature and develop biases to bound the data (Ref. 2.6, Section 4.5). A lower bound for heat transfer through the containment shell to the ultimate heat sink is therefore used.

One of the more complex issues is the coupling of circulation and stratification, break direction and momentum, and intercompartment flow, and the impact of those parameters on internal heat sink utilization. Circulation and stratification are complex physical processes that are not easily solved by numerical methods. Since both the AP600 and AP1000 rely on passive cooling by natural circulation, there are no active systems to force the atmosphere to homogenize. Based on a study of plausible break scenarios (mass and energy, momentum, direction, and elevation), bounding, or extreme cases are identified for further study. The extreme cases are studied using first principles calculations and sensitivities to specific flow patterns of interest. The lumped parameter plant model, with above-deck noding based on noding frozen for the LST evaluations, is used to calculate the containment response for the specified flow patterns. Based on the sensitivities, a limiting scenario is chosen for use as the PCS DBA to bound the impact on mass transfer of the strongly coupled phenomena. Biases are introduced with lumped parameter compartment nodes to bound the effects of stratification, and an assessment of stratification effects on PCS heat removal through the shell shows that no net penalty on heat removal from the above-deck region need be applied. This is discussed in more detail in Section 9 (See Table 9-1).

Similar evaluations have led to the definition of a bounding Evaluation Model for important phenomena identified in the PIRT and documented in Reference 2.2 Section 4.4.

2.5 ELEMENT 4 - PERFORM DBA CALCULATIONS AND COMPARE TO SUCCESS CRITERIA

The Evaluation Model was developed as previously described to produce conservative, bounding pressure transients for each accident phase. The acceptance criteria are that the peak pressure must remain below the design pressure and pressure should be rapidly reduced, consistent with assumptions in radiological release calculations, which is typically interpreted as the pressure at 24 hours should be less than one half of the design pressure. Documentation is provided in Reference 2.2 that shows for each phenomenon:

- Relevant model in the code
- Test basis
- Report references
- Summary report conclusions
- Validation basis summary
- How validation results are used
- How uncertainty is addressed

2.6 CONCLUSIONS

A structured, traceable approach has been followed to develop the PCS DBA Evaluation Model. The PIRT has been used to develop a bounding Evaluation Model and the PIRT has been used as the basis for a road map to relevant supporting information for each phenomenon.

2.7 REFERENCES

- 2.1 Boyack, B.E., et al., "An Overview of the Code Scaling, Applicability, and Uncertainty Evaluation Methodology," Nuclear Engineering and Design, Volume 119 (1990) No. 1, May 1990, pp 1-15
- 2.2 WCAP-14812, "Accident Specification and Phenomena Evaluation for AP600 Passive Containment Cooling System," Rev. 2, April 1998
- 2.3 NTD-NRC-95-4563, "GOTHIC Version 4.0 Documentation," September 21, 1995
- 2.4 NTD-NRC-95-4577, "Updated GOTHIC Documentation," October 12, 1995
- 2.5 NTD-NRC-95-4595, "AP600 WGOTHIC Comparison to GOTHIC," November 13, 1995
- 2.6 WCAP-14326, "Experimental Basis for the AP600 Containment Vessel Heat and Mass Transfer Correlations," Rev. 2, April 1998
- 2.7 WCAP-14135, "Final Data Report for PCS Large-Scale Tests, Phase 2 and Phase 3," Revision 1, April 1997
- 2.8 WCAP-14382, "WGOTHIC Code Description and Validation," May 1995
- 2.9 WCAP-14845, "Scaling Analysis for AP600 Containment Pressure During Design Basis Accidents," Rev. 3, March 1998
- 2.10 WCAP-15613, "AP1000 PIRT and Scaling Assessment," February 2001

Section 3

Overview of WGOTHIC

TABLE OF CONTENTS

LIST OF TABLES iii

LIST OF FIGURES iii

3.1 INTRODUCTION 3-1

3.2 OVERVIEW OF THE CODE DEVELOPMENT AND VALIDATION 3-1

3.3 THE WGOTHIC CLIME MODEL 3-11

3.4 GENERAL CLIME EQUATIONS 3-14

3.5 INTEGRATION OF THE WESTINGHOUSE CLIME MODEL
INTO GOTHIC 3-19

3.6 REFERENCES 3-22

LIST OF TABLES

Table 3-1 GOTHIC Validation Tests 3-5

Table 3-2 GOTHIC Phenomenological Models Validated by Test 3-6

Table 3-3 Operating Range Comparison for AP600 and AP1000 Heat and
Mass Transfer Parameters 3-10

LIST OF FIGURES

Figure 3-1 Summary of GOTHIC Historical Development 3-2

Figure 3-2 GOTHIC Modeling Features 3-3

Figure 3-3 Summary of WGOTHIC Historical Development 3-7

Figure 3-4 Westinghouse-GOTHIC Clime Wall Source Term Models 3-13

Figure 3-5 Clime Finite Difference Model Definitions 3-15

Figure 3-6 Clime Routines Flow Control Outline 3-21

3.1 INTRODUCTION

The passive containment cooling system (PCS) phenomena were identified and ranked by order of importance in determining the vessel pressure in a phenomena identification and ranking table (PIRT). The important phenomena are summarized in Section 2. Existing containment analysis codes were reviewed to determine which most closely met the requirements identified in the PIRT. Although none of the codes met all of the requirements, the GOTHIC code package (Reference 3.1) was selected for further development based on its validation history and modeling capability. This section provides an overview of the GOTHIC code and describes the changes made to the GOTHIC solver program to incorporate the special heat and mass transfer correlations, liquid film tracking, and the wall-to-wall radiation model for performing design basis analyses for PCS-type containments.

3.2 OVERVIEW OF THE CODE DEVELOPMENT AND VALIDATION

The GOTHIC code is a state-of-the-art program for modeling multi-phase flow. The GOTHIC code has been developed through a long history from other qualified thermal-hydraulic computer codes (as shown in Figure 3-1).

GOTHIC consists of three separate programs, the preprocessor, solver, and postprocessor. The preprocessor allows the user to rapidly create and modify an input model. The solver performs the numerical solution for the problem. The postprocessor, in conjunction with the preprocessor, allows the user to rapidly create graphic and tabular outputs for most parameters in the model.

The GOTHIC solver program calculates the solution for the integral form of the conservation equations for mass, momentum, and energy for multi-component, two-phase flow. The conservation equations are solved for three fields: continuous liquid, liquid drops, and the steam/gas phase. The three fields may be in thermal nonequilibrium within the same computational cell. This would allow the modeling of subcooled drops (for example, containment spray) falling through an atmosphere of saturated steam. The gas component of the steam/gas field can be comprised of up to eight different noncondensable gases with mass balances performed for each component. Relative velocities are calculated for each field, as well as the effects of two-phase slip on pressure drop. Heat transfer between the phases, surfaces, and the fluid are also allowed.

The GOTHIC solver program is capable of performing calculations in three modes. A model can be created in the lumped-parameter nodal-network mode, the two-dimensional distributed parameter mode, or the three-dimensional distributed parameter mode. Each of these modes may be used within the same model (as shown in Figure 3-2). The lumped parameter nodal-network mode is used for the containment Evaluation Model.

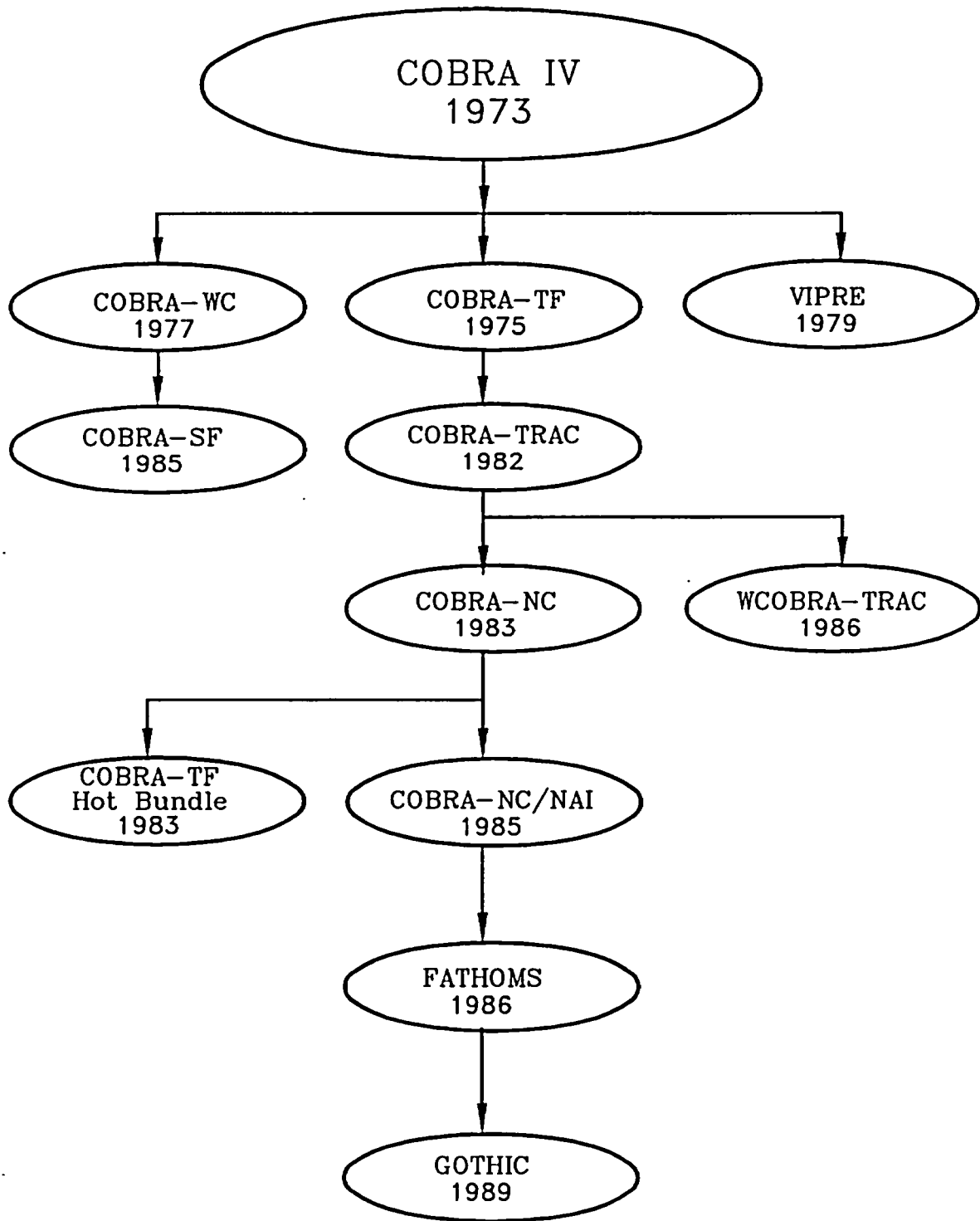


Figure 3-1 Summary of GOTHIC Historical Development

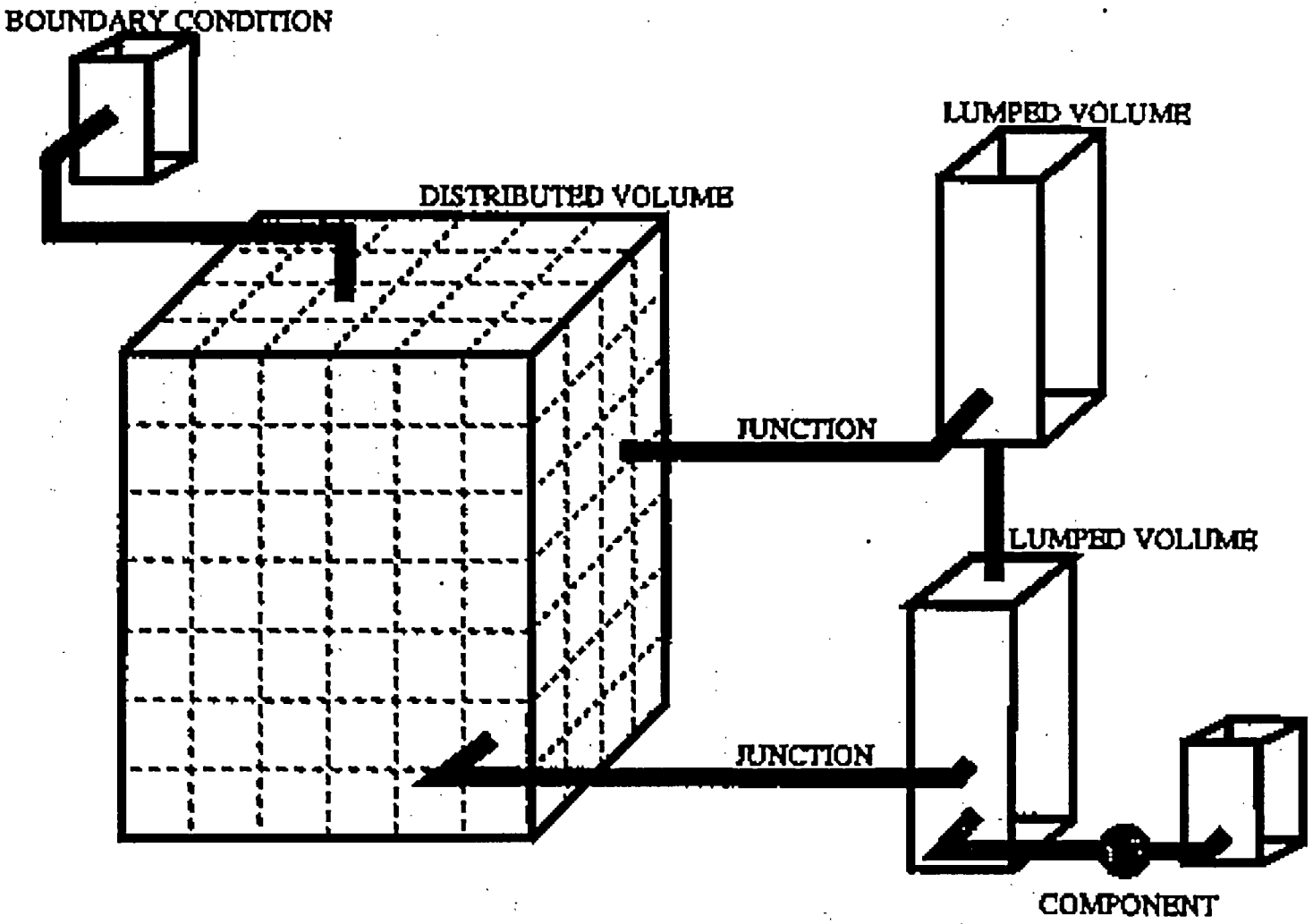


Figure 3-2 GOTIHC Modeling Features

The GOTHIC code also contains the options to model a large number of structures and components. These include, but are not limited to, heated and unheated conductors, pumps, fans, a variety of heat exchangers, and ice condensers. These components can be coupled to represent the various systems found in any typical containment. They are not used in the AP600 or AP1000 analyses described in this report.

The GOTHIC code has an extensive validation history which was an important consideration in the selection of the code for further development for modeling of the PCS. The GOTHIC code validation program includes both a comparison of code-calculated results with analytical solutions to specified standard problems and a comparison of code-calculated results with experimental data. The results of the EPRI-sponsored GOTHIC code validation program are presented in Reference 3.1, Enclosure 1. Table 3-1 lists some of the tests used in the GOTHIC code validation program. The phenomenological models validated by each test are cross-referenced and presented in Table 3-2. In addition, industry experience using GOTHIC in the lumped parameter mode, as well as attempts to improve results using multi-dimensional analyses, are described in Appendix 9.C.3.

Westinghouse purchased Version 3.4c of the GOTHIC code in 1991 and began modifying it to include mechanistic convection heat and mass transfer correlations, a liquid film tracking model, a one-dimensional wall conduction model, and wall-to-wall radiant heat transfer to model heat removal by the PCS. The code with modifications, is called Westinghouse-GOTHIC and is abbreviated as WGOTHIC.

The WGOTHIC development history is shown in Figure 3-3. The PCS heat and mass transfer models developed by Westinghouse were incorporated into the GOTHIC version 3.4c pre-processor and solver programs to create the WGOTHIC version 1.0 pre-processor and solver programs in 1993.

Between 1991 and 1993, while Westinghouse was developing the PCS heat and mass transfer models, GOTHIC version 3.4d underwent an EPRI-sponsored peer review. The purpose of the review was to establish a reference point for placing the GOTHIC code package under a 10 CFR 50, Appendix B Quality Assurance Program. The peer design review group reviewed the documentation, coding, convergence, pre/post-processor, code qualification package, and the code's adequacy for containment analysis. The conclusions from the review are presented in Section 2.2 of the GOTHIC Design Review Final Report (Reference 3.2).

Overall, the GOTHIC containment analysis package was found to be adequate for containment analyses, and that the code package offered the ability to provide more accurate and mechanistic results than with other currently available containment codes. This conclusion was qualified with the statements that the nodal and junction treatment, as well as the range of the qualification database, need to be justified for each intended application; as was done via the large-scale (LST) and separate effects tests (SETs) (Reference 3.3) and various scale integral tests (Appendix 9.C.3) used to qualify WGOTHIC.

| Table 3-1 GOTHIC Validation Tests | |
|--|---|
| Battelle-Frankfurt Tests D-1, D-15, D-16 | Modeling: 7 lumped parameter volumes, junctions Phenomena: Blowdown transients, subcompartment pressurization, wall differential pressures |
| Battelle-Frankfurt Test 6 | Modeling: 1 distributed parameter volume (55 cells), conductors, junctions Phenomena: Hydrogen transport by convection and diffusion |
| Battelle-Frankfurt Tests 12, 20 | Modeling: Combination of 5 lumped and 1 distributed parameter volumes (2 cells), conductors, junctions Phenomena: Hydrogen transport by convection and diffusion |
| Battelle-Frankfurt Tests C-13, C-15 | Modeling: 10 lumped parameter volumes, conductors, junctions Phenomena: Main steamline break, pressure/temperature response |
| Hanford Engineering Development Laboratory Tests HM-5, HM-6 | Modeling: 1 distributed parameter volume (300 cells), conductors, junctions Phenomena: Hydrogen mixing in a large, simulated containment |
| Light Water Reactor Aerosol Containment Experiments Tests LA-5, LA-6 | Modeling: Combination of 1 lumped and 1 distributed parameter (2 cells) volumes, conductors, junctions Phenomena: Severe accident response to sudden containment failure |
| Marviken Full-Scale Containment Tests 17, 24 | Modeling: 21 lumped parameter volumes, conductors, junctions Phenomena: Pressurized high temperature steam blowdown |
| Carolina's Virginia Tube Reactor Tests 3, 4, 5 | Modeling: 2 lumped volume and a 2 distributed parameter volume (20 cells) models, conductors, junctions Phenomena: Steam blowdowns (T31.5 includes hydrogen/helium) |
| Heissdampfreaktor Tests V21.1, T31.1, T31.5, V44 | Modeling: 37 lumped parameter volumes, conductors, junctions Phenomena: Steam blowdowns (T31.5 includes hydrogen/helium) |

| Table 3-2 GOTHIC Phenomenological Models Validated by Test | | | | | | |
|---|-------------|-------------|-------------|-------------|-------------|------------|
| Item | BFMC | HEDL | LACE | MARV | CVTR | HDR |
| Fluid momentum | X | | X | X | | |
| Energy transport | X | | X | X | | |
| Noncondensable gases | X | X | X | X | X | X |
| Equations of state | X | | X | X | | |
| Pressure response | X | X | X | X | X | X |
| Temperature response | X | X | X | X | X | X |
| Humidity response | X | X | X | X | X | X |
| Hydrogen transport | X | | | | | |
| Energy sources | X | X | X | | X | X |
| Subcompartment analysis | X | | | X | | |
| High energy line breaks | X | | | | | |
| PWR standard containment | | | X | | | |
| BWR pressure suppression | | | | X | | |
| Fluid/structure interaction | X | | | | | |
| Conductors | X | | | | | |
| Subdivided volumes | X | | | | | |
| Turbulence | X | | | | | |
| 3-D calculations | X | X | | X | | |

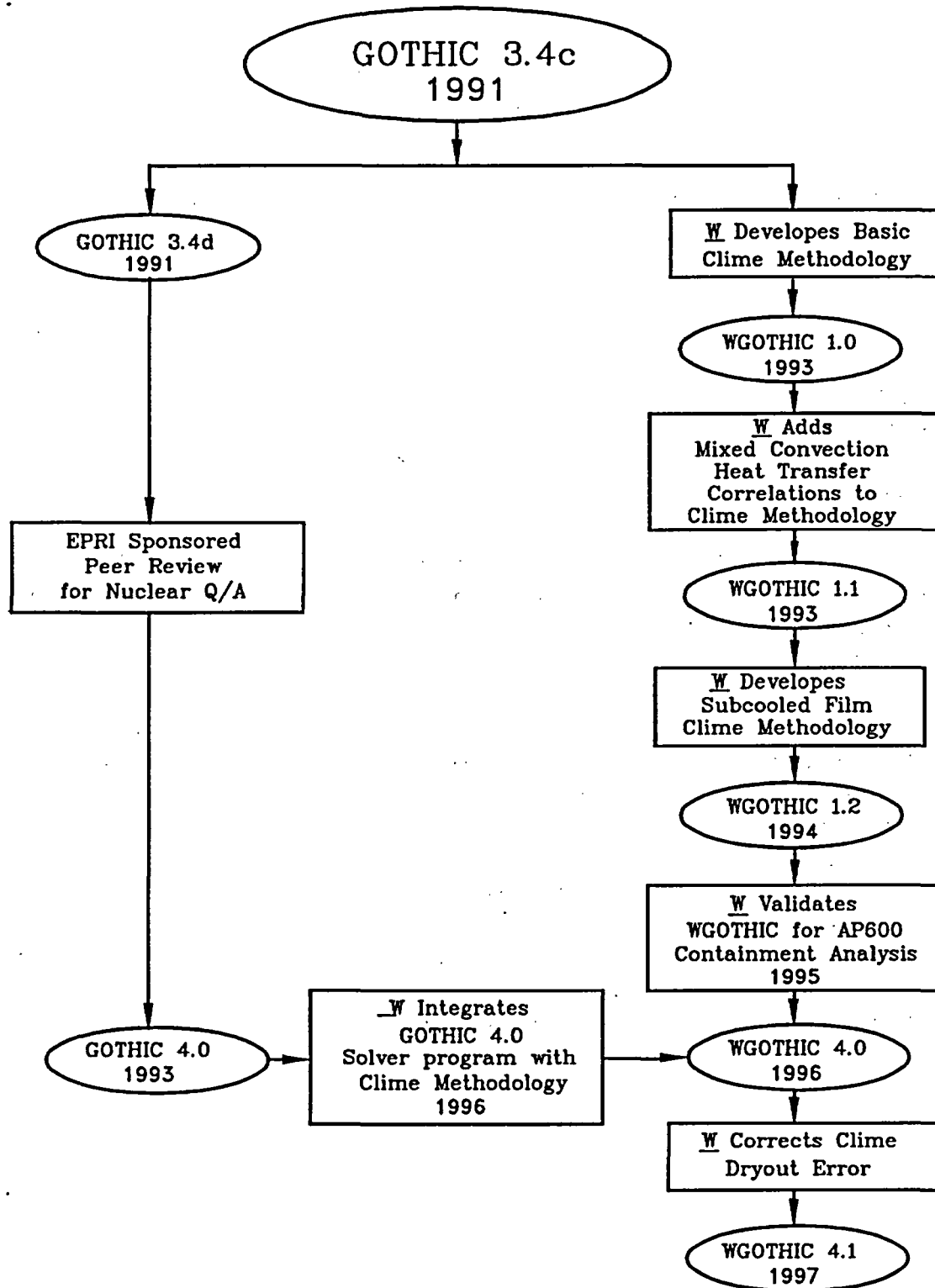


Figure 3-3 Summary of WGOETHIC Historical Development

The review group had three recommendations. The first was the addition of dynamic memory allocation, so that the code would not need to be recompiled for different sizes of models. The second was the inclusion of an iterated Newton method to aid in convergence. The third was to incorporate a fog model to simulate condensation of vapor when regions go from superheated to saturated.

As described in Reference 3.4, the conclusions and recommendations from the GOTHIC design review also apply to WGOTHIC. None of the recommended changes were incorporated in WGOTHIC. The first recommendation, dynamic memory allocation, wasn't incorporated in WGOTHIC, since it is a user convenience option and does not affect the solution technique. The second recommendation, to include an iterated Newton solution option to aid in convergence, was not incorporated in WGOTHIC, since satisfactory convergence was supported by the comparisons presented in the GOTHIC code qualification test report (Reference 3.1) and the WGOTHIC validation report (Reference 3.3). The third recommendation, to include a fog model, was not incorporated in WGOTHIC because it was concluded that, based on the GOTHIC CVTR qualification test case results (Reference 3.1) and an assessment of fog modeling as it relates to the AP600 (Reference 3.5, Sections 4.4.2D and 4.4.9C), it is conservative with respect to the prediction of containment temperature and pressure to not include the fog model.

Westinghouse updated the PCS models to account for subcooled films and incorporated the GOTHIC software error corrections that were provided by NAI to create WGOTHIC pre-processor version 2.0 and solver version 1.2 in 1994. Westinghouse validated this version of WGOTHIC for performing AP600 analyses in 1995 (Reference 3.3). The WGOTHIC validation program consisted of four parts:

1. The subset of GOTHIC validation tests that was identified as sensitive in the original acceptance tests was rerun with WGOTHIC. These tests were run with the same input options selected in the original GOTHIC validation calculation (that is, the PCS models were not exercised) to determine if any of the code changes made to incorporate the PCS models would affect the transient results. This comparison is presented in Appendix D of Reference 3.3. It shows that the code changes Westinghouse made to incorporate the PCS models do not affect the GOTHIC calculation results.
2. The PCS model one-dimensional conduction equation solution technique was validated by comparison with an analytical solution for a test problem. This comparison is presented in Section 4.1 of Reference 3.3. The code calculated results match the analytical solution.

3. The PCS model heat and mass transfer correlations were validated by comparison with separate effects test data from the Westinghouse Flat Plate Tests, the Westinghouse Large-Scale Tests, the Wisconsin Condensation Tests, and publicly available published reports. These comparisons are documented in Reference 3.6. The range of the important dimensionless parameters from the test program bounds both the AP600 and AP1000 operating range, as shown in Table 3-3. Therefore, the correlations are acceptable for modeling heat and mass transfer in both the AP600 and AP1000 PCS.
4. WGOTHIC, including the PCS models and nodalization, was verified to be coded correctly by comparison with transient test data from the Westinghouse Large-Scale tests. Comparison with steady state test data from the LSTs assessed the ability of WGOTHIC to represent internal flow fields and noncondensable gas distributions and to calculate the net heat removal from the vessel in an integral system. The comparisons provided insight for the applicability of documented lumped parameter biases (Appendix 9.C.3) that are applied to the AP600 and AP1000 containment Evaluation Models and identified a bounding approach to address compensating errors. This comparison is presented in Section 8 of Reference 3.3. Section 9, Table 9-1 summarizes how lumped parameter biases have been addressed.

In 1996, the source code for the PCS heat and mass transfer models for WGOTHIC solver version 1.2 and pre-processor version 2.0 was incorporated into the GOTHIC solver and pre-processor version 4.0 source code to create the WGOTHIC version 4.0 pre-processor and solver programs. This was done to incorporate all of the GOTHIC design review code changes into WGOTHIC.

A series of verification tests, including the most sensitive GOTHIC code qualifications test cases, were run to validate WGOTHIC version 4.0. The results of the GOTHIC code qualification test cases that were run using the WGOTHIC version 4.0 all compared very well with the results obtained using GOTHIC version 4.0, indicating that the incorporation of the Westinghouse PCS model did not significantly affect the GOTHIC calculations.

Version 4.1 of the WGOTHIC pre-processor, solver, and post-processor programs was created in 1997 to correct an error that was discovered in the PCS heat and mass transfer model and several other non-calculational code problems. The error caused the PCS heat removal to be overpredicted at the point of dryout. Verification test cases performed using WGOTHIC version 4.1 demonstrated that the dryout error was corrected. Version 4.1 of WGOTHIC has been used for all of the analyses presented in this report except as specifically noted for sensitivity studies in Section 11.

Table 3-3 Operating Range Comparison for AP600 and AP1000 Heat and Mass Transfer Parameters

| Heat Transfer Correlation | Parameter | Composite of Test Data | AP600 Range | AP1000 Range |
|---|-------------------|--|-------------------------|-------------------------|
| Internal Free Convection: $h = 0.13 k/(v^2/g)^{1/3} [\Delta\rho/\rho]^{1/3} Pr^{1/3}$ | $\Delta\rho/\rho$ | 0.08 to 0.55 | <0.40 | <0.42 |
| | Pr | 0.72 to 0.90 | 0.72 to 0.90 | 0.72 to 0.90 |
| | Sc | ~0.52 | ~0.52 | ~0.52 |
| External Mixed Convection: $Nu_{force} = 0.023 Re_d^{0.8} Pr^{1/3}$ $Nu_{free} = 0.13 (Gr_d Pr)^{1/3}$ For Opposed Mixed Convection: $Nu_{mix} = (Nu_{force}^3 + Nu_{free}^3)^{1/3}$ For Assisted Mixed Convection: $Nu_{mix} = \text{Max} \{ (Nu_{free}^3 - Nu_{force}^3)^{1/3}, Nu_{free}, 0.75 * Nu_{force} \}$ | Re_d Riser | <120000 evap. <500000 dry | <189000 | <210000 |
| | Re_d Downcomer | | <151000 | <190000 |
| | Re_d Chimney | | <1400000 | <1800000 |
| | Gr_d Riser | <7.0x10 ¹⁰ evap. <1.0x10 ¹¹ dry | <1.2 x 10 ⁹ | <1.5 x 10 ⁹ |
| | Gr_d Downcomer | | <6.2 x 10 ⁹ | <2.1 x 10 ¹⁰ |
| | Gr_d Chimney | | <2.1 x 10 ¹² | <8.0 x 10 ¹² |
| | Pr | ~0.72 | ~0.72 | ~0.72 |
| Sc | ~0.52 | ~0.52 | ~0.52 | |
| Liquid Film Heat Transfer: $Nu_{turb} = 0.0038 Re^{0.4} Pr^{0.65}$ $Nu_{wavy\ laminar} = 0.822 Re^{-0.22}$ | Re | 10000 | <3200 | <3500 |
| | Pr | 1.77 to 5.9 | 1.5 to 3.0 | 1.5 to 3.0 |

3.3 THE WGOTHIC CLIME MODEL

A solution technique that includes wall-to-wall radiation at the conditions expected for the passive plant design necessitates a close coupling of the participating walls. This coupling is accomplished by assigning boundaries that define the portions of the various walls that radiate to one another. Consistent with the basic formulation implemented for the GOTHIC code that considers conductors or heat sinks to be energy sink or source terms, code modifications that include wall-to-wall radiant heat transfer can be thought of as the addition of a special type of conductor group. This special conductor type or group consists of a set of walls that radiate to each other and interface with GOTHIC fluid cells through mass and energy source terms. The term *clime*, meaning *region*, is used to differentiate and distinguish this special conductor type from those already existing in GOTHIC terminology.

For the passive containment model, a clime is a horizontal slice of the containment structure consisting of the following:

- The heat and mass transfer source terms from the containment volume to the shell
- Liquid film mass and energy conservation and thermal resistance on shell, baffle, or shield building surfaces.
- Conduction through the shell
- Heat and mass transfer source terms from the exterior shell to the riser air flow channel
- Radiation from the exterior shell to the interior baffle
- Heat and mass transfer source terms to the interior baffle from the riser air flow channel
- Conduction through the baffle
- Heat and mass transfer source terms from the exterior baffle to the downcomer air flow channel
- Radiant heat transfer from the exterior baffle to the interior surface of the shield building
- Heat transfer source terms to the interior surface of the shield building from the downcomer air flow channel
- Conduction through the wall of the shield building
- Both radiant and convective heat transfer from the exterior surface of the shield building to the environment

A representative three-conductor clime is shown schematically in Figure 3-4. The internal containment vessel volume, riser air flow channel volume, downcomer air flow channel volume, and environment volume are separate computational cells or fluid volumes in the model. The shell, baffle, and shield building walls are one-dimensional conductors representing solid wall structures between the computational cells. These conductors are further subdivided into regions of different materials with different mesh sizes. Each conductor surface may have a liquid film present (not shown) depending on thermodynamic conditions.

The climes are stacked vertically through the PCS to model the effects of changing properties both inside and outside the containment shell. Usually there are at least two stacks of climes a wet stack and a dry stack. The only difference between a wet and dry stack is that a time-dependent, water flow rate boundary condition is specified for each conductor surface of the top clime in a wet stack. Because condensation can occur on either wet or dry conductor surfaces, an initially dry stack of climes could contain some wet conductor surfaces and/or a partially wet conductor surface due to condensation. Likewise, an initially wet stack of climes could contain some dry conductor surfaces and/or a partially dry conductor surface due to evaporation.

The user must specify values for the area and circumferential perimeter for each conductor of each clime in both the wet and dry stacks. The input values for the area and circumferential perimeter for the clime conductors in the wet stacks are based on measurements of the water coverage from the full-scale Water Distribution Tests. The PCS film coverage model, which conservatively bounds results from several test facilities, is described in Section 7.

The WGOTHIC clime model calculates the temperature, flow rate, and thermal resistance of the water films on the various conductor surfaces of a clime. Liquid mass is conserved whenever the film reaches the bottom clime in a stack or a conductor surface dries out. The clime model takes the film flow rate from each conductor surface of the previous clime in the stack as input, then adds the local condensation rate, or subtracts the local evaporation rate to determine the output water flow rate on each of its corresponding conductor surfaces. Any liquid film remaining on the conductor surfaces of the last clime in a stack is added to the liquid field of the GOTHIC cell in contact with the conductor surface, or an alternate drain cell specified by user input.

Dryout occurs when either the film flow rate is low enough or the heat flux is high enough to result in complete evaporation of the film before it can exit the conductor. The clime model calculates the evaporation heat and mass transfer and the location of the dryout elevation; the remainder of the conductor surface below the dryout elevation is treated as a dry surface.

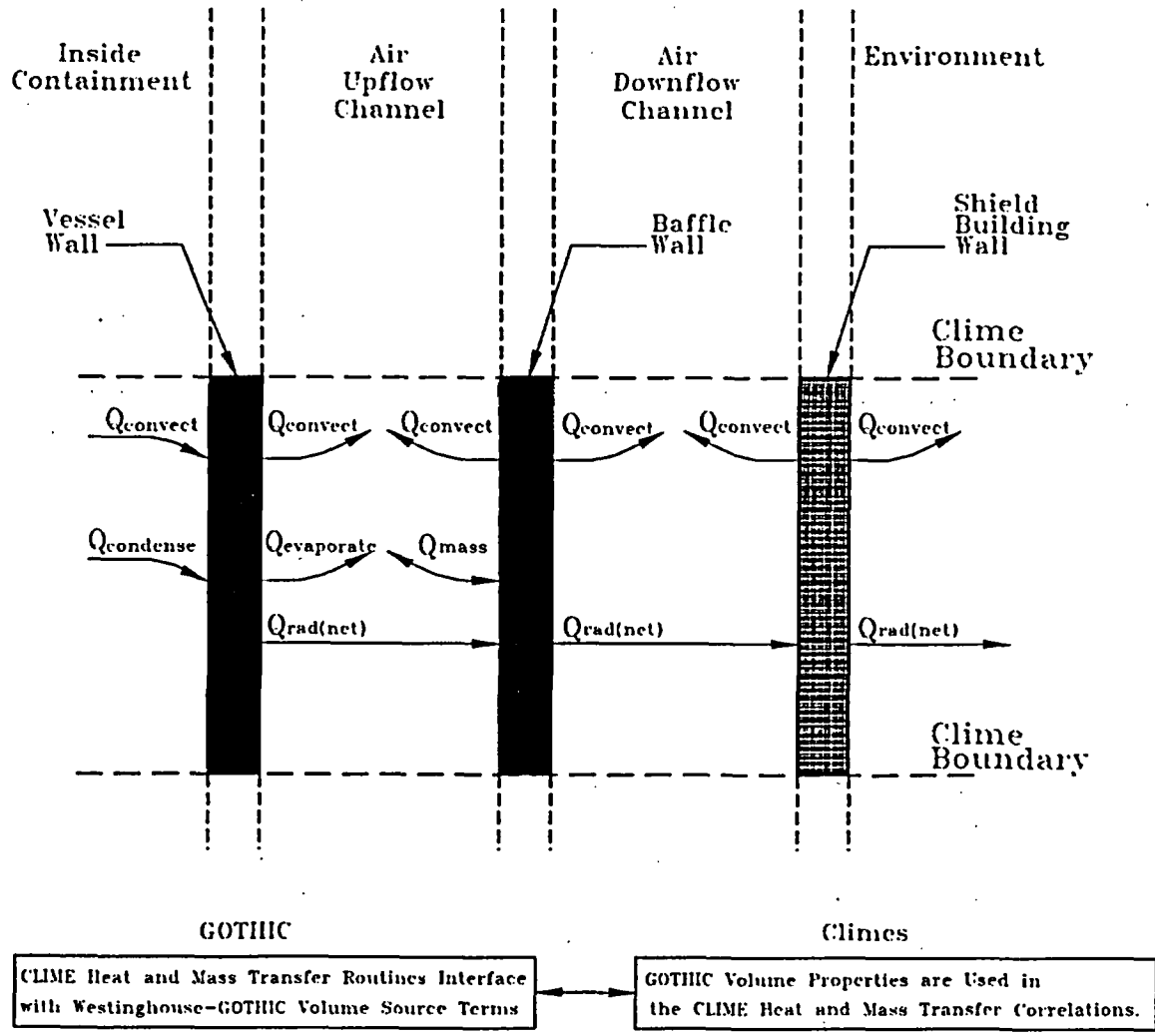


Figure 3-4 Westinghouse-GOTHIC Clime Wall Source Term Models

3.4 GENERAL CLIME EQUATIONS

The energy equation for the film must balance the heat from the wall into the film, the heat conduction through the film, and the heat and mass transfer from the film surface to the ambient, with the change in energy of the flowing film. Assuming constant fluid properties over the node surface, one-dimensional film flow along the wall, one-dimensional conduction across the film, and that the viscous dissipation term can be neglected, the general energy transport equation for the film can be written in terms of temperature as:

$$\frac{\partial T}{\partial t} = \frac{k}{\rho c_p} \frac{\partial^2 T}{\partial x^2} + v_z \frac{\partial T}{\partial Z} \quad (3-1)$$

For computational purposes, the water film is divided into 3 control volumes as shown in Figure 3-5. The boundary control volume of the film includes the outer 1/2 layer of the wall and its temperature equals the wall temperature. The outer surface of the outer control volume touches the atmosphere and its temperature is coupled to the temperature of the atmosphere through the heat and mass transfer boundary layer correlations. The temperature in the central control volume represents the average heat stored in the film. Note that all convected energy is transported in the central control volume. This simplification improves numerical stability. Referring to Figure 3-5, the film energy transport equation can be expressed in a finite difference form as follows:

$$\frac{T_{avg} - T_{avg, old}}{\Delta t} = \frac{4k_{film}}{\rho_{film} c_{p, film}} \frac{T_{surf,1} - 2T_{avg} + T_{wall,1}}{\delta x_{film}^2} + v_z \frac{T_{in} - T_{out}}{\Delta Z} \quad (3-2)$$

where:

- k_{film} = film thermal conductivity (Btu/ft-sec-°F)
- δx_{film} = film thickness (ft)
- $c_{p, film}$ = film heat capacity (Btu/lbm-°F)
- ρ_{film} = film density (lbm/ft³)
- T_{in} = inlet temperature of film at the top of the clime (°F)
- T_{out} = exit temperature of film at the bottom of the clime (°F)
- T_{avg} = temperature of the center of the film (°F)
- $T_{wall,1}$ = temperature of first wall node (°F)
- $T_{surf,1}$ = film surface temperature (°F)
- ΔZ = height of the clime (ft)
- v_z = film velocity (ft/sec)

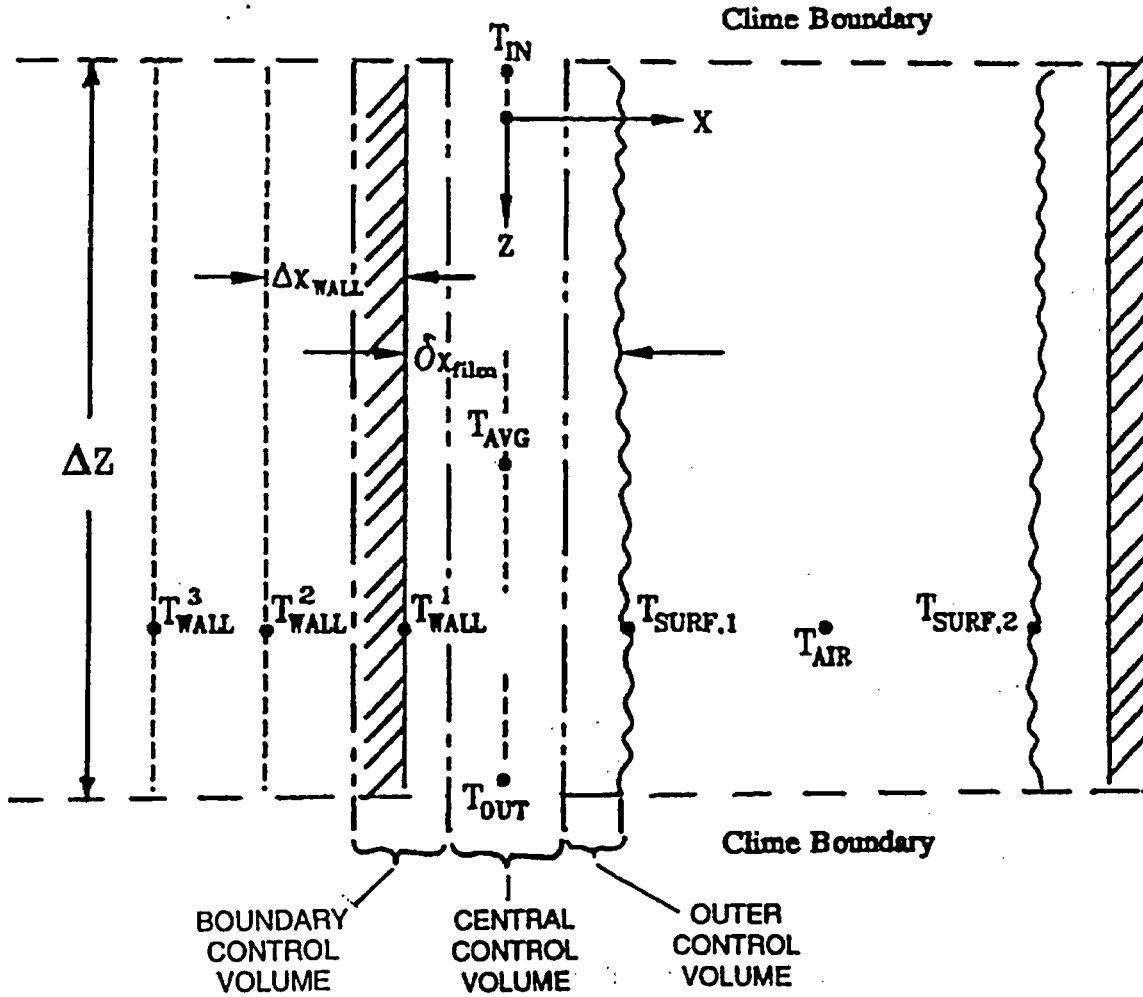


Figure 3-5 Clime Finite Difference Model Definitions

The film inlet temperature is given, either from a boundary condition or from the outlet temperature of the preceding clime in the stack. To ensure stability, the film outlet temperature is defined to be the same as the average temperature.

$$T_{\text{out}} = T_{\text{avg}} \quad (3-3)$$

The inner film surface boundary condition forces the heat flux from the outer surface of the conductor wall to equal the heat flux into the film. The solid film interface boundary condition is:

$$k_{\text{wall}} \frac{\partial T}{\partial x} \Big|_{\text{wall}} = k_{\text{film}} \frac{\partial T}{\partial x} \Big|_{\text{film}} \quad (3-4)$$

The outer film surface boundary condition equates the energy leaving the outer film layer surface to the energy entering the atmosphere. The energy leaving the film surface may enter the atmosphere through a combination of convection, evaporation, and radiation. The outer film surface boundary condition is:

$$-k_{\text{film}} \frac{\partial T}{\partial x} \Big|_{\text{film}} = h_c (T_{\text{surf},1} - T_{\text{air}}) + h_M h_{fg} (P_{\text{stm}}^{\text{air}} - P_g^{\text{film}}) + \epsilon \sigma (T_{\text{surf},1}^4 - T_{\text{surf},2}^4) \quad (3-5)$$

where:

- h_c = convection heat transfer coefficient from the film to the air (Btu/sec-ft²-°F)
- T_{air} = air temperature (°F)
- h_M = mass transfer coefficient (lbm/sec-ft²-psi)
- h_{fg} = latent heat of vaporization of the film (Btu/lbm)
- $P_{\text{stm}}^{\text{air}}$ = partial pressure of steam in the air (psi)
- P_g^{film} = saturation pressure of steam at the film surface temperature, $T_{\text{surf},1}$ (psi)
- ϵ = emissivity of film surface
- σ = Stefan-Bolzman constant
- $T_{\text{surf},2}$ = temperature of second radiative surface (°R)

The four film equations are:

$$\frac{T_{avg} - T_{avg,old}}{\Delta t} = \frac{4k_{film}}{\rho_{film}c_{p,film}} \frac{T_{surf,1} - 2T_{avg} + T_{wall,1}}{\delta x_{film}^2} + v_z \frac{T_{in} - T_{out}}{\Delta Z} \quad (3-6)$$

$$k_{wall} \frac{\partial T}{\partial x} \Big|_{wall} = k_{film} \frac{\partial T}{\partial x} \Big|_{film} \quad (3-7)$$

$$-k_{film} \frac{\partial T}{\partial x} \Big|_{film} = h_c (T_{surf,1} - T_{air}) + h_M h_{fg} (P_{stm}^{air} - P_g^{film}) + \epsilon \sigma (T_{surf,1}^4 - T_{surf,2}^4) \quad (3-8)$$

$$T_{out} = T_{avg} \quad (3-9)$$

The wall conduction equation is tightly coupled to these film equations. For points within the wall, the conduction equation is simply a one-dimensional partial differential equation:

$$\frac{\partial T}{\partial t} = \frac{k}{\rho c_p} \frac{\partial^2 T}{\partial x^2} \quad (3-10)$$

By replacing the derivatives with finite differences, this partial differential equation is replaced with a system of algebraic equations. The superscript "n" identifies the point (node) at which the derivatives are to be calculated.

$$\frac{T_{wall,n} - T_{wall,n,old}}{\Delta t} = \frac{k_{wall}}{\rho_{wall}c_{p,wall}} \frac{T_{wall,n+1} - 2T_{wall,n} + T_{wall,n-1}}{\Delta x_{wall}^2} \quad (3-11)$$

This equation, along with Equations (3-6 through 3-9), can be considered to be the system of equations for a clime.

Although the differential Boundary Condition Equation (3-7) is mathematically complete and correct, numerical stability in a finite difference formulation is improved by defining an alternate control volume containing the boundary between solid and liquid. This control volume is defined to contain the wall material from the surface to a point halfway between the surface and the first internal calculational point (that is, between wall nodes 1 and 2) into the control volume and the inner quarter of the film. A single energy balance equation for the boundary control volume is,

$$\left[\rho_{\text{wall}} c_{p,\text{wall}} \frac{\Delta x_{\text{wall}}}{2} + \rho_{\text{film}} c_{p,\text{film}} \frac{\delta x_{\text{film}}}{4} \right] \frac{dT_{\text{wall},1}}{dt} =$$

$$k_{\text{wall}} \frac{T_{\text{wall},2} - T_{\text{wall},1}}{\Delta x_{\text{wall}}} - 2k_{\text{film}} \frac{T_{\text{wall},1} - T_{\text{avg}}}{\delta x_{\text{film}}} \quad (3-12)$$

Note that we neglect film convective energy transport for the boundary control volume. Because the film velocity at the wall is zero, the effect of neglecting this is small. A similar control volume and heat flux equation is defined for the outer half of the outer film layer to model the air/film interface in Equation (3-8). In this case, the film surface heat flux is the sum of the convection, radiation, and mass transfer heat fluxes.

$$\rho_{\text{film}} c_{p,\text{film}} \frac{\delta x_{\text{film}}}{4} \frac{dT_{\text{surf}}}{dt} = 2k_{\text{film}} \frac{T_{\text{avg}} - T_{\text{surf}}}{\delta x_{\text{film}}} - h_c (T_{\text{surf},1} - T_{\text{air}})$$

$$- h_M h_{fg} (P_{\text{stm}}^{\text{air}} - P_g^{\text{film}}) - \epsilon \sigma (T_{\text{surf},1}^4 - T_{\text{surf},2}^4)^{a,c} \quad (3-13)$$

Most of the convective energy transport by the film as it flows down the shell is carried in the central flow region of the film. At the wall, the film velocity is zero so there is little transport next to the wall even though the temperature gradient is greatest there. At the film surface, the vertical temperature gradient is smallest because the film surface temperature is strongly coupled to the surrounding atmosphere which has a relatively small vertical temperature gradient.

In the WGOTHIC Containment Evaluation Model, most of the water film on the outside of the containment is expected to evaporate. The latent heat of evaporation of water is around 1000 Btu/lbm. Compare this with the heat required to heat water from its initial temperature to the dewpoint temperature of the surrounding air which is around 20-50 Btu/lbm. At most, the subcooling of a completely evaporating film accounts for about 5 percent of the total energy removal. The numerical error introduced by neglecting the transport in the control volumes at the wall and on the film surface is estimated to be less than 20 percent of the total energy transport. Thus the total energy imbalance introduced by neglecting these transport terms is less than 1 percent of the total energy removal from containment.

On the inside of containment, the water film temperature is very closely tied to the partial pressure of steam. During the large-scale tests, the internal steam concentration vertical gradient was observed to be nearly zero. The numerical error in the transport equation on the inside is smaller than the 1 percent of total energy on the outside of containment.

In principle, the effects of the numerical modeling assumptions could be reduced more by including the film surface vertical convective energy transport term. During the development of the model, this term was included and appeared to be linked to an instability that arose through the interaction between the transport energy and the non-linear radiation and convective heat and mass transfer models. As a result, a decision was made to accept the small numerical error to maintain the stability of the model.

The second numerical assumption made is that the film instantly covers the containment as soon as film flow is introduced in the code, i.e., no tracking of a film front is performed. The film flow is initiated by a high-pressure signal inside containment. At this time, the outer surface of the containment is still cold. It takes several minutes for the film to entirely cover the containment. It also takes about 10-15 minutes for the outer surface of the containment to heat sufficiently for the heat and mass transfer models to start to have any effect. As a result, by the time evaporation could contribute to heat removal, the containment would be covered with water anyway. The only other time that this could have an impact on transient results would be if there is a step change in the flow. Given that the transient involving large changes in the film flow occur over a period of more than a day, the error in assuming an instantaneous step change instead of a change over several minutes can be considered to be small. In addition, it can be compensated for by ramping the flow rate over a period of several minutes instead of introducing the step change.

Equations 3-6, 3-9, and 3-11 through 3-13 represent the complete system of equations for a clime as used in WGOTHIC. See Sections 4 and 13 for a description of how climes are implemented for the AP600 and AP1000 Containment Evaluation Models.

3.5 INTEGRATION OF THE WESTINGHOUSE CLIME MODEL INTO GOTHIC

The Westinghouse clime model is composed of a set of subroutines. These subroutines were added to the GOTHIC solver program to create the WGOTHIC solver program. The GOTHIC solver program logic was modified to incorporate the clime model as follows:

- A call to the subroutine that reads the clime input was added
- A call to the subroutine "gshell", the main calling routine for the clime model, was added
- A call to the subroutine that generates the clime output was added

The clime model flow control outline is shown in Figure 3-6. Subroutine "gshell" is the main calling routine for the other subroutines of the clime model. Separate subroutines in the clime model compute the heat and mass transfer coefficients between the conductor surfaces and the corresponding volumes, the surface-to-surface radiation heat transfer, the conductor wall temperature distribution, and the changes to the source terms for the GOTHIC mass and energy conservation equations.

The interface between the climate model and GOTHIC takes place through the source terms for the GOTHIC mass and energy conservation equations. The GOTHIC vapor mass and energy source terms are updated to include the mass and energy transfer due to convection, radiation, evaporation, and condensation within the climes. The GOTHIC liquid mass and energy source terms are updated to include the liquid mass and energy transfer due to runoff or stripping of the liquid film from the climes.

a,b,c

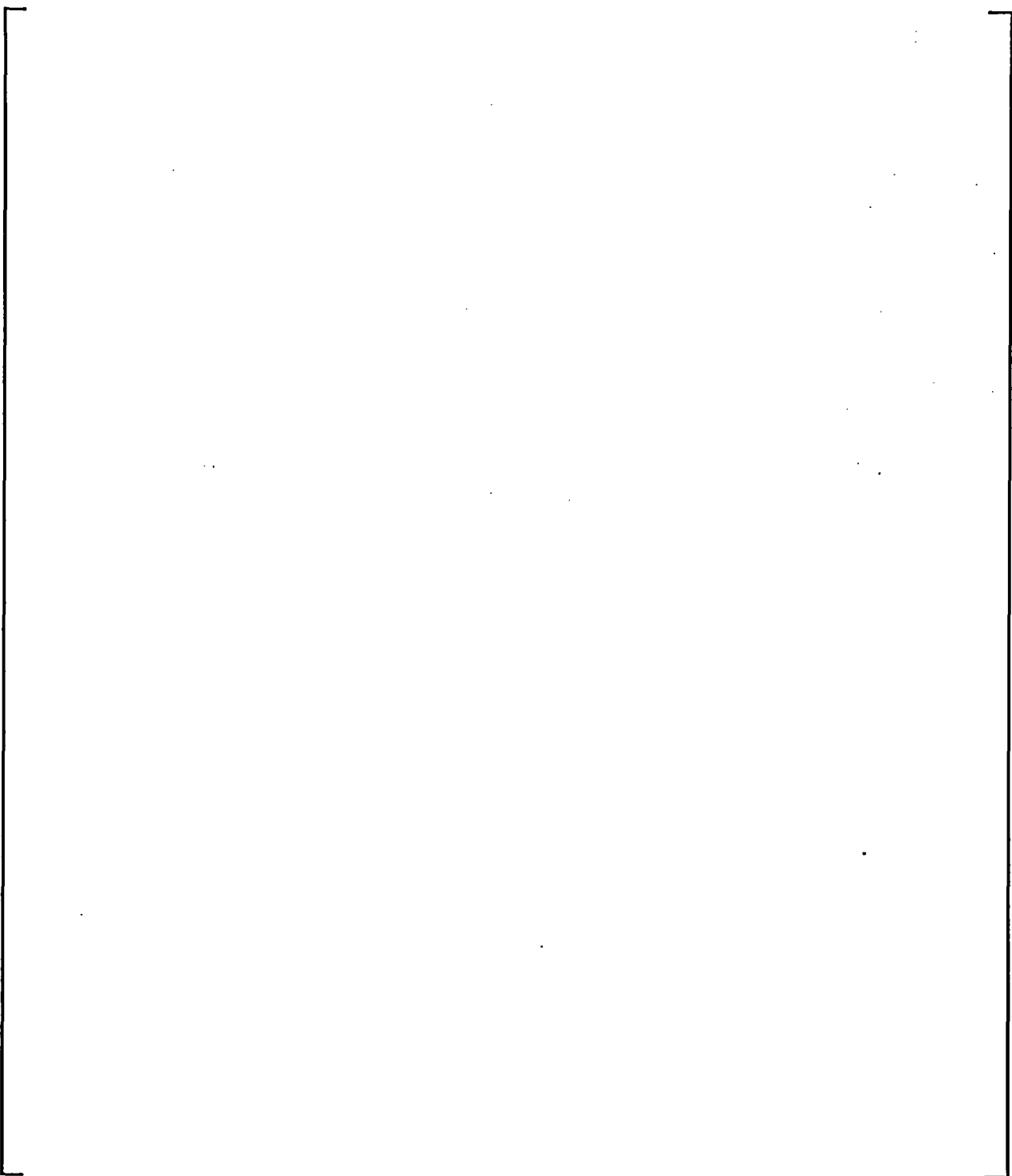


Figure 3-6 Clime Routines Flow Control Outline

3.6 REFERENCES

- 3.1. Westinghouse Letter NTD-NRC-95-4563, B.A. McIntyre to Quay (NRC), "GOTHIC Version 4.0 Documentation," September 21, 1995
- 3.2. Westinghouse Letter NTD-NRC-95-4462, N.J. Liparulo to T.R. Quay (NRC), EPRI Report RA-93-10, "GOTHIC Design Review, Final Report," May 15, 1995
- 3.3. WCAP-14382, "WGOTHIC Code Description and Validation," M. Kennedy, et al., May 1995
- 3.4. Westinghouse Letter NTD-NRC-95-4595, B.A. McIntyre to Quay (NRC), "AP600 WGOTHIC Comparison to GOTHIC," November 13, 1995
- 3.5. WCAP-14812, "Accident Specification and Phenomena Evaluation for AP600 Passive Containment Cooling System," Revision 2, April 1998
- 3.6. WCAP-14326, Rev. 2, "Experimental Basis for the AP600 Containment Vessel Heat and Mass Transfer Correlations," F. Delose, et al., April 1998

Section 4

**Description of AP600 Plant Geometry in
WGOTHIC Evaluation Model**

This entire section (4) is proprietary to Westinghouse Electric Company.(a,c)

Section 5

Initial and Boundary Conditions

TABLE OF CONTENTS

LIST OF TABLES iv

LIST OF FIGURES v

5.1 INTRODUCTION 5-1

5.2 INITIAL CONDITION SENSITIVITY CASES 5-1

5.3 INITIAL CONTAINMENT HUMIDITY 5-3

5.4 INITIAL CONTAINMENT PRESSURE 5-4

5.5 INITIAL CONTAINMENT TEMPERATURE 5-9

5.6 AMBIENT HUMIDITY 5-12

5.7 AMBIENT TEMPERATURE 5-15

5.8 SENSITIVITY TO DROP MODELING ASSUMPTIONS 5-20

5.9 CONCLUSIONS 5-20

LIST OF TABLES

| | | |
|-----------|---|-----|
| Table 5-1 | Initial Conditions | 5-1 |
| Table 5-2 | Initial Conditions Sensitivity Analysis Cases | 5-2 |
| Table 5-3 | Summary of Pressure Results for LOCA Initial Condition Sensitivity Studies | 5-3 |
| Table 5-4 | Summary of Pressure Results for MSLB Initial Condition Sensitivity Studies | 5-3 |

LIST OF FIGURES

Figure 5-1 Case 1 - Initial Containment Humidity Sensitivity - LOCA 5-5

Figure 5-2 Case 8 - Initial Containment Humidity Sensitivity - MSLB 5-6

Figure 5-3 Case 2 - Initial Containment Pressure Sensitivity - LOCA 5-7

Figure 5-4 Case 9 - Initial Containment Pressure Sensitivity - MSLB 5-8

Figure 5-5 Case 3 - Initial Containment Temperature Sensitivity - LOCA 5-10

Figure 5-6 Case 10 - Initial Containment Temperature Sensitivity - MSLB 5-11

Figure 5-7 Case 4 - Ambient Humidity Sensitivity at 115°F Ambient
Temperature - LOCA 5-13

Figure 5-8 Case 11 - Ambient Humidity Sensitivity at 115°F Ambient
Temperature - MSLB 5-14

Figure 5-9 Case 5 - Ambient Temperature Sensitivity - LOCA 5-16

Figure 5-10 Case 12 - Ambient Temperature Sensitivity - MSLB 5-17

Figure 5-11 Case 7 - Film Temperature Sensitivity - LOCA 5-18

Figure 5-12 Case 14 - Film Temperature Sensitivity - MSLB 5-19

Figure 5-13 Blowdown Drop Fraction Sensitivity - LOCA 5-21

5.1 INTRODUCTION

The purpose of this section is to describe a series of sensitivity analyses performed using the AP600 containment model to examine the effect of initial conditions on containment pressure response for the LOCA and MSLB events. Sensitivity evaluations are performed on initial containment humidity, pressure, and temperature, as well as ambient (outside containment) humidity and temperature. In addition, a sensitivity to drop modeling assumptions – a boundary condition for LOCA – is presented in this section.

Initial conditions assumed in the WGOTHIC Evaluation Model are conservatively set to maximize containment pressure response and are consistent with Technical Specifications and site interface parameter limits. Initial conditions assumed in the sensitivity evaluations are set at the opposing end of the Technical Specifications and site interface parameter limits for all sensitivity cases in this section except for the external temperature sensitivity, which was examined over a more limited range to be consistent with the film temperature range.

5.2 INITIAL CONDITION SENSITIVITY CASES

The initial conditions considered in the sensitivity studies are summarized in Table 5-1. The reference values for the initial condition parameters were selected in the Evaluation Model to maximize peak containment pressure. The reference value in Table 5-1 corresponds to the Evaluation Model.

| Table 5-1 Initial Conditions | | |
|--|------------------------|--------------------------|
| Initial Condition Sensitivity Case | Reference Value | Sensitivity Value |
| Containment Relative Humidity, % | 0 | 100 |
| Containment Pressure, psia | 15.7 | 14.5 |
| Containment Temperature, °F | 120 | 50 |
| Ambient (Outside) Relative Humidity, % (Based on 80°F wet bulb temperature at 115°F) 100% Relative Humidity is the maximum value when the ambient temperature is 40°F | 22 | 0 0/100 |
| Ambient (Outside) Temperature, °F | 115 | 40 |
| Water Film Temperature on Outside Shell Surface, °F | 120 | 40 |

The sensitivity cases considered for the LOCA and MSLB transients are summarized in Table 5-2 with the initial condition parameters assumed in each case. Only values noted in Table 5-2 were varied in each of the cases. The reference cases for the LOCA and MSLB are described in Sections 4.5.2.1 and 4.5.2.2, respectively. The mass and energy releases are the same for all LOCA and MSLB cases. A summary of the pressure results are summarized in Table 5-3 for the LOCA and Table 5-4 for the MSLB. A discussion of each sensitivity case is provided in the following sections.

| Table 5-2 Initial Conditions Sensitivity Analysis Cases | | | | | | | | |
|---|-----------|--------------------|----------|--------|-----------------|---------------------|-------------|--------|
| Case | Transient | Inside Containment | | | | Outside Containment | | |
| | | T-air (°F) | P (psia) | RH (%) | T-ht. sink (°F) | T-air (°F) | T-film (°F) | RH (%) |
| Reference | | 120 | 15.7 | 0 | 120 | 115 | 120 | 22 |
| 1 | LOCA | 120 | 15.7 | 100 | 120 | 115 | 120 | 22 |
| 2 | LOCA | 120 | 14.5 | 0 | 120 | 115 | 120 | 22 |
| 3 | LOCA | 50 | 15.7 | 0 | 50 | 115 | 120 | 22 |
| 4 | LOCA | 120 | 15.7 | 0 | 120 | 115 | 120 | 0 |
| 5 | LOCA | 120 | 15.7 | 0 | 120 | 40 | 40 | 100 |
| 6 | LOCA | 120 | 15.7 | 0 | 120 | 40 | 40 | 0 |
| 7 | LOCA | 120 | 15.7 | 0 | 120 | 115 | 40 | 22 |
| 8 | MSLB | 120 | 15.7 | 100 | 120 | 115 | 120 | 22 |
| 9 | MSLB | 120 | 14.5 | 0 | 120 | 115 | 120 | 22 |
| 10 | MSLB | 50 | 15.7 | 0 | 50 | 115 | 120 | 22 |
| 11 | MSLB | 120 | 15.7 | 0 | 120 | 115 | 120 | 0 |
| 12 | MSLB | 120 | 15.7 | 0 | 120 | 40 | 40 | 100 |
| 13 | MSLB | 120 | 15.7 | 0 | 120 | 40 | 40 | 0 |
| 14 | MSLB | 120 | 15.7 | 0 | 120 | 115 | 40 | 22 |

| Table 5-3 Summary of Pressure Results for LOCA Initial Condition Sensitivity Studies | | | |
|---|---|---|--|
| | Peak Pressure During Blowdown (psig) | Peak Post-Blowdown Pressure (psig) | Pressure at 24 Hours (psig) |
| Eval. Model | 34.4 | 43.9 | 18.9 |
| Case 1 | 34.0 | 42.5 | 16.6 |
| Case 2 | 33.0 | 42.1 | 17.2 |
| Case 3 | 35.2 | 42.5 | 19.4 |
| Case 4 | 34.4 | 43.9 | 18.9 |
| Case 5 | 34.4 | 43.7 | 16.6 |
| Case 6 | 34.4 | 43.7 | 16.6 |
| Case 7 | 34.4 | 43.7 | 16.6 |

| Table 5-4 Summary of Pressure Results for MSLB Initial Condition Sensitivity Studies | |
|---|-----------------------------|
| | Peak Pressure (psig) |
| Evaluation Model | 44.8 |
| Case 8 | 43.6 |
| Case 9 | 42.9 |
| Case 10 | 44.6 |
| Case 11 | 44.7 |
| Case 12 | 44.7 |
| Case 13 | 44.7 |
| Case 14 | 44.7 |

5.3 INITIAL CONTAINMENT HUMIDITY

The purpose of this sensitivity analysis is to illustrate the effect of initial containment humidity on containment pressure response. Initial humidity affects the initial mass of air in the containment and the concentration of air inside containment during the accident. In general, the

presence of noncondensable gases reduces the effectiveness of internal heat sink structures to absorb energy, since the condensing vapor must diffuse through the gas before it can condense on the surface.

The upper and lower bounds on relative humidity are 100 percent and 0 percent, respectively. The minimum, initial containment relative humidity (0 percent) is used for the Evaluation Model, since this value produces a higher peak containment pressure. The maximum relative humidity (100 percent) is assumed for the sensitivity case in order to quantify the effect of initial containment relative humidity on containment pressure response.

The sensitivity of containment pressure to initial containment humidity is illustrated in Figure 5-1 for the LOCA (Case 1) and Figure 5-2 for the MSLB (Case 8). The sensitivity and reference cases are compared, corresponding to 100 percent and 0 percent relative humidity, respectively. A higher containment pressure response is predicted for zero percent relative humidity than for the sensitivity case at 100 percent relative humidity. The effect of relative humidity on containment pressure is explained by the influence of air on the rate of condensation on internal heat sink structures, and the additional mass of air in containment. Lower relative humidity corresponds to lower vapor partial pressure and hence, to lower water vapor concentration. Since the total initial pressure is fixed, the partial pressure and, therefore, the concentration of air is greater at 0 percent than at 100 percent relative humidity. The higher mass of air also contributes to the pressurization as it heats up in thermal equilibrium with the steam. A greater quantity of air in the condensing vapor also results in greater resistance to heat transfer, since the vapor must diffuse through the gas before it can condense on the surface. This factor reduces the overall heat removal capability of internal heat sink structures, and results in greater containment pressures for the initial 0 percent relative humidity case.

5.4 INITIAL CONTAINMENT PRESSURE

Initial containment pressure directly affects the containment pressure response. The range of initial containment pressures is bounded by the Technical Specifications limits. The initial internal containment pressure is set to the maximum Technical Specifications limit of 15.7 psia (1.0 psig) in the Evaluation Model. The lower bound (sensitivity case) initial containment pressure is set at the minimum Technical Specification limit of 14.5 psia (-0.2 psig).

The sensitivity of containment pressure to the initial containment pressure is shown in Figure 5-3 for the LOCA (Case 2) and Figure 5-4 for the MSLB (Case 9). As expected, greater initial containment pressure results in greater containment pressure response throughout the transient. A higher initial pressure results in a greater mass (and hence concentration) of air and results in higher containment pressures.

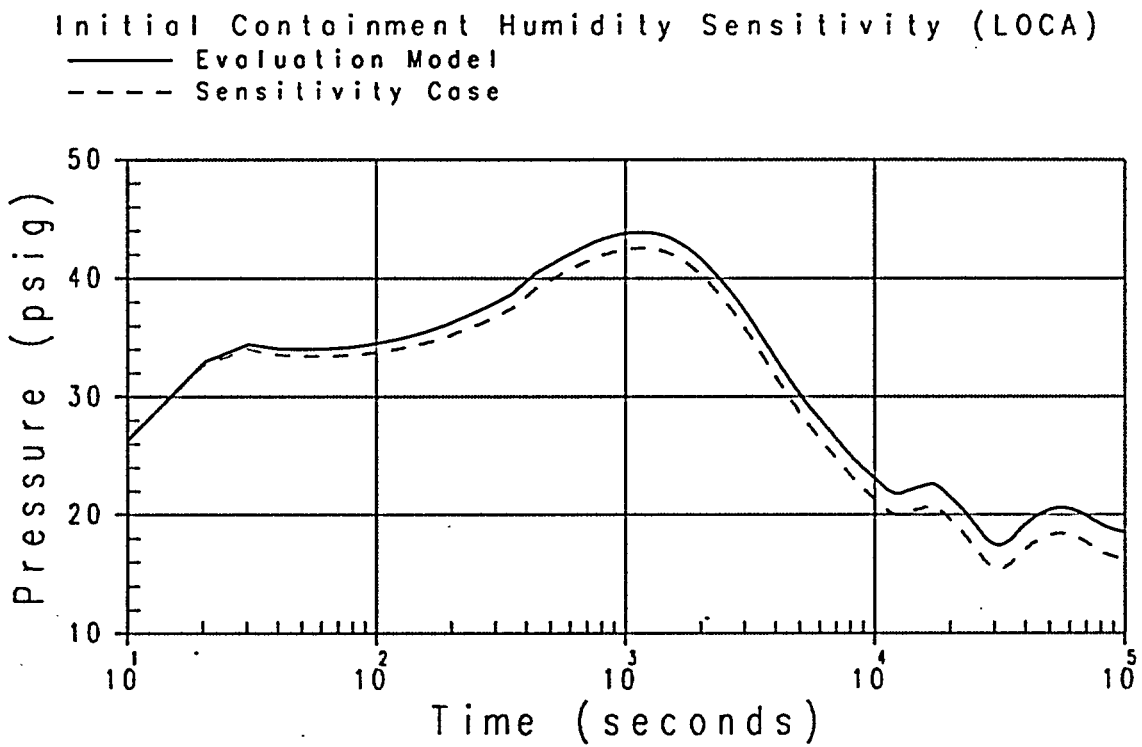


Figure 5-1 Case 1 - Initial Containment Humidity Sensitivity - LOCA

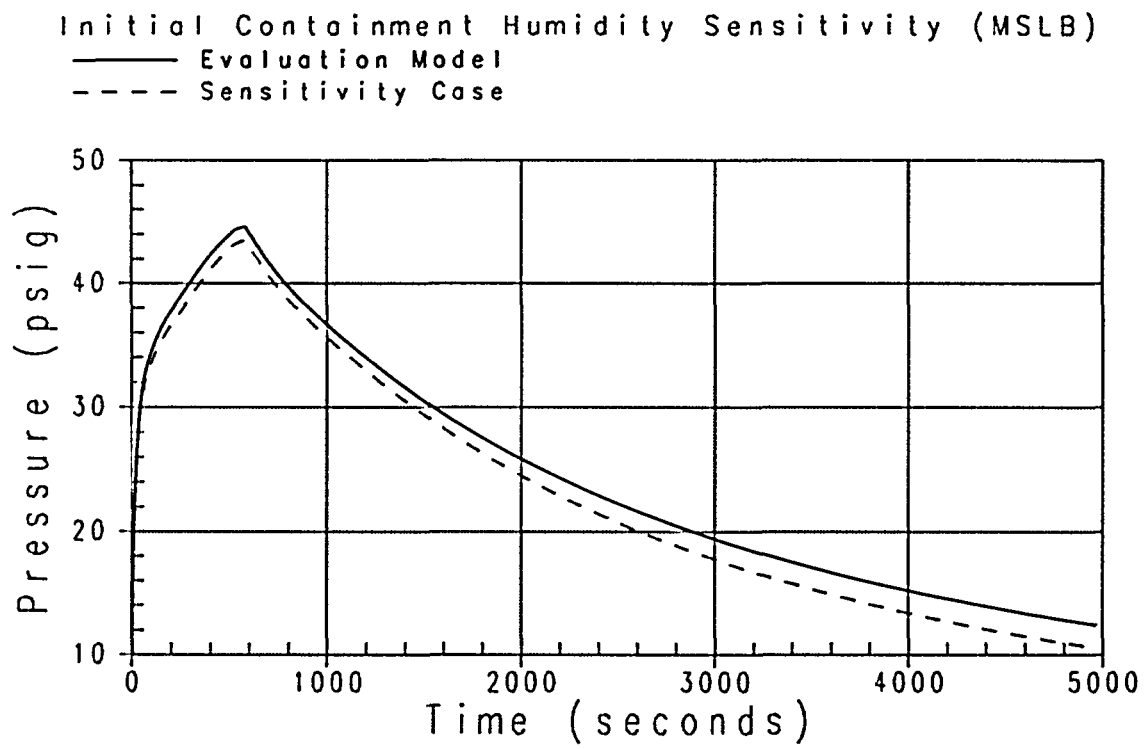


Figure 5-2 Case 8 - Initial Containment Humidity Sensitivity - MSLB

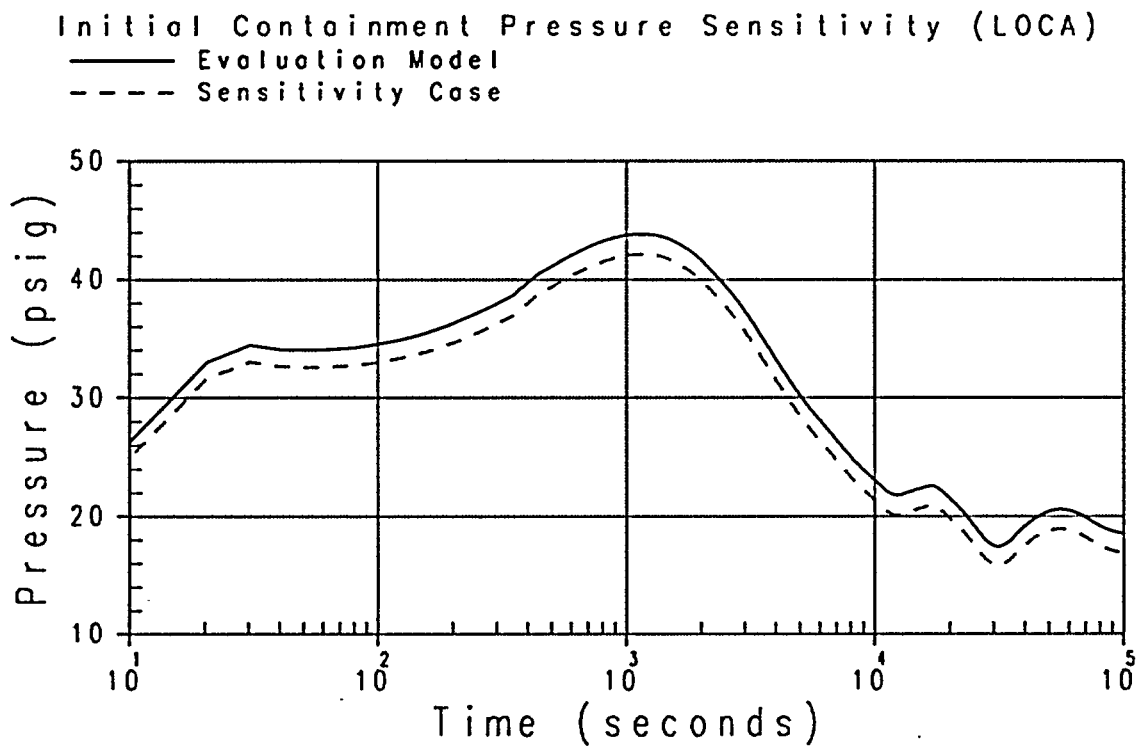


Figure 5-3 Case 2 - Initial Containment Pressure Sensitivity - LOCA

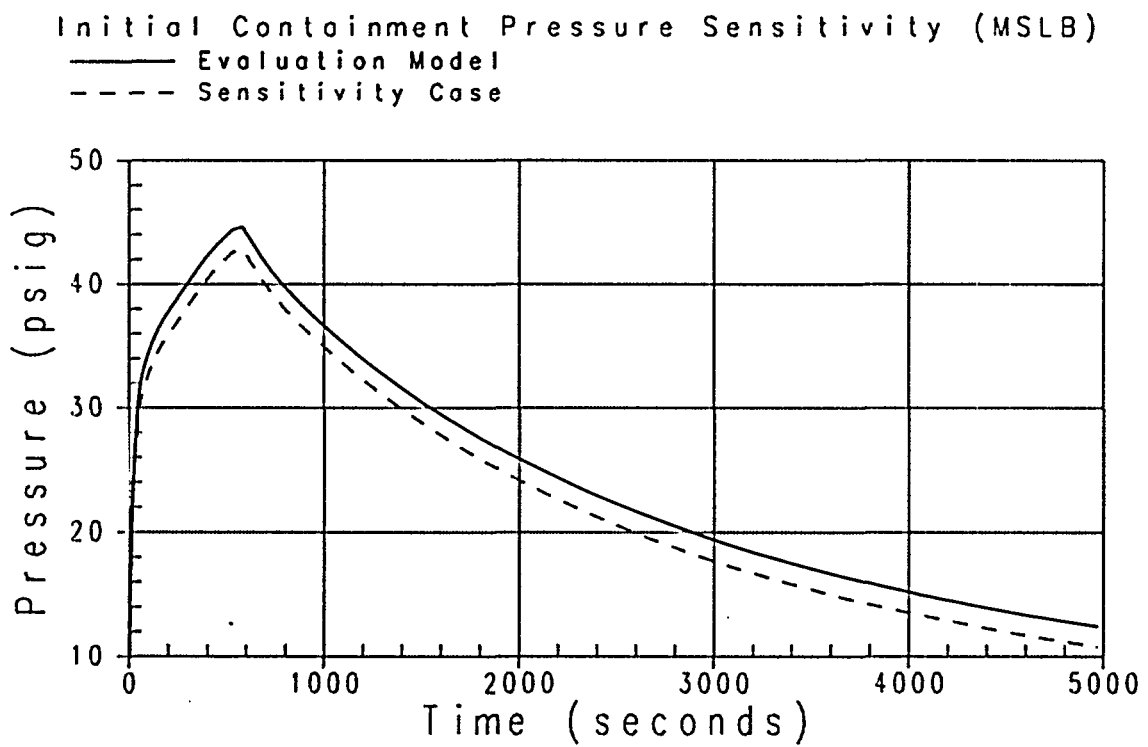


Figure 5-4 Case 9 - Initial Containment Pressure Sensitivity - MSLB

5.5 INITIAL CONTAINMENT TEMPERATURE

The purpose of this sensitivity analysis is to quantify the effect of initial containment temperature on containment pressure response. Containment air, internal heat sink, and containment shell initial temperature are simultaneously varied. A change in the initial air temperature affects the concentration of air inside containment. A change in the initial containment heat sink temperature directly affects the heat absorption capacity of these structures.

The initial containment temperature is set to the maximum Technical Specification limit of 120°F in the Evaluation Model. The lower bound (sensitivity case) initial containment temperature is set to a value of 50°F.

The sensitivity of containment pressure to initial containment temperature is shown in Figure 5-5 for the LOCA (Case 3) and Figure 5-6 for the MSLB (Case 10). As indicated, a higher peak containment pressure is predicted for the Evaluation Model case at 120°F, than for the sensitivity case at 50°F initial temperature. As illustrated in Figure 5-5, the pressure is higher for the 50°F initial temperature case during the blowdown phase of the transient, lower at the time of maximum pressure, and higher beyond approximately 5000 seconds. For the MSLB case shown in Figure 5-6, the peak pressure is slightly lower for the 50°F initial temperature case, but is higher during the initial pressure rise and beyond approximately 2000 seconds.

This pressure response behavior is predominately due to two competing influences: (1) the effect of initial temperature on the amount of air in the containment, and (2) the effect of initial temperature on the heat absorption capacity of internal heat sink structures. A lower initial temperature results in a higher air mass which contributes to the pressurization as the containment heats up. The increased concentration inhibits condensation of vapor on internal heat sinks and results in higher containment pressures. In contrast, a lower initial temperature results in increased heat absorption capacity of internal heat sinks that tend to lower containment pressures. Initially the noncondensable gas concentration factor dominates, and the sensitivity case exhibits a slightly higher containment pressure. When the heat absorption capacity of internal heat sinks becomes the more dominant factor, a higher containment pressure results for the Evaluation Model case. As the internal heat sinks saturate, the air concentration factor again becomes the governing influence, and the pressure for the sensitivity case exceeds that for the Evaluation Model. The Evaluation Model uses the maximum temperature assumption in order to maximize the more limiting post-blowdown peak containment pressure.

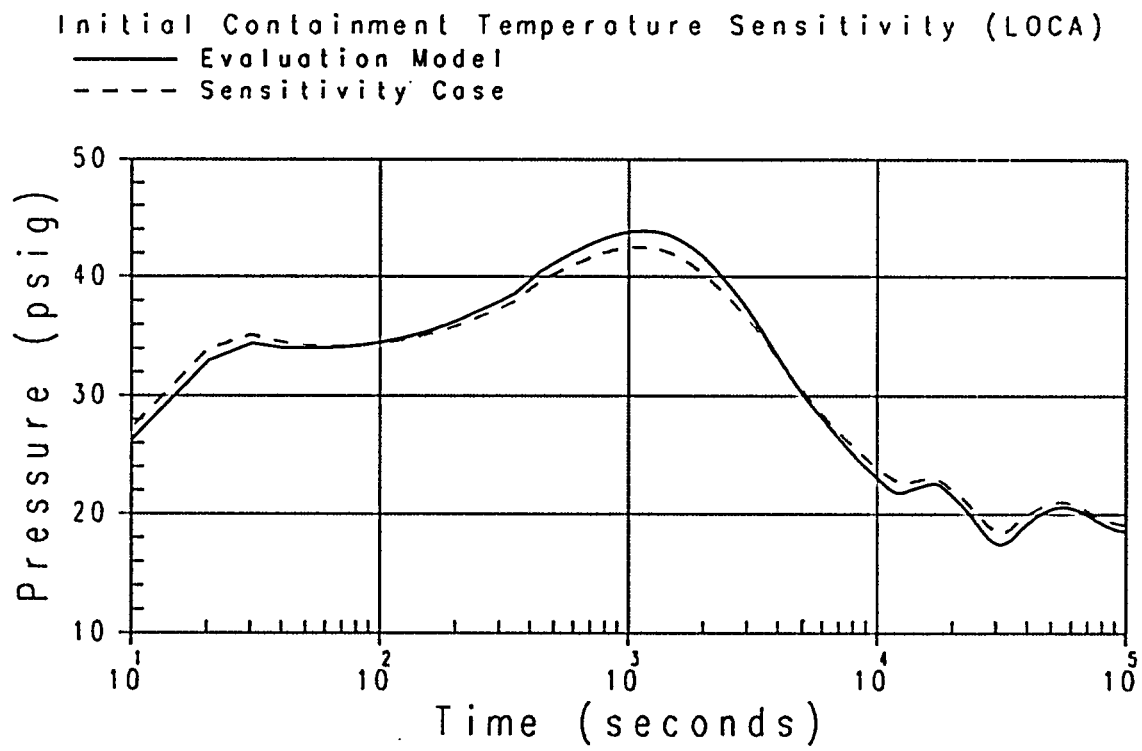


Figure 5-5 Case 3 - Initial Containment Temperature Sensitivity - LOCA

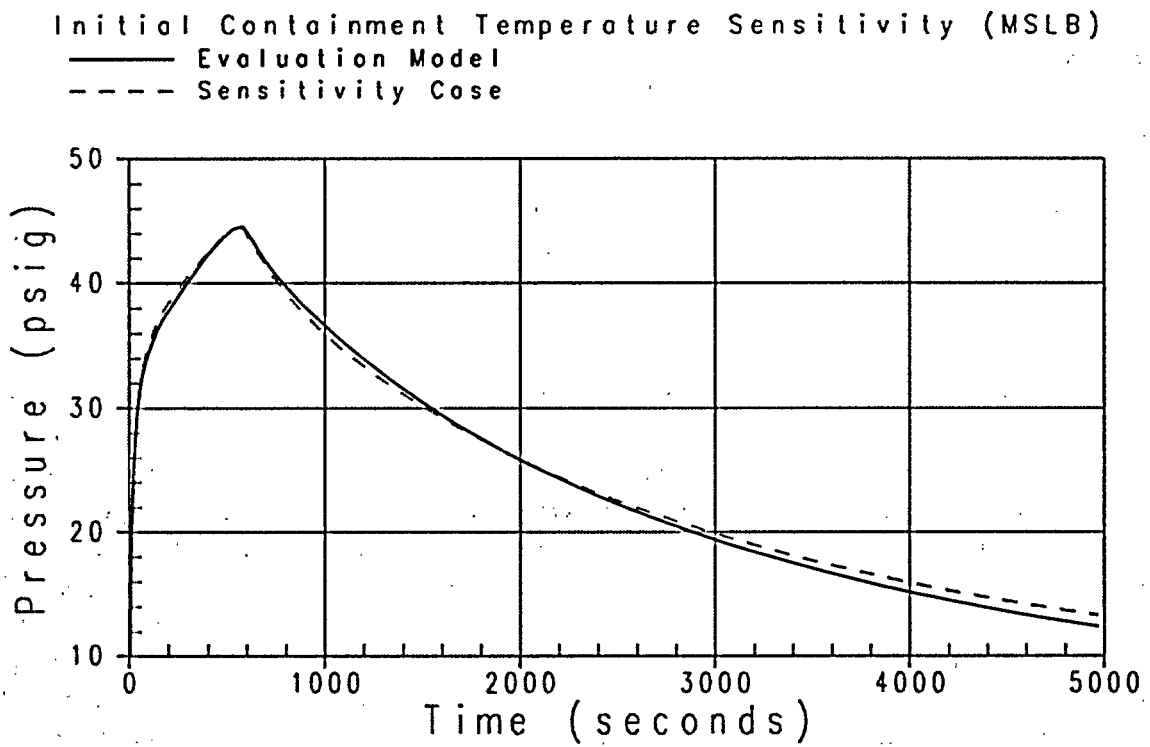


Figure 5-6 Case 10 - Initial Containment Temperature Sensitivity - MSLB

5.6 AMBIENT HUMIDITY

Heat is removed from the containment atmosphere by condensation and convection heat transfer to the shell, where it is conducted through the shell and rejected to the atmosphere on the outside of containment. Heat rejection to the atmosphere is achieved by convection to the buoyant cooling air, radiation to the baffle, and evaporation of the external PCS film to the cooling air. Evaporation of PCS water is the most significant of these heat removal mechanisms. Evaporation mass transfer is driven by the concentration gradient, or equivalently, the vapor partial pressure difference between the film and riser air. Changes in ambient or outside atmospheric conditions (e.g., relative humidity) can influence, to some degree, the vapor partial pressure difference. The purpose of this sensitivity analysis is to evaluate the effect of ambient humidity on containment pressure response.

The upper limit of ambient humidity is defined by the site interface parameters to be a maximum wet bulb temperature of 80°F. This corresponds to a relative humidity of 22 percent when the ambient temperature is 115°F. These boundary conditions are assumed in the Evaluation Model.

Two sets of sensitivities to relative humidity are presented. The first provides a comparison of the Evaluation Model to the case with 0 percent relative humidity at an ambient temperature of 115°F. The second sensitivity compares relative humidity of 0 percent and 100 percent at an ambient temperature of 40°F.

The sensitivity of containment pressure to ambient humidity is depicted in Figure 5-7 for the LOCA (Case 4) and Figure 5-8 for the MSLB (Case 11). The sensitivity and reference cases are compared corresponding to 0 and 22 percent relative humidity, respectively. These figures illustrate that containment pressure is not sensitive to initial inlet humidity. This result is consistent with the small effect of inlet humidity on the main factors governing the process of evaporation between the wetted shell and the riser air flow. The rate of evaporation is principally driven by the concentration gradient or, equivalently, the difference in vapor partial pressure between the film interface and the bulk air mixture. The partial pressure of vapor at the film interface is equal to the saturation pressure at the film temperature. Because the concentration of water vapor in the bulk air mixture is small in comparison, the partial pressure gradient is essentially given by the saturation pressure at the film interface. Consequently, initial inlet humidity has no significant effect on the rate of film evaporation or on containment pressure.

The sensitivity performed at 40°F, comparing 0 and 100 percent relative humidity, exhibited the same behavior, indicating almost no sensitivity to ambient humidity. A comparison of Case 5 to Case 6 for LOCA, and Case 12 to Case 13 for MSLB indicates a nearly identical pressure response. A comparison plot for these cases is not provided. The differences in these cases compared to the Evaluation Model are due to ambient temperature differences which are discussed in the Section 5.7.

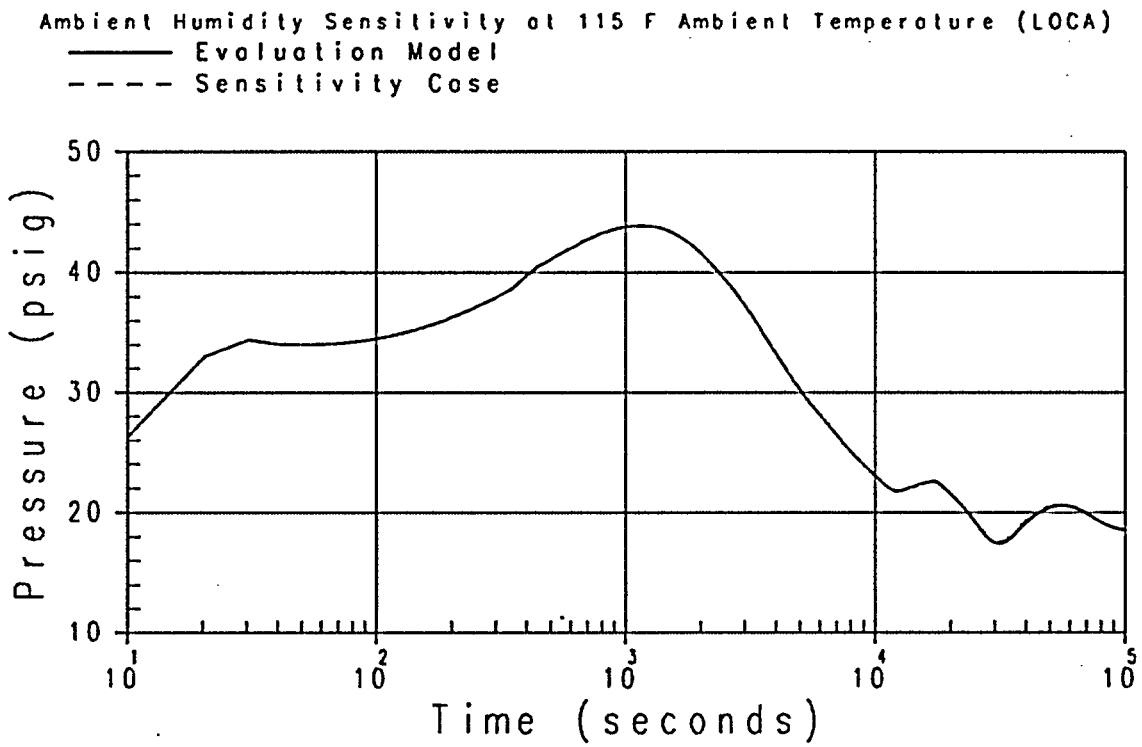


Figure 5-7 Case 4 - Ambient Humidity Sensitivity at 115°F Ambient Temperature - LOCA

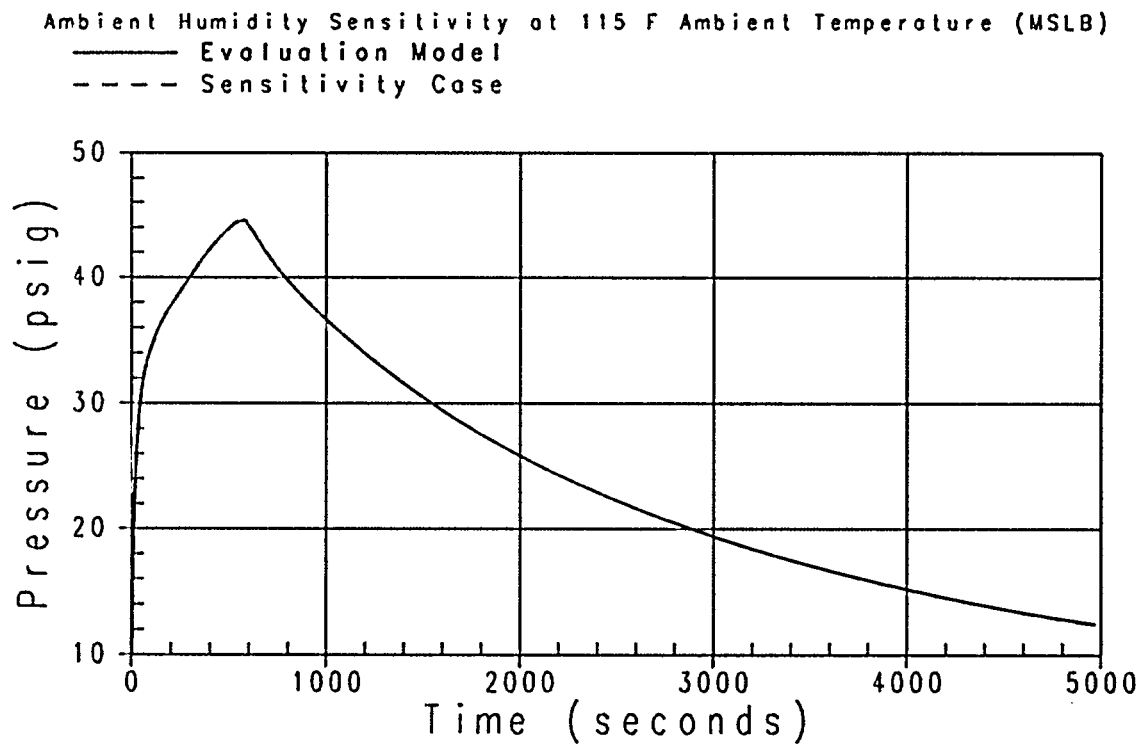


Figure 5-8 Case 11 - Ambient Humidity Sensitivity at 115°F Ambient Temperature - MSLB

5.7 AMBIENT TEMPERATURE

The purpose of this sensitivity analysis is to illustrate the effect of ambient temperature on containment pressure response. Cooling air and PCS water temperature are simultaneously and independently varied in order to investigate the effects. A change in the ambient air temperature primarily affects heat rejection by convection to the riser air flow. A change in the PCS water temperature affects the amount of energy absorbed by sensible heating.

The site interface parameter limits on ambient air temperature are 115°F and -40°F. The minimum PCS water temperature is limited by the Technical Specifications to a value of 40°F. Since a higher ambient temperature and PCS water temperature produces a slightly greater containment pressure, the maximum ambient temperature (115°F) and PCS water temperature (120°F) are assumed for the Evaluation Model. The temperature for both inlet air and PCS water (sensitivity case) is set equal to 40°F.

The sensitivity of containment pressure to ambient temperature is shown in Figure 5-9 for the LOCA (Case 5) and Figure 5-10 for the MSLB (Case 12). As indicated, lower containment pressures are predicted for the sensitivity case at lower ambient temperatures late in the transient for the LOCA case. There is little impact on the peak pressure or pressure early in time. The containment pressure for an MSLB is less sensitive to external conditions and therefore, there is a smaller impact on pressure for the entire transient.

The reduction in the long-term pressure is primarily attributed to liquid subcooling with a small contribution due to forced convection heat transfer effects. The external liquid film absorbs sensible heat from the point of PCS flow application to the point where significant film evaporation occurs. The subcooled heat capacity is dependent on water source temperature and external water flow rate. A lower source temperature results in greater subcooled heat capacity of the external film and, hence, more energy removed from containment. Forced convection heat transfer exists in the riser post-wetting as a result of the high buoyancy-driven air flow rate. The rate of energy transfer by forced convection is dependent on the heat transfer coefficient and the temperature difference between the liquid film and bulk air. Of these parameters, the temperature difference is influenced to a greater extent by bulk air temperature. A lower bulk air temperature results in greater forced convection heat transfer and, therefore, more energy removal from containment. The combined energy absorbed by liquid subcooling and forced convection represents a small fraction of the total energy removed from containment. Consequently, lowering the ambient air and source water temperatures to 40°F results in more total energy removed from containment, and, therefore, results in a decrease in containment pressure relative to the Evaluation Model.

Case 7 (LOCA) and Case 14 (MSLB) considered only the change in PCS water temperature, shown in Figures 5-11 and 5-12, respectively. These cases confirm that the air temperature impact is less important than the PCS water temperature.

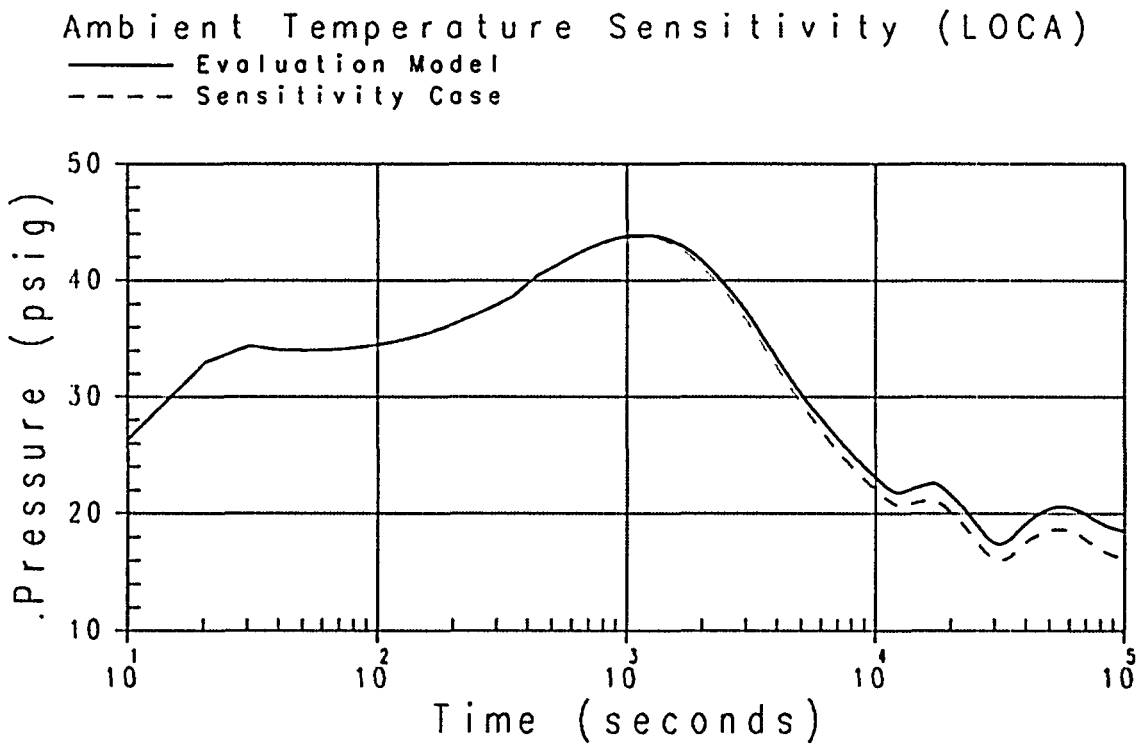


Figure 5-9 Case 5 - Ambient Temperature Sensitivity - LOCA

Ambient Temperature Sensitivity (MSLB)

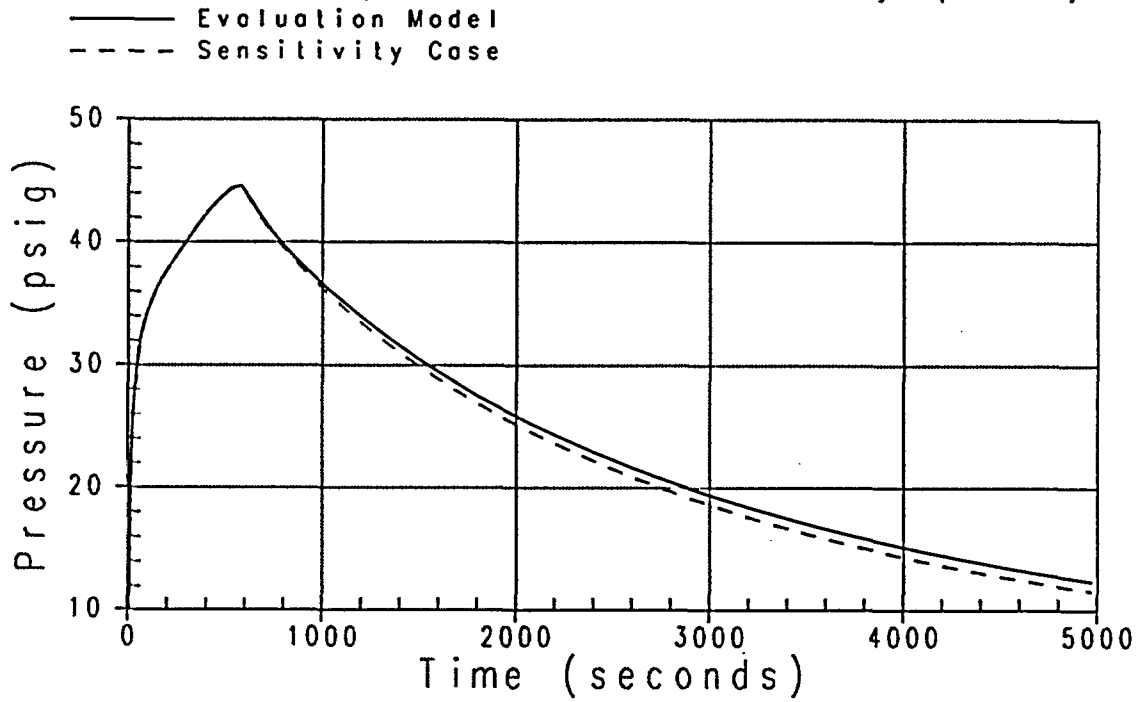


Figure 5-10 Case 12 - Ambient Temperature Sensitivity - MSLB

Film Temperature Sensitivity (LOCA)

— Evaluation Model
- - - Sensitivity Case

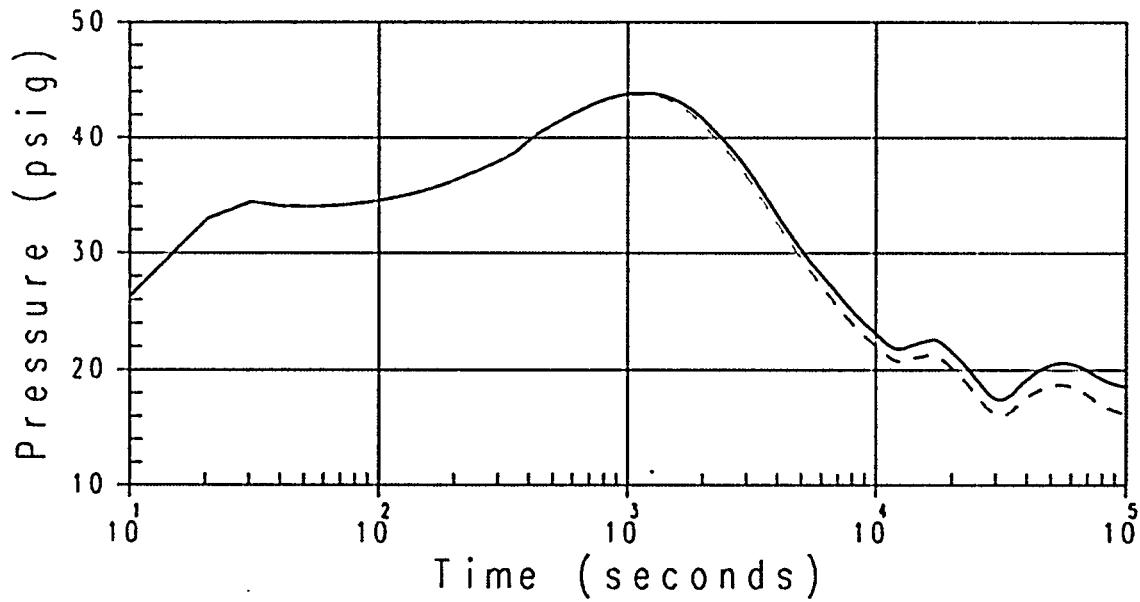


Figure 5-11 Case 7 - Film Temperature Sensitivity - LOCA

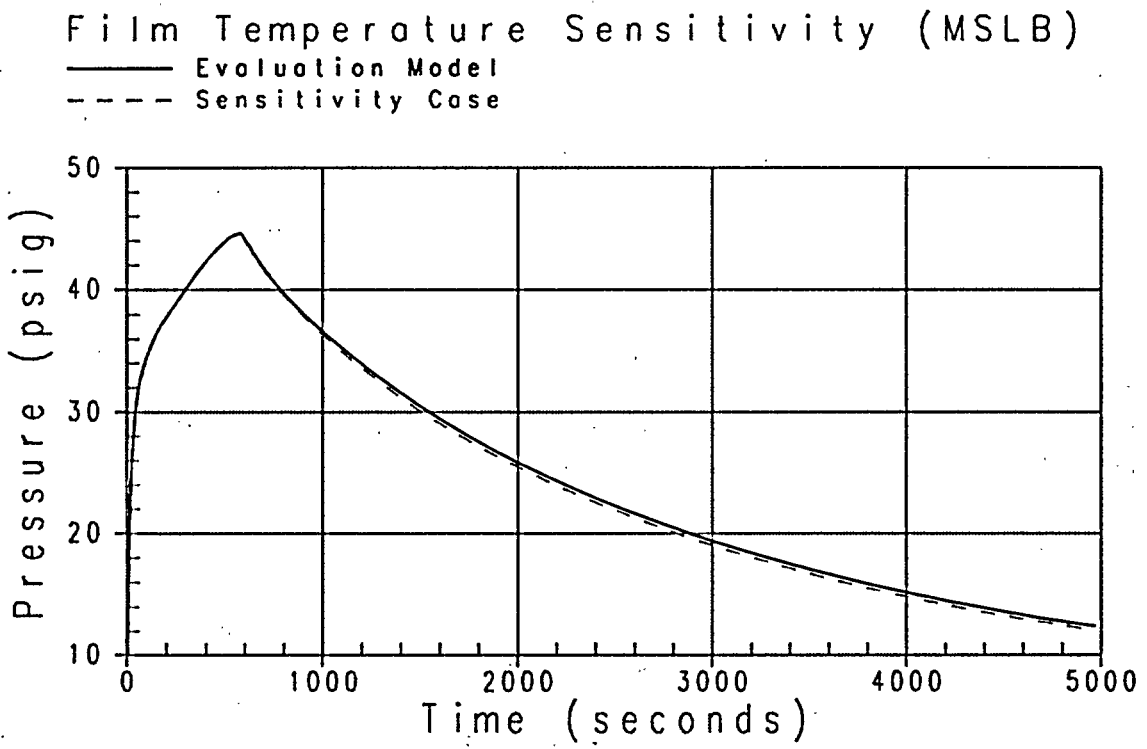


Figure 5-12 Case 14 - Film Temperature Sensitivity - MSLB

5.8 SENSITIVITY TO DROP MODELING ASSUMPTIONS

During a LOCA blowdown, the liquid and entrained droplets enter the atmosphere saturated at the containment total pressure where they are exposed to the containment gas mixture of air and steam at the steam partial pressure. Since the liquid and drops are initially superheated, they evaporate quickly to reach thermal equilibrium with the gas mixture. A sensitivity study was performed for the LOCA to determine the impact of the modeling assumption in WGOTHIC of the fraction of liquid converted to drops on the containment pressure. The mass released during the MSLB does not contain droplets.

The fraction of liquid assumed to be turned into droplets during the LOCA blowdown was varied from 0 to 100 percent. These sensitivities showed that the impact of assuming no droplets released, had a significant impact on the calculated pressure response compared to the cases where droplets were modeled. With no droplets assumed, the blowdown pressure was higher, but the peak pressure was lower. However, the sensitivity to the assumed fraction of droplets was very weak above a level of approximately 5 percent. The drops are strongly coupled to the containment atmosphere temperature due to the large surface area of the drops. The presence of drops in the atmosphere at approximately the 5 percent level maintains the atmosphere in a saturated condition and the presence of additional drops has little impact on containment pressure.

This sensitivity indicates that it is important to model the presence of drops in the containment atmosphere but the specific fraction assumed has a minor impact on the resulting pressure. The containment pressure response for assumed droplet fractions of 0 and 100 percent along with the Evaluation Model assumptions for drops (discussed in Section 4.5.2.1) is illustrated in Figure 5-13.

5.9 CONCLUSIONS

A series of sensitivity analyses has been carried out using the AP600 containment model to determine the effect of initial conditions on containment pressure response for the LOCA and MSLB events. Sensitivity evaluations were performed on initial containment humidity, pressure, and temperature, as well as ambient humidity and temperature and PCS water (film) temperature. These sensitivities demonstrate that the initial conditions assumptions in the Evaluation Model result in a conservative prediction of containment pressure. The containment pressure is more sensitive to internal conditions than to ambient conditions. The sensitivity to internal conditions is due primarily to the effect of these conditions on the amount of air in the containment.

A sensitivity was performed for the LOCA to determine the impact of the drop modeling assumption in WGOTHIC on the calculated containment pressure. The results show that it is important that the droplet formation be modeled, but at fractions above approximately 5 percent, the fraction assumed to be released as drops has a small impact on the calculated pressure.

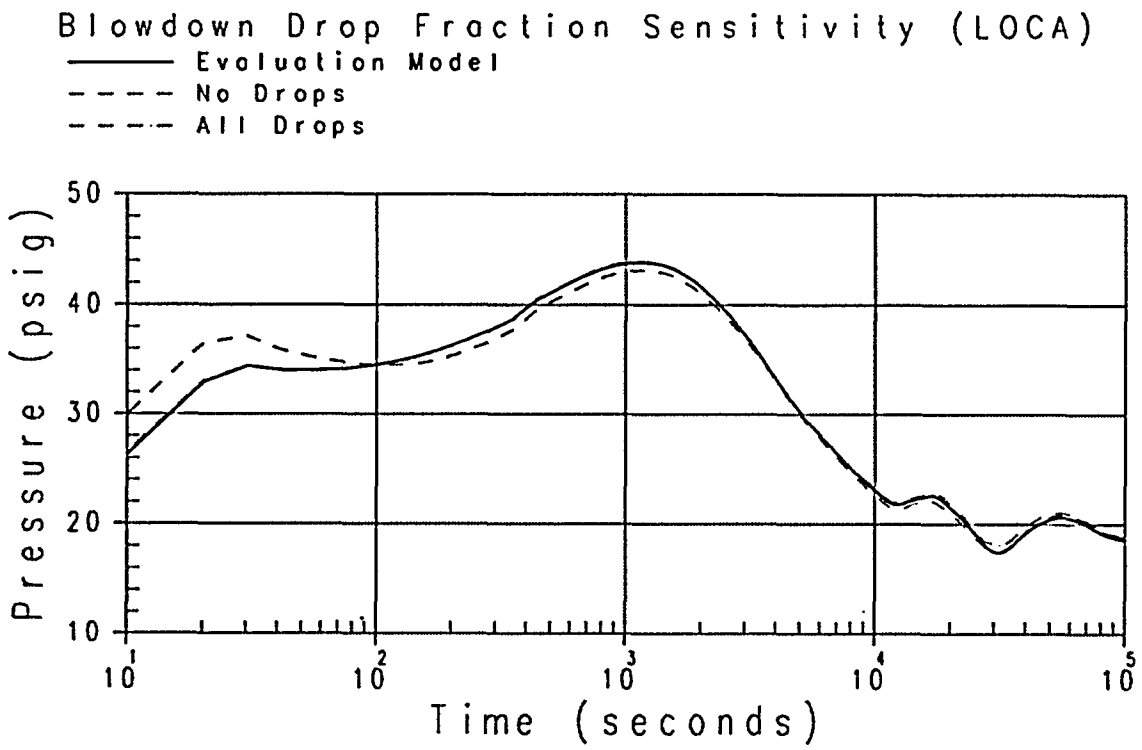


Figure 5-13 Blowdown Drop Fraction Sensitivity - LOCA

Section 6

Meteorological Effects on PCS Performance

TABLE OF CONTENTS

LIST OF FIGURES iii

6.1 INTRODUCTION 6-1

6.2 WIND-INDUCED TURBULENCE 6-1

 6.2.1 Summary of Wind Tunnel Tests 6-1

 6.2.2 Tracking of a Wind-Driven Particle 6-3

 6.2.3 Containment Time Constants 6-3

 6.2.4 Wind-Induced Oscillation Effect on Heat Transfer Coefficient 6-5

 6.2.5 WGOthic Evaluation Model Basis 6-5

6.3 RECIRCULATION OF CHIMNEY EFFLUENT 6-7

 6.3.1 Summary of Literature Review 6-7

 6.3.2 Evaluation of Effect of Recirculation 6-8

 6.3.3 WGOthic Evaluation Model Basis 6-9

6.4 CONCLUSIONS 6-10

6.5 REFERENCES 6-10

LIST OF FIGURES

Figure 6-1 Particle Path Through AP600 PCS With and Without Wind 6-4

Figure 6-2 1D Containment Shell Model Inside Temperature Results 6-6

6.1 INTRODUCTION

Meteorological conditions which could be postulated to degrade the performance of the PCS design have been investigated. The design includes, within the chimney, a shield plate which protects the containment surface from direct impingement of rain. Screens on the PCS inlets and around the entrance to the chimney protect the PCS from birds or larger debris which may be blown by wind. Meteorological effects that are evaluated, are wind-induced turbulence and the potential for recirculation due to wind or temperature inversions. This chapter shows that the assumption of a quiescent atmosphere in the evaluation model conservatively neglects enhancements to heat and mass transfer due to wind. It is also shown that the potential effects of recirculation produce a negligible effect on containment pressure.

6.2 WIND-INDUCED TURBULENCE

6.2.1 Summary of Wind Tunnel Tests

A goal of the containment building design is that wind not adversely impact heat removal from the building. The PCS is designed for wind to either have a nominal effect on PCS flow (wind neutral) or enhance PCS flow (wind positive). To verify the wind positive performance, a series of wind tunnel tests were performed. The wind tunnel tests, performed at the Boundary Layer Wind Tunnel Laboratory at the University of Western Ontario (UWO), were designed to test the aerodynamic response of air flow past the AP600 containment under a variety of conditions. The tests occurred in four phases.

Phase 1 testing (~1:100 scale) examined the effects of various design options on the wind-induced pressures. In Phase 1 testing, although the flow through the building annulus was not modeled, the pressure difference between inlets and chimney, Δp , was measured. The inlet-minus-chimney Δp is the pressure driving flow through the PCS, and a pressure coefficient, c_p , is defined based on free stream wind velocity and Δp :

$$\Delta p = 1/2 c_p \rho_{amb} V_{roof}^2$$

where

ρ_{amb} = ambient air density
 V_{roof} = free stream wind velocity

In Phase 2 tests, the air flow path was modeled for two different building designs: the most wind-neutral design found in Phase 1 testing and the current design of the building. The purpose of the Phase 2 testing was to provide information for the design of the baffle wall. Buoyancy was not considered in the wind tunnel

tests, since the driving pressure due to buoyancy amounts to only about 1 to 5 percent of the wind-induced driving pressure for the design wind cases.

At the end of Phase 2 of the wind tunnel program, several questions remained. In Phase 3, analysis was used to address the potential effects of wind and thermal inversion on recirculation of the chimney effluent back into the inlet, using available literature from mechanical and natural draft cooling towers.

Three additional questions were addressed with testing in Phase 4. The first question regards the effect of Reynold's number on the results. Reynold's number effects could only be addressed definitively by testing a larger model (1:30 scale) in a higher wind speed tunnel, such that the Reynold's numbers were in the same range as expected full-scale values. The second question was the effect of a tornado wind profile (near uniform) on the results. Tornado profile effects could be obtained using the same test model as in previous phases, but with a uniform flow model. The third question addressed the blockage effects of a hyperbolic cooling tower relative to the UWO wind tunnel size. Cooling tower blockage could be addressed by testing the model in a larger wind tunnel where blockage would be small.

The final question, the effect of severe terrain, was the subject of Phase 4 testing, in which a smaller scale (1:800 scale) was chosen to allow modeling of larger areas around the site.

Test results indicated that the AP600 design was wind positive for average PCS flow. The testing included a variety of terrain and conditions, including open country terrain, tornado loading, modeling of the cooling tower(s), and simulation of several types of severe terrain. Open country terrain yielded the most beneficial results for PCS heat removal, indicating a significant contribution to PCS air flow due to wind-induced driving pressures. The effect of the cooling tower, however, was to reduce static pressure at both the chimney and the inlets, resulting in lower mean wind Δp . Thus, the likelihood of flow in the PCS changing direction (flow reversal) was greater when the plant was in the wake of the cooling tower, giving the least positive mean PCS driving force due to wind.

The three Phase 4 severe terrain scenarios included an escarpment with mountain backdrop, a river valley site, and a river valley site with two cooling towers. Each terrain scenario caused durations and magnitudes of negative wind Δp , which could lead to flow reversals within the PCS flow path.

The wind-positive response of the PCS has been shown (Ref. 6.1) to be beneficial for containment heat removal for the limiting terrain configuration. Increased wind speed drives more flow through the PCS annulus and increases heat and mass transfer coefficients. Three questions have been addressed regarding the results of the wind tunnel tests:

- The model scale aerodynamic response versus full-scale response

- The effects of wind-induced flow oscillations on PCS heat removal and containment pressure response
- The effect of near-zero average wind Δp for certain wind angles in some of the severe terrain tests

Due to the shape of the containment shield building (sharp edges initiate flow separation), the model-to-full-scale aerodynamic response is relatively insensitive to model size in the range tested. A review of the literature has indicated that pressure oscillations in heat transfer generally improve heat transfer rates. In addition, time constants associated with the containment shell and internal volume minimize any benefit or penalty on containment pressure due to oscillations. The effect of wind-induced pressure oscillations has been evaluated with simple calculations.

6.2.2 Tracking of a Wind-Driven Particle

Using the measured pressure coefficients, density of air, and design wind speed of 214 mph, wind Δp was calculated and converted into annulus velocities using the momentum equation, which balances the driving force with the unrecoverable losses. Figure 6-1 presents the calculated path of the first element to travel from the inlet to the outlet of the PCS. Figure 6-1 also presents the path of the element neglecting the wind, and using an assumed buoyancy-driven annulus velocity of 15 ft/sec. Note that the wind-driven element shows a net positive flow response to pressure oscillations (net flow is from the inlet to the chimney).

6.2.3 Containment Time Constants

A review of the literature has indicated that oscillating flows generally increase heat transfer. The effect of the wind Δp oscillations on the containment post-LOCA pressure response is limited by time constants associated with the containment shell and the containment volume. The shell time constant gives the response of the containment shell to changes in its environment. Using a lumped mass approach, the time constant compares the thermal capacitance of the shell to the heat removal rate from its surface and has a value of about 255 seconds. The shell time constant is significantly higher than the frequency of pressure fluctuations, which are on the order of several seconds for high wind speed cases. The time constants show that the thermal response of the containment shell is sufficiently slow so that high speed oscillations will not significantly affect PCS heat removal. At lower wind speeds, oscillations are much slower. However, at lower wind speeds, the wind Δp is much lower. As wind speed reduces, the wind Δp decreases rapidly, as a function of the square of the wind velocity. Thus, oscillations will not have a significant impact on PCS heat removal. Since PCS heat removal is relatively unaffected, containment pressure response to a postulated LOCA will not be significantly affected by pressure oscillations. Thus, heat transfer fluctuations occur relatively faster than the ability of the wall material to transmit oscillations through the shell.

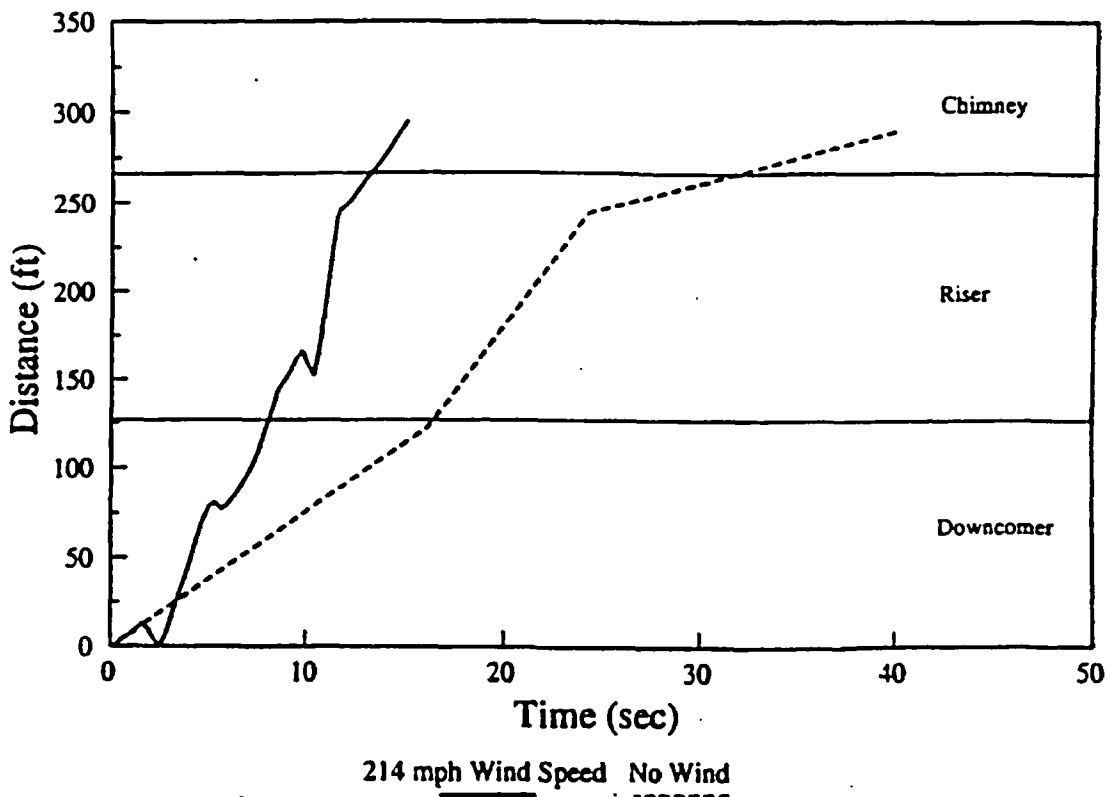


Figure 6-1 Particle Path Through AP600 PCS With and Without Wind

6.2.4 Wind-Induced Oscillation Effect on Heat Transfer Coefficient

Pressure fluctuations affect the heat transfer coefficient on the containment surface. In particular, oscillations result in short periods where the heat transfer coefficient may be lower than the value assumed in the no-wind case, followed by periods of higher heat transfer coefficients. The heat transfer response to wind oscillations has been investigated using a 1-D plane wall conduction model. The conduction model was used to estimate the effect of pressure oscillations on heat transfer through the containment shell. The model simulates the containment shell and a liquid water film on the outside of the shell. The 1-D conduction model was subjected to the heat and mass transfer coefficient on the outside of the plane wall calculated from the time-varying annulus velocity. Only forced convection correlations were used, so that heat and mass transfer rates on the outside of the plane wall approached zero as annulus velocities approached zero. The use of a forced convection correlation is conservative since, even as velocities in the annulus pass through zero, heat transfer would still occur. To further impose a conservative bias in the calculation, heat and mass transfer rates on the outside of the wall were assumed to be zero whenever the annulus velocity was negative.

The response of the containment shell to the imposed velocity was calculated. Figure 6-2 presents the surface temperature of the inside of the plane wall versus time. The figure compares the response of the wall to the annulus velocity oscillations versus the response assuming a steady buoyancy-driven annulus velocity. Note that, despite neglecting heat removal from the wall during periods of negative annulus velocity, the temperature of the inside of the plane wall is still about the same as a typical steady velocity case, showing that the response of the containment shell is limited by the time constants discussed in previous sections.

6.2.5 WGOthic Evaluation Model Basis

The wind tunnel testing of the AP600 indicates that the average wind Δp tends to be positive under a variety of conditions. Wind flowing towards and over the containment building will tend to increase average flow rates through the PCS. The wind-induced flow rate increase will improve heat transfer rates in the PCS.

In addition to the open-country terrain, several highly turbulent severe terrain scenarios were tested to obtain data on the AP600 subjected to limiting site conditions. For the severe terrain, positive wind Δp that averages near zero may be seen. In addition, the wind Δp tends to oscillate, giving periods of negative wind Δp . Negative pressures indicate the possibility of flow reversals within the PCS annulus. Assessment of the current literature has indicated that flow oscillations will tend to increase heat transfer primarily by enhancing mixing across the riser annulus flow channel. While periods of negative pressure may result in short periods of flow reversal within the annulus, the literature indicates that turbulent conditions may continue to exist. Turbulent conditions would continue to provide significant heat transfer rates despite the oscillating flow. Time constants were calculated for the containment shell which indicated that the shell time constants were of significantly higher magnitude than the period of the pressure oscillations. Thus the

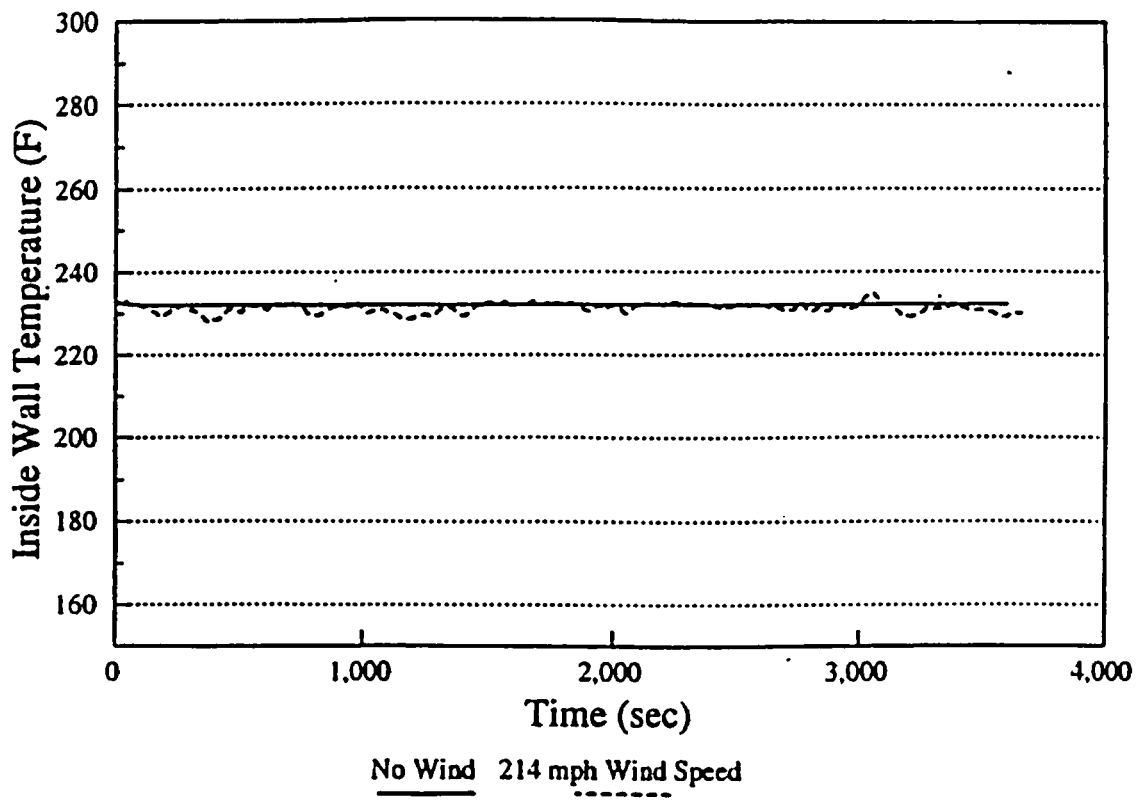


Figure 6-2 1D Containment Shell Model Inside Temperature Results

pressure oscillations in the annulus would be damped in their effects on the containment heat removal rates at the inside of the containment shell. A 1-D conduction model of the containment shell, subjected to oscillating heat transfer rates, was solved using the wind Δp from a particularly turbulent angle of the limiting test site. The 1-D conduction calculation used the forced convection correlation to conservatively determine heat transfer rates in the annulus. Heat transfer was also assumed to be zero when the flow reversed. The results of the calculation indicate a slight benefit in PCS heat removal and containment pressure due to wind for the limiting case. The effect of the containment shell was to dampen the oscillations occurring on one side of the shell. Thus, a conservative calculation of the passive containment response to a LOCA could assume a quiescent atmosphere.

6.3 RECIRCULATION OF CHIMNEY EFFLUENT

After the PCS cooling air flow passes over the containment shell surface, the air and evaporated water exhaust through an opening in the roof of the shield building and through the chimney. The potential for recirculation of the chimney effluent back to the PCS inlets, due to temperature inversions or strong winds has been evaluated (Ref. 6.2) through a review of literature and shows the negligible effect of a conservatively high assumed recirculation.

6.3.1 Summary of Literature Review

Many references were found in the literature to address potential recirculation due to strong winds or thermal inversions. References are available for natural draft hyperbolic cooling towers, typically hundreds of feet tall, and for mechanical draft cooling towers, typically 10 to 20 feet tall.

Strong winds can cause the formation of a recirculation cavity on the leeward side of a building or cooling tower. It was found that there are some intermediate wind speeds which can be sufficient to bend the plume horizontally, yet not strong enough to carry all the effluent away. Analytical and experimental research in the literature was conducted to determine the extent of the recirculation cavity behind a natural draft cooling tower and its effect on the plume. Curves are provided in the literature based on a normalized temperature difference that indicates the increase in the mixed mean ambient inlet temperature due to mixing with the plume. Such curves suggest a maximum normalized temperature increase of 10 percent for recirculation. Similar studies for mechanical draft towers suggest recirculation of 3 to 7 percent reaching a maximum of 15 percent.

Thermal inversions, and combinations of wind and temperature inversions were cited. Results showed that an inversion, by itself, does not induce the downflow necessary to recirculate chimney effluent. Adverse inversion conditions are associated with calm or light winds. Using simplified plume rise equations, the approximate effluent conditions resulted in plume rise above the shield building chimney for stable atmospheric conditions (inversions). The plume rise was sufficient to raise the plume, in light wind, above

the recirculation zone of structures the size of those associated with the passive containment design. Consequently, the maximum expected recirculation would be determined from the strong wind case.

Based on the literature review and evaluations of the AP600, the upper limit for recirculation of the passive containment chimney effluent is []°C. To account for the uncertainty in choosing a value for recirculation, the more conservative value of []°C has been assessed, which would result in the mixed mean ambient inlet temperature increasing from the safety analysis basis of 115°F to []°C.

6.3.2 Evaluation of Effect of Recirculation

The effect of a recirculation ratio of [] has been assessed with WGOTHIC sensitivity calculations. The base case calculation used an inlet temperature of 115°F and inlet humidity of 20 percent. Two sensitivities were run: one with only the inlet temperature increased, based on the recirculation ratio, and one with both the inlet temperature and inlet humidity increased. Results show that the pressure transient is insensitive to temperature and humidity in this range due to the self-regulating performance of the PCS.

The base case used for recirculation sensitivity differs from the evaluation model in the details of internal nodding, azimuthal segregation of the annulus into quadrants, modified mass and energy releases, the use of 22 percent relative humidity, an initial PCS flow profile starting at 220 gpm, and in the use of nominal heat and mass transfer correlations. Since these sensitivity results are used to examine relative effects of changes in the annulus inlet conditions, the sensitivity results are judged to provide a reasonable estimate of the potential effect of recirculation. The base case chimney outlet temperature reaches a maximum of []°C at about 2100 seconds and decreases almost linearly to []°C at about 8700 seconds, after which it gradually reduces to []°C at 24 hours. For simplicity, a conservative assessment of the potential effect can be based on an assumed chimney outlet temperature of []°C, which includes []°C to account for the increase in outlet temperature when the inlet temperature is increased in the sensitivity run. Using the definition of the recirculation ratio, the mixed mean inlet temperature, accounting for the effect of effluent recirculation, is

$$T_{in} = T_a + R(T_{out} - T_a)$$

$$T_{in} = 115 + []$$

So the inlet temperature to be assumed in the sensitivity cases is []°C which is applied for all annulus quadrants, consistent with the definition of R from the literature. The first sensitivity case used a constant []°C inlet temperature and essentially unchanged inlet humidity []

Results from the sensitivity show that the pressure transient changed by a negligible (<0.1 percent) amount due to the []°C increase in inlet temperature, and confirmed the initial guess for the corresponding increase in outlet temperature. The second sensitivity included the increase in inlet temperature combined with the inlet humidity set to 98 percent. Again, there is a negligible effect on

the containment pressure. The lack of sensitivity of the pressure response is due to the self-regulating performance of the PCS. By comparing the annulus conditions in going from 20 to 98 percent inlet humidity, it is seen that the annulus mass flow rate increased by about []%. The higher mass flow increases the capacity to move vapor out of the annulus and is due to the increase in vapor pressure at the annulus outlet from []% of the approximately 14.7 psia total pressure. Since steam density is more sensitive to temperature increases than air density is, and steam density is less than air density at annulus conditions, the increased steam content provides a greater density driving head for flow through the annulus. The increased mass flow results in a greater velocity through the annulus, which increases the PCS mass transfer coefficient. Thus, the mass flow increase offsets increases in inlet humidity. Similar, self-regulating performance results from an increase in inlet temperature alone.

It may be expected that an increase in inlet humidity would suppress the evaporation rate from the film. Such an effect is actually small since the driving force for evaporation is the difference between the vapor pressure of the film and the bulk saturation pressure in the annulus. Since the vapor pressure of the film is on the order of ten times that of the annulus, a relatively large percentage change to annulus humidity corresponds to a relatively small percent of the driving force.

Sensitivities to the effects of increasing both inlet temperature and humidity to account for potential recirculation show that there is a negligible effect on the containment pressure transient.

6.3.3 WGOTHIC Evaluation Model Basis

Since the effect of effluent recirculation is negligible, the WGOTHIC evaluation model does not consider any additional penalty due to recirculation.

6.4 CONCLUSIONS

Wind-induced pressure oscillations have been shown to provide a benefit to PCS heat removal because of the wind-positive design; that is, wind induces more heat removal than a quiescent atmosphere. The effects of recirculation due to thermal inversions or strong winds has been shown to have a negligible impact on PCS heat removal. The WGOTHIC evaluation model bounds the postulated effects with no input modifications.

6.5 REFERENCES

- 6.1 NTD-NRC-95-4467, J. Narula, "Analysis of AP600 Wind Tunnel Testing for PCS Heat Removal," June 2, 1995.
- 6.2 NTD-NRC-94-4166, R. Haessler, "AP600 Passive Containment Cooling System Letter Reports," June 10, 1994.

Section 7

**Basis and Method for Calculating the PCS
Water Evaporation Rate for the
AP600 and AP1000 Containment DBA Evaluation Models**

TABLE OF CONTENTS

LIST OF TABLES v

LIST OF FIGURES vi

EXECUTIVE SUMMARY vii

7.1 INTRODUCTION 7-1

7.2 WATER APPLICATION AND DISTRIBUTION 7-3

7.2.1 Containment Shell Surface Coating 7-3

7.2.2 PCS Water Distribution Weir Description and Operation 7-5

7.2.3 PCS Water Distribution Testing Results 7-8

7.2.4 Delivered PCS Water Flow Rate versus Time 7-10

7.2.5 Time to Establish Steady State Water Coverage 7-10

7.3 WATER COVERAGE BASIS 7-14

7.3.1 Water Distribution Film Flow Rate, Γ_{dist} 7-14

7.3.2 Minimum Film Flow Rate, Γ_{min} 7-16

7.4 EFFECT OF TWO-DIMENSIONAL (2-D) HEAT CONDUCTION THROUGH THE CONTAINMENT SHELL 7-18

7.4.1 Geometry of the Wet and Dry Vertical Stripes on the Containment Outside Steel Surface 7-18

7.4.2 Inside and Outside Heat Transfer Boundary Conditions for the Conduction Model 7-19

7.4.3 2-D Conduction (ANSYS) Model Description 7-20

7.4.4 Enhanced Evaporation due to 2-D Conduction 7-21

7.4.5 Insights from the PCS Large-Scale Testing 7-21

7.5 THE CONTAINMENT EVALUATION MODEL TREATMENT OF WATER COVERAGE 7-31

7.5.1 PCS Film Coverage Model 7-31

7.5.2 WGOTHIC Model 7-36

7.6 SUMMARY OF SUPPORTING TESTS AND SELECTED ANALYSIS 7-39

7.6.1 Westinghouse Wet Flat Plate Test 7-39

7.6.2 Small-Scale Tests 7-39

7.6.3 Large-Scale Tests (LSTs) 7-40

7.6.4 Estimated Range of Film Coverage Parameters 7-49

7.6.5 Containment Shell Heatup Analysis 7-51

TABLE OF CONTENTS (Cont.)

7.7 AP600 CONTAINMENT DBA EVALUATION MODEL
FILM COVERAGE SENSITIVITIES 7-54
7.7.1 Sensitivity of the Evaluation Model to the Input PCS Film
Flow Rate 7-54
7.7.2 Sensitivity to the Water Coverage Area 7-54
7.7.3 Conservatism in the Assumed Time Delay for Application
of the PCS Film 7-60
7.8 CONCLUSIONS AND SUMMARY 7-63
7.9 NOMENCLATURE 7-65
7.10 REFERENCES 7-66
APPENDIX 7A PHYSICS OF LIQUID FILMS ON THE AP600
CONTAINMENT SHELL 7A-1

LIST OF TABLES

| | | |
|------------|--|------|
| Table 7-1 | Ranges of the Film Coverage Parameters in the PCS Tests | 7-4 |
| Table 7-2 | Summary of the Phase 3 Water Distribution Test | 7-9 |
| Table 7-3 | Elevation D Heat Flux Comparison From PCS Large-Scale Tests RC048C and RC050C | 7-29 |
| Table 7-4 | Elevation E Heat Flux Comparison From PCS Large-Scale Tests RC048C and RC050C | 7-30 |
| Table 7-5 | Clime Wetted Perimeter and Basis for <u>WGOTHIC</u> Model | 7-37 |
| Table 7-6 | Summary of STC Heated Flat Plate Tests | 7-41 |
| Table 7-7 | Summary of Small-Scale Tests | 7-43 |
| Table 7-8 | Summary of Large-Scale Tests | 7-47 |
| Table 7-9 | Estimated Shell Heat Flux and Film Temperature | 7-50 |
| Table 7-10 | Comparison of the Range of Film Coverage Parameters | 7-51 |
| Table 7-11 | Transient Dry Shell Temperature Increase | 7-53 |

LIST OF FIGURES

Figure 7-1 Illustration of PCS Water Distribution Weir Assembly 7-7

Figure 7-2 Minimum Delivered PCS Water Flow Rate 7-11

Figure 7-3 Weir Outflow 7-12

Figure 7-4 Comparison of Water Distribution Model to Phase 3 Water Distribution
Test Results 7-15

Figure 7-5 Determination of Gamma-Min from LST, SST, and Flat Plate Data 7-17

Figure 7-6 Normalized Water Evaporation Rate (2-D/1D Conduction) versus
Overall Containment Wetted Fraction 7-22

Figure 7-7 Containment Steel Shell Temperature Gradients (°F) with 2-D Heat
Conduction; 20 psig, 25% Wetted 7-23

Figure 7-8 Containment Steel Shell Thermal Flux Gradients (Btu/hr-ft²) in
Y-Direction; 20 psig, 25% Wetted 7-24

Figure 7-9 Containment Steel Shell Total Thermal Flux (Btu/hr-ft²); 20 psig,
25% Wetted 7-25

Figure 7-10 Thermal Flux in Y-Direction on Outside Surface of Containment Wall
[Btu/hr-ft²] 7-26

Figure 7-11 Thermal Flux in Y-direction on Inside Surface of Containment
Wall [Btu/hr-ft²] 7-27

Figure 7-12 Large-Scale Test Water Coverage Pattern 7-45

Figure 7-13 Sensitivity to the Input PCS Film Flow Rate 7-55

Figure 7-14 Comparison of Peak Containment Pressure as Function of PCS
Coverage Area 7-57

Figure 7-15 PCS Runoff Flow Rates as a Function of Coverage Area 7-58

Figure 7-16 Comparison of Evaporation Model Peak Pressure with 100% and
50% Constant Coverage Models 7-59

Figure 7-17 Comparison of Evaporation Model PCS Runoff Flow Rate with
100% and 50% Constant Coverage Models 7-61

Figure 7-18 Difference in the Integrated Energy Transferred to the Top of the
Dome (with PCS Film Applied at 35 and 337 Seconds) 7-62

EXECUTIVE SUMMARY

The basis and calculational method used to determine the amount of water that evaporates from the containment steel shell during the operation of the passive containment cooling system (PCS) are conservative; both with respect to the individual elements of the WGOTHIC code and the PCS film coverage model, as well as the method of combining these elements in the Evaluation Model.

The amount of water that can be evaporated from the containment shell is input to the WGOTHIC portion of the containment Evaluation Model. The amount of water evaporated determines the calculated effectiveness of the PCS in limiting peak containment pressure, as well as the capability of the PCS to reduce and maintain low containment pressure following postulated limiting design basis events.

The basis for determining the amount of water that is evaporated has been developed based on PCS test data. Since the water evaporated at a given containment pressure (temperature) is dependent on the containment surface area that is wetted, the area used in the Evaluation Model is conservatively determined using the following:

- The portion of the containment shell perimeter that is wetted versus the amount of water being delivered from the PCS water storage tank to the containment dome has been based on testing of the Phase 3 Water Distribution Test (Reference 7.2). This test was performed with prototypic water distribution devices on a full-sized segment of the dome and the top of the sidewall, using cold water. PCS tests performed with heated surfaces with evaporating water have demonstrated that cold water on a cold surface conservatively underpredicts the coverage that occurs with heated water on a heated surface.
- The minimum water film flow rate per foot of wetted perimeter used to determine when water streams begin to narrow in width, conservatively bounds the minimum film flow rates observed in the PCS tests over the range of anticipated heat fluxes.

The calculational methods for determining the evaporated water flow rate have been developed and are consistent with or conservatively bound PCS test data and observations, and include the following:

- The evaporation of water due to the conduction of heat in the circumferential direction through the containment steel shell (i.e., 2-D conduction) has been calculated for the alternating, vertical, wet and dry stripes observed in the PCS testing at reduced delivered water flow rates.

- The decrease in the dry surface convective and radiative heat transfer that is calculated to occur with alternating, vertical, wet and dry stripes on the containment shell has been conservatively considered in the containment Evaluation Model.

Bounding assumptions and conservatisms for the operational characteristics of the PCS have been incorporated in the Evaluation Model. The most significant of these is that the portion of the containment shell surface wetted by the initial PCS-delivered water flow rate is assumed to be no greater than the []^o percent coverage observed in Phase 3 Water Distribution tests with a 220 gpm equivalent PCS water flow rate. A sensitivity study has shown that the AP600 containment design pressure will not be exceeded when only 70 percent of the containment surface is wetted.

7.1 INTRODUCTION

The energy released to the containment atmosphere following a postulated design basis high energy line break is removed from the exterior containment shell surface by a combination of convection and radiation from dry surface areas and by convection, radiation, and water evaporation from wetted surface areas, to a naturally circulating air stream. The energy removal due to water evaporation dominates the PCS total heat removal and is a function of the PCS flow rate, the wetted area, and the external shell temperature. Since these parameters vary with time, the energy removal rate due to evaporation also varies with time.

The containment shell outer surface is wetted with water that is stored in a tank located above the containment. Piping and two parallel valves provide a flow path from the tank to the top of the containment shell. The valves open upon receipt of a high pressure signal, allowing water from the tank to drain by gravity through the piping to a central distribution bucket located above the center of the containment shell. This water flow fills the distribution bucket, overflows out onto the dome, and spreads outward on the nearly horizontal surface at the top of the containment shell. As the applied water spreads outward from the center of the dome, it runs down the increasingly sloped dome surface where it is collected and redistributed by weirs located at the ~24-foot and ~51-foot radius of the dome. These water distribution weirs reapply the collected water at a regular uniform spacing around the containment shell perimeter.

The PCS water flow rate into the distribution bucket and onto the containment surface is controlled by the inlet elevations of standpipes within the PCS water storage tank. As the tank drains and each standpipe is uncovered, the PCS flow to the containment surface is reduced in a step-wise fashion. The standpipes are located so that the PCS flow results in sufficient heat removal to match the decreasing rate of heat release to the containment, and to achieve the desired decrease in containment pressure.

Because the ability of the PCS to remove heat at a given containment pressure (temperature) is largely dependent on the amount of water applied and the surface area that is wetted, the method of water application and the behavior/stability of the liquid film are important. Therefore, this section describes the testing and analyses utilized to define a conservative water flow rate input to the WGOTHIC Evaluation Model, including:

1. Water distribution testing used to demonstrate the weir design and how the resulting wetted surface area is affected by the applied water flow rate and surface irregularities in the containment shell structure.
2. PCS testing performed with heated wetted surfaces to determine how the water film is affected by post-accident containment operating conditions, including the steel shell surface temperature, the water film temperature, the water film mass flux (mass flow rate per foot of wetted perimeter, hereafter referred to simply as film flow rate), and cooling air flow velocity.

3. The method used to predict the containment shell wetted area and water film behavior conservatively compares with test data in order to conservatively calculate the amount of water that can be evaporated from the containment shell.
4. The method used to calculate the effect of heat conduction, in the circumferential direction through the steel containment shell (2-D conduction), on the water evaporation rate from the surface with vertical wet stripes.

The liquid film application, flow rate, area wetted, and film behavior are evaluated in the "PCS film coverage model," separate from the WGOTHIC Evaluation Model. This model permits a conservative determination of the amount of supplied water that evaporates from the shell, considering the aspects of water application, and film behavior and stability. The resulting amount of water is input to the WGOTHIC Evaluation Model.

The methodology bounds data from tests of an unheated, full-scale portion of the containment dome and 4 feet of sidewall, and from various scale heated tests. The evaporation-limited PCS water flow rate input for the WGOTHIC Containment Evaluation Model is calculated using a simple model that is consistent with test observations and uses as inputs the parameters Γ_{dist} and Γ_{min} which are selected to conservatively bound test data. Γ_{dist} represents the film flow rate (mass flow rate per unit wetted perimeter) of water applied by the weir distribution system at the second weir. Γ_{min} represents the minimum stable film flow rate, below which water coverage is assumed to decrease, and is selected to bound heated film stability test data. The database from which conservative values for Γ_{dist} and Γ_{min} are determined is discussed, as well as how these parameters are implemented into the model.

The Evaluation Model conservatively neglects heat removal during the initial period from the first spillage from the bucket to the time when steady-state coverage has developed on the containment shell (Section 7.5.2.2). The time to develop steady-state coverage is conservatively estimated. The effects of surface temperature during the initial application are also addressed (Section 7.6.5).

The supporting tests for water coverage are shown to span the range of AP600 and AP1000 nondimensional parameters, so that the database is sufficient.

7.2 WATER APPLICATION AND DISTRIBUTION

The wetting characteristics of the containment coating and the application and distribution of water onto the containment steel shell outer surface are important design features of the passive containment design. The containment is covered with an inorganic zinc coating, and an assembly of devices on the containment dome are used to collect and redistribute water to maximize the containment surface wetted area at a given delivered water flow rate.

The Phase 3 Water Distribution Test (Reference 7.2) was performed to demonstrate the operation of the prototype of the AP600 water distribution devices on a full-scale sector of the containment dome. Other PCS tests were performed to quantify the heat removal capability of the PCS. The test results provided information to understand and characterize the behavior of water films on the outside of the containment surface. In addition to the containment coating and the water distribution devices, other parameters that characterize the water film behavior are the delivered water flow rate, the water film flow rate (per foot of wetted perimeter), the water film temperature, and the evaporative heat flux. The film Reynold's number provides a dimensionless measure of the film flow rate, and the Marangoni number is a dimensionless measure of heat flux. The range of dimensioned and dimensionless parameters for PCS testing used to understand and characterize containment surface wetting are summarized in Table 7-1.

7.2.1 Containment Shell Surface Coating

The containment shell surface is covered with an inorganic zinc coating for corrosion protection. Prototypical coated surfaces were obtained for testing by following the manufacturers' specifications for preparation of the metal surface and for application of the coating for each test article in the tests described in Sections 7.2.3 and 7.6.

- The surface was prepared for coating application according to the coating manufacturer's requirements by sandblasting to a white metal surface finish. The coating was then sprayed onto the surface to a thickness range within the required specification of 4 to 10 mils. Coating thickness measurements were taken to verify that the coating thickness was within specification.
- Local or spot recoating of the surfaces was performed if the surface of the test article was affected by changes to the facility, such as the installation of additional instrument penetrations.

Note:

(1) Dimensionless groups are defined in Nomenclature, Section 7.9.

Although no specific aging simulation of the surfaces was performed prior to testing, matrix tests were performed over a period of time using the original coated surface, where aging of the surfaces occurred due to operation and exposure to the environment. For example, the small-scale test vessel was erected in 1986 and tests were performed until late 1992 using the same test vessel with the original coating. The LST matrix tests were conducted from late 1991 until the end of 1993 and further operation took place through 1996, with the original coating. An estimate of the equivalent service time cannot be evaluated since a large number of tests were performed during this period. In each test facility, no noticeable degradation of the surface was noted during the testing.

In consideration of the above, the surfaces tested are considered prototypic of the AP600 and AP1000 containment shell exterior surfaces. Measurement and/or observations of film coverage on the prototypical surface were made in each of the PCS tests.

7.2.2 PCS Water Distribution Weir Description and Operation

An assembly of devices for distributing the water applied to the containment shell is provided to maximize the outside surface area of the containment shell that is wetted during PCS operation. The PCS water distribution devices include a distribution bucket located above the center of the containment dome, eight divider plates that extend radially from the center of the dome to the first set of water distribution weirs, the first set of water distribution weirs located at the ~24 foot radius of the dome, and the second set of water distribution weirs located at the ~51 foot radius of the dome.

The PCS water is delivered to the water distribution bucket at the center of the containment dome. The bucket has 16 vertical slots, such that two slots meter water flow to each of the eight pie-shaped segments on the dome created by the eight divider plates that originate at the distribution bucket and extend radially along the surface of the dome to the first distribution weir ring. These divider plates are required because the center of the dome is relatively flat, and maldistribution of flow due to localized imperfections in plate welds or alignment, or variations in the slope at the center of the dome could otherwise occur. Thus, the dividers distribute the water applied to each one-eighth dome segment and to the corresponding one of eight weir assemblies that comprise the first ring of weirs.

The first weir ring consists of eight weir assemblies located at the ~24 foot radius. This radial position is just below a circumferential weld around the containment dome at the 22-foot radius from the dome center. Thus this discontinuity will have no lasting effect on water distribution, since this first set of weirs, just below the weld line, will collect the applied water and redistribute it. Each of the eight first weir assemblies consist of two water collection dams that direct the applied water, in its one-eighth segment from the dome center, into a collection box. Each of the eight collection boxes meters flow to two distribution troughs, one on either side of the collection box. Each distribution trough meters the water from the collection box back onto the dome surface via nine V-notches spaced at 1-foot intervals. The eight weir assemblies are installed with the distribution boxes end-to-end, so that each forms one-eighth of the weir ring which completely

circles the containment dome at the ~24 foot radius, and which apply water at the 24-foot radius in 144 streams with an ~1 foot stream spacing. Because the containment dome has sufficient downward slope at the 24-foot radius, radial dividers are not required below the first weir ring and the water applied at the first set of weirs will follow the natural fall line to the second weir ring.

The second weir ring is located circumferentially on the containment shell at 50.7 feet from the center of the dome, just below the second circumferential weld on the containment shell. This assembly again corrects any uneven distribution of flow that may have occurred below the first weir ring due to weld discontinuities or deviations in the dome shape from the ideal shape. Also, since the containment dome is steeply sloped at this radial position, the water applied by this second weir ring is not significantly affected by local surface imperfections or deviations from ideal shape, since gravity rather than allowable surface variations becomes controlling. Thus, the second weir ring creates an even distribution over the rest of the dome and the vertical portion of the containment shell. The second weir ring consists of sixteen weir assemblies; each with two collection dams, a collection box, and two distribution troughs. The 16 weir assemblies are again arranged end-to-end to form a distribution system that completely circles the containment. Water that runs down the dome from each of the 16 distribution troughs in the first weir ring is collected by the dams, flows into the collection box, and is metered to two distribution troughs. In this second weir ring, the distribution troughs each have 18 V-notches spaced at 6.5-inch intervals.

Figure 7-1 is an illustration of a weir assembly. The dams collect all the water flowing from above them and direct this water into their corresponding collection box. As the water rises in the collection boxes, it overflows via three V-notches on either side of the top of the box, effectively dividing the collected water into six equal portions. Each portion of the water overflowing through the six collection box V-notches, flows into one of the three parallel flow channels in each of the two distribution troughs. As the parallel flow channels fill with water, each flow channel overflows via another set of V-notches arranged equidistantly along the back wall (facing the containment axial center-line) of the distribution trough, onto the containment shell. The eight weir assemblies comprising the first weir ring, have 16 distribution boxes, each with nine V-notches equally spaced at 1-foot intervals; resulting in 144 individual streams of water applied to the dome at the 24-foot radius. The 16 weir assemblies comprising the second weir ring, has 32 distribution boxes, with each having 18 V-notches equally spaced at 6.5-inch intervals; resulting in 576 individual streams of water applied to the containment dome at the 50.7-foot radius. Note that in each weir assembly the spacing of the two streams, one on either side of the collection box, is greater than the uniform V-notch spacing along the distribution boxes.

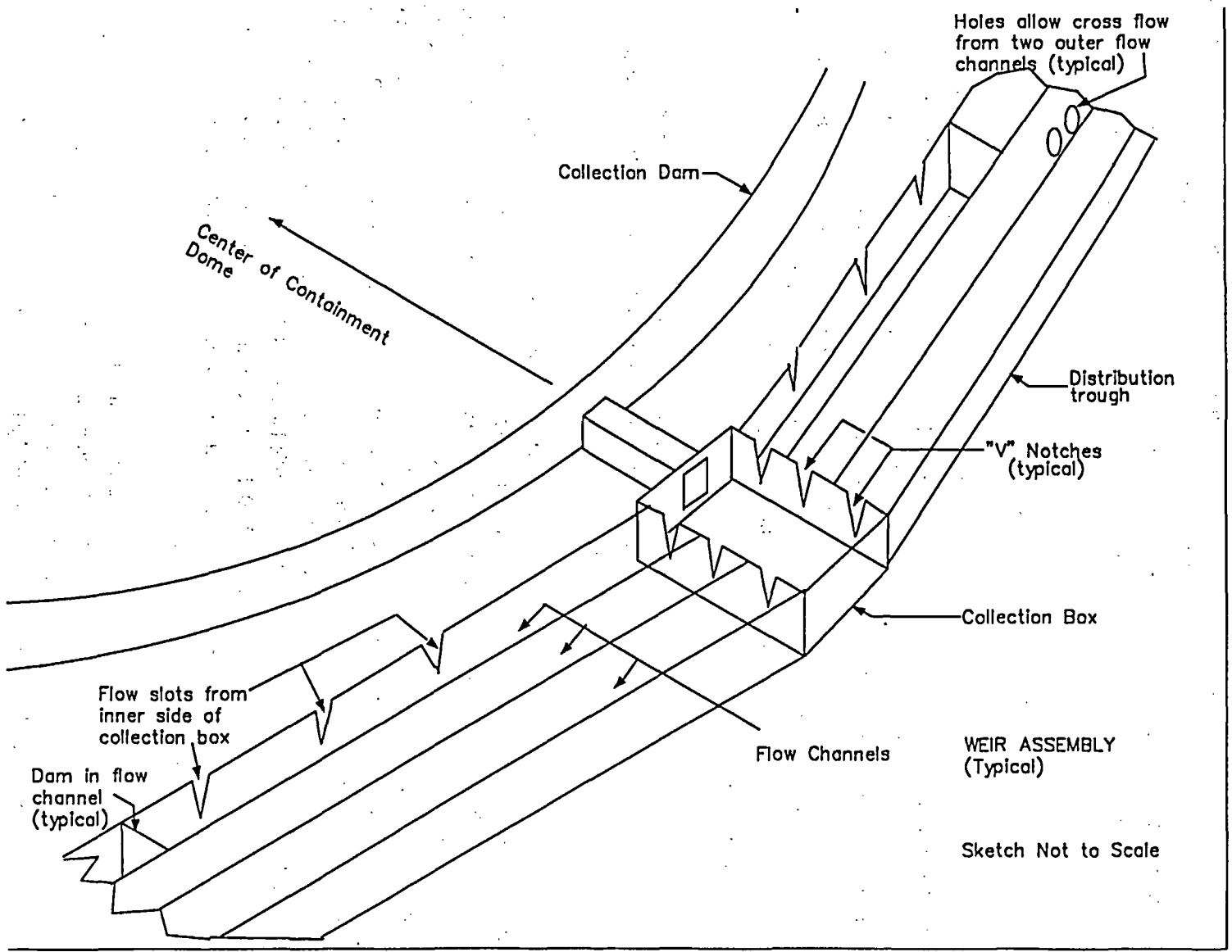


Figure 7-1 Illustration of PCS Water Distribution Weir Assembly

All components of the water distribution system are seismic category I, and designed to withstand thermal and pressure expansion/contraction of the containment without failure. The system is capable of functioning adequately during PCS accident operation under extreme low or high ambient temperatures. The weir distribution systems are constructed of stainless steel to limit concerns over blockage due to corrosion products or paint/coating degradation. The water distribution weir system is designated a safety class C component based on its containment cooling function.

7.2.3 PCS Water Distribution Testing Results

The Water Distribution Test (Reference 7.2) was used to determine the effectiveness of water distribution devices, to determine the water coverage as a function of the flow rate on the prototypical surface, and to determine the time to establish steady-state coverage. A full-scale test section, representing a 1/8 sector of the containment dome to the ~50 foot radius and a 1/16 sector of the full containment dome and a 4-foot long portion of the vertical sidewall, was built. The test section included both meridional and circumferential joints, with the maximum allowable plate misalignment, and was coated with the prototypic inorganic zinc coating. Testing included simulation of the maximum allowable deviation in dome shape from ideal shape, by tilting the distribution troughs.

There was no source of heat to simulate mass and energy removal by evaporation for these tests. Two water distribution weir designs were tested. The final weir design was tested in Phase 3 of the Water Distribution Test (Reference 7.2) and is the weir described in Section 7.2.2.

These tests demonstrated that the water coverage just below the weirs consisted of discrete streams after the water was collected, redistributed, and re-applied at a fixed spacing around the containment dome perimeter by the water distribution weirs. These individual streams were sufficiently wide at the higher applied flows (35 and 27.5 gpm) to join just below the weirs and provide high water film coverage over the portion of the test section below the weir. However, at reduced applied water flow rates, the streams were sufficiently narrow in width that the water coverage consisted of vertical alternating wet and dry stripes. Below the second set of weirs at the ~51 foot radius, where the downward slope of the containment dome is 35°, the stripes remained discrete from the weir to the springline and down the vertical sidewall. At the lowest flow rate tested, 6.9 gpm (equivalent to 55 gpm of water applied to the full dome), the 32 weir V-notches in the lower weir ring distribution troughs produced 29-30 discrete vertical wet stripes with an average width of ~2.5 inches. It is noted that several streams joined together only because of specific worst case surface defects that were simulated on the test section.

The water coverage was measured just above the second weir (at the 49-ft radius) and at the springline (65-ft radius at the top of the vertical sidewall). Measurements of stripe widths accounted for only the traverse where flowing water was observed, not the wider wetted traverse. The Phase 3 test data are summarized in Table 7-2, where the wetted perimeter of the flowing water was observed and is listed as a percent of total area or water coverage.

a,c

| [Redacted Table Header] | | | | | | | |
|-------------------------|--|--|--|--|--|--|--|
| | | | | | | | |
| | | | | | | | |
| | | | | | | | |
| | | | | | | | |
| | | | | | | | |
| | | | | | | | |
| | | | | | | | |

The coverage listed at 49-ft and 65-ft are the measured coverage just above the second weir and at the springline and for the water flow rates delivered in Phase 3 of the Water Distribution Test. The coverage decreases as the delivered flow rate decreases. The flow rate was not adjusted to account for the water lost at sampling points upstream of the springline. This correction would increase the water coverage percentages slightly.

The surface area that was wetted at a flow rate of 27.5 gpm (equivalent to 220 gpm on the full dome) was estimated to be []^{a,c} from the top of the dome down to the first weir, based on a review of the video tapes for the Phase 3 Water Distribution Tests. About []^{a,c} of the vessel was wet between the first and second weirs, and the entire vessel was wet at the bottom of the test section.

This test also demonstrated the time required to fill the prototypic water distribution devices and establish steady-state water coverage on the containment shell at a PCS flow rate equivalent to 220 gpm. Based on a review of the video tapes of the test, water began to spill from the first set of weirs at about 2.5 minutes, and spilled from the second weir ring at about five minutes after flow into the bucket was initiated. The total time to completely fill the weir devices and establish steady-state coverage on the dome and sidewall was conservatively estimated to be about 10 minutes. Since the initial PCS-delivered flow rate has been increased, the time required to achieve steady-state water coverage will be decreased, as discussed in Section 7.2.5.

7.2.4 Delivered PCS Water Flow Rate versus Time

The AP600 and AP1000 minimum delivered PCS water flow rates are shown as a function of time in Figure 7-2. The minimum delivered PCS water flow rate was calculated assuming a single failure of one of the parallel PCS tank discharge valves to open. This single failure assumption reduces the gravity-driven flow rate by less than 2 percent since flow orifices in the discharge lines limit the flow rate from the tank.

The amount of water required for evaporative heat removal from the PCS shell decreases as the core decay heat decreases. Therefore, the PCS flow rate is designed to vary with time. The gravity-driven flow rate decreases as the water level in the PCS tank decreases. A series of standpipes are located within the PCS tank. The delivered PCS water flow rate decreases substantially whenever the water level falls below the top of a standpipe.

7.2.5 Time to Establish Steady State Water Coverage

Some period of time is required to establish steady state water coverage after the PCS has been actuated. This is an important input for the containment Evaluation Model. The delivered PCS water must fill the distribution bucket, two sets of distribution dam/weirs, and then cover the vertical containment shell.

The time needed to establish steady state water coverage was observed on the video tape recording of the 220 gpm equivalent full-scale PCS flow Water Distribution test. The first distribution dam/weir filled and began spilling about 2.5 minutes after flow initiation and the second distribution dam/weir filled and began spilling about 5 minutes after flow initiation. A steady flow and coverage pattern was observed about 10 minutes after flow initiation.

As shown in Figure 7-2, the initial delivered PCS water flow rate is about twice as high as the tested value (about 440 gpm for AP600 and about 469 gpm for AP1000). Therefore, the time to establish steady state water coverage will be less than measured in the Water Distribution tests.

A simple analytical model was developed to estimate the weir outflow rates for a constant 440 gpm PCS water flow rate. The results are shown in Figure 7-3. This figure helps illustrate the various components of the time needed to establish steady state flow from the bucket, first, and second weirs. The steady state water coverage delay time input values for the AP600 and AP1000 containment Evaluation Models are based on the actual prototype test results, rather than these calculations.

The time to establish steady state coverage is the sum of the valve stroke time, the time to fill the lines and distribution bucket, the time to fill and spill over the two sets distribution dam/weirs, and the time to cover the vertical containment shell. The PCS discharge valve stroke time is 20 seconds and the time to fill the lines and bucket at 440 gpm was calculated to be 17 seconds. As described above, about 10 minutes after flow initiation, a steady state flow and coverage pattern was observed in the 220 gpm equivalent full-scale PCS flow Phase 3 Water Distribution test. Therefore, for AP600, the steady state coverage delay time input value is calculated to be $20 + 17 + 600 \cdot 220 / 440 = 337$ seconds.

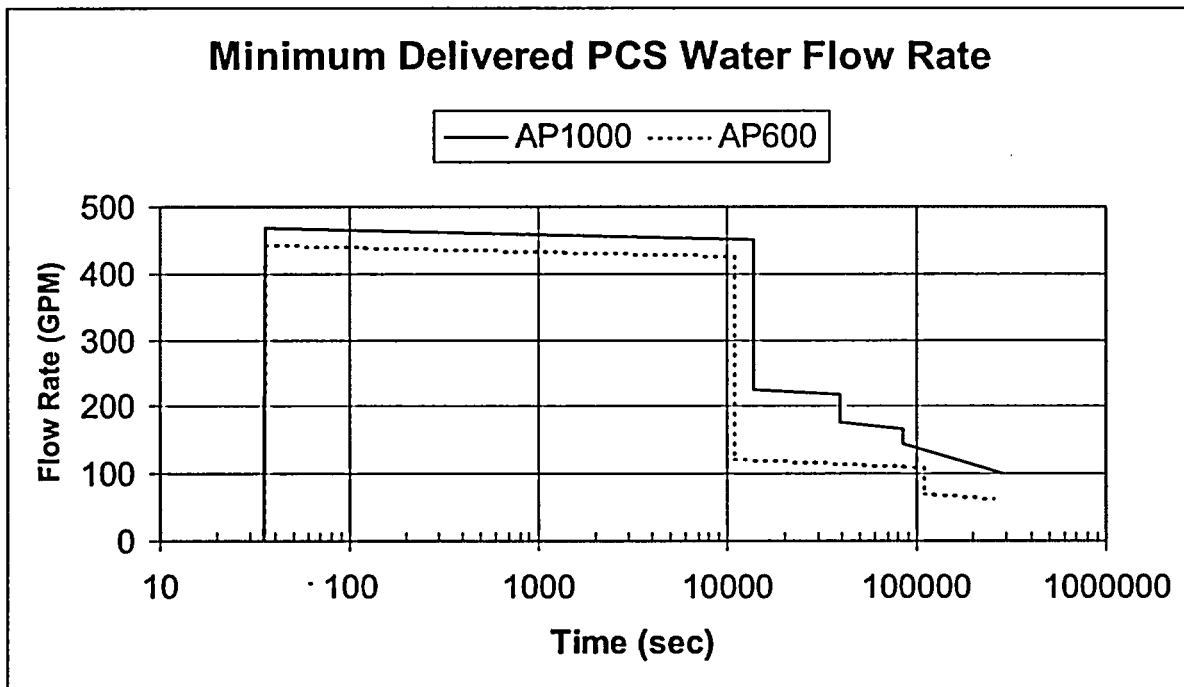


Figure 7-2 Minimum Delivered PCS Water Flow Rate



Figure 7-3 Weir Outflow

The AP1000 containment diameter, dome geometry, and water distribution system are the same as AP600, but the containment sidewall is 25.5 feet higher. Also, the initial delivered PCS water flow rate is higher for AP1000, 469 gpm vs. 440 gpm. Since the water distribution system is the same, scaling the AP600 steady state coverage delay time input value by the change in flow rate yields:

$$t_{\text{PCS-AP1000}} = t_{\text{STROKE}} + t_{\text{PCS-AP600}} * Q_{\text{PCS-AP600}} / Q_{\text{PCS-AP1000}}$$

where: $t_{\text{PCS-AP1000}}$ is the time to reach steady state coverage for AP1000
 $t_{\text{PCS-AP600}}$ is the time to reach steady state coverage for AP600
 $m_{\text{PCS-AP1000}}$ is the initial PCS flow for AP1000, 469 gpm
 $m_{\text{PCS-AP600}}$ is the initial PCS flow for AP600, 440 gpm
 t_{STROKE} is the valve stroke time, 20 seconds.

Using this information, $t_{\text{PCS-AP1000}} = 20 + 317 * 440 / 469 = 317.4$ seconds.

The average velocity of the falling laminar film is needed to calculate the time to cover the additional 25.5-ft fall height in AP1000. The average velocity and film thickness for a falling laminar film is:

$$v_{\text{avg}} = g * d^2 * \cos(\beta) / (3 * \nu)$$

where

$$\delta = (3 * \nu * Q / \{ g * \pi * D * \cos(\beta) \})^{1/3}$$

- Q is the film flow rate = 469 gpm = 1.04494 ft³/s
- G is the gravitational constant (32.2 ft/s²),
- β is the surface angle relative to vertical (0° for cylindrical shell surface)
- ν is the kinematic viscosity (ft²/s) (4.77E-06 @ 150°F, 3.41E-06 @ 200°F)
- D is the shell diameter (ft) = 130.2917 ft
- δ film thickness (ft)

$\delta @ 150^\circ\text{F} = 0.001043$ ft
 $\delta @ 200^\circ\text{F} = 0.000933$ ft

$v_{\text{avg}} @ 150^\circ\text{F} = 2.45$ ft/s
 $v_{\text{avg}} @ 200^\circ\text{F} = 2.74$ ft/s

Using an average film velocity of 2.5 ft/s, the film should take an additional 10 seconds to cover the 25.5 feet of shell height, yielding a total steady state coverage delay time of 327.4 seconds for AP1000. This is not significantly different than the AP600 steady state coverage delay time input value, so the AP600 value of 337 seconds was used for AP1000 as well.

7.3 WATER COVERAGE BASIS

The PCS film coverage model was developed to calculate the amount of water that evaporates from the AP600 shell, consistent with conservative models for film stability. Inputs to the PCS film coverage model are the delivered PCS flow rate, the sidewall height and diameter, and an estimated evaporation mass flux. The output from the model is the evaporation rate from the containment shell. The evaporation-limited PCS water flow rate is input to the WGOTHIC Containment Evaluation Model, rather than the total delivered PCS flow rate. The WGOTHIC code calculation is used to determine an average evaporation mass flux that is input to the PCS film coverage model. Thus, an iteration is required. The iteration is made to converge on the conservative side, i.e., the evaporation flux input to the PCS film coverage model is underestimated. This results in an overestimated amount of water runoff, and therefore underestimates the evaporation-limited PCS water flow rate input to the WGOTHIC Containment Evaluation Model.

The PCS film coverage model described in Section 7.5 assumes there is no evaporation from the center of the dome to the second weir. The surface area for evaporation is modeled as a right circular cylinder with the same area as the containment shell surface below the second weir.

The "film flow rate", represented by the parameter Γ , is the water mass flow rate divided by the circumferential wetted perimeter, that is, $\Gamma = m/W$. Water is distributed on to the containment shell by a series of streams around the circumference. At the high initial delivered PCS flow rate, these streams merge into a continuous film. After the first stand pipe uncovers and the delivered PCS flow rate decreases, the streams remain separate and flow down as stripes from the weirs. The stripes start with a film flow rate, Γ_{dist} and flow down the wall at a constant width until evaporation causes the film flow rate to reach the film stability limit, Γ_{min} . Once Γ_{min} is reached, film stability causes the width of the stripe to reduce as additional evaporation takes place. The bases for Γ_{dist} and Γ_{min} are presented in this section.

7.3.1 Water Distribution Film Flow Rate, Γ_{dist}

Values of water coverage at the springline were measured in Phase 3 of the Water Distribution Test (Reference 7.2). The data, presented in Figure 7-4, show the coverage increased with the total water flow rate to []^{a,b} percent coverage at 220 gpm, then increased to []^{a,b} percent at 280 gpm. Thus, a model that limits the coverage at the top of the side wall to []^{a,c} percent bounds the test data at flow rates greater than 280 gpm. Modeling the coverage at lower flow rates with a value of $\Gamma_{dist} = []$ ^{a,b} lbm/hr-ft bounds the test data for lower flow rates.



Figure 7-4 Comparison of Water Distribution Model to Phase 3 Water Distribution Test Results

The room temperature, isothermal Water Distribution Test data are applicable to both AP600 and AP1000. The basis for using the data is that the water applied to the shell beyond the second weir during actual PCS operation is heated to the shell temperature while flowing down to the second weir. The AP600 scaling analysis estimated less than 1600 ft² of heat transfer surface area is required to heat up the subcooled water, whereas there is 4400 ft² of wetted surface area above the second weir (Reference 7.8, Section 7.6.6). Consequently, heated water is applied to a heated shell at approximately the same temperature at the second weir, so the water and shell are nearly isothermal, as in the Water Distribution Test. The decreased stability exhibited by the application of cold water to a hot surface (References 7.10 and 7.12) is not an issue in this case, so it is assumed that the coverage measured in the cold, isothermal tests is conservative for the nearly isothermal application below the second weir in both AP600 and AP1000.

The room temperature (65° to 68°F) Water Distribution Test coverages are a conservative basis for Γ_{dist} due to the effect of increased temperature on the film properties. The film spreads where the water spills from the weir V-notch and impinges on the shell surface. The spreading is a momentum-dominated process that is opposed by friction and surface tension. At higher temperatures, the film viscosity is decreased by a factor of 2 to 3, and the surface tension is decreased by 15-20 percent, while the impingement momentum is essentially unchanged. The reduction of the friction and surface tension both allow the film to spread more at high temperature than at low temperature.

7.3.2 Minimum Film Flow Rate, Γ_{min}

Observations of the evaporating film flow on heated surfaces show the film flows in constant width stripes until evaporation causes the film flow rate to reach a minimum value, Γ_{min} after which, the film width narrows with additional evaporation. Most of the LST, SST, and Westinghouse Flat Plate tests produced constant width stripes, or constant coverage. The lowest values of film flow rate, Γ , either were above Γ_{min} , or at most were close to Γ_{min} . Consequently, the film measurement data for each of the tests is a record of values of $\Gamma \geq \Gamma_{min}$. Several of the lowest measured values of Γ are presented in Figure 7-5.

A conservative upper limit for the minimum stable film flow rate, Γ_{min} , is needed for the PCS film coverage model. The minimum stable film flow rate increases as the heat flux increases, as demonstrated by the work of Bohn and Davis (Reference 7.10). The Westinghouse test data cover a heat flux range that is greater than the maximum expected operating value for both the AP600 and AP1000 (see Table 7-10).

A constant Γ_{min} value of []^{4c} lbm/hr-ft was selected to bound the various Westinghouse test data as shown in Figure 7-5. The comparison presented in Figure 7-5 shows this value to be much higher than the lowest stable measured Γ values of each test.

a,c

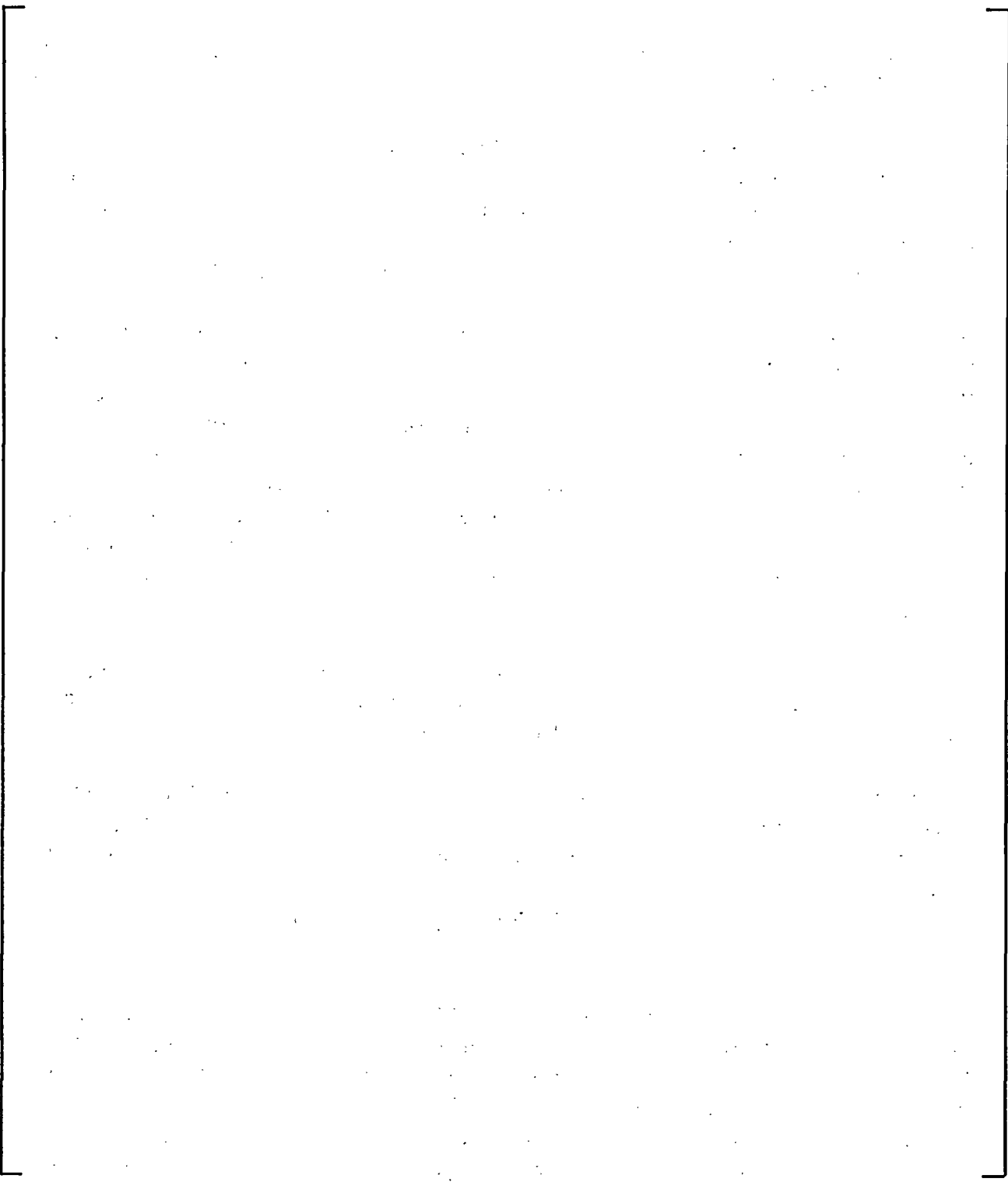


Figure 7-5 **Determination of Gamma-Min from LST, SST, and Flat Plate Data**

7.4 EFFECT OF TWO-DIMENSIONAL (2-D) HEAT CONDUCTION THROUGH THE CONTAINMENT SHELL

The PCS transfers heat from the containment atmosphere to the outside environment. Cooling water is applied to the outside surface of the shell to facilitate the heat removal process by evaporation of the applied water. Early in the postulated event, the water applied to the shell exterior provides at least 90 percent coverage of the external surface. As the transient progresses, the applied flow rate is reduced and the water coverage of the external surface area of the shell is reduced as discussed in Section 7.2 and 7.3.

As evidenced by test data, the flow distribution weirs develop alternating wet and dry vertical "stripes" on the containment surface. These stripes become clearly segregated as the applied water flow rate is reduced. Heat removal from the wetted areas is greater than from the dry areas and results in the wetted surface area being cooler than the dry surface (evaporative cooling in the wetted area is much greater than convection and radiation from the dry surface). This difference in temperature results in heat conduction in the circumferential direction through the thickness of the containment shell. Thermal energy is conducted from the hotter dry stripe areas into the adjacent portions of the containment shell cooled by a wet stripe. The transfer of additional thermal energy to the wet stripe increases the temperature of the wetted steel which increases the water film temperature, which increases the water evaporation rate, the containment heat removal rate, and the use of the delivered water.

Since the water evaporation rate calculated by WGOTHIC only considers heat conduction in the radial direction through the containment steel shell, evaporation rates calculated by WGOTHIC are enhanced by considering the effects of circumferential two-dimensional heat conduction.

A description follows of the method used to calculate the effect of circumferential two-dimensional heat conduction on the water evaporation. Section 7.5 describes how this is applied in the PCS film coverage model to calculate the evaporation-limited PCS water flow rate input for the Containment Evaluation Model.

7.4.1 Geometry of the Wet and Dry Vertical Stripes on the Containment Outside Steel Surface

The Water Distribution Tests, as discussed in Section 7.2.3, showed that the outside surface of the containment shell will be partially wet when the PCS-delivered water flow rate is reduced below the high initial flow rate. At cold, unheated conditions, the observed side wall wetting was []^{a,c} percent with 100 gpm and []^{a,c} percent with 55 gpm equivalent delivered PCS flow. The limited percentages of wetted area were a consequence of the water being applied to the surface at discretely spaced locations, and the fact that the water spread to a stream width that resulted in a bounding Γ_{dist} of []^{a,b} lb/hr-ft. Therefore, the observed

stream width and wetted surface areas were directly proportional to the water flow rate. At these lower flow rates, the stream widths were observed to be less than the distance between weir slots and therefore alternating, vertical, dry and wetted stripes formed down the containment below the second distribution weir.

The occurrence of alternating wet and dry vertical stripes on the containment outside surface was also documented on a hot surface with evaporation in progress in the PCS large-scale test (Reference 7.7).

In the Water Distribution Test, the streams initiated by the second (lower) set of weirs had a center-to-center spacing on the vertical sidewall that corresponded to the spacing of applied water streams at the weir, multiplied by the ratio of the containment radius at the sidewall to the radius at the weir. For example, the 6-inch weir slot spacing at the ~50-foot radius of the dome produced stripes at a spacing of ~8-inches at the sidewall radius of 65-feet. In the LST, with heat transfer occurring, wet stripes were observed to flow vertically at constant width to the bottom of the sidewall unless almost all of the applied water was evaporated.

This evaluation of the effects of two-dimensional conduction on the wet steel surface temperature, and resulting water evaporation rate was based on the same alternating wet and dry stripe pattern and spacing produced by the weir(s) in the water distribution test. However, the location of the second weir ring and the weir ring slot spacing used were updated to correspond to the AP600 plant. Specifically, the weir slots on the backwall of the distribution troughs in the second weir ring are at the 50.7 foot radius, and the spacing between weir slots is 6.5 inches. This results in an 8.35-inch center-line to center-line stripe spacing at the vertical sidewall. In addition, a wider dry stripe directly under the 16-weir collection boxes was taken into account.

7.4.2 Inside and Outside Heat Transfer Boundary Conditions for the Conduction Model

The boundary conditions used in the two-dimensional heat conduction model were established by a series of one-dimensional, steady-state calculations of the PCS heat transfer process performed at steady-state containment pressures ranging from 10 psig to 65 psig (24.7 to 79.7 psia). These calculations were performed using the same heat and mass transfer correlations as used in WGOTHIC. The heat transfer and the temperature differences from the steam/air mixture inside containment through the steel shell, and from the wet and dry outside containment surfaces to the air are provided. The heat transfer and temperature differences were used to establish heat transfer coefficients for each containment pressure condition for both the inside heat transfer to the inside water film, and for the outside heat transfer from the outside water film. These heat transfer coefficients were reduced based on the conservative multiplication factors (Reference 7.11, WCAP-14326, Rev. 1) applied in WGOTHIC, and were then further decreased to account for the water film and paint layer conductivities and thicknesses. The outside heat transfer coefficient versus the outside steel shell temperature obtained for each pressure condition for the wetted surface, was fitted using a second degree polynomial for use in the conduction model. A constant dry surface heat transfer coefficient (with a fixed outside cooling air temperature) that accurately modeled the pressure conditions

analyzed, established the outside heat transfer boundary conditions. These boundary conditions were reviewed to assure that the heat transfer rates at all containment pressure/temperature conditions were higher than the corresponding heat transfer calculated by WGOTHIC in the containment analysis. This assures that any increase in heat transfer, as compared to the heat transfer with only radial conduction through the containment steel shell, is underpredicted.

7.4.3 2-D Conduction (ANSYS) Model Description

The effect of circumferential conduction through the AP600 steel containment shell on the shell surface temperatures and the resulting effects on the condensing heat transfer on the inside surface, the evaporative heat transfer on outside wetted surfaces, and the convective heat transfer from the dry outside surface; were quantified using the ANSYS computer code. The ANSYS computer code is a multi-purpose, finite element program that has been used commercially since 1970. For this calculation ANSYS revision 5.3 was used.

The ANSYS calculation was a two-dimensional, thermal, steady-state analysis of a periodic half-cell (cross-section) that consisted of a two-dimensional block []^{ac} thick and 0.3479-foot (4.174 inches) wide; corresponding to the AP600 containment steel shell thickness and the spacing of water streams at the containment sidewall perimeter imposed by the PCS water distribution weirs. A thermal conductivity of 24 Btu/hr-ft-°F was used for the steel material. Adiabatic boundary conditions were used for the right and left side of the half-cell model to represent symmetry and periodicity of the cell.

For each steady-state containment pressure analyzed, a half-cell model was established for each water coverage fraction ranging from 0.05 to 0.95. The noding density was increased on each side of the wet/dry interface on the outside surface to increase the accuracy of the heat transfer calculation near the wet/dry interface.

In addition to these partially wetted half-cell models, the heat transfer with a completely wetted and completely dry half-cell model was analyzed for each containment pressure using the same inside and outside boundary conditions. Since the half-cell has a 1-D solution when fully wet or dry, these cases provide the heat flux with only radial conduction through the containment shell. The heat flux rate results of these fully wetted and fully dry cases were used to normalize the heat flux rate obtained from the partially wetted cases, where 2-D heat conduction occurs.

7.4.4 Enhanced Evaporation due to 2-D Conduction

The heat flux from the wetted portion of the half-cell model was compared with the wetted heat flux that occurs when only radial heat conduction (one-dimension) is assumed. Figure 7-6 shows the water evaporation rate with two-dimensional conduction versus the fraction of wetted area, normalized to the evaporation rate, calculated with only radial heat conduction (one-dimensional) outward through the steel shell, for containment pressures of 10, 15, 20, and 25 psig. These calculational results are bounded by the following polynomial expression which is used in the PCS film coverage model to determine the evaporation-limited applied water flow rate that is input to WGOTHIC (See Section 7.5):

$$[\quad]^{a,c} \quad (7-1)$$

where

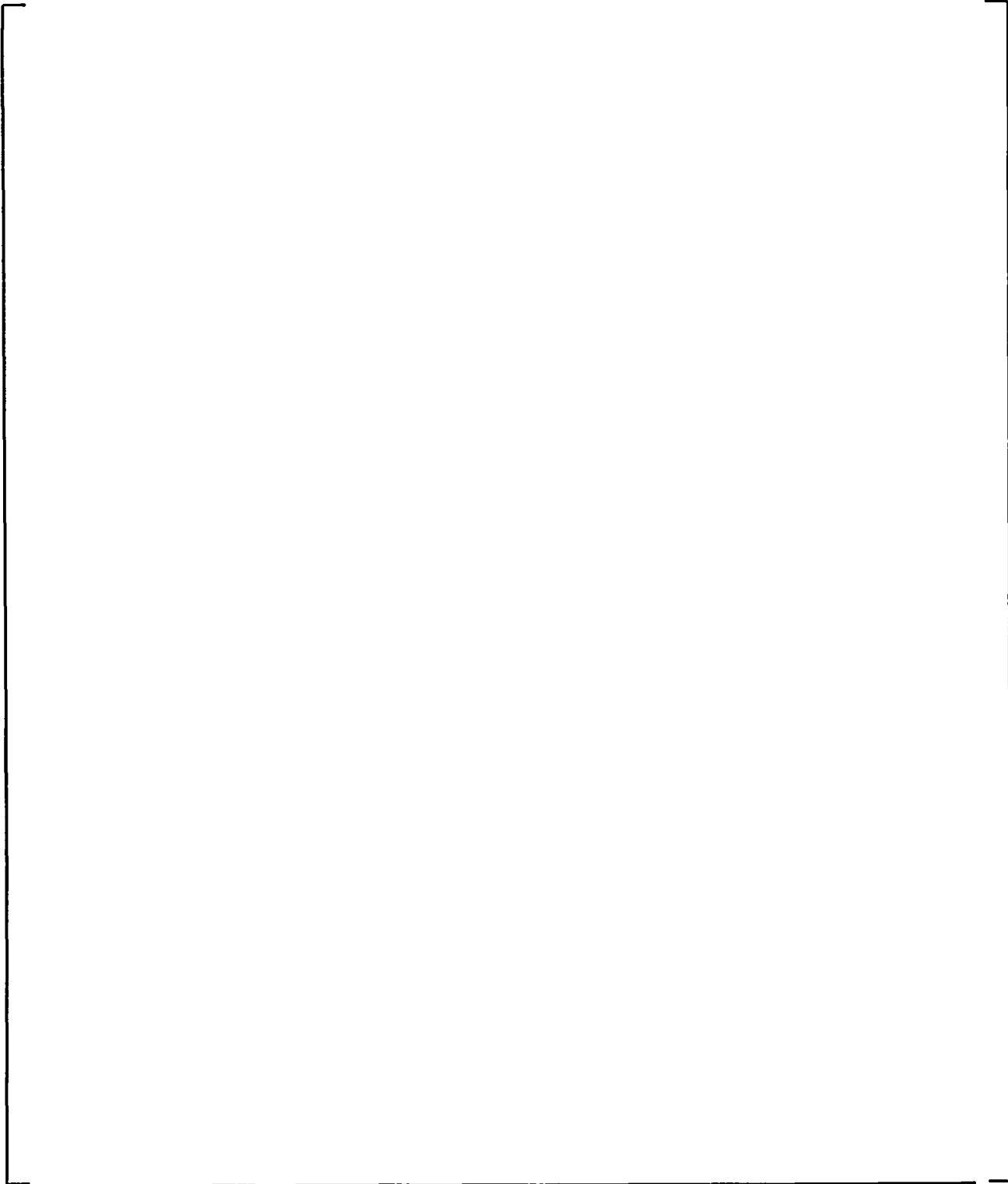
- M = the wetted area heat transfer rate enhancement or multiplication factor
- x = fraction of containment surface wetted, = W/W_o

Several additional plots to illustrate the effect of two-dimensional conduction on the PCS heat transfer process are provided for the 20 psig containment pressure, 25 percent wetted case. A temperature distribution contour plot is shown for the ANSYS half-cell model in Figure 7-7, with the surface inside containment at the top of the page. Figure 7-8 shows the thermal flux from the inside to outside surface (-y direction), perpendicular to the containment shell, and Figure 7-9 shows the total heat flux (x, -y directions) that occur in the steel shell. Figures 7-10 and 7-11 show the thermal flux distribution on the outside and inside surface of the wall, respectively.

7.4.5 Insights from the PCS Large-Scale Testing

The large-scale PCS heat transfer tests were largely conducted with high water coverage fractions such that circumferential conduction would have little or no effect on the water evaporation rate. An exception is test run RC050C of matrix test 213.1. A clear indication of 2-D conduction effects is seen by comparing the results of RC050C with test run RC048C of matrix test 212.1. In these tests, the containment pressure and other boundary conditions were essentially the same, with the exception that the amount of water applied to the external surface of the test vessel was []^{a,b} gpm in test RC048C and only []^{a,b} gpm in test RC050C.

The reduced water flow rate in test RC050C resulted in a reduction in the wetted area observed at the bottom of the test vessel sidewall, []^{a,b} percent for test RC050C versus []^{a,b} percent for test RC048C. In spite of the reduced wetted area in test RC050C, the total heat removed from the test vessel and the amount of water evaporated in this test was equal to test RC048C.



a,c

Figure 7-6 Normalized Water Evaporation Rate (2-D/1D Conduction) versus Overall Containment Wetted Fraction

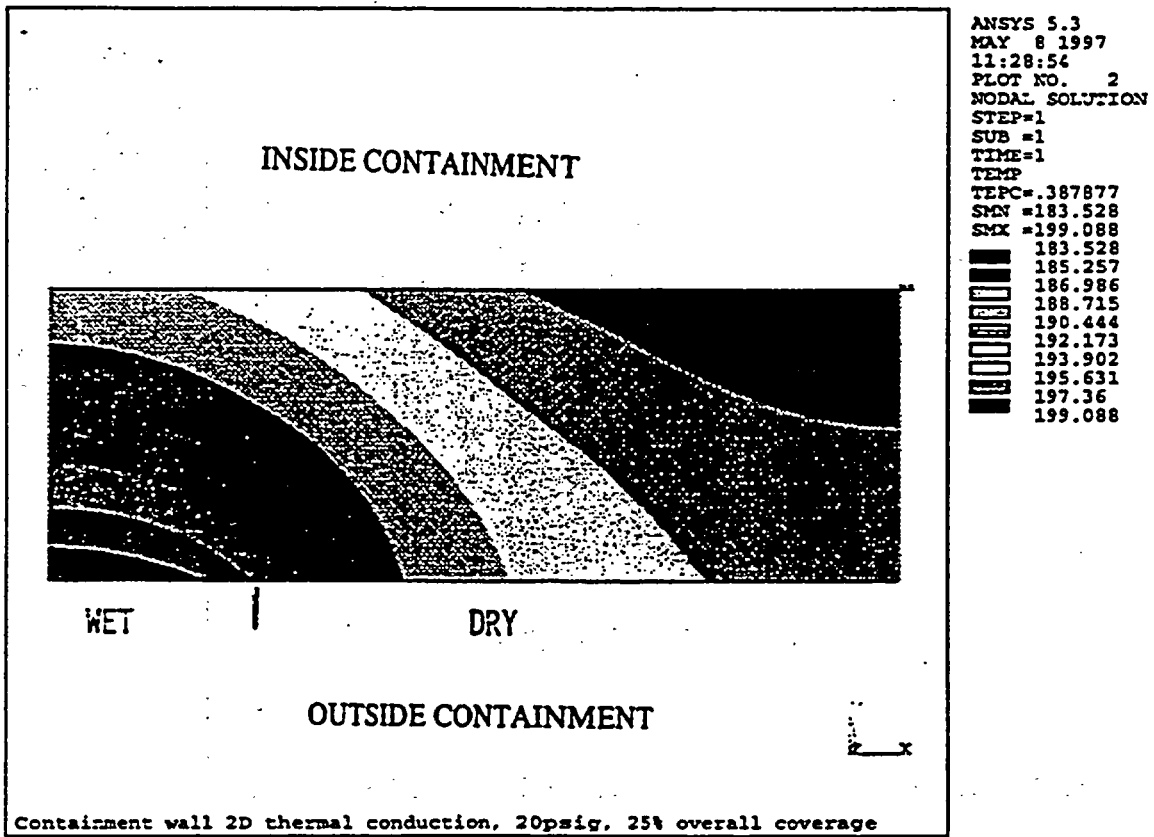


Figure 7-7 Containment Steel Shell Temperature Gradients (°F) with 2-D Heat Conduction; 20 psig, 25% Wetted

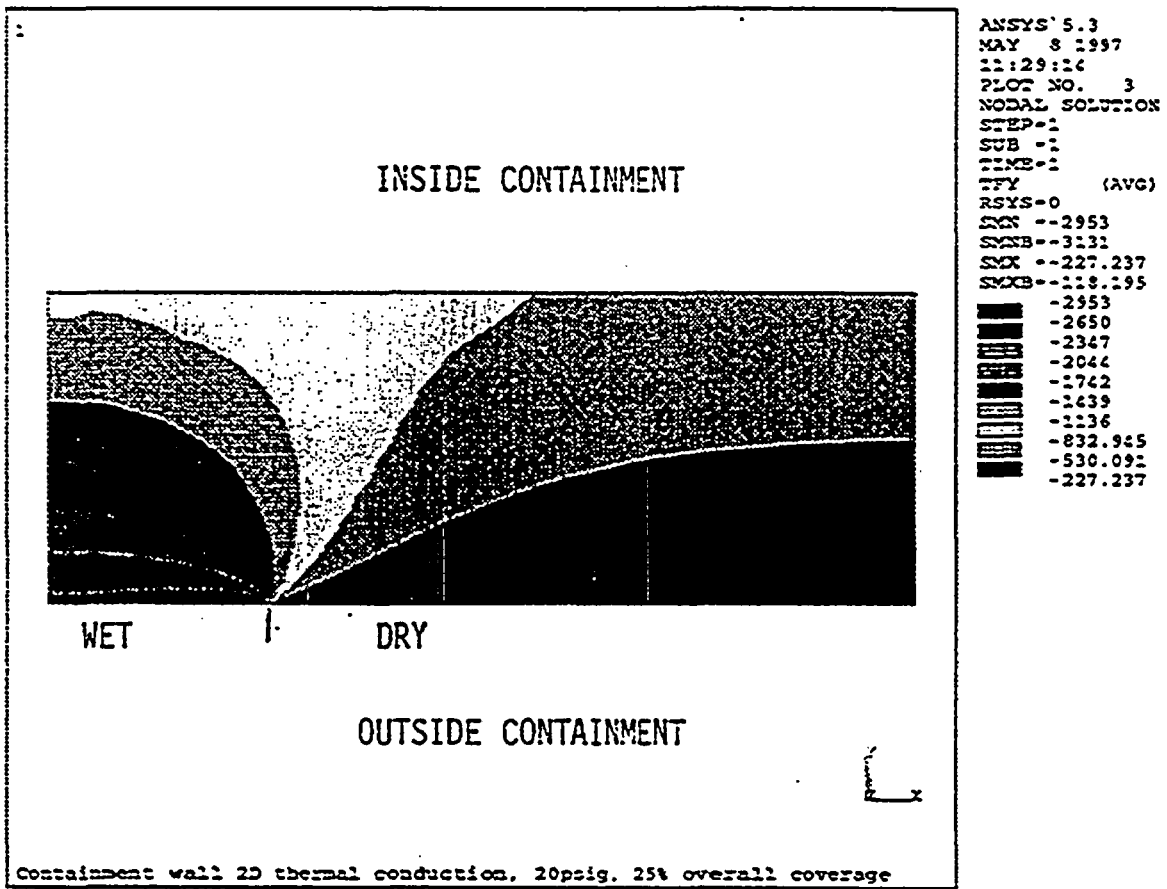


Figure 7-8 Containment Steel Shell Thermal Flux Gradients (Btu/hr-ft²) in Y-Direction; 20 psig, 25% Wetted

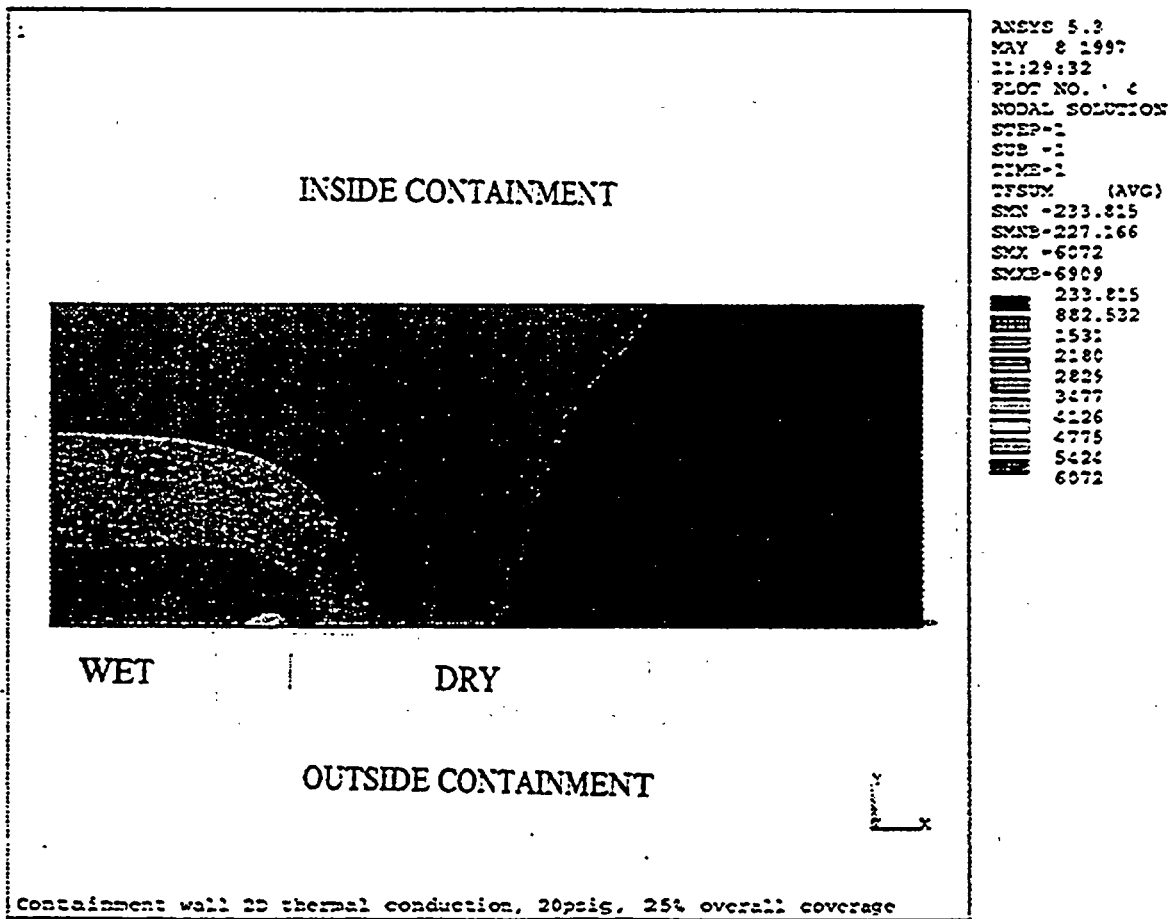


Figure 7-9 Containment Steel Shell Total Thermal Flux (Btu/hr-ft²); 20 psig, 25% Wetted

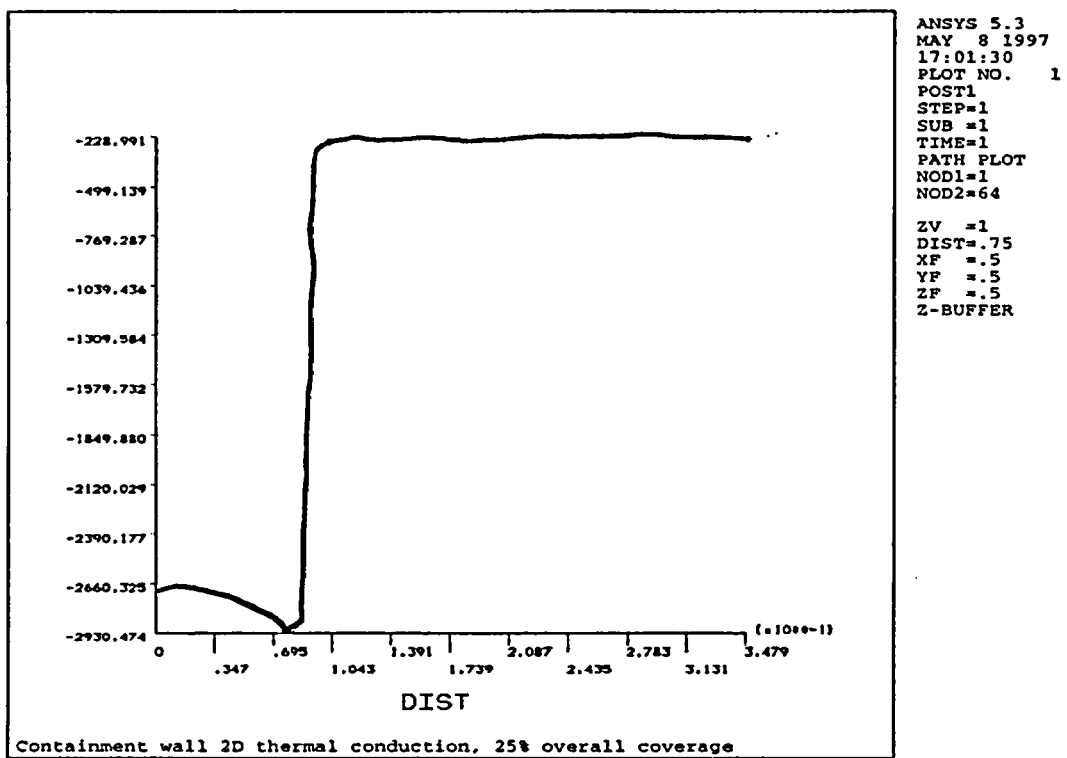


Figure 7-10 Thermal Flux in Y-Direction on Outside Surface of Containment Wall [Btu/hr-ft²]

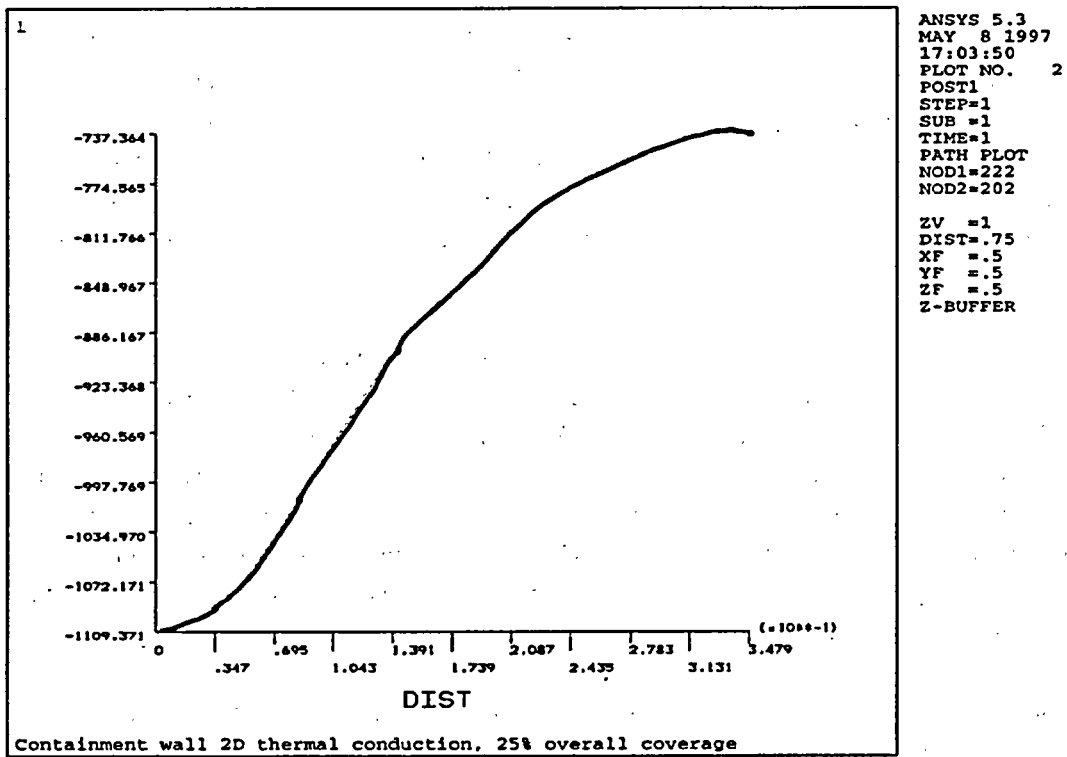


Figure 7-11 Thermal Flux in Y-direction on Inside Surface of Containment Wall [Btu/hr-ft²]

Furthermore, the lower portion of the vertical sidewall in test run RC050C was wetted with []^{a,b}. This stripe geometry is similar to that observed in the water distribution test discussed in Section 7.2.3 and assumed for the 2-D conduction model.

A comparison of the LST vessel shell wall temperatures for these two test runs using the thermocouple pairs (one thermocouple at the inside wall surface matched to a thermocouple at the outside wall surface), used to derive local heat flux rates, provides insight to the effect of circumferential conduction. Tables 7-3 and 7-4 provide comparisons of the inside and outside LST shell temperatures, and the local heat flux derived from the temperature difference across the 7/8-inch thick steel shell; for the two lowest elevations on the LST sidewall.

Table 7-3 shows that at the Level D elevation in test run RC048C all the inside and outside wall temperatures are relatively uniform. This indicates that the outer wall is wetted at all the thermocouple pair locations. The average outside wall surface temperature is []^{a,b}°F, and the average local heat flux is []^{a,b} Btu/hr-ft² based on the thermocouple pair ΔT s. In comparison, only four of seven outside wall thermocouples appear to be wetted in test run RC050C (dry outside wall temperatures are very high, []^{a,b}°F, and the wall ΔT is small). In this test run the average wetted outside wall temperature is []^{a,b}°F, and the average wetted local heat flux is []^{a,b} Btu/hr-ft².

Similarly, Table 7-4 shows that at the Level E elevation (just above the runoff collection gutter) the test run RC048C uniformly wetted outside wall average temperature is []^{a,b}°F and the average heat flux is []^{a,b} Btu/hr-ft². In comparison, test run RC050C which is []^{a,b} percent wetted at this elevation; indicates that only two of the outside wall thermocouples are clearly wetted, and the average wetted outside wall temperature is []^{a,b}°F and the average heat flux is []^{a,b} Btu/hr-ft². Note that the test run RC050C thermocouples at the 240° circumferential location show an outside wall temperature and heat flux that is intermediate to the clearly wetted or dry locations. This thermocouple pair may be adjacent to a wet stripe, where circumferential heat conduction would cause these observed intermediate temperatures and ΔT .

These tables show that with the striped water coverage on the outside surface, the wall temperatures and heat flux of the wet portions of the shell are higher than when the outside surface is completely wet.

7.5 THE CONTAINMENT EVALUATION MODEL TREATMENT OF WATER COVERAGE

The PCS heat removal at a given containment pressure is largely determined by how much of the delivered water evaporates. Heat removal is maximized if all the water delivered to the shell evaporates. Consequently, the determination of how much water evaporates from the containment shell is necessary to determine the containment heat removal. The flow rate of water that runs off the shell is the difference between the delivered water flow rate and the evaporation rate.

The containment Evaluation Model includes the PCS film coverage model and the WGOTHIC code. The PCS film coverage model calculates how much of the delivered flow evaporates and how much runs, unevaporated, off the shell. The evaporation and runoff calculation is performed consistent with the PCS film coverage model described in Section 7.5.1. Since the PCS film coverage model requires heat flux as an input, iterations on heat flux are performed between the PCS film coverage model and the WGOTHIC code. The PCS film coverage model calculates a transient evaporation-limited PCS flow rate for input to the WGOTHIC code. The WGOTHIC code calculates the resulting containment pressure history as discussed in Section 7.5.2.

The PCS film coverage model eliminates the need for the WGOTHIC code to determine the wetted area as a function of time. The use of the evaporation-limited PCS flow to calculate containment pressure introduces conservatism because it discounts sensible heating of any runoff flow, and because a heat flux lower than the heat flux calculated by WGOTHIC is used to calculate the amount of water evaporated.

As the water coverage of the containment shell decreases due to the decrease in the delivered PCS flow rate with time, alternate wet and dry stripes are formed on the containment shell exterior surface and two-dimensional (radial and circumferential) heat conduction is established in the containment shell. Accounting for two-dimensional conduction increases the temperature of the wetted steel surface, and therefore also increases the temperature of the liquid film, over what is calculated for one-dimensional (radial) conduction only. The increase in the temperature of the liquid film, in turn, results in the evaporation of more water, reducing the calculated runoff from the shell. Section 7.5.1.3 describes how the increase in water evaporation effectiveness of the PCS is accounted for in the PCS film coverage model, when both radial and circumferential heat conduction are important in the steel containment shell.

7.5.1 PCS Film Coverage Model

The PCS film coverage model, which is used to calculate the rate at which water evaporates from the sidewall of the containment shell, is described in this section. The model assumes water is delivered to the sidewall consistent with the initial distribution spreading data described in Section 7.3.1. That is, []^{a,b} percent of the shell circumference is wet for delivered flow rates greater than []^{a,b} gpm. When the delivered flow rate decreases to less than []^{a,b} gpm, the wetted circumference is calculated using a water

film flow rate of []^{a,b} lbm/hr-ft (Γ_{dist}). The water flows in constant width stripes down the sidewall as the water evaporates, until Γ is reduced to Γ_{min} , defined in Section 7.3.2. Thereafter, evaporation reduces the film width while Γ remains constant at Γ_{min} .

The PCS film coverage rate model starts with a simple definition that relates the total film flow rate, m ; the wetted circumference, or width of the wetted surface, W ; and the film flow, or mass flow rate per unit width, Γ . Each of these is assumed to be a function of the parameter Z , the distance below the top of the sidewall. The equation is:

$$m = \Gamma W \tag{7-2}$$

which, rearranged, also defines Γ . The derivative of the mass flow rate with respect to vertical distance is also used. Using the chain rule for derivatives:

$$\frac{dm}{dZ} = W \frac{d\Gamma}{dZ} + \Gamma \frac{dW}{dZ} \tag{7-3}$$

The wetted coverage and runoff flow rate are calculated based on the following assumptions and boundary conditions:

- The delivered PCS water flow rate boundary condition at the top of the sidewall, m_{on} is presented in Figure 7-2. The initial film flow rate at the top of the sidewall is specified to be []^{a,c}, where W_o is the containment circumference, for delivered flow rates greater than []^{a,b} gpm. For delivered flow rates less than []^{a,b} gpm, the film flow rate at the top of the sidewall is specified to be $\Gamma_{dist} = []$ ^{a,b} lbm/hr-ft. The other boundary condition, the width of coverage at the top, W_{top} is determined from []^{a,c}, or []^{a,c}, depending on the delivered flow rate.
- The water is assumed to flow in constant width stripes below each weir slot as long as the film flow rate Γ remains greater than Γ_{min} . The film flow rate decreases due to evaporation as the film travels down the sidewall.
- After the film flow rate reaches Γ_{min} , evaporation is assumed to cause the stripe width to narrow while Γ remains constant at Γ_{min} .

7.5.1.1 Constant Width Coverage

After the water distribution is established at the top of the sidewall by the weir, the film evaporates at mass flux, ϕ_m , as it flows down the shell in stripes of constant width. The basis for the constant width stripe is the observations of the stripes on the LST, and the physical explanation in Appendix 7.A-3. For a constant width stripe $dW/dZ = 0$, and $d\Gamma/dZ = -\phi_m$. The change equations for m , Γ , and W for the constant width portion of the stripe are:

$$\frac{dm}{dZ} = -\phi_m W \quad (7-4)$$

$$\frac{d\Gamma}{dZ} = -\phi_m \quad (7-5)$$

$$\frac{dW}{dZ} = 0 \quad (7-6)$$

With the boundary conditions listed above, and Equations 7-4, 7-5, and 7-6, the water mass flow rate, m , and the film flow rate, Γ , can be calculated for the constant width evaporation portion of the coverage. For the case with $\phi_m = \text{constant}$, the simple analytical expression for the mass flow rate is:

$$m = m_{on} - \phi_m W_{top} Z \quad (7-7)$$

Equation (7-4) can be written in terms of difference equations for a numerical solution where $\Delta m = m_2 - m_1$, $\Delta Z = Z_2 - Z_1$, and ϕ_m is a variable:

$$\Delta m = -W_{top} \phi_m \Delta Z \quad (7-8)$$

or

$$m_2 = m_1 - W_{top} \phi_m (Z_2 - Z_1) \quad (7-9)$$

Knowing m , the film flow rate is determined from Equation (7-2) where $\Gamma = \Gamma_{dist} = m/W$.

The value of Z when Γ reduces to Γ_{\min} is Z_{\min} . The value of Z_{\min} can be determined from Equation (7-7) when ϕ_m is constant:

$$Z_{\min} = \frac{m_{\text{on}}/W_{\text{dist}} - \Gamma_{\min}}{\phi_m} \quad (7-10)$$

7.5.1.2 Constant Γ_{\min} Coverage

When $\Gamma = \Gamma_{\min}$, the stripe width W begins to narrow, while Γ_{\min} is maintained at a constant value. The resulting change equations for m, Γ , and W for this portion of the stripe are:

$$\frac{dm}{dZ} = -\phi_m W \quad (7-11)$$

$$\frac{d\Gamma}{dZ} = 0 \quad (7-12)$$

$$\frac{dW}{dZ} = -\frac{\phi_m W}{\Gamma} \quad (7-13)$$

When $\phi_m = \text{constant}$ and $\Gamma = \Gamma_{\min} = \text{constant}$, the solution to Equation 7-13 is the simple exponential function:

$$W = W_{\text{dist}} e^{-\phi_m(Z_2 - Z_1)/\Gamma_{\min}} \quad (7-14)$$

When ϕ_m is not constant with height, the analytical expression for W depends on the functional form of ϕ_m and a general expression is written for numerical integration where ϕ_m is calculated for each ΔZ :

$$\Delta W = -\frac{W \phi_m \Delta Z}{\Gamma_{\min}} \quad (7-15)$$

or

$$W_2 = W_1 - \frac{W_1 \phi_m (Z_2 - Z_1)}{\Gamma_{\min}} \quad (7-16)$$

Knowing W from Equations (7-14) or (7-16), the mass flow rate at any Z is simply calculated from Equation (7-2). The runoff flow rate is $m_{\text{off}} = W\Gamma_{\min}$, where W is the wetted circumference at the bottom of the containment shell, $Z = Z_{\text{max}}$.

By inspection of Equation (7-14), it is noted that W , the film flow per unit width, is always greater than zero. Thus, for constant values of ϕ_m and Γ_{\min} , Equation (7-14) always predicts some water runs off the wall without evaporating. However, from experimental observations, all the water delivered to the containment shell is evaporated for some transient conditions. Thus, the preceding calculation method is conservative in its execution.

7.5.1.3 Spreadsheet Calculation

The equations developed in Sections 7.5.1.1 and 7.5.1.2 are solved in a spreadsheet for both one-dimensional and two-dimensional shell heat transfer. During the initial high flow PCS period when water coverage is high and two-dimensional effects are small, only one-dimensional heat transfer is calculated. However, after the first standpipe uncovers, the PCS-delivered flow is reduced and the wetted circumference at the top of the containment shell is predicted to decrease. Figure 7-6 shows the two-dimensional conduction enhances evaporation at reduced coverages. Thus, as the delivered flow rate continues to decrease, two-dimensional conduction is included in the calculation of the evaporation rate.

The two-dimensional conduction model discussed in Section 7.4 calculated the evaporation rate for a range of wet stripe widths for both one- and two-dimensional conduction. The calculation used the same overall temperature difference (and steam partial pressure difference) between the bulk containment and the bulk riser as boundary conditions for both cases. The effective heat transfer coefficients, for mass transfer, were determined for each case. The comparison shows for a given stripe width, the enhancement of the evaporation rate when the real physical case of two-dimensional conduction is considered. It was found that the enhancement varied with stripe width, but had little effect on the overall temperature difference between the bulk containment and riser. Consequently, the family of curves representing the bulk temperature difference were lower bounded, thereby eliminating the dependence on the bulk temperature difference. The only dependent variable is the wet stripe width. The enhancement of evaporation is characterized by the multiplier, M , that is a polynomial function of the wet stripe width. M is defined by Equation 7-1.

The multiplier, M is used in the spreadsheet as a multiplier on ϕ_m to produce a better estimate of the actual evaporation flux from the film stripes.

The evaporation-limited PCS flow rate calculated with the PCS film coverage model spreadsheet is input to the WGOTHIC code. The WGOTHIC pressure calculation is thereby limited to the amount of flow that is independently shown to evaporate.

7.5.2 WGOTHIC Model

The WGOTHIC AP600 containment model is described in detail in Section 4. The WGOTHIC AP1000 Containment Model is described in detail in Section 13. Features specific to water coverage are discussed in this section.

The WGOTHIC code uses a special type of heat conductor called a "clime" to model the convection, radiation, conduction, evaporation, and condensation heat and mass transfer processes from the inside of containment to the outside of containment. Each clime consists of a horizontal slice of the shell, riser, baffle, downcomer, and shield building of the PCS. []^{a,c} climes are used to represent the PCS in the AP600 containment DBA Evaluation Model. []^{a,c} climes are used to represent the PCS in the AP1000 containment DBA Evaluation Model.

The WGOTHIC model uses the following input to compute the evaporation heat removal rate from the shell: the evaporation-limited PCS water flow rate, the PCS water temperature, and the area and wetted perimeter for each clime. The vertical variation in the wetted perimeter and the resulting wetted area were conservatively calculated in the PCS film coverage model, so the WGOTHIC code does not calculate the change in these values as a function of time or position. Rather, the evaporation-limited PCS water flow rate is determined in the PCS film coverage area model, and is input to WGOTHIC to account for changes in the evaporation rate due to anticipated changes in the coverage area with time and location on the shell. The WGOTHIC code uses wetted perimeter inputs for each clime as described in Section 7.5.2.1.

The evaporation-limited PCS flow rate that is input to the WGOTHIC code is calculated in the PCS film coverage model described in Section 7.5.1. The application of the PCS flow is assumed to be delayed until 337 sec, based on the estimated time required to reach steady-state coverage at a PCS flow rate of 440 gpm as described in Section 7.2.5.

7.5.2.1 Wetted Perimeter Inputs

The wetted perimeter for each clime is input to the WGOTHIC model. The clime model allows the water to flow at constant width until it reaches the next lower clime, or it evaporates entirely. When it evaporates entirely before reaching the bottom of the clime, the code tracks the distance traveled and breaks the clime vertically into wet and dry portions with temperatures calculated using the appropriate wet or dry heat and mass transfer models. The wetted perimeter input values for the WGOTHIC Model are based on the measured water coverage values from the Phase 3 Water Distribution Tests on the dome, and 90 percent of the shell circumference wetted on the sidewall. Use of the evaporation-limited PCS water flow rate from the film coverage model as input to the WGOTHIC model, as described in Section 7.5.1, eliminates the need to vary the wetted perimeter input values with time. The sensitivity analyses, presented in Section 7.6, demonstrate that this approach is conservative as compared to using the actual PCS film flow rate with variable coverage area.

The fixed wetted perimeters input for the WGOTHIC climes provide a conservative coverage fraction for the initial PCS operation when the delivered flow rate is high. Since the amount of water that is evaporated is calculated in the PCS film coverage model, the area used by WGOTHIC to evaporate the evaporation-limited PCS flow does not affect the evaporation rate.

The wetted perimeter value for the top of the dome down to the first weir is estimated from the video tapes of the Phase 3 Water Distribution Test. The coverage area and wetted perimeter change over the diverging area between the first and second weirs. The wetted perimeter specified for this region is based on the average of the value just below the first weir and the minimum measured value just above the second weir. The wetted perimeter does not change much over the steeply sloped region between the second weir and the top of the vertical sidewall. The wetted perimeter input values are the same for each clime representing the vertical sidewall.

The percent of the perimeter wetted is summarized in Table 7-5. The values listed represent the measurements at the 27.5 gpm flow rate (which is equivalent to a 220 gpm PCS water flow rate). The use of these wetted perimeter percentages for the higher initial PCS flow rate is a conservatism in the containment Evaluation Model.

| Table 7-5 Clime Wetted Perimeter and Basis for <u>WGOTHIC</u> Model | | | |
|---|------------|----------|--|
| Clime | Percentage | Location | Method of Determination |
| [| |] | ^{a,c} Visual inspection and calculation |
| | | | Measured |
| | | | Measured |

7.5.2.2 WGOTHIC Iteration with Spreadsheet

An iteration between the PCS film coverage model spreadsheet and the WGOTHIC model is necessary to converge on the same evaporation rate in both. The iteration between the PCS film coverage model spreadsheet and the WGOTHIC calculations proceed as follows:

1. An average evaporation heat flux, ϕ_h , at selected times is determined from the wet WGOTHIC climes below the second weir.
2. The evaporation mass flux, $\phi_m = \phi_h/h_{fg}$, is input to the spreadsheet. The evaporation rate, m_{evap} is calculated in the spreadsheet for each time using Equations (7-7) and (7-14) for problems with constant evaporation mass flux, and Equations (7-8) and (7-15) for problems with variable evaporation flux.

3. WGOTHIC is run with m_{evap} from the spreadsheet and the calculated results are used to define ϕ_h for input to Step 2 to recalculate the water evaporation rate.

When the WGOTHIC calculated values of ϕ_h are sufficiently close to, but higher than, the values assumed for input to the spreadsheet under Step 2, the solution is converged. That is because a higher heat flux input to the spreadsheet will predict more water evaporated. The use of the lower evaporation rate input results in WGOTHIC pressure predictions that are slightly high.

7.5.2.3 Dry Convection and Radiation Heat Transfer Predictions

The ANSYS two-dimensional heat conduction results show that the temperature of the dry surface area is decreased compared to the dry surface temperature when only one-dimensional radial heat conduction is used. This results in less radiation and convection from the dry regions. Although WGOTHIC utilizes one-dimensional radial heat conduction, the dry area convection and radiation is not overpredicted because WGOTHIC must use a wet surface area that corresponds to the evaporated water flow rate calculated by the PCS film coverage model. The evaporated water flow rate calculated by the PCS film coverage model includes the enhanced evaporation characterized by the multiplier, M (Section 7.5.1.3). Thus, WGOTHIC must use more cooler wet surface area to evaporate the water flow rate from the PCS film coverage model. This results in less hotter dry surface area, and therefore, WGOTHIC underpredicts the net radiation and convection from the dry surface.

The WGOTHIC conservatism can be estimated using values from the ANSYS two-dimensional calculation, which is the best representation of the heat conduction through the shell. It is assumed the WGOTHIC temperatures and heat fluxes are the same as ANSYS one-dimensional cases.

- At containment pressures of 15 and 25 psig, and with 50 percent wet coverage, the two-dimensional ANSYS model predicts dry heat transfer (radiation and convection) is 73 and 82 percent respectively, of the one-dimensional value. WGOTHIC will predict 67 percent of the one-dimensional dry heat transfer, since it reduces the dry surface area available by 33 percent.
- For the same containment pressures, at 25 percent wet coverage, the two-dimensional model predicts the actual dry heat transfer (radiation and convection) is 83 to 91 percent of the one-dimensional value. WGOTHIC will predict 57 percent of the one-dimensional dry heat transfer, since it reduces the dry surface area by 43 percent. Thus, WGOTHIC again predicts less dry energy removal than two-dimensional model predicts.

It is concluded that the WGOTHIC model predicts less dry heat transfer than the two-dimensional ANSYS model.

7.6 SUMMARY OF SUPPORTING TESTS AND SELECTED ANALYSIS

This section provides a summary of the PCS tests and data that are relevant to water film coverage and film behavior, and which support the Evaluation Model. In addition Section 7.6.4 provides an estimate of the range of film coverage parameters that can occur in the AP600 and AP1000, and compares this parameter range to a composite of the ranges tested.

Section 7.6.5 summarizes an estimate of the heatup of the AP600 and AP1000 containment shell versus time. This heatup versus time is utilized in the sensitivity study of PCS flow initiation time presented in Section 7.7.3.

7.6.1 Westinghouse Wet Flat Plate Test

The primary purpose of the Westinghouse wet flat plate test was to generate heat and mass transfer data for evaporative cooling with parameters that bound the expected conditions on the AP600 containment shell. A secondary purpose was to observe the film hydrodynamics including possible formation of dry patches due to surface tension instabilities. The test article is described in Reference 7.3.

Tests were performed in two orientations, vertical (to represent the sidewall) and 15 degrees from horizontal (to represent the upper portion of the dome) with various combinations of air velocity, film flow rate, and heat flux. A stable, wavy laminar water film was formed easily on the hot, coated, steel surface, even in the vertical orientation. A description of the test section and results from the various tests are given in Reference 7.3. The test data are summarized in Table 7-6.

Two of the heated flat plate tests were run with very low film flow rates at relatively high heat flux (6000 - 8000 BTU/hr-ft²) to force the film to completely evaporate before reaching the end of the test section. The observations given in Reference 7.3 state the following: "The upper part was 80 percent wetted and fingers of water film extended down 4 feet to within 2 feet of the end of the heated plate. The bottom of the fingers slowly moved up and down. The dry patch between fingers was between 1/4-inch and 1-1/2 inches wide. As the width varied in time, the lateral, slow flow of liquid could be seen feeding the thinnest parts of evaporating film. These two tests showed that the end point of water films on the containment would still be stable film evaporation, even with very thin films and high heat fluxes."

7.6.2 Small-Scale Tests

The small-scale tests were designed to provide heat and mass transfer data for both the inside and outside of the test vessel. The test apparatus consisted of a 3-foot diameter, 24-foot high steel pressure vessel filled with air at atmospheric pressure into which steam was supplied to maintain various pressures. Water was applied to the external surface to simulate evaporation in the PCS annulus. The pressure vessel was surrounded by a clear, plexiglass shield that formed a 15-inch wide annulus for either forced or natural circulation-driven air flow and allowed observation of the applied external film flow.

The tests were conducted with varying steam supply flow rates, water film flow rates, water film temperatures, cooling air flow rates, and cooling air inlet temperature and humidity. Instrumentation was provided to measure internal steam condensation rates, external water evaporation rates, inner and outer wall temperatures, film temperatures, air velocity, temperatures, and humidity. A summary of the test data from Reference 7.4 (for tests with measured water coverage) is provided in Table 7-7.

The following observations and conclusions (with respect to the water film) were drawn from these tests:

- A stable, uniform, wavy laminar film was formed on the inorganic zinc-coated steel surface using simple weirs.
- The film remained stable and uniform on the vertical sidewall of the vessel at average evaporating heat fluxes in the range of those expected on the AP600.

7.6.3 Large-Scale Tests (LSTs)

The Westinghouse large-scale PCS test facility was built to provide heat and mass transfer test data for a geometrically similar model of the AP600 containment vessel. The tests provided experimental data used for evaluating the physics in containment, determining the relative importance of various parameters that affect heat and mass transfer, and validating computer codes and models. The following provides a discussion focused on the use of LST data to develop a bounding film coverage model.

Three series of tests were run at the Westinghouse large-scale PCS test facility. The steady-state pressure, annulus air flow rate, external water flow rate, injected steam flow rate, injection velocity, location and orientation, and noncondensable gas concentration were varied between the tests. Test conditions were selected to provide heat and mass transfer validation over a range of post-accident containment operating conditions for the AP600.

a,c

a,c

The large-scale PCS test facility is a 20-foot tall, 15-foot diameter pressure vessel that simulates the AP600 containment vessel. The geometry is approximately a 1/8-scale of the AP600 containment vessel. A plexiglass cylinder is installed around the vessel to form the air cooling annulus. Air flows upward through the annulus via natural convection to cool the vessel, resulting in condensation of the steam inside the vessel. A fan is located at the top of the annulus shell to provide the capability to induce higher air velocities than can be achieved with purely natural convection. Water is applied to the elliptical dome surface by two rings of J-tubes. This method of application resulted in a series of spaced, wavy laminar flow stripes. At low test pressures the stripes spread within a few inches of their application point to form a continuous wavy laminar film. At high pressure the continuous film separated to form discrete stripes.

The following important observations with respect to film behavior were made during the tests:

- The J-tubes resulted in a non-uniform distribution of water on the surface of the LST, similar to that observed in the Water Distribution Test.
- Some J-tubes dripped and others had noticeably lower flow rates. This resulted in some regions of the dome and sidewall that were just wet or had a very low film flow rate.
- As the pressure and temperature increased inside the pressure vessel, dry spots first began to form in the wet, but low flow regions on the dome and sidewall.
- With increased pressure and heat flux, the dry spots grew vertically (both upward from the gutter and downward from the dome, between dripping or low flow J-tubes), separating the original continuous film into wavy laminar flow stripes.
- At higher heat fluxes, dry spots also formed just below, and in line with the J-tube location. A typical coverage pattern for high heat flux and high flow rate is shown in Figure 7-12.
- The central, wavy laminar flow region of the individual film stripes was surrounded by a region of laminar flow (with no visible waves). The thickness of the laminar flow region appeared to continually decrease out to the very edge (or bottom) of the film stripe.
- The widths of both the wavy laminar and laminar flow regions of the stripe were observed to decrease with increasing heat flux. At high flow rates, the width of the stripe was observed to remain relatively constant with elevation as the film flowed down the vertical sidewall. At lower flow rates, the stripe width was observed to taper uniformly with elevation as the film flowed down the vertical sidewall.

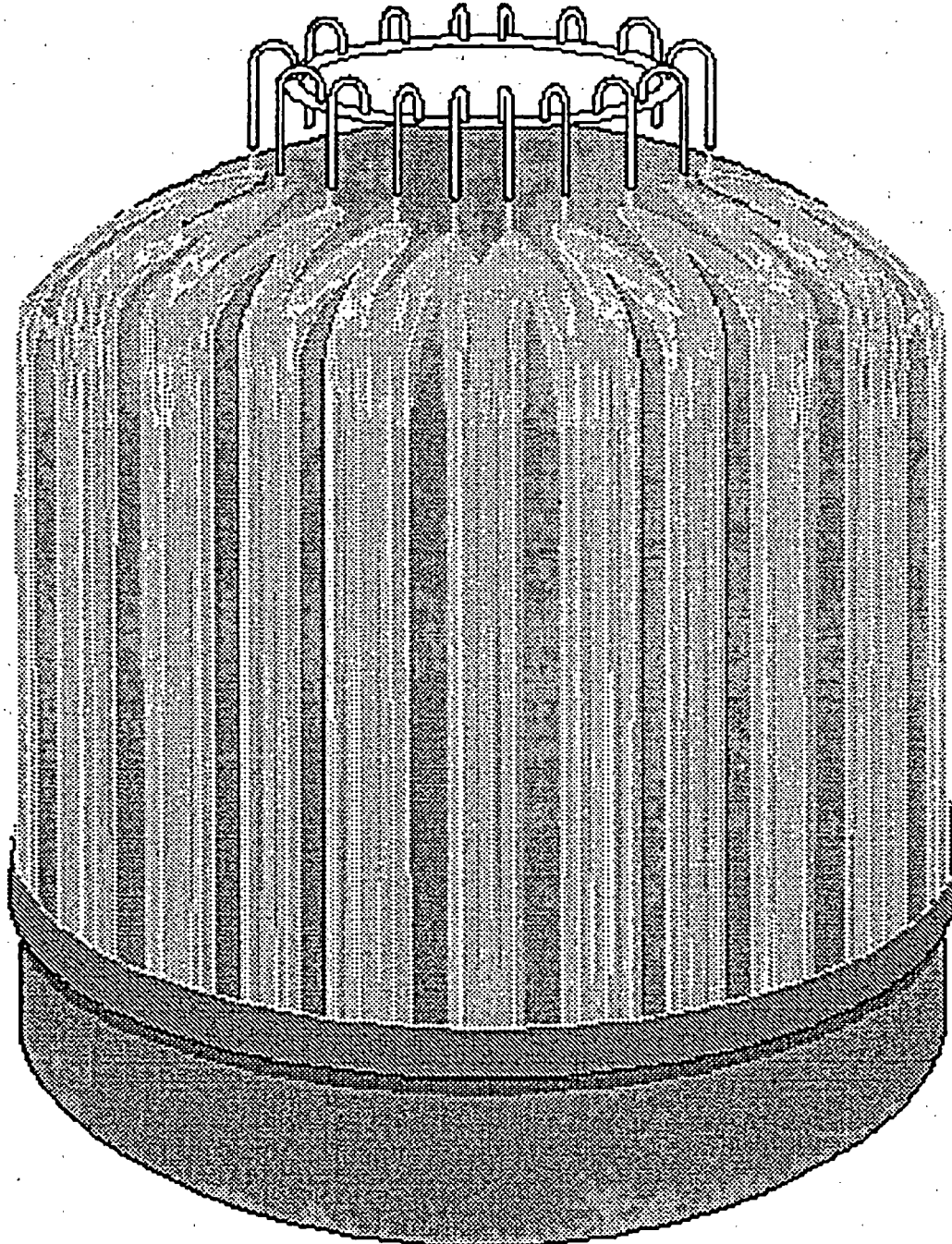


Figure 7-12 Large-Scale Test Water Coverage Pattern

- The film stripes remained stable (i.e., they did not split or bunch up to form thick, narrow rivulets) as they evaporated on the vertical sidewall.

The applied PCS flow rate was observed to vary or oscillate at a slow but regular period during some tests. This phenomenon was the result of sharing a common water source with a boiler feedwater valve that opened every two minutes, thereby reducing the PCS flowrate to the J-tube header. From observations made during testing, the flow oscillations had an effect on the water coverage fraction; it was most noticeable at the bottom of the sidewall. The length of the narrow film stripes and the width of the wider film stripes both decreased when the flow was observed to decrease. The dryout point of the narrow film stripes was observed to rise up and fall down the sidewall as the flow oscillated. At no time were the stripes observed to become unstable due to the oscillations; the process remained well-behaved and repeated itself with the periodicity of the applied flow.

After the Baseline LSTs were completed, instrumentation was added so the transient inlet and outlet cooling water flow rates could be measured and recorded by the data acquisition system. All of the Phase 2 and Phase 3 tests, with the exception of the blind test, (220.1, RC062) were included in the evaluation. The steam injection location, velocity, and initial pressure were much different in the Phase 3 tests, and subsequently, the level of stratification within the vessel was different than the Phase 2 tests. The differences in stratification resulted in changes in the coverage from the top to the bottom of the vessel; the top was less well covered than the bottom during some of the Phase 3 tests. The test numbers that were evaluated are listed in Table 7-8.

Measurements of the dry stripes on the vessel were taken just above the gutter during the defined steady-state periods of each test. The time the measurement was recorded on the data sheets for each test. This could have been either the time the measurement was started or finished. In test 221.1B, the time of measurement does not match with the stated steady-state time period. The test engineer postulated the recorded time to be one hour off, i.e., 12:45 was recorded as 1:45 by mistake. The following assesses the effects of variations in flow during the time taken to record coverage data at the gutter.

From recorded test data the maximum and minimum exit mass flow rates were determined over the approximate time the wetted perimeter measurement was made. The time taken to perform these measurements was related to the number of dry stripes; more stripes took longer to measure. A 15-minute band on either side of the stated time of measurement was used in this evaluation to bound the time it took to make the measurement.

The maximum and minimum exit film flow rates were calculated by dividing the maximum and minimum mass flow rate by the measured wetted perimeter value. Because the film flow rate is calculated by dividing the mass flow rate by the wetted perimeter, if the wetted perimeter were slightly less than measured (due to a reduction in the mass flow rate), the film flow rate would be higher than calculated with this method.

Similarly, if the wetted perimeter were slightly higher than measured (due to an increase in the mass flow rate), the film flow rate would be lower. In either case, the difference between the maximum and minimum film flow rates would be smaller than calculated. The maximum and minimum film flow rates for the tests are tabulated in Table 7-8.

An evaluation of the LST data (Reference 7.5) yielded some additional important conclusions with respect to film coverage and heat removal:

- Evaporation is the primary mode of heat removal from the outside of the vessel. Sensible heating of the subcooled liquid film, convection, and radiation are second order.
- Striped film coverage provided better heat removal than forced quadrant coverage for the same wetted coverage.
- The highest heat flux occurred near the top of the dome at the elevation where the external film was applied for all of the wetted LSTs (except the horizontal, high-velocity, steam jet injection case). Although the dome represents about 30 percent of the heat transfer surface area, approximately 40 percent of the total heat removal occurred on the dome and 60 percent on the cylindrical sidewalls.
- Injection of high-velocity steam (similar to a steamline break) resulted in a well-mixed vessel (both above and below the operating deck), and thus, a relatively uniform wall temperature and heat flux over the evaporating surface.

The test data related to water coverage from References 7.6 and 7.7 are summarized in Table 7-8. Tests 207.1, 207.3, 208.1, 216.1A, and 216.1B were conducted with water coverage by quadrants and are not representative of AP600 conditions and are therefore excluded from the table. The data of Table 7-8 are used to develop a bounding film stability model as described in Section 7.3.2.

7.6.4 Estimated Range of Film Coverage Parameters

The estimates for the maximum and minimum values for the range of AP600 and AP1000 film coverage parameters during a DBA are calculated using the simple approach described below. The range of film coverage parameters is compared with the range of the PCS tests and is shown in Table 7-10.

To determine a maximum sidewall film flow rate, none of the initial PCS water is assumed to evaporate on the dome. Measurements from the unheated, Phase 3 Water Distribution Tests indicate that approximately []% percent of the perimeter at the top of the sidewall will be wetted with 220 gpm, assuming this same wetted parameter at the higher actual PCS delivered flow rate results in an estimated maximum sidewall film flow rate of []^{sc} lbm/hr-ft for AP600 and AP1000 respectively. The maximum sidewall Re_{film} would

be []^{ac} respectively at the estimated maximum 200°F film temperature. The liquid film Reynolds numbers range up to []^{ac} in the test data (Reference 7.11).

The shell heat flux provides the boundary conditions for the evaporating film. The steady-state, shell average heat flux and film temperature were estimated for the subcooled, evaporating, and dry portions of the shell, assuming an initial ambient air and film temperature of 120°F. These estimates were made at the containment design pressure to bound conditions at the expected DBA peak pressure and at half containment design pressure, for conditions representative of 24 hours after blowdown. The results are presented in Table 7-9.

| Table 7-9 Estimated Shell Heat Flux and Film Temperature | | | | | | | |
|--|------|-------------------------------------|---------------|-------------------------------------|---------------|-------------------------------------|----------------|
| Containment Pressure (psig) | | Avg. Subcooled | | Avg. Evaporating | | Avg. Dry | |
| | | Heat Flux (BTU/hr-ft ²) | Film Temp (F) | Heat Flux (BTU/hr-ft ²) | Film Temp (F) | Heat Flux (BTU/hr-ft ²) | Shell Temp (F) |
| AP1000 | 59 | 9500 | 160 | 4800 | 195 | 400 | 275 |
| AP600 | 45 | 7500 | 155 | 3800 | 190 | 320 | 250 |
| AP1000 | 29.5 | 6000 | 150 | 2800 | 180 | 290 | 240 |
| AP600 | 22.5 | 3500 | 150 | 1500 | 170 | 165 | 215 |

To account for stratification, the maximum wet shell heat flux is estimated to be 50 percent higher than the average subcooled value. The minimum wet shell heat flux would be 0 BTU/hr-ft².

The initial PCS film temperature will be between 40°F and 120°F. The 120°F value is used in the DBA Evaluation Model to minimize the benefit of heat removed by heating the subcooled film. The film temperature will increase as the film flows down the dome. The maximum evaporating film temperature was estimated to be less than 212°F.

The resulting estimated range of the AP600 film parameters during a DBA is summarized in Table 7-10 and compared with the composite test data range.

The test data parameter ranges are sufficient for evaluating the film stability model. It is important for the test data to cover the higher range of heat flux and the lower range of the sidewall film Reynolds number for evaluating the film stability model. Films with high Reynolds number values on low heat flux surfaces are more stable than films with low Reynolds number values on high heat flux surfaces. The maximum tested heat flux is almost 50% higher than the estimated maximum AP1000 value. Tests were run at low film flow rates and to dryout, so the lower range of film Reynolds numbers are also covered.

| | | | | | | |
|--|--|--|--|--|--|--|
| | | | | | | |
| | | | | | | |
| | | | | | | |
| | | | | | | |

a,c

7.6.5 Containment Shell Heatup Analysis

This section summarizes an analysis of the heatup of the containment shell versus time. This analysis will be utilized in the sensitivity study on the importance of the time at which PCS flow is put on the containment dome following a DBA (see Section 7.7.3).

The shell surface temperature begins to increase following a DBA. The time for the dry outer shell to reach a given temperature is a function of the internal containment gas temperature, the internal energy transfer coefficient, and the shell thickness. The time can be calculated using the properties of the steel shell and Figure 4-8 from Kreith (Reference 7.9).

The initial shell temperature is assumed to be 120°F. The time for the dry external shell surface temperature to reach the boiling point (212°F) can be calculated with the following input:

- T = 212°F (external shell surface temperature)
- T_i = 120°F (initial shell temperature)
- T_∞ = 250°F (internal containment gas temperature for AP600)
- T_∞ = 270°F (internal containment gas temperature for AP1000)
- ζ = (T - T_∞)/(T_i - T_∞)

So, ζ = 0.292 for AP600 and ζ = 0.387 for AP1000.

The Biot number is given by

$$Bi = h * L / k$$

where h is the heat transfer coefficient on the inside wall, Btu/hr-ft²-°F
 k is the thermal conductivity of the shell
 and L is the shell thickness

The Fourier number is given by

$$Fo = \alpha * t / L^2$$

where α is the thermal diffusivity and is given by

$$\alpha = k / (\rho * c_p)$$

ρ is the shell density

c_p is the shell specific heat

and t is the time to reach the target temperature

The properties of the steel shell are given below:

- k = 23.6 BTU/hr-ft-F (AP1000)
- = 25 BTU/hr-ft-F (AP600)
- L = []^{sc} ft (AP1000)
- = []^{sc} ft (AP600)
- ρ = 490 lbm/ft³
- c_p = 0.107 BTU/lbm-F (AP1000)
- = 0.104 BTU/lbm-F (AP600)

By assuming a heat transfer coefficient on the inside wall, the Biot number is calculated then used to determine the Fourier number and the time for the outer surface to reach 212°F.

| h (BTU/hr-ft ² -F) | 1/Bi | | Fo | | t (sec) | |
|-------------------------------|-------|--------|-------|--------|---------|--------|
| | AP600 | AP1000 | AP600 | AP1000 | AP600 | AP1000 |
| 5 | 36.9 | 32.4 | 43 | 28 | 5792 | 4373 |
| 10 | 18.5 | 16.2 | 22 | 18 | 2963 | 2811 |
| 50 | 3.7 | 3.2 | 5 | 3.5 | 673 | 547 |
| 100 | 1.8 | 1.6 | 2.6 | 2.2 | 350 | 344 |

The shell internal heat transfer coefficient is likely in the range of 50-100 BTU/hr-ft²-F. Thus, the external shell surface temperature is estimated to reach 212 F between 350 and 670 seconds for AP600 and between 340 and 550 seconds for AP1000.

The WGOTHIC AP600 Evaluation Model calculated shell surface temperatures at the top of the dome, before application of the PCS film, can be compared to the hand calculated results. During the initial 5.5 minutes of the transient, the containment gas temperature (and therefore the maximum possible internal shell surface temperature) is maintained at about 250°F by condensation on the heat sinks inside containment. The dome surface temperature is predicted to be 174°F at 337 sec, and without external water is projected

to reach 212°F at 500 sec, which is in reasonable agreement with the estimates above. The heatup rate from the WGOTHIC calculation is about 0.2°F/sec and falls between the 50 and 100 BTU/hr-ft²-F internal energy transfer coefficient values assumed in the hand calculation.

The calculated temperature increase in the AP600 dry external shell surface is compared to water coverage events as a function of time in Table 7-11.

At the maximum time delay for initial water application to the shell (36 seconds, from Table 7-11), the outer shell temperature is calculated to increase less than 4°F. The temperature increase of the dry portion of the outer shell is less than 70°F at the time the weirs are filled and steady-state coverage is established (337 seconds, from Table 7-11). Therefore, the external shell surface temperature is less than 190°F at the time steady-state coverage is established.

Water coverage is not adversely affected by application of the film to a hot, dry, shell surface. Both the STC wet flat plate tests and the LSTs verified the ability of the water film to wet and rewet a hot, dry surface (temperature exceeding 240°F) with the inorganic zinc coating. Video tape records of the Westinghouse wet flat plate tests show the initial wetting, dryout, and re-wetting of a hot, dry plate in both a vertical and inclined position. The dry plate temperature was estimated to be about 240°F (based on the maximum heating fluid temperature). An applied wavy laminar film quickly covered the hot, dry plate. As the flow rate was reduced, the waves in the film became smaller and eventually disappeared. The plate remained visibly wet until after the film flow was turned off, then dry patches appeared and grew in circumference as the plate dried out. Video tapes also show the initial wetting of the LST vessel. The measured shell surface temperature was about 260°F at the time the water was applied. The film front was observed to "sizzle" as it quickly advanced downward and covered the surface of the elliptical dome.

| Table 7-11 Transient Dry Shell Temperature Increase | | |
|---|------------|--|
| Event | Time (sec) | Increase in Dry, External Shell Temp. (°F) |
| Signal Actuation | 0 | 0 |
| Valve Strokes Open | 20 | 0 |
| Piping Fills | 34 | 2 |
| Bucket Fills & Spills | 36 | 4 |
| Weirs are filled and steady-state coverage is established | 337 | 68 |

7.7 AP600 CONTAINMENT DBA EVALUATION MODEL FILM COVERAGE SENSITIVITIES

Sensitivity analyses performed with the AP600 containment DBA Evaluation Model are provided in this section. The model's sensitivity to the PCS film flow rate and water coverage are studied. An estimate of the conservatism in the assumed time delay for PCS film application is also studied.

7.7.1 Sensitivity of the Evaluation Model to the Input PCS Film Flow Rate

Calculations were performed using the WGOTHIC code with the AP600 containment Evaluation Model described in Section 4. The delivered PCS flow rate presented in Figure 7-2 was applied to the WGOTHIC model. Sensitivity calculations were performed by decreasing the input PCS flow rates to 75, 60, 50, and 25 percent of the nominal value. Recalling that the time it takes to fill the headers and weirs is inversely proportional to the film flow rate, the time of film application was adjusted in each case to account for the decreased film flow rate. The water wetted perimeter input value was kept the same for each case, assuring the difference in calculational results was due only to applied PCS flow.

Figure 7-13 presents the change in peak containment pressure as a function of percent change in applied PCS flow rate. As expected, the peak containment pressure increases as PCS flow rate decreases from its nominal value. Decreasing the PCS flow rate results in the following;

- The time of film application is increased.
- The heat removed from the containment to heat the cool applied PCS water is reduced.
- The amount of evaporation from the containment shell decreases.

The containment pressure increase is very modest until the applied flowrate is significantly decreased. This is because the initial decreases in applied flow only decrease the runoff flow rate, the amount of water evaporated remains constant.

7.7.2 Sensitivity to the Water Coverage Area

A sensitivity study was performed to determine the effect that the PCS water coverage area has on the AP600 peak containment pressure for a DBA LOCA as calculated by WGOTHIC. The AP600 containment Evaluation Model described in Sections 4 and 7.5 was used to perform the calculations with only one-dimensional heat conduction through the shell. The sensitivity study considered a range of sidewall water coverage fractions from 20 to 100 percent. These input coverage fractions were kept constant over the entire transient. The delivered PCS water flow rate shown in Figure 7-2 was used in each case.

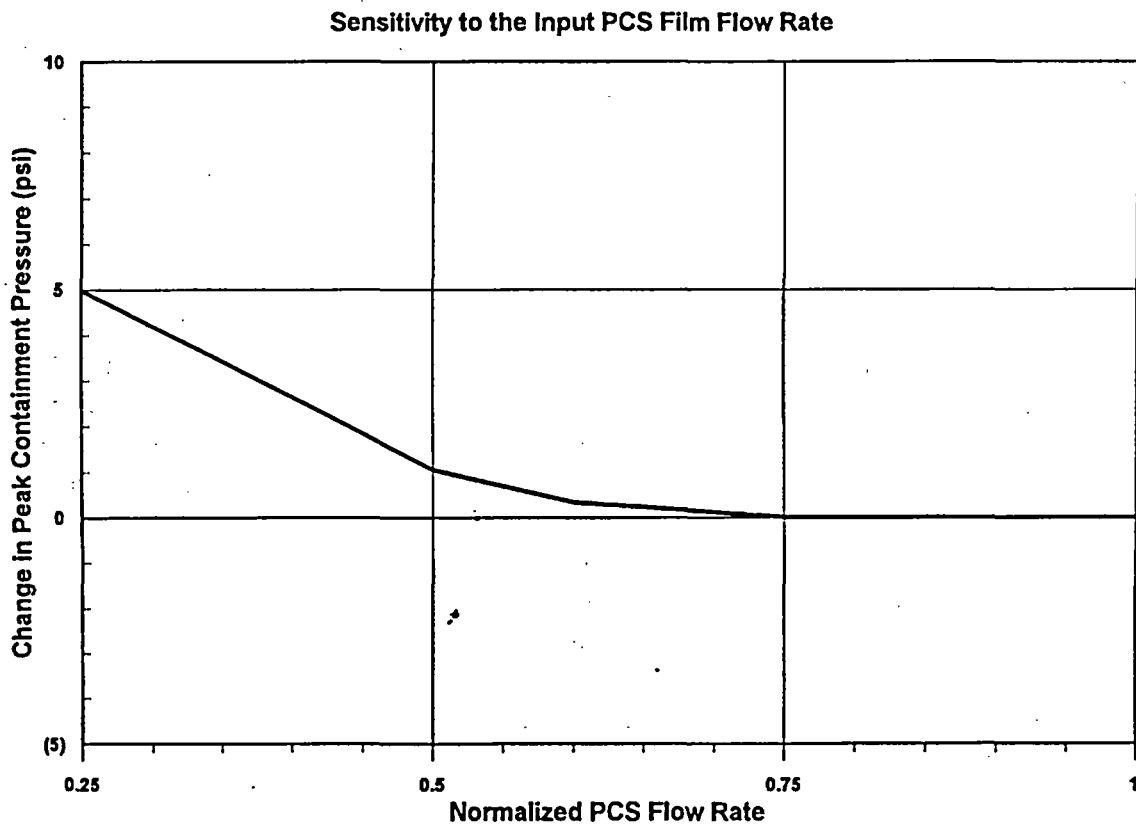


Figure 7-13 **Sensitivity to the Input PCS Film Flow Rate**

The transient pressure comparison is shown in Figure 7-14. As the water coverage fraction decreases, the peak containment pressure increases. For the 100 percent coverage case, the peak pressure is about 43 psig. The containment design pressure limit, 45 psig, is exceeded at 70 percent and lower coverage.

Decreasing the coverage fraction results in a decrease in the amount of evaporation at a given containment pressure (temperature). As the coverage fraction decreases, the reduced evaporative heat removal causes the containment pressure to increase until the evaporation rate per unit area increases sufficiently to remove enough heat to match the energy input into containment.

The transient PCS runoff flow rate is shown in Figure 7-15. The runoff flow rate is the difference between the PCS delivered flow rate and the evaporation rate. As the input coverage area decreases, the amount of evaporated water decreases and the runoff flow increases.

Figure 7-16 presents a comparison of the pressure transients for the 50 and 100 percent coverage cases to the Evaluation Model.

The level in the PCS water storage tank drops below the first standpipe at about 10,800 seconds causing a substantial reduction in the PCS flow rate (from 423 gpm to 123 gpm). For the 100 and 50 percent coverage cases, this results in a large decrease in the runoff flow rate, but no change in the evaporation rate, which is dictated by the containment pressure (temperature). Note that all the delivered water is not being used. Pressure continues to decrease, although at a slower rate in both the constant coverage cases since in both cases evaporation is removing more heat than is being released to containment. But in the Evaluation Model, the containment pressure increases when the delivered flow decreases. This occurs because the PCS film coverage model decreases the wetted perimeter, (i.e., the wetted surface area is decreased in accordance with the decrease in the applied water flow rate). The increase in pressure reflects the increase in the evaporation rate required to achieve a balance between the heat removed from and the heat input to the containment. Therefore, the Evaluation Model containment pressure approaches the same pressure as the 50 percent fixed coverage case. Pressure then begins to decrease again when the evaporative heat removed at the area dictated by the delivered flow rate exceeds the heat input.

At about 40,000 seconds, the IRWST is predicted to empty. After the IRWST empties, the flow for core cooling is provided by the sump, which is assumed to be at saturation. Since most of the internal heat sinks (except concrete) are saturated, the PCS is the primary heat sink at this time and must now absorb the energy that had previously been absorbed by sensible heat addition to the cool IRWST water. The containment pressure increases until the heat removal rate (primarily evaporation from the PCS) exceeds the heat generation rate. The pressures for all three cases remained below the 24-hour goal of 1/2 design pressure.

PCS Coverage Sensitivity

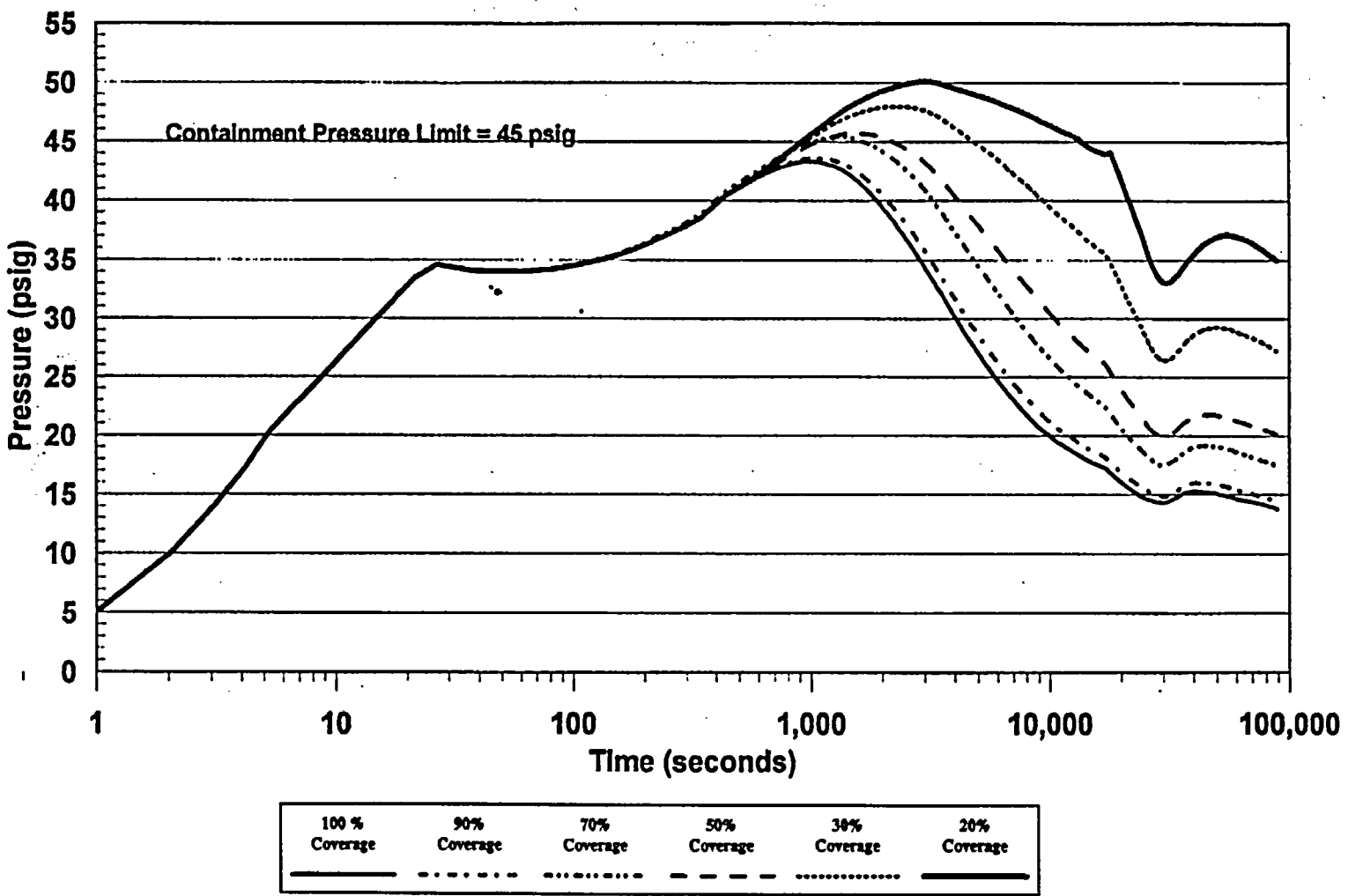


Figure 7-14 Comparison of Peak Containment Pressure as Function of PCS Coverage Area

PCS Runoff Flowrates as a Function of Coverage Area

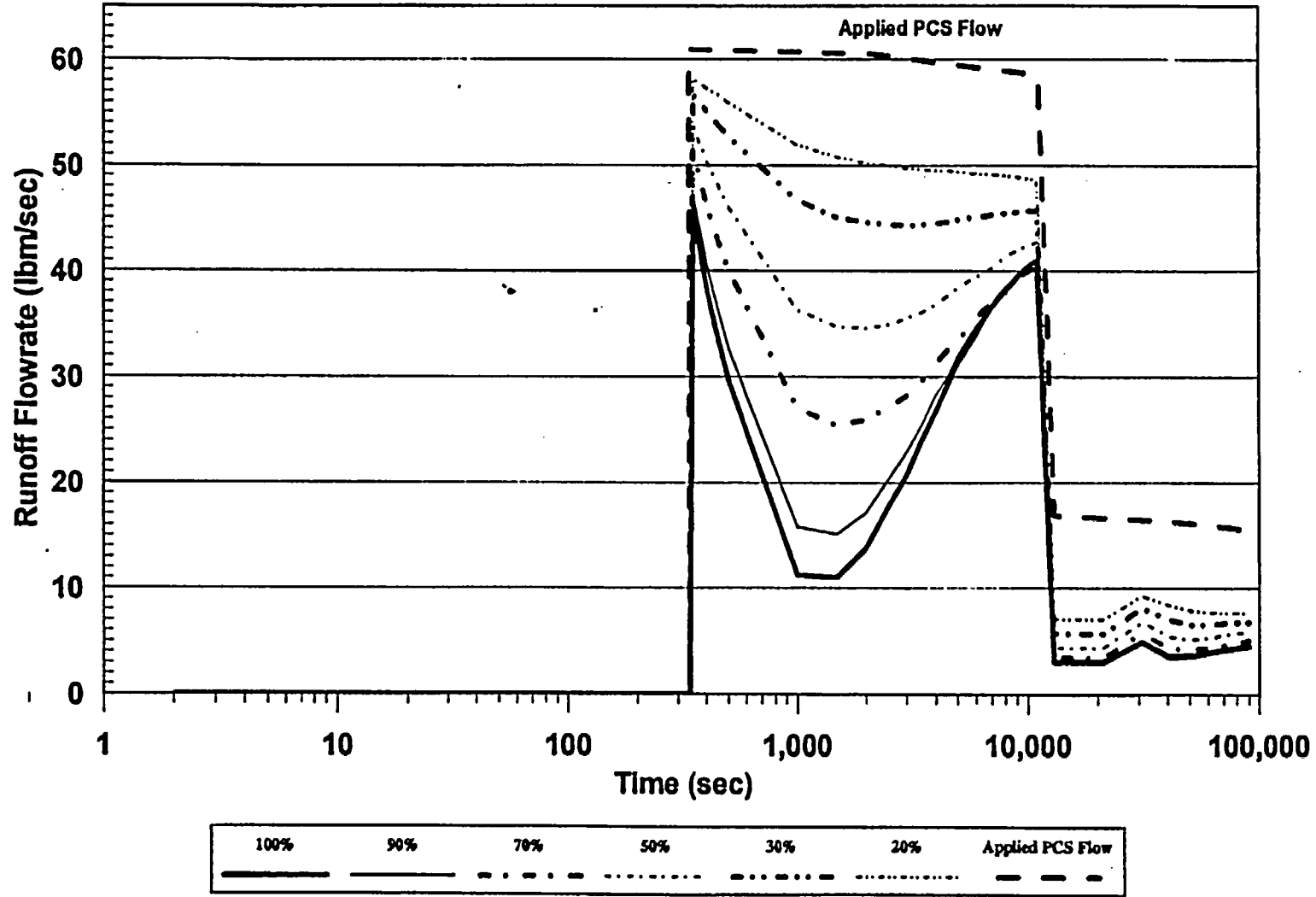


Figure 7-15 PCS Runoff Flow Rates as a Function of Coverage Area

Comparison of Evaluation Model Peak Pressure with 100% and 50% Constant Coverage Models

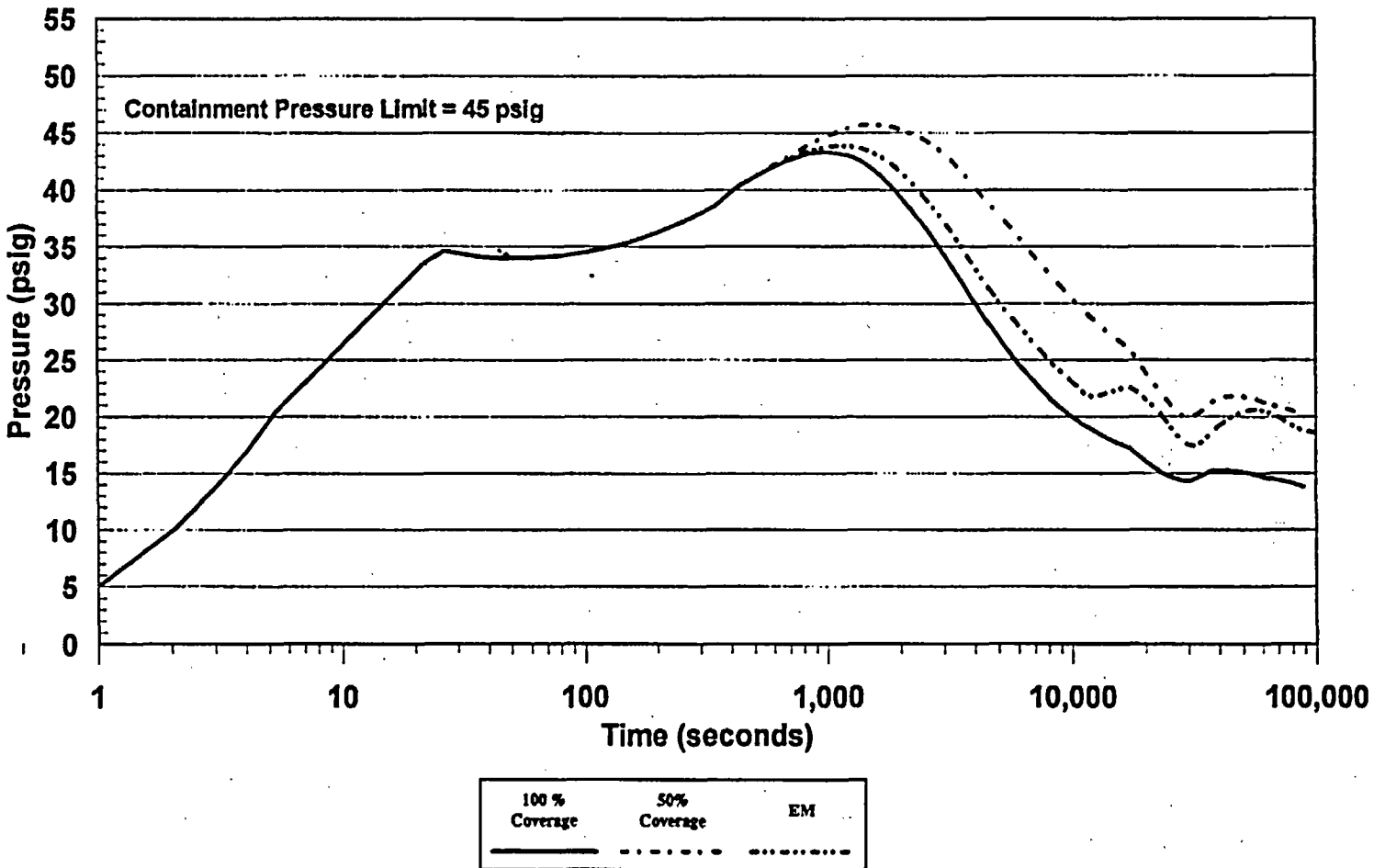


Figure 7-16 Comparison of Evaporation Model Peak Pressure with 100% and 50% Constant Coverage Models

The transient runoff flow rate for these three cases is shown in Figure 7-17. The runoff flow rate for the 50 percent coverage case is higher than the 100 percent coverage case. The lower evaporative heat removal in this case results in a sustained higher containment energy content and subsequently higher pressure. Note that there is virtually no runoff flow in the Evaluation Model case since the water coverage portion of the model limits the applied water to the amount that can evaporate.

7.7.3 Conservatism in the Assumed Time Delay for Application of the PCS Film

A delay in application of the PCS film is assumed in the DBA Evaluation Model to cover the time it takes to fill the weirs and establish steady-state coverage, as described in Section 7.2. The coverage delay time is conservative in that it neglects energy removal from the shell while steady-state film coverage is being developed. The following assessment shows the amount of conservatism in the predicted energy removal is small.

To quantify the amount of energy removal neglected during the development of steady-state film coverage, the WGOTHIC calculation used to assess the heatup of the containment shell, described in Section 7.6 was extended to 1,800 seconds. The heat removal results from this case with the water film applied at 337 seconds were compared to the results from a second case in which the assumed water coverage delay time was reduced to 35 seconds. The same input water coverage fractions were used in both cases.

Note that the WGOTHIC Evaluation Model assumes that steady-state water coverage develops instantaneously after a specified time required to fill the weirs and develop steady-state coverage. The 35-second delay case is a more realistic estimate of the film application delay time for the top of the dome, but will overestimate heat removal from the rest of the dome and sidewall. Therefore, only the heat removal from the top of the dome will be compared for the two cases to estimate the effect on heat removal.

Figure 7-18 compares the integrated energy removal rate from the top of the dome as a function of time. There is very little difference in the energy removal rates for either case. This is because the time required to significantly heat the containment external shell is much greater than the 33-second delay time for water application. Recall that, from Table 7-11, the external shell surface is calculated to heat up about 68°F after ~5 minutes when steady flow conditions develop.

The energy release difference at the lower portions of the dome and sidewalls will be even less. Therefore, the assumed water coverage delay time, although conservative, has a minor effect on containment pressure.

Comparison of Evaluation Model PCS Runoff Flow Rate with 100% and 50% Constant Coverage Models

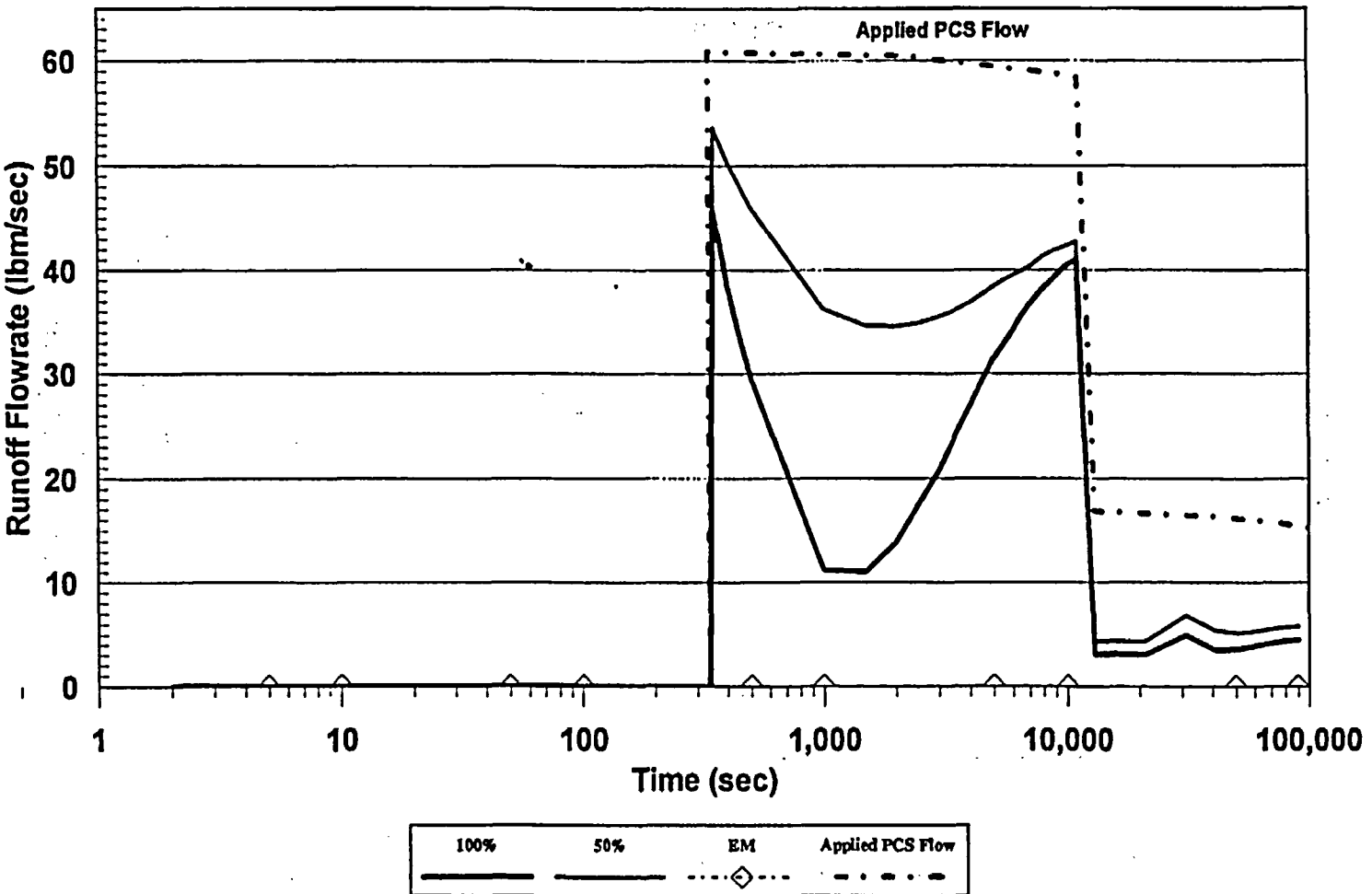


Figure 7-17 Comparison of Evaporation Model PCS Runoff Flow Rate with 100% and 50% Constant Coverage Models

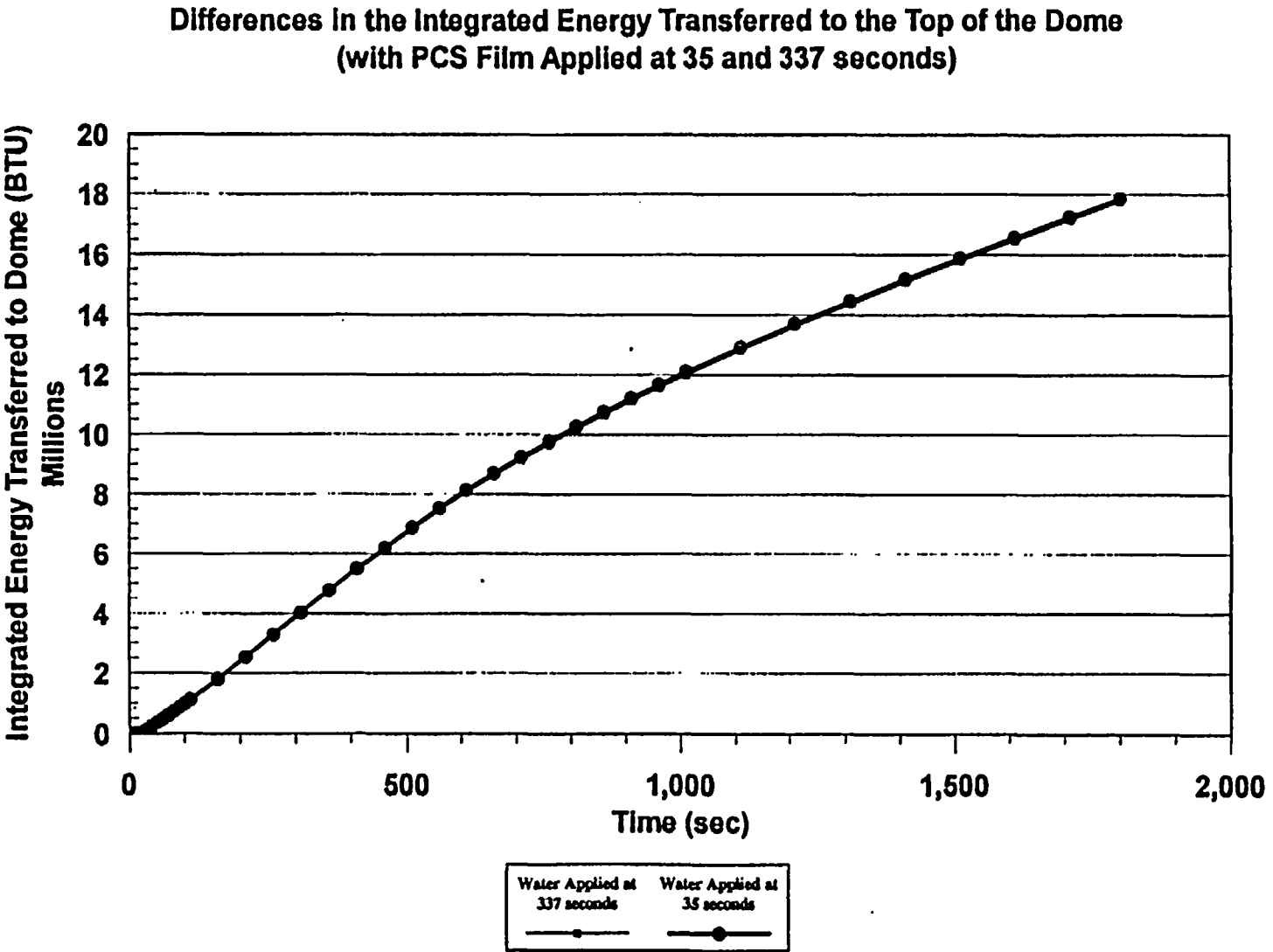


Figure 7-18 Difference in the Integrated Energy Transferred to the Top of the Dome (with PCS Film Applied at 35 and 337 Seconds)

7.8 CONCLUSIONS AND SUMMARY

The basis and calculational method used to determine the amount of water that is evaporated from the AP600 containment steel shell during the operation of the passive containment water cooling system is conservative; both with respect to the individual elements of the WGOTHIC code and the PCS film coverage model, as well as the method of combining these elements in the Evaluation Model.

The amount of water that can be evaporated is the important input parameter to the WGOTHIC portion of the Evaluation Model. The amount of water evaporated determines the effectiveness of the PCS in limiting peak containment pressure, as well as the capability of the PCS to reduce and maintain low containment pressure following postulated limiting design basis events.

The basis for determining the evaporation-limited PCS flow rate input for WGOTHIC has been developed based on PCS test data and observations, and includes the following:

- The portion of the containment shell perimeter that is wetted versus the amount of water being delivered from the PCS water storage tank to the containment dome has been based on data from the Phase 3 Water Distribution Test. This test was performed with prototypic water distribution devices on a full sized segment of the dome and top of sidewall.
- The relationship of wetted perimeter to delivered flow is conservatively bounded by the linear equation,

$$\Gamma_{\text{dist}} = \text{Delivered Flow/Wetted Perimeter}$$

where: Γ_{dist} is a constant = []^{ac} lb_m/hr-ft for PCS flow rates less than 220 gpm

The wetted perimeter used in the PCS film coverage model is limited to []^{ac} percent of the containment circumference.

- The several PCS tests performed with hot evaporating surfaces have demonstrated that the value for Γ_{dist} obtained with cold water on a cold surface conservatively bounds the Γ_{dist} that will occur with heated water on a heated surface during operation of the PCS.
- In the heat flux range of PCS operation, water streams on the containment surface are observed to become narrower in width only when most of the water in the stream has been evaporated. The Evaluation Model uses a Γ_{min} of []^{ac} lb_m/hr-ft, as the film flow rate at which water streams will become narrower. This minimum film flow rate conservatively bounds the observed minimum film flow rates observed in the PCS tests over the entire range of anticipated heat fluxes.

- Water or streams of water on the containment below the second water distribution weir ring and on the vertical containment sidewall are always observed to flow downward, following the natural fall line of the dome surface.

The calculational methods for determining the amount of water evaporated have been developed and are consistent with or conservatively bound PCS test data and observations, and include the following:

- The evaporation of water due to the conduction of heat in the circumferential direction through the containment steel shell has been calculated for the alternating, vertical, wetted and dry stripes that were observed in the PCS testing at reduced delivered water flow rates.
- The reduction in dry surface convective and radiative heat transfer that is calculated to occur with alternating, vertical, wet and dry stripes on the containment shell has been determined to be conservatively considered in the WGOthic portion of the Evaluation Model.

Bounding assumptions and conservatisms for the operational characteristics of the PCS delivering and applying water to the containment surface have been incorporated in the Evaluation Model including:

- The portion of the containment shell surface wetted by the initial delivered PCS water flow rate is conservatively assumed to be []^{ac} percent, although, at the high initial flow rate, 100 percent coverage is expected. A sensitivity study has shown that the containment design pressure will not be exceeded when only 70 percent of the containment surface is wetted. Coverage at lower flow rates is based on cold water data, which are believed to underestimate the coverage area.
- The minimum delivered PCS flow rate used in the Evaluation Model assumes the single failure of one of two parallel valves in the PCS water storage tank discharge flow path to open.
- A 337-second delay time is used to account for filling the water distribution devices and for establishing steady-state water coverage over the containment shell. No credit is taken for any containment heat removal due to heating the delivered water or due to evaporation, prior to the time when the steady-state water coverage is established.
- The temperature of the delivered PCS water is assumed to be 120°F, 5°F higher than the design basis maximum ambient temperature, to minimize the amount of containment heat removed in heating the water to the temperature at which it is being evaporated.
- The evaporation-limited PCS water flow rate calculated by the PCS film coverage model neglects the subcooled heat capacity of the runoff flow.

7.9 NOMENCLATURE

Dimensionless Groups

Biot Number:
$$Bi = \frac{\text{Convection}}{\text{Conduction}} = \frac{hL}{k}$$

Marangoni Number:
$$Ma = \frac{\text{Surface Tension Force}}{\text{Viscous Force}} = \frac{\partial\sigma}{\partial T} \frac{\delta T}{\delta L} \frac{\delta^2}{\mu\alpha}$$

Reynold Number:
$$Re = \frac{\text{Momentum Force}}{\text{Viscous Force}} = \frac{4\Gamma}{\mu}$$

Parameters

| | | |
|-----|---|---|
| g | = | gravitational constant |
| h | = | convection heat transfer coefficient |
| k | = | conductivity |
| L | = | characteristic length, |
| m | = | mass flow rate |
| M | = | multiplier representing the ratio of 2-D to 1-D heat transfer |
| q'' | = | surface heat flux |
| T | = | film temperature; |
| W | = | width of water film stripe |
| Z | = | vertical distance from top of sidewall |

Greek Characters

| | | |
|-----------|---|---|
| α | = | thermal diffusivity, |
| β | = | surface angle of inclination relative to horizontal |
| Γ | = | film flow rate = mass flow rate per unit width of film, |
| δ | = | film thickness, |
| ρ | = | liquid density |
| σ | = | liquid surface tension |
| φ | = | heat or mass flux |
| θ | = | contact angle between the surface and film |
| μ | = | liquid viscosity |

7.10 REFERENCES

- 7.1 A. T. Pieczynski, W. A. Stewart, WCAP-13884, "Water Film Formation on AP600 Reactor Containment Surface," February 1988
- 7.2 J. E. Gilmore, WCAP-13960, "PCS Water Distribution Phase 3 Test Data Report," December 1993
- 7.3 W. A. Stewart, A. T. Pieczynski, L. E. Conway, WCAP-12665 Rev 1, "Tests of Heat Transfer and Water Film Evaporation on a Heated Plate Simulating Cooling of the AP600 Reactor Containment," April 1992
- 7.4 R. E. Batiste, WCAP-14134, "AP600 Passive Containment Cooling System Integral Small-Scale Tests Final Report," August 1994
- 7.5 R. P. Ofstun and D. R. Spencer, PCS-T2R050, "Large-Scale Test Data Evaluation," May 1995, Westinghouse Electric Corporation
- 7.6 F. E. Peters, WCAP-13566, "AP600 1/8th Large-Scale Passive Containment Cooling System Heat Transfer Test Baseline Data Report," October 1992
- 7.7 F. E. Peters, WCAP-14135, Rev. 1, "Final Data Report for PCS Large-Scale Tests, Phase 2 and Phase 3," April 1997
- 7.8 D. R. Spencer, WCAP-14845, Rev. 3, "Scaling Analysis for AP600 Containment Pressure During Design Basis Accidents," March 1998
- 7.9 Frank Kreith, "*Principles of Heat Transfer*," 3rd Edition, 1973
- 7.10 M. S. Bohn and S. H. Davis, "Thermocapillary breakdown of Falling Liquid Films at High Reynolds Numbers," *International Journal of Heat and Mass Transfer*, Vol. 36, pp 1875-1881 (1993)
- 7.11 F. Delose, R. P. Ofstun, D. R. Spencer, WCAP-14326, Rev. 2, "Experimental Basis for the AP600 Containment Vessel Heat and Mass Transfer Correlations," April 1998, Westinghouse Electric Corporation
- 7.12 T. Fujita and T. Ueda, "Heat Transfer to Falling Liquid Films and Film Breakdown Parts I and II," *International Journal of Heat and Mass Transfer*, Vol. 21, pp. 97-108 and 109-118 (1978)

APPENDIX 7A

PHYSICS OF LIQUID FILMS ON THE AP600 AND AP1000 CONTAINMENT SHELLS

TABLE OF CONTENTS

7.A.1 INTRODUCTION 7.A-2

7.A.2 SUMMARY OF GENERAL LIQUID FILM BEHAVIOR 7.A-3

7.A.3 CONTACT ANGLE AND SURFACE WETTABILITY 7.A-8

7.A.4 DESCRIPTION OF LST OBSERVATIONS 7.A-14

7.A.5 CONCLUSIONS 7.A-19

7.A.6 REFERENCES 7.A-20

LIST OF TABLES

Table 7.A-1 Summary of Test Results to Determine Static Contact Angle 7.A-12

LIST OF FIGURES

Figure 7.A-1 Variation in Surface Tension Over the Surface of a Heated
Liquid Film 7.A-6

Figure 7.A-2 Typical Qualitative Contact Angles for Advancing and Receding
Contact Lines 7.A-10

Figure 7.A-3 Sketch of Qualitative Wavy Laminar Film Flow Characteristics on
Heated LST Shell Water Stripe 7.A-15

Figure 7.A-4 Large-Scale Test Water Coverage Pattern at High PCS Flows 7.A-17

Figure 7.A-5 Sketch of LST Observation of Vessel Exterior at Water Flows
Similar to LST 213.1 Showing Complete Dryout of Some Stripes 7.A-18

7.A.1 INTRODUCTION

The total evaporation from the external shell is the parameter of interest for mass transfer, the dominant means of removing heat from the containment. Total evaporation is equal to the integral of the mass flux over the covered, or wetted, area. The mass flux for a given set of parameters (surface and film temperature, film flow rate, annulus conditions) is given by correlations presented in Reference 7.A.1. The subject of this appendix is the wetted area of the external shell surface, and how the wetted area is limited by film stability effects.

Note that the initial application of water to the external surface at safety analysis basis surface temperatures is discussed in Section 7.6.5, so that quasi-steady water coverage is assumed to be established in the discussions of this appendix.

The introduction and Section 7.2 provide a brief overview of the PCS design, as it relates to film stability considerations. The test program is discussed in Section 7.6, where it is shown that the range of nondimensional parameters for AP600 and AP1000 is adequately covered in the test program. Subsequent Appendix 7A sections give a summary of literature findings on film stability, a discussion of the contact wetting angle that addresses the wettability of the coated surface in the context of surfaces studied in the literature, and a description of LST observed liquid film behavior for high and low flow tests. The physics summarized in this appendix were considered in the development of the PCS film coverage model. The PCS film coverage model is biased to conservatively bound test data that include cold full-scale tests and smaller-scale heated surface tests.

The double dam-weir system is designed to evenly distribute the PCS water onto the surface of the dome. The elliptical shape of the dome and corresponding area divergence helps spread the stripes of water flowing from the individual V-notches in the weirs. Water coverage on the top of the dome is the most difficult to quantify, but water coverage on this portion of the dome is also the least important to the successful operation of the PCS; the area between the top of the dome and the second weir is only about 20 percent of the total shell external surface area and is neglected in the PCS film coverage model calculation of the evaporation-limited PCS flow rate input for the WGOTHIC model.

The distribution system applies water to the shell in discrete, evenly spaced streams. Water from the PCCWST discharge header falls into a bucket suspended just above the center of the dome. Slots on the side of the bucket allow water to spill at discrete locations around the circumference onto the containment dome. From there, the water flows outward and downward, spreading due to the area divergence, until it is collected and redistributed by a series of two weir rings. Weir outflow rates as a function of time, including the initial filling of the bucket and dams, are shown in Figure 7-3. The method of water application, by weir slots, induces discrete water streams that can remain discrete at low PCS water flow rates and merge to form continuous circumferential water coverage at higher PCS water flow rates.

The initial application of water flowing from a weir slot hits the surface and spreads until surface tension and skin friction dissipate the momentum. If the film is significantly subcooled relative to the surface at that point, thermocapillary effects (see Section 7.A.2.2) may also affect how wide the stripe is as it flows down from the point of application. The PCS water distribution system employs two weir rings on the dome. By the time the water exits the second weir ring, the water has been heated to a temperature relatively close to that of the shell, so that thermocapillary effects are less important. Therefore, the focus for film stability is on evaporating film stability.

Evaporation of the PCS water results in a reduction of the mass flow rate as the film advances down the containment structure from the second weir. As the mass flow rate decreases, the wetted perimeter of the stable film also changes. From observation of tests, the wetted perimeter typically decreases only after the mass flow rate decreases below a certain point. The physical processes that limit the amount of stable film coverage on the containment shell are discussed in this appendix.

7.A.2 SUMMARY OF GENERAL LIQUID FILM BEHAVIOR

This section provides a summary of available literature on models and data for liquid films and provides a discussion of the various aspects of liquid film behavior.

7.A.2.1 Literature Summary

The study of movement in a fluid interface has been studied over 150 years. In studying the spreading of a drop of alcohol on the surface of water, British engineer and physicist James Thompson correctly explained the phenomena as a surface-tension-driven flow. The name of Italian physicist Carlo Marangoni has been associated with two distinct but related surface effects. The first is motion in a fluid interface caused by local variations in interfacial tension which were, in turn, caused by differences in composition or temperature. The second phenomenon is a conjugate of the first; it is the departure from equilibrium surface tension that is produced by the extension or contraction of an interface. Both of these phenomena are important to the understanding of the behavior of liquid films.

The stability of liquid films has been studied by many analysts and experimenters within the last 50 years. These studies may be grouped in two general categories;

1. Determining the minimum flow rate required to rewet a stable dry patch.
2. Examining the thermocapillary breakdown of a thin film.

Films are generally categorized as saturated films or subcooled films, due to differences in stability, or wetting performance. Films that are applied at or near the temperature of the surface are typically referred to as "saturated films." Such films, when applied to heated surfaces as is done on AP600 and AP1000, have a significant evaporation component and are thus called "evaporating films." Norman and McIntyre (Ref. 7.A.2) reported data showing that a large increase in the minimum film wetting rate was required as the temperature difference between the surface and film was increased (that is, subcooling of the liquid film relative to the surface was increased). Hallet (Ref. 7.A-3) also observed this phenomenon and developed a film breakdown correlation that was related to the film surface tension difference, the wave number, and the heat transfer coefficient. Fujita and Ueda (Ref. 7.A-4) measured the breakdown of both subcooled and saturated liquid films on heated, vertical, polished, stainless steel tubes. A comparison of the results from their tests also showed that the highly subcooled films are unstable at flow rates several times higher than that observed for saturated films. More recently, Bohn and Davis (Ref. 7.A-5) measured the breakdown of subcooled water films on heated, vertical, polished, stainless steel tubes and developed a film breakdown correlation that was dependent on thermocapillary effects. Thus, there is clearly a basis for separately considering film stability for subcooled and evaporating films.

The conclusion that thermocapillary effects influence the early breakdown of subcooled films is based on the following. Subcooled films having liquid temperatures much lower than the solid surface temperature absorb heat, causing the film temperature to increase. Evaporating films that are more nearly in thermal equilibrium with the solid surface, transfer mass and energy from the film surface to the gas atmosphere. Thus, one explanation for the apparent reduced stability of subcooled films is the existence of significantly higher temperature gradients through the film that give rise to increased thermocapillary forces (see Section 7.A.2.2).

The manner in which data has been presented in the literature is also of interest. In general, the surface heat flux is recognized as the dominant independent parameter, and properties have a strong influence on film behavior. The literature presents data most often as film flow rate (mass flow rate per unit wetted perimeter) versus heat flux. To account for the effect of viscosity on wettability, the Westinghouse test data reduction uses film Reynold's number as the dependent parameter, with surface heat flux as the independent parameter.

The performance of the coated surface to be used for AP600 and AP1000 can be compared to the performance of the typical surfaces studied in the literature, polished steel and polished copper. The use of polished materials in laboratory tests allows careful characterization of the important parameter, the wetting angle. The coated surface does not lend itself to characterization of a single local wetting angle (Section 7.A.3.2). Therefore, the data for film flow rate versus heat flux give an appropriate means of comparison of film stability data. Stable film flow rates on the order of 20 to 50 lb_m/hr-ft are noted on the LST and other test surfaces, even with heat fluxes up to 10,000 Btu/hr-ft². Comparison to Fujita-Ueda data shows that the coated surface is significantly better at wetting, and is less sensitive to heat flux than the polished surfaces.

The list of papers reviewed and considered for application to the containment Evaluation Model is extensive and will not be given here. However, in a summary article (Ref. 7.A-6), Bankoff provided an extensive list of relevant papers. The current state of the art is focused on the "moving contact line," which was also considered for application to the containment Evaluation Model, but is generally not very practical for engineering application.

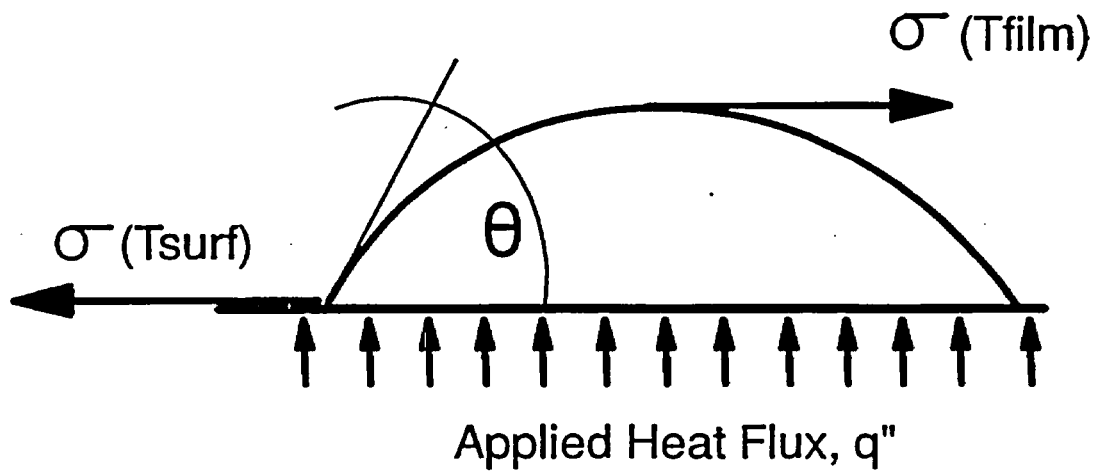
7.A.2.2 Thermocapillary Effect

Based on discussions with Bankoff (Reference 7.A-8), the thermocapillary effect is a result of the variation of surface tension with temperature in moving from the contact line to the free film surface (see Figure 7.A-1). For a stable stripe shape, the forces in the horizontal direction must sum to zero. The surface tension decreases as temperature increases, so the minimum stable film flow rate has to be greater to prevent the hotter liquid at the surface from causing the film stripe width to contract. The thermocapillary effect on the force balance is sometimes estimated (as in equation 7.A-2) by replacing the actual $\sigma(T)$ function with a much simpler function using the temperature drop through the film which can be related to the heat flux as

$$\sigma_{\text{surf}} - \sigma_{\text{film}} \approx \sigma_{\text{surf}} - \left(\sigma_{\text{surf}} + \frac{d\sigma}{dT} \Delta T_{\text{film}} \right) \approx - \frac{d\sigma}{dT} \frac{q''}{k_{\text{film}}} \quad (7.A-1)$$

This simplification becomes increasingly inaccurate as the film subcooling increases, since the sensible temperature increase of the film invalidates the approximation q''/k , used to estimate the film surface temperature.

Overall, investigators have identified momentum, surface tension, body (hydrostatic) force, thermocapillary, and vapor thrust as the dominant forces affecting film stability. These forces are typically expressed as functions of flow rate, heat flux, fluid properties, and wetting angle. Vapor thrust can be neglected in AP600 and AP1000 because the heat flux is low, less than 10,000 BTU/hr-ft². Consequently, film stability may be considered to be controlled by a balance between momentum, surface tension, hydrostatic, and thermocapillary forces.



$$T_{\text{surf}} > T_{\text{film}}$$

$$\sigma_{\text{surf}} < \sigma_{\text{film}}$$

Figure 7.A-1 Variation in Surface Tension Over the Surface of a Heated Liquid Film

7.A.2.3 Available Theoretical Analytical Models

The available analytical theoretical models have not been found to be practical for determining the film coverage on the passive containment design. Rather, the Evaluation Model includes a film coverage model that is consistent with the physics of liquid films, and is developed to provide a conservatively bounded total water coverage. However, models proposed in the literature can be used to gain insight into film behavior.

The Zuber-Staub model (Ref. 7.A-7) considers the stability of a dry patch located within a uniform, flowing film, i.e., the inability of the liquid film to rewet the dry patch. The mathematical formulation of the model includes three of the dominant terms identified above: momentum, surface tension, and thermocapillary. The model uses a vertical force balance at the tip of a postulated dry patch to determine the minimum uniform film thickness required to rewet the dry patch. This minimum film thickness is a function of the surface heat flux, the film properties (including the contact angle between the film and surface).

One of the Zuber-Staub formulations treats the film thickness as the dependent parameter from which film stability criteria can be derived. Although film thickness is not easily measured, film thickness is related to the film flow rate through continuity. Therefore, the discussions that follow will treat the film flow rate as the controlling parameter from which film stability criteria may be derived.

According to the Zuber-Staub model, if the film flow rate is greater than the minimum stability value, any dry patch created in the film would be washed over and would readily disappear after formation due to the momentum of the flowing film. Conversely, if the film flow rate was equal to or less than the minimum stability value, a dry patch, if formed, would be predicted to be stable (i.e., the film would not be able to recover the dry patch). The Zuber-Staub model does not consider the effects of waves in recovering the dry patch.

The concept of a force balance can be used to develop insight into controlling parameters for film stability. A force balance more specific to the passive containment design that includes momentum, surface tension, thermocapillary, and body forces (and thus, surface inclination angle, β) to account for spreading on the inclined surface of the elliptical dome, but neglects the vapor thrust term, may be written in terms of the film flow rate, Γ . Since the relationship is for a stable film width, equilibrium between the various forces is assumed. If the film flow rate is greater than the value of Γ in the equation, the film will wash over any dry patch which happens to form. The equation, which can be used to examine the minimum stable film flow, Γ_{\min} , is:

$$\frac{1}{15} \left[\frac{9g \sin\beta \Gamma_{\min}^2}{\rho\mu} \right]^{\frac{2}{3}} + \left[\frac{3\rho g^2 \cos^3\beta \mu \Gamma_{\min}}{8 \sin\beta} \right]^{\frac{1}{3}} = \frac{\sigma(1-\cos\theta)}{\left[\frac{3\mu\Gamma_{\min}}{g \sin\beta \rho^2} \right]^{\frac{1}{3}}} - \frac{d\sigma}{dT} \frac{q''}{k} \cos\theta \quad (7.A-2)$$

Note that the formulation given above assumes a laminar film with uniform film thickness and does not consider the effect of waves in wavy laminar flow. Waves in wavy laminar flow typically have a peak to valley distance of about 3 times the average film thickness, but occupy only a small fraction of the flowing volume. Waves carry momentum as they pass, but do not significantly affect the calculated average film thickness. Waves will wash through the region of flowing film, effectively wiping out any history effect of the method of application or other upstream effects. Therefore, film stability can be considered to be a local phenomenon, governed by local force balances at the point of interest on the contact line.

Equation 7.A-2 predicts higher values for the minimum stable film flow rate on surfaces that wet poorly, that is, those that have large contact angles, than for surfaces that wet readily. For surfaces that are heated, heat flux is destabilizing. The equation also shows that as the film heats up, it becomes more stable due to property changes.

Since the theoretical models available in the literature are not practical for determining the film coverage on the passive containment design, the insight gained from examining those approaches is used to support development of an empirical bulk coverage model. That is, the film stability can be characterized using a criterion for a minimum film flow rate, Γ_{min} , that will maintain a stable stripe. Data from tests at different scales, wherein the range of AP600 and AP1000 dimensionless parameters is sufficiently covered, can be used to empirically derive a bounding value for Γ_{min} . As discussed in 7.A.2.1, data can be represented using the film flow rate, and plotted against the dominant independent parameter, heat flux.

7.A.3 CONTACT ANGLE AND SURFACE WETTABILITY

A discussion of contact angles in general and observations from test coupons are provided to gain insight into the performance of the coated surface relative to surfaces in the literature. Finally, factors which can affect surface wettability are discussed.

7.A.3.1 Advancing and Receding Contact Angles

The place where the wet and dry regions intersect is called the contact line. For example, in a liquid film flowing down a wall in a constant width stripe, the contact lines are the two vertical lines defining the width of the stripe. The contact angle is defined as the angle between the solid and the liquid surface at the contact line. The contact angle between a water film and the surface to which it is applied is an indication of the surface wettability. Typically, better wetting occurs on surfaces with small contact angles. In practice, contact angles are measured for both advancing and receding films. Usually the two values are quite different, with the advancing contact angle being much larger than the receding contact angle. The relation between contact angle and velocity is qualitatively depicted in Figure 7.A-2. Of interest is the hysteresis between advancing and receding contact angles. There is actually a range of stable contact angles for a static contact line. Thus, if a droplet starts out by spreading, such as when it is dropped onto the surface, it will spread to a diameter governed by the advancing contact angle. Then as the droplet evaporates, it may be expected to remain at a constant diameter, with the contact line anchored, until the mass lost contracts the

droplet such that the receding contact angle is reached. Further evaporation would then cause the droplet diameter to decrease.

It is general practice to measure contact angles of a liquid on a smooth or polished surface, such as glass or polished steel having surface profiles measured in microns. High magnification is used to measure the contact angle as it meets the surface. The surface on the external containment shell is an inorganic zinc coating applied on a carbon steel structure. The surface of the inorganic zinc coating is not smooth, having a surface profile of several mils. With a surface profile of several mils, the magnified image shows significant peaks and valleys, making it impossible to measure a single contact angle that is applicable over the entire surface. Thus, the significance of a representative contact angle for the organic zinc coating used for the exterior of the containment shell is diminished. The interest is on bulk coverage performance over a large surface area, so larger scale integral tests are used. It is desired, however, to understand and relate the bulk wetting performance of the coated surface to that of surfaces in the literature. Therefore, measurements were taken to characterize a bulk static contact angle on the prototypic surface by observing a drop on sample coupons under various conditions as described below.

7.A.3.2 Static Contact Angle Measurements of Coated Surface

The bulk contact angle for a drop of water was measured as a function of temperature and age of the surface coating selected for the AP600 and AP1000. Two samples were prepared for these measurements. The first test coupon was supplied to Westinghouse by the coating vendor. This sample was prepared by the vendor and was not subjected to weathering. The second sample was a 12-in² section of a steel plate that was painted by Westinghouse and weathered for two years.

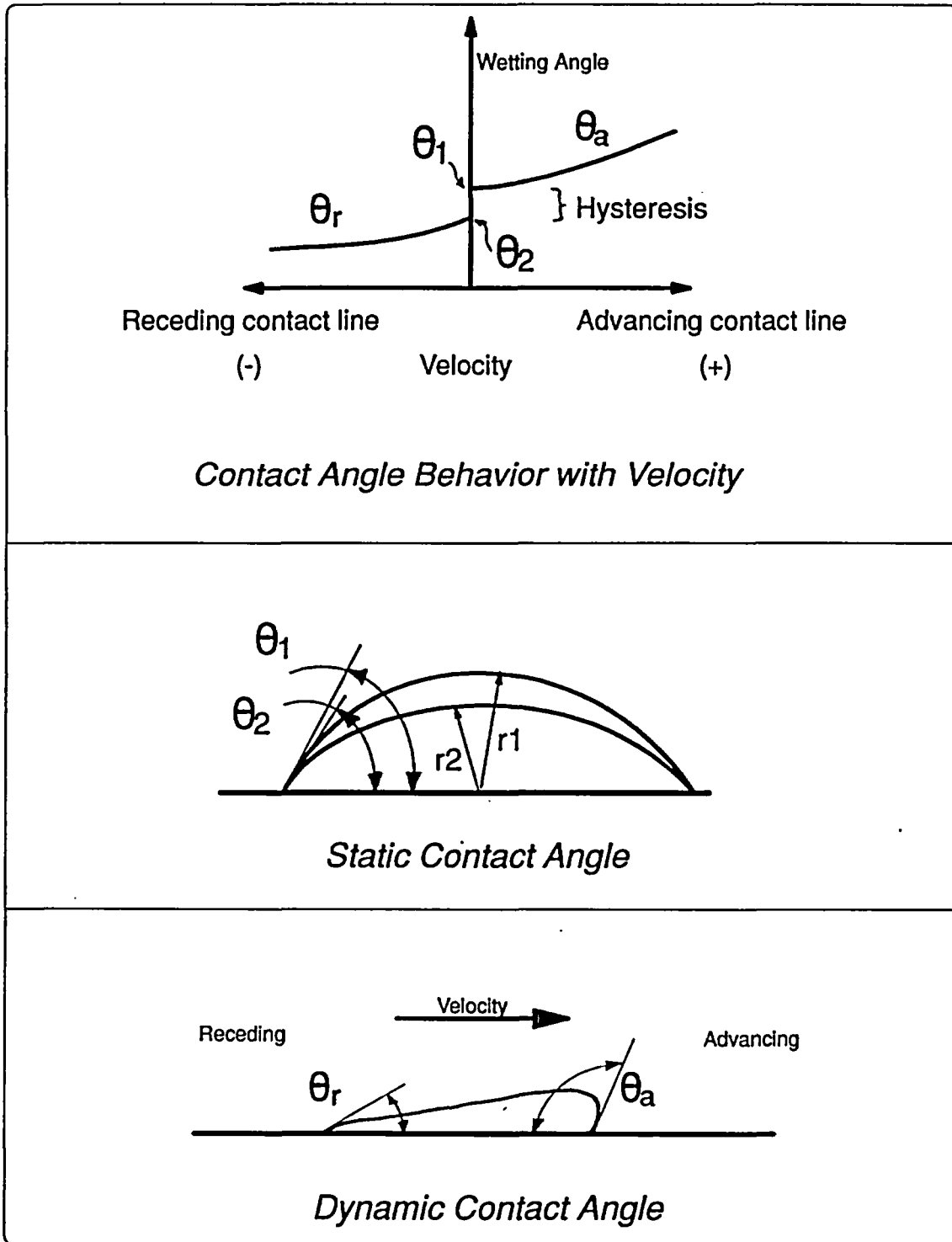


Figure 7.A-2 Typical Qualitative Contact Angles for Advancing and Receding Contact Lines

The following procedure was used to determine the static contact angle for both samples at ambient conditions:

- The test coupons were cleaned per coating vendor specifications and dried.
- The test coupon was placed in a horizontal position.
- A drop of water was placed on the test coupon.
- Using an optical comparator, the average angle between the sample surface and the drop at the interface.
- Measurements were repeated using several drops to ensure repeatability and consistency in the measurements.

Additional measurements were taken with the test coupons held at different temperatures. This was done to evaluate the effect of the surface temperature on the contact angle. The test coupons were heated with either hot water or a heat gun.

The static contact angle measurements taken are summarized in Table 7.A-1. They show that the contact angle for inorganic zinc coated surface decreases both with an increase in age and an increase in temperature. At high temperatures, the contact angle was observed to be initially larger than that observed for lower temperatures. It was observed, however, that the drops quickly spread and flattened out to a quasi-steady shape, thereby reducing the measured contact angle.

From the measurements listed in Table 7.A-1, it is concluded that a representative bulk or average contact angle for the inorganic zinc coated containment shell surface is between [][°] for a new surface, and between [][°] after just two years of weathering.

| | | |
|--|--|--|
| | | |
| | | |
| | | |
| | | |
| | | |
| | | |
| | | |
| | | |
| | | |
| | | |

a,c

A small drop of water spread around on the inorganic zinc-coated surface was not observed to contract, or snap back into a drop. This observation indicates that the receding contact angle for this surface is nearly zero. These observations also suggest that the film breakdown to form a dry spot occurs at a lower film Reynolds number than the critical Reynolds number for rewetting.

Static wetting angle measurements indicate that the coated surface is clearly more wettable than surfaces reported in the literature, and based on the force balance it is expected to be less sensitive to heat flux.

7.A.3.3 Relative Magnitude of Surface Tension Effects

A solid surface will be wet with liquid if the free surface energy of the solid is greater than the free surface energy of the liquid. Surface tension, σ , is defined as the work required to expand the surface of a liquid by a unit of area. It is a measure of the strength of the intermolecular forces in the fluid, similar to the latent heat of vaporization.

Hydrogen bonding is the strongest type of intermolecular force. Liquid water has relatively strong intermolecular forces due to the strong hydrogen bonds; 80 percent of the intermolecular attraction in water is attributed to hydrogen bonding. In a water molecule, the electrons spend more time in the vicinity of the oxygen atom than the hydrogen atoms because oxygen is more electro-negative than hydrogen (3.5 versus 2.1 for hydrogen on a scale of 4.0). This results in an electric dipole within the molecule. For this reason water is said to be a polar molecule.

As its temperature increases, the mean spacing between molecules in a liquid increases, causing the density to decrease and a reduction in the intermolecular forces. Therefore, both surface tension, σ , and the latent heat of vaporization, h_{fg} , decrease with increasing liquid temperature. For example, the surface tension of water is about 4.97×10^{-3} lbf/ft and the latent heat of vaporization is about 1054 BTU/lbm at room temperature. The value of these two parameters decreases to 4.0×10^{-3} lbf/ft and 970 BTU/lbm, respectively, at 212°F.

7.A.3.4 Factors Affecting Surface Wettability

The wetting of a solid surface by water is improved by reducing the surface tension of the water (by use of a wetting agent such as a detergent), by making the surface more porous (to improve the spreading by capillary action), or by using a polar surface (increasing the intermolecular forces between the surface and the polar liquid water). The use of a surfactant was examined during the Water Distribution Tests. It was found that surfactants offered no effective improvement in coverage. This has been postulated to be due to the turbulence of the flowing film which would not allow the surfactant to influence the surface of the film significantly. The porosity of the inorganic zinc coating is believed to be the primary factor affecting wetting early in the coating's life, adding a significant capillary effect at the contact line. It was postulated that the buildup of polar molecules (e.g., oxides of zinc) on the solid surface improved its wettability with age. Photographs were taken of both new and weathered surface coating samples using a scanning electron microscope with an energy dispersive X-ray spectrometer to identify the chemical species present on the surface. More oxides of zinc were found on the weathered surface than the new surface, supporting the hypothesis that the increase in wetting is due to the surface becoming more polar as it ages.

A buildup of some surface contaminants can result in a reduction in wettability. The worst surface contaminant for the inorganic zinc coating is silicone; it has both low surface energy and low polarity. Sources of silicone in air pollution are rare. Other surface contaminants that could result in reduced wetting include hydrocarbons such as oils, members of the PTFE family (Teflon), polypropylene, and polyethylene residues. To combat surface contaminants, the coatings vendor has developed and made available a standard cleaning procedure and a specially developed detergent that emulsifies these types of surface contaminants so they can be washed away.

Although the number of potential contaminants that would adversely affect wetting of the inorganic zinc coating surface is probably limited to a dozen or so, it would be very difficult to analytically predict the wetting degradation over time. The degradation of surface wettability would have to be estimated as a function of the concentration of each potential contaminant, the deposition rate of each as a function of the local or worst case atmospheric conditions, and the assumption that the degradation is additive, etc. Therefore, periodic in-service inspections will be performed to look for corrosion and surface contaminant buildups to assure surface wettability. The frequency and procedures for testing and the minimum acceptance criteria prior to cleaning the surface are defined in the Reliability Assurance Program.

7.A.3.5 Summary of Wetting Angle Assessment

The contact angle between a water film and the surface to which it is applied is an indication of the surface wettability. Although the surface provided by the inorganic zinc coating applied to the external surface of the containment is not smooth relative to other materials used to measure contact angles such as glass or polished steel, measurements were taken to characterize a bulk static contact angle of a spreading film on the prototypic surface to relate to literature data. The static angle was measured by observing the spreading of a drop on two coupons, one weathered and one not weathered, under ambient and heated conditions. Results showed that a surface weathered for two years is significantly more wettable []^{a,b} than surfaces for which data exists in the literature (in the range of 60 degrees).

7.A.4 DESCRIPTION OF LST OBSERVATIONS

LST observations to characterize wetting behavior were made during shakedown tests, video tapes were recorded, and sketches were made for the test records. During these shakedown tests, quasi-steady heat flux and water flow rate conditions were achieved, and then water flow was slowly valved down in stages with constant steam flow. At each stage, when quasi-steady conditions again were reached, observations and notes were taken. Subsequent similar cycles were done at several steam flows (heat fluxes). The objective was to observe the behavior of the liquid film as it varied from a moderately high flow down to nearly complete evaporation. Since the majority of the LST matrix tests were run with a high flow rate, the qualitative discussion starts with a description of water coverage on a high flow test. Finally, the water coverage on a low flow test is described. Observations are consistent with the physics of liquid films discussed above.

7.A.4.1 High Flow LST

As discussed in Section 7.6.3, the water is applied to the shell in stripes around the circumference of the test vessel. Stripe widths for a given steady state test were relatively constant, varying by fractions of an inch as the delivered flow rate varied (see Section 7.6.3). Based on Reynolds number, the flow regime is wavy laminar, which has been confirmed by test observations. The wavy laminar regime is discussed in the literature. A simple sketch is provided in Figure 7.A-3, showing qualitative characteristics observed for a representative film stripe on a heated LST surface with a high flow rate. High flow rate LST typically exhibited constant width stripes, as discussed further below. Stripe widths varied from an inch or an inch or less to complete circumferential coverage, depending on the test delivered flow and heat flux. Within a stripe, the majority of the width is flowing water with wavy laminar conditions. In that portion, waves are generated by upstream disturbances and advance down the stripe with a velocity faster than the average film speed, consistent with continuity flow theory. The waves generally alternate with slight left and right horizontal velocity components.

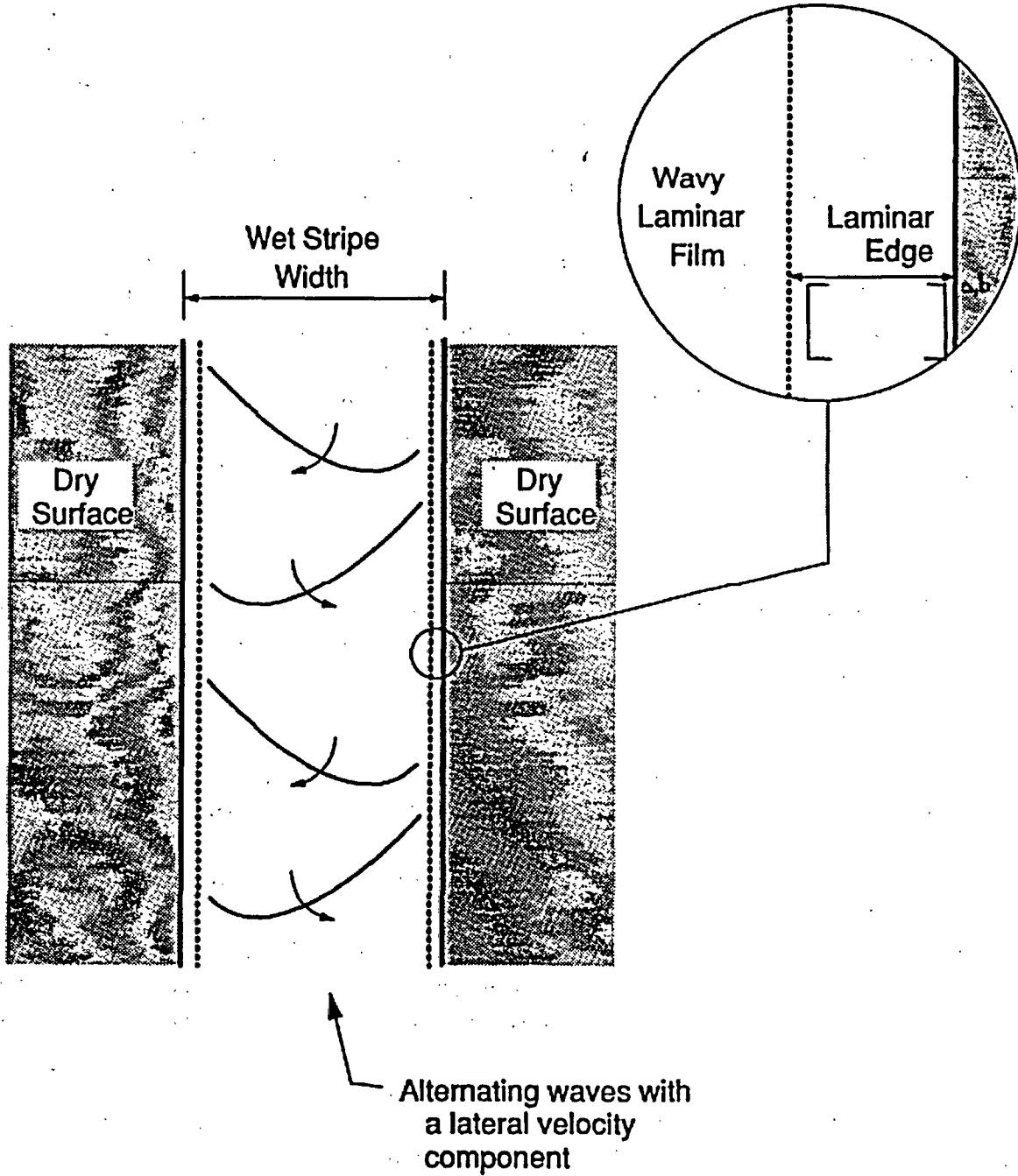


Figure 7.A-3 Sketch of Qualitative Wavy Laminar Film Flow Characteristics on Heated LST Shell Water Stripe

Water stripe edges exhibited a narrow []^{a,b} region of laminar flow. Visual observation indicated that the edges were wetted but not obviously flowing. When an obstruction was placed within a wet edge, a "bow wave" built up above the obstruction, confirming that indeed liquid was flowing downward in that region. The film flow, and thus thickness, in that region is small enough that viscous forces damp out any disturbances. For example, the waves are damped by viscous forces in the stripe edge. Note that the laminar edge was also observed to occur on stripes which narrowed as their film flow rates decreased due to evaporation. This indicates that there is a very thin layer near a stripe edge, or in fact the equivalent wetting angle at the contact line is very small. This is consistent with the consideration in 7.A.3 that the receding wetting angle likely governs film stability of an evaporating stripe on the containment shell.

Since the water is applied as stripes at the dome with J-tubes (see Figure 7.A-4), and there is significant liquid film subcooling over much of the LST dome for high flow tests, the width of stripes that reach the vertical sidewall is less than can be supported by a stable film at the given film flow rate. Therefore, it can be postulated that the initial width at the top of the vertical sidewall is sufficiently greater than the evaporating film stability limit and that evaporation from the stripes does not cause the receding contact angle to be reached. Rather the film stripes in high flow LST tests are believed to remain within the region of hysteresis over the entire height, consistent with the observed constant width stripes.

7.A.4.2 Low Flow LST

Figure 7.A-5 shows a composite of typical film characteristics on a portion of the LST shell at relatively low flows typical of the water flow applied to LST 213.1. The tests described here have film flows that are low enough that evaporation causes the receding contact angle to be reached, and further evaporation leads to narrowing of the stripes.

As for the high flow LST, the water is delivered to the vessel shell surface via J-tubes, as a subcooled film. The application method and subcooled film stability set the initial stripe width, similar to the high flow tests. However, the film heats up to become an evaporating film before it reaches the sidewall. Observations were made of shakedown tests at conditions (steam flow, external water flow) similar to those for LST 213.1. During the initial setup prior to heating the vessel, the film flow was established and gradually valved down. As very low flows were reached, some J-tubes were seen to stop delivering water before others, indicating that there was some asymmetry in delivered flow per stream. This is consistent with observations of heated tests that indicated stripe widths and vertical extents varied around the circumference of the vessel.

In Figure 7.A-5 the width of the two outer stripes shown remain approximately constant down to a certain elevation, varying only as the delivered flow rate varied. At some elevation on the sidewall, which may be different for different stripes, the film width began to narrow until the gutter was reached.

For some stripes, shown as the two innermost stripes in Figure 7.A-5, the delivered flow was low enough that the stripes completely evaporated before reaching the gutter elevation.

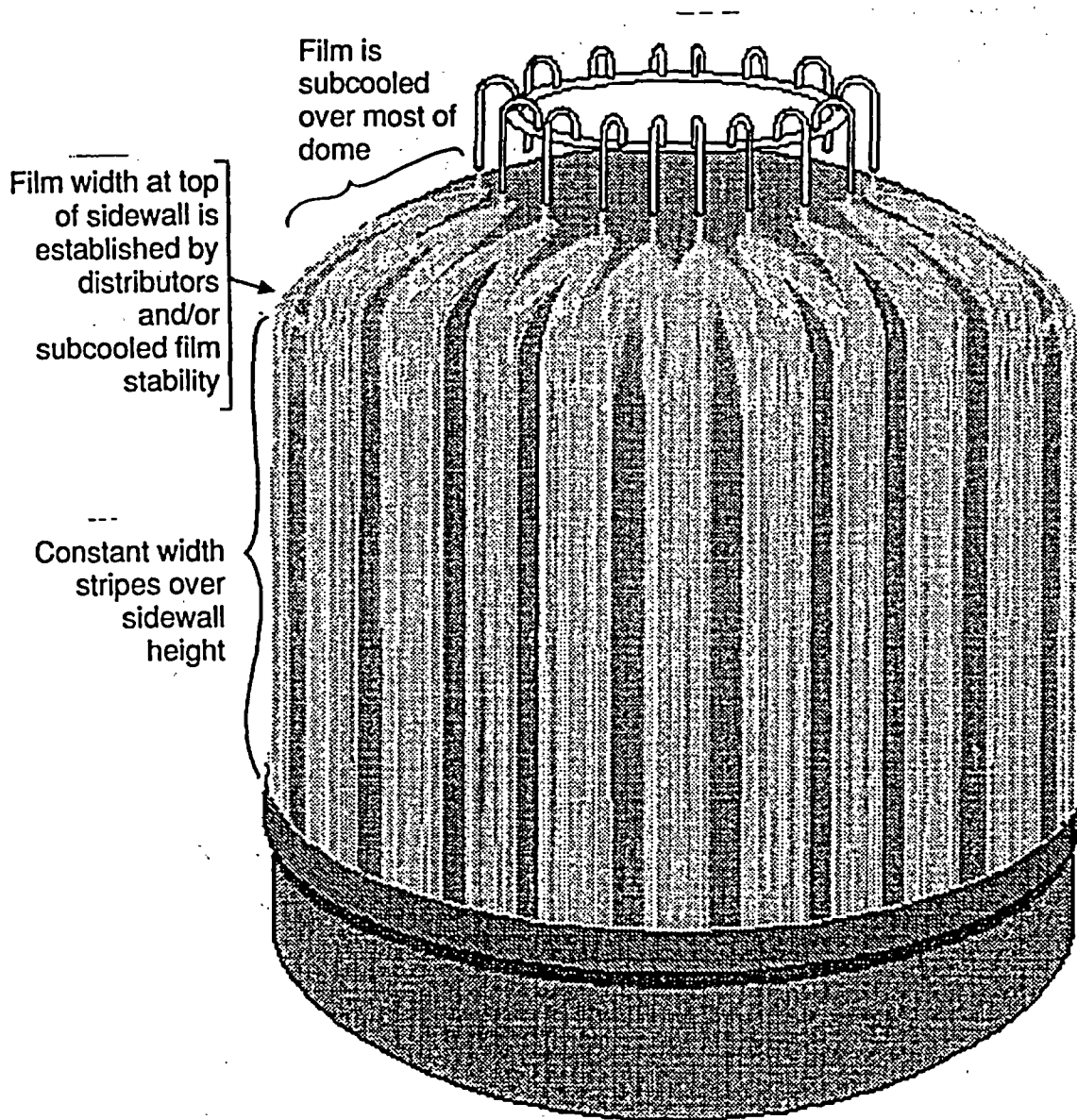


Figure 7.A-4 Large-Scale Test Water Coverage Pattern at High PCS Flows

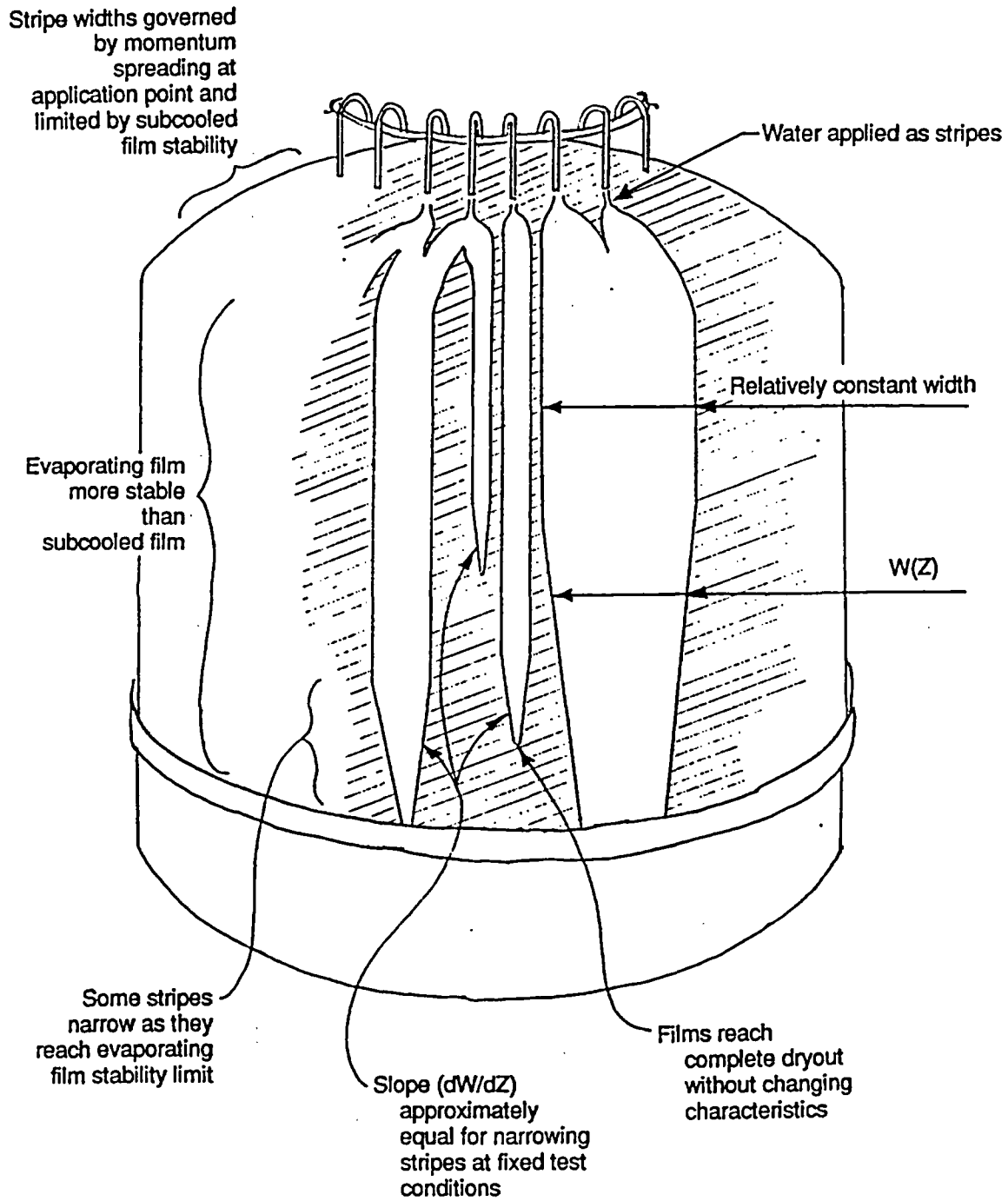


Figure 7.A-5 Sketch of LST Observation of Vessel Exterior at Water Flows Similar to LST 213.1 Showing Complete Dryout of Some Stripes

The slope of the changing width as a function of height, dW/dZ , was carefully observed. Qualitative observation indicated that the dW/dZ of each stripe around the circumference was nearly constant at a specific quasi-steady-state test condition.

Of most interest in these tests, relative to water coverage, is the fact that stripes that evaporated completely did so without changing their characteristics near the point of complete dryout. Thus, for the surface tested, the liquid films did not snap, or draw up, into a thick film. The edges of the film, including the bottom edge remained as wavy laminar film up to within a fraction of an inch from the edge, including the lower edge. As the water flow rate was valved down, the bottom edge moved gradually up, and when the flow was increased to its original value, the vertical extent of the stripe returned to a consistent elevation. Therefore, the film was well behaved as it completely evaporated.

7.A.5 CONCLUSIONS

A comparison of coated surface data with polished surface data from the literature shows the coated surface is more wettable.

Models from the literature are not sufficiently developed to be considered reliable. The literature provides an indication of the appropriate parameters to study film breakdown data: Re_{film} or Γ and heat flux. A practical approach taken to bound the data from the various tests is to establish a minimum stable film flow rate, Γ , that can be used to define a minimum coverage.

History effects are washed out by waves, so breakdown can be considered to be a local phenomenon. Therefore, LST (Section 7.6.3), SST (Section 7.6.2), and heated flat plate tests (Section 7.6.1) can be said to represent the bottom portions of liquid film stripes on the containment shell that dry out due to evaporation.

Observations of tests are explained based on physics of liquid films on heated surfaces. At high enough applied flows, the applied stripe maintains constant width until the film stability limit is reached, governed by the receding contact angle, then the stripe begins to narrow consistent with the minimum film flow rate required to maintain a stable film.

Observations of tests show that complete dryout occurs while maintaining a stable stripe geometry, gradually decreasing in width until it disappears.

7.A.6 REFERENCES

- 7.A.1 WCAP-14326, Revision 2, "Experimental Basis for the AP600 Containment Vessel Heat and Mass Transfer Correlations," April 1998.
- 7.A.2 W. S. Norman and V. McIntyre, "Heat Transfer to a Liquid Film on a Vertical Surface," *Trans. Inst. Chem. Engrs.* Vol. 38, pp 301-307 (1960).
- 7.A-3 V. A. Hallett, "Surface Phenomena Causing Breakdown of Falling Liquid Films During Heat Transfer," *International Journal of Heat and Mass Transfer*, Vol. 9, pp 283-294 (1966).
- 7.A-4 T. Fujita and T. Ueda, "Heat Transfer to Falling Liquid Films and Film Breakdown Parts I and II," *International Journal of Heat and Mass Transfer*, Vol. 21, pp 97-108 and 109-118 (1978).
- 7.A-5 M. S. Bohn and S. H. Davis, "Thermocapillary breakdown of Falling Liquid Films at High Reynolds Numbers," *International Journal of Heat and Mass Transfer*, Vol. 36, pp 1875-1881 (1993).
- 7.A-6 S. G. Bankoff, "Dynamics and Stability of Thin Heated Liquid Films," *Transactions of the ASME—Journal of Heat Transfer*, Vol. 112, pp 538-546, (1990).
- 7.A-7 N. Zuber and F. W. Staub, "Stability of Dry Patches Forming in Liquid Films Flowing over Heated Surfaces," *International Journal of Heat and Mass Transfer*, Vol. 9, pp 897-905 (1966).
- 7.A-8 Dr. S. G. Bankoff, discussions held at Westinghouse Science and Technology Center during observations of LST, 1996.

Section 8

**Containment Pressure Sensitivity
During Blowdown**

TABLE OF CONTENTS

LIST OF FIGURES iii

8.1 INTRODUCTION 8-1

8.2 METHOD 8-1

8.3 ANALYSIS 8-2

8.4 CONCLUSIONS 8-2

LIST OF FIGURES

Figure 8-1 Comparison of Single-Node Model with EM Pressure Curve 8-3

Figure 8-2 Comparison of Response with No Heat Sinks to EM Response 8-4

8.1 INTRODUCTION

The purpose of performing the single-node WGOTHIC analysis is to show that the containment pressure during the blowdown phase (predicted using the WGOTHIC code) is essentially the same as if Standard Review Plan (SRP) methodologies were utilized for the analysis. This comparison supports the use of WGOTHIC during the analysis of the blowdown phase of the transient, since it is expected that the presence of external heat removal from the containment shell during the first 50 seconds of the transient has little impact on the pressure transient. The containment shell time constant is long, as compared to the transient time, and passive cooling system (PCS) film flow is assumed to be delayed until well after the end of blowdown.

The purpose of performing the sensitivity to heat sinks during blowdown is to confirm that volume compliance is the dominant means of mitigating pressure increase during blowdown.

8.2 METHOD

The AP600 evaluation model (EM) described in Section 4 was used for comparison in this study. The EM was converted to a single-node containment model, consistent with SRP 6.2.1 methodology and comparable to the licensed Westinghouse methodology by the following input modifications:

- All of the climes were removed.
- All of the flow paths, except for those associated with the mass and energy release forcing functions, were deleted. The mass and energy forcing functions were not changed.
- All control volumes which represent the outside containment regions were deleted.
- A single-node containment control volume, containing all of the thermal conductors from the base case and the two mass and energy release forcing functions, was created.
- A conductor representing the containment shell was added to the single-node containment control volume.
- The Uchida heat transfer correlation with revaporization was used on the shell and conductors.

The EM was modified to eliminate heat removal from the containment gas volume by internal heat sinks and the steel shell. The only modification to the EM was to delete all thermal conductors within containment and to effectively eliminate the clime conductors for the shell itself by assuming an adiabatic inner surface.

8.3 ANALYSIS

The blowdown phase pressure results for the single-node analysis are compared to the EM containment pressure in Figure 8-1.

The blowdown phase pressure response without heat sinks is compared to the EM results in Figure 8-2.

8.4 CONCLUSIONS

The conclusion of the blowdown noding sensitivity is that the single-node model (utilizing SRP 6.2.1 methodologies) essentially provides the same results during the blowdown phase as the EM.

The conclusion of the sensitivity to eliminating heat sinks during blowdown shows a relative pressure increase at the end of blowdown of only 3.6 psi relative to the EM. This compares to the EM pressure increase of about 33 psi during the blowdown phase, which confirms the dominant pressure mitigation during blowdown is energy storage due to pressure increase of the volume, or volume compliance.

Single Node Model Versus Evaluation Model

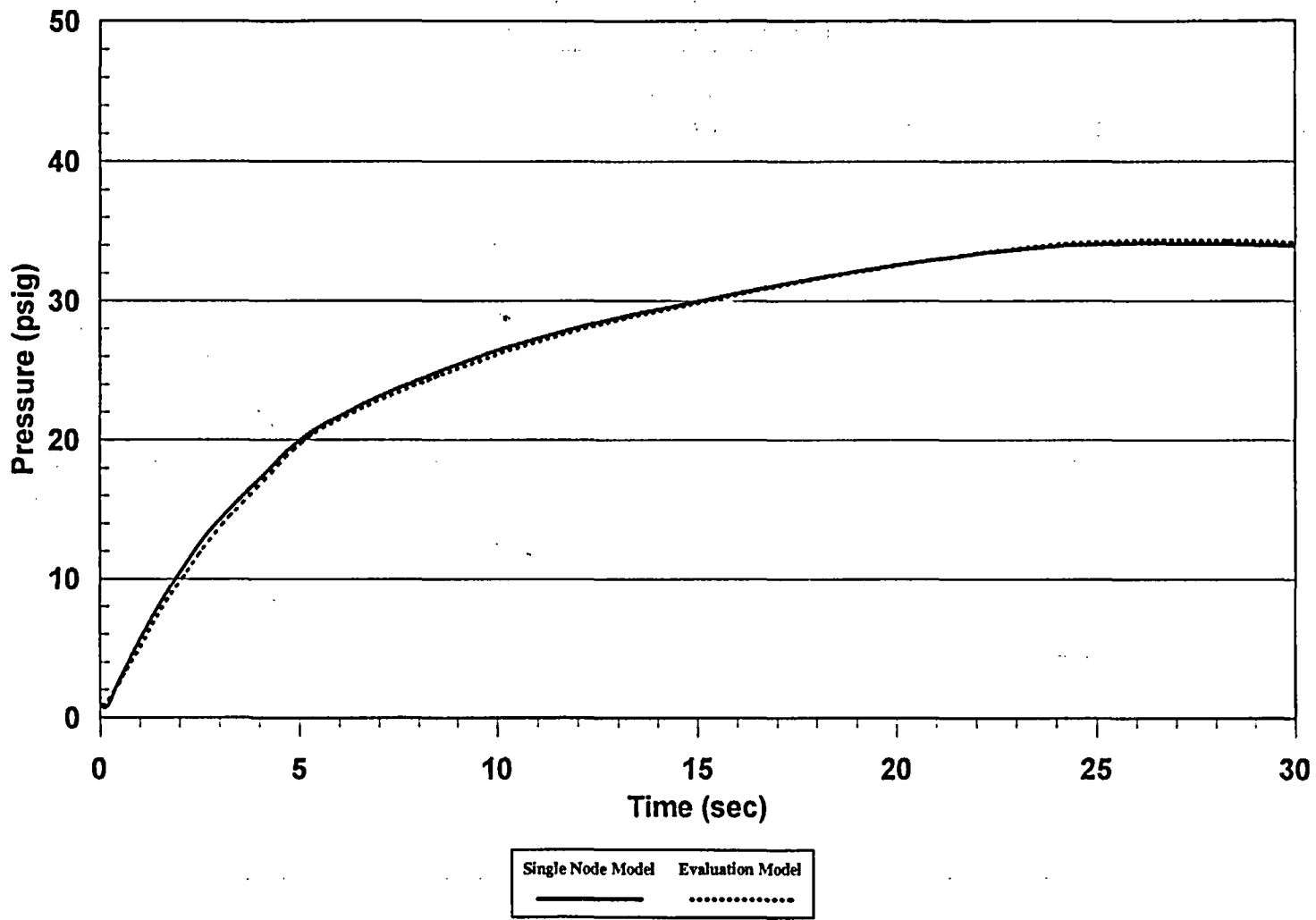


Figure 8-1 Comparison of Single-Node Model with EM Pressure Curve

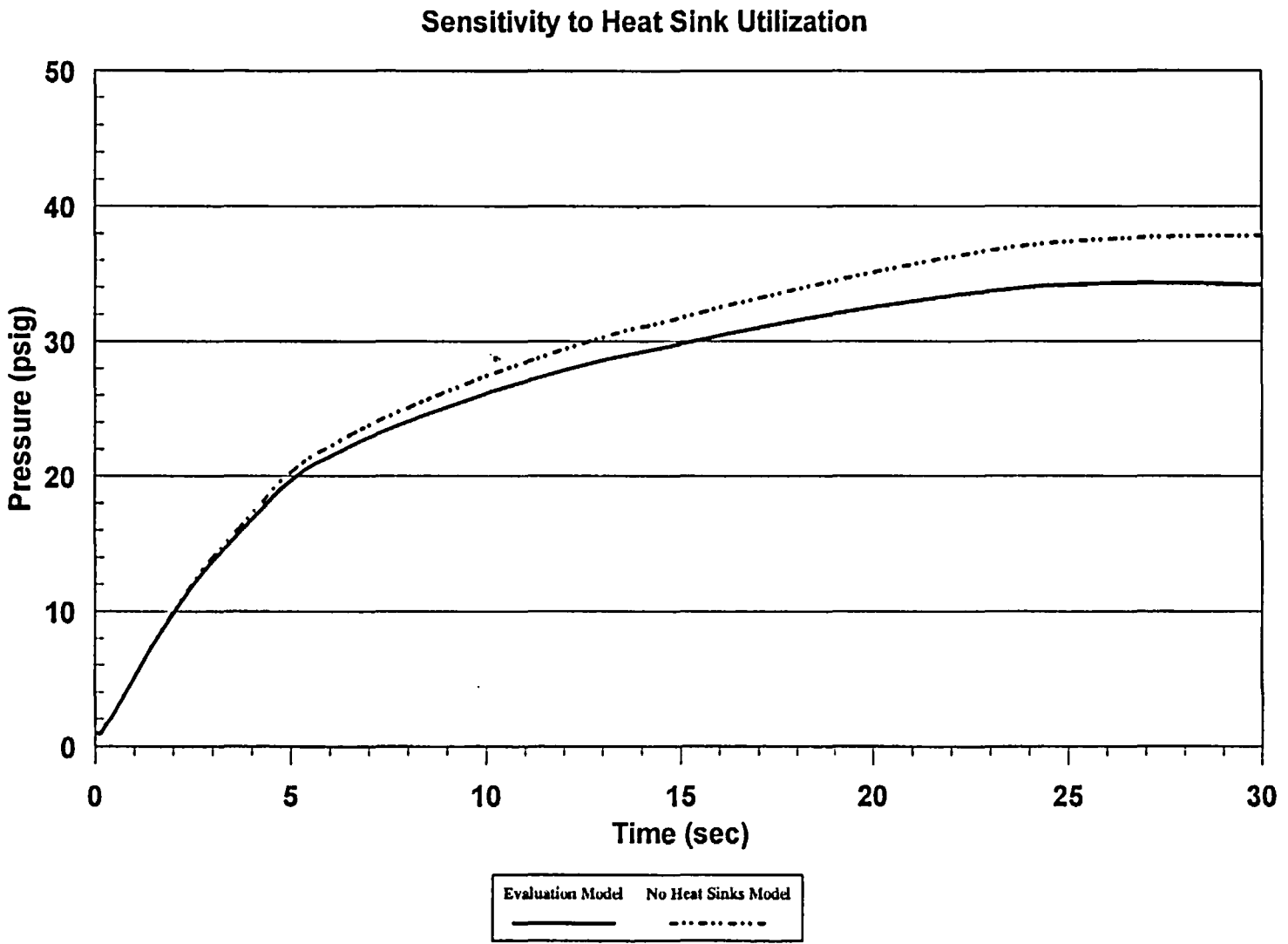


Figure 8-2 Comparison of Response with No Heat Sinks to ENI Response

Section 9

Circulation and Stratification Within Containment

TABLE OF CONTENTS

LIST OF TABLES iv
LIST OF FIGURES v

9 CIRCULATION AND STRATIFICATION WITHIN CONTAINMENT 9-1

9.1 INTRODUCTION 9-4
9.1.1 Definitions 9-14
9.1.2 Lumped Parameter Biases and Capabilities 9-14

9.2 LARGE-SCALE TEST RESULTS 9-17
9.2.1 LOCA Configuration 9-18
9.2.2 MSLB Configuration 9-19
9.2.3 Method to Address Distortions in LST Stratification Data 9-20
9.2.4 Application of Modeling Methods Developed
for NUPEC M-4-3 Lumped Parameter Model 9-22

9.3 CIRCULATION AND STRATIFICATION ASSESSMENT FOR THE
LOSS-OF-COOLANT ACCIDENT 9-26
9.3.1 LOCA Break Scenarios 9-27
9.3.2 WGOOTHIC Containment Evaluation Model for LOCA 9-34

9.4 MAIN STEAMLINE BREAK (MSLB) 9-44
9.4.1 Break Locations 9-44
9.4.2 WGOOTHIC Containment Evaluation Model for MSLB 9-45
9.4.3 MSLB Sensitivity Results 9-46

9.5 CONCLUSIONS 9-48

9.6 REFERENCES 9-50

APPENDIX 9.A THERMAL AND CIRCULATION EFFECTS OF DROPS
DURING A LOCA 9.A-1

APPENDIX 9.B EFFECTS OF STRATIFICATION ON HEAT SINK
UTILIZATION 9.B-1

APPENDIX 9.C ADDITIONAL INFORMATION ON CONTAINMENT
CIRCULATION AND STRATIFICATION 9.C-1

TABLE OF CONTENTS (Cont.)

APPENDIX 9.D **BASIS FOR ASSUMING HOMOGENEOUS BULK
CONDITIONS FOR AP600 AND AP1000
CONTAINMENT PRESSURE DESIGN BASIS ANALYSIS 9.D-1**

LIST OF TABLES

Table 9-1 **Circulation and Stratification Evaluation Summary 9-5**

Table 9-2 **AP600 Flow Areas Connecting to North and South CMT Compartments
(excluding Dead-Ended Compartment Connections) 9-24**

LIST OF FIGURES

Figure 9-1 Measured Steam Concentrations for LST 9-52

Figure 9-2 LST with Diffuser Under Steam Generator - Steam Flow
0.11-0.17 lb/sec - Internal Fluid Temperature - Group 1 9-53

Figure 9-3 LST with Diffuser Under Steam Generator - Steam Flow
0.11-0.17 lb/sec - Saturation Temperature - Group 1 9-54

Figure 9-4 LST with Diffuser Under Steam Generator - Steam Flow
0.11-0.17 lb/sec - Internal Steam Pressure Ratio - Group 1 9-55

Figure 9-5 LST with Diffuser Under Steam Generator - Steam Flow
0.11-0.17 lb/sec - Internal Fluid Temperature - Group 2 9-56

Figure 9-6 LST with Diffuser Under Steam Generator - Steam Flow
0.11-0.17 lb/sec - Saturation Temperature - Group 2 9-57

Figure 9-7 LST with Diffuser Under Steam Generator - Steam Flow
0.11-0.17 lb/sec - Internal Steam Pressure Ratio - Group 2 9-58

Figure 9-8 LST with Diffuser Under Steam Generator - Steam Flow
0.27-0.36 lb/sec - Internal Fluid Temperature 9-59

Figure 9-9 LST with Diffuser Under Steam Generator - Steam Flow
0.27-0.36 lb/sec - Saturation Temperature 9-60

Figure 9-10 LST with Diffuser Under Steam Generator - Steam Flow
0.27-0.36 lb/sec - Internal Steam Pressure Ratio 9-61

Figure 9-11 LST with Diffuser Under Steam Generator - Steam Flow
0.49-0.62 lb/sec - Internal Fluid Temperature - Group 1 9-62

Figure 9-12 LST with Diffuser Under Steam Generator - Steam Flow
0.49-0.26 lb/sec - Saturation Temperature - Group 1 9-63

Figure 9-13 LST with Diffuser Under Steam Generator - Steam Flow
0.49-0.62 lb/sec - Internal Steam Pressure Ratio - Group 1 9-64

Figure 9-14 LST with Diffuser Under Steam Generator - Steam Flow
0.49-0.62 lb/sec - Internal Fluid Temperature - Group 2 9-65

Figure 9-15 LST with Diffuser Under Steam Generator - Steam Flow
0.49-0.62 lb/sec - Saturation Temperature - Group 2 9-66

Figure 9-16 LST with Diffuser Under Steam Generator - Steam Flow
0.49-0.62 lb/sec - Internal Steam Pressure Ratio - Group 2 9-67

LIST OF FIGURES (Cont.)

Figure 9-17 LST with Diffuser Under Steam Generator - Steam Flow
0.76-0.84 lb/sec - Internal Fluid Temperature 9-68

Figure 9-18 LST with Diffuser Under Steam Generator - Steam Flow
0.76-0.84 lb/sec - Saturation Temperature 9-69

Figure 9-19 LST with Diffuser Under Steam Generator - Steam Flow
0.76-0.84 lb/sec - Internal Steam Pressure Ratio 9-70

Figure 9-20 LST with Diffuser Under Steam Generator - Steam Flow
1.10-1.20 lb/sec - Internal Fluid Temperature 9-71

Figure 9-21 LST with Diffuser Under Steam Generator - Steam Flow
1.10-1.20 lb/sec - Saturation Temperature 9-72

Figure 9-22 LST with Diffuser Under Steam Generator - Steam Flow
1.10-1.20 lb/sec - Internal Steam Pressure Ratio 9-73

Figure 9-23 LST with Diffuser Under Steam Generator - Steam Flow
1.54-1.68 lb/sec - Internal Fluid Temperature 9-74

Figure 9-24 LST with Diffuser Under Steam Generator - Steam Flow
1.54-1.68 lb/sec - Saturation Temperature 9-75

Figure 9-25 LST with Diffuser Under Steam Generator - Steam Flow
1.54-1.68 lb/sec - Internal Steam Pressure Ratio 9-76

Figure 9-26 LST with Diffuser Up 6 Feet - Steam Flow 0.76 &
1.68 lb/sec - Internal Fluid Temperature 9-77

Figure 9-27 LST with Diffuser Up 6 Feet - Steam Flow 0.76 &
1.68 lb/sec - Saturation Temperature 9-78

Figure 9-28 LST with Diffuser Up 6 Feet - Steam Flow 0.76 &
1.68 lb/sec - Internal Steam Pressure Ratio 9-79

Figure 9-29 LST with Steam Injection: 3 Inch Pipe - Steam Flow
0.76 - 0.95 lb/sec - Internal Fluid Temperature 9-80

Figure 9-30 LST with Steam Injection: 3 Inch Pipe - Steam Flow
0.76 - 0.95 lb/sec - Saturation Temperature 9-81

Figure 9-31 LST with Steam Injection: 3 Inch Pipe - Steam Flow
0.76 - 0.95 lb/sec - Internal Steam Pressure Ratio 9-82

LIST OF FIGURES (Cont.)

Figure 9-32 LST with Steam Injection: 3 Inch Pipe - Steam Flow
1.25 - 1.31 lb/sec - Internal Fluid Temperature 9-83

Figure 9-33 LST with Steam Injection: 3 Inch Pipe - Steam Flow
1.25 - 1.31 lb/sec - Saturation Temperature 9-84

Figure 9-34 LST with Steam Injection: 3 Inch Pipe - Steam Flow
1.25 - 1.31 lb/sec - Internal Steam Pressure Ratio 9-85

Figure 9-35 CMT Compartment Layout 9-86

Figure 9-36 Simplified AP600 Containment Diagram 9-87

Figure 9-37 WGOTHIC Calculated LOCA Blowdown Steam Pressure Ratio for
Jet Momentum Dissipated in SG East Compartment 9-88

Figure 9-38 WGOTHIC Calculated AP600 Containment Pressure - Sensitivity to Loss
Coefficients for LOCA Jet Momentum Dissipated in SG East Compartment 9-89

Figure 9-39 WGOTHIC Calculated Flow Pattern - Sensitivity to Loss Coefficients
for LOCA Jet Momentum Dissipated in SG East Compartment at
20 Seconds 9-90

Figure 9-40 WGOTHIC Calculated Flow Pattern - Sensitivity to Loss Coefficients for
LOCA Jet Momentum Dissipated in SG East Comp. at 1000 Seconds 9-91

Figure 9-41 WGOTHIC Calculated Flow Pattern - Sensitivity to Loss Coefficients for
LOCA Jet Momentum Dissipated in SG East Comp. at 1550 Seconds 9-92

Figure 9-42 WGOTHIC Calculated Flow Pattern - Sensitivity to Loss Coefficients for
LOCA Jet Momentum Dissipated in SG East Comp. at 80050 Seconds 9-93

Figure 9-43 WGOTHIC Calculated AP600 Containment Heat Removal Rates - LOCA
Jet Momentum Dissipated in SG East Compartment 9-94

Figure 9-44 WGOTHIC Calculated AP600 Containment Steam Pressure Ratio for
LOCA Jet Momentum Dissipated in SG East Compartment 9-95

Figure 9-45 WGOTHIC Calculated AP600 Cont. Pressure - Sensitivity to Heat Transfer
Coefficient for Study of Undissipated Jet Effects During a LOCA 9-96

Figure 9-46 WGOTHIC Calculated AP600 Containment Pressure-LOCA Jet
Momentum Dissipated in SG East Compartment 9-97

LIST OF FIGURES (Cont.)

Figure 9-46A WGOTHIC Calculated AP600 Containment Below-Deck Compartment Pressure for LOCA Jet Momentum Dissipated in SG East Compartment 9-98

Figure 9-47 WGOTHIC Calculated Flow Pattern - LOCA Jet Momentum Dissipated in SG East Compartment at 20 Seconds 9-99

Figure 9-48 WGOTHIC Calculated Flow Pattern - LOCA Jet Momentum Dissipated in SG East Compartment at 1000 Seconds 9-100

Figure 9-49 WGOTHIC Calculated Flow Pattern - LOCA Jet Momentum Dissipated in SG East Compartment at 1500 Seconds 9-101

Figure 9-50 WGOTHIC Calculated Flow Pattern - LOCA Jet Momentum Dissipated in SG East Compartment at 8000 Seconds 9-102

Figure 9-51 Details of WGOTHIC Flow Paths to Above-Deck Region from CMT, Refueling Canal, and IRWST 9-103

Figure 9-52 WGOTHIC Calculated AP600 Containment Pressure - LOCA Plume Rising into CMT Room 9-104

Figure 9-53 WGOTHIC Calculated Flow Pattern - LOCA Plume Rising into CMT Room at 1000 Seconds 9-105

Figure 9-54 WGOTHIC Calculated Flow Pattern - LOCA Plume Rising into CMT Room at 1400 Seconds 9-106

Figure 9-55 WGOTHIC Calculated AP600 Containment Heat Removal Rates - LOCA Plume Rising into CMT Room 9-107

Figure 9-56 WGOTHIC Calculated AP600 Containment Pressure - LOCA Plume Rising into CMT Room and SG Compartments 9-108

Figure 9-57 WGOTHIC Calculated Flow Pattern - LOCA Plume Rising into CMT Room and SG Compartments at 1000 Seconds 9-109

Figure 9-58 WGOTHIC Calculated Flow Pattern - LOCA Plume Rising into CMT Room and SG Compartments at 1500 Seconds 9-110

Figure 9-59 WGOTHIC Calculated AP600 Containment Heat Removal Rates - LOCA Plume Rising into CMT Room and SG Compartments 9-111

Figure 9-60 WGOTHIC Calculated AP600 Containment Steam Pressure Ratio for MSLB Above-Deck 9-112

LIST OF FIGURES (Cont.)

Figure 9-61 WGOTHIC Calculated AP600 Containment Pressure - MSLB
Above Operating Deck 9-113

Figure 9-62 WGOTHIC Calculated AP600 Containment Pressure - MSLB
in CMT Room 9-114